New Perspectives on Surface Passivation: Understanding the Si–Al_2O_3 Interface

Lachlan E. Black

April 2015

A thesis submitted for the degree of Doctor of Philosophy
of The Australian National University

For my parents

The French chemists have given a new name to this pure earth; alumine in French, and alumina in Latin. I confess I do not like this alumina.

— Joseph Black
LECTURES ON THE ELEMENTS OF CHEMISTRY

Declaration

The work in this thesis is my own except where otherwise stated.

Lachlan E. Black

Acknowledgements

Many people must be thanked for helping to bring this thesis to fruition, and helping me to survive it!

I have been extremely fortunate to have had a succession of outstanding mentors who have helped to guide and shape me through my early research career. Firstly, I must thank Dr Keith McIntosh, my primary supervisor for the last four odd years and previously for my undergraduate thesis. I owe an enormous debt to Keith for originally stimulating my interest in photovoltaics research, and for doing so much to foster my abilities. Keith's principled approach to scientific writing and research has been a huge influence on me, and his unfailing enthusiasm and encouragement have been a constant source of motivation. Our discussions were always a pleasure to partake in, and almost invariably produced fresh insights.

Another large debt is owed to Professor Andrés Cuevas, who stepped in to assume a significant supervisory role in my PhD following Keith's departure from ANU. Andrés' infectious enthusiasm and good humour, coupled with his immense knowledge of the field, have been a great source of support. His readiness to challenge conventional misconceptions is a particular source of inspiration.

Another early mentor who must be acknowledged is Dr Frank Lenzmann, who supervised me during my stay as an intern at ECN, prior to commencing my PhD. Frank allowed me a great deal of initiative in pursuing research objectives, giving me the space to spread my wings, and influenced my attitude to both life and research through his own example. His passionate commitment to renewable energy is an inspiration.

This project could not have been undertaken without the expert support of Ken Provancha, Jeff Simpson, and all the team at Schmid Thermal Systems (formerly SierraTherm), in connection with the design, installation, operation, and maintenance of the prototype atmospheric pressure chemical vapour deposition (APCVD) Al_2O_3 deposition system at ANU. Ken in particular devoted countless hours to the design and testing of the system, and his invaluable advice helped keep things running through thick and thin.

In the same vein, James Cotsell, perhaps the handiest man I know, provided invaluable technical support, and shared the many hours spent maintaining and trouble-shooting the APCVD system. James' willing enthusiasm and relentless optimism were a great asset. Bruce Condon provided able assistance with all matters electrical, particularly with several technical aspects of the C–V measurement system.

A major mention must go to Thomas Allen who contributed invaluable practical assistance with a number of experiments. This work would be significantly poorer without his many hours spent preparing samples and profiling diffusions.

Many other colleagues gave freely of their time and expertise. I have benefited from discussions with and practical assistance from Simeon Baker-Finch, James Bullock, Andreas Fell, Nicholas Grant, Anthony Hill, Teng Kho, Wensheng Liang, Daniel Macdonald, Fiacre Rougieux, Pheng Phang, Andrew Thomson, Yimao Wan, Klaus Weber, Di Yan, and Xinyu Zhang, among others.

I have been fortunate to have had more than one opportunity to collaborate with colleagues at other research groups during the course of my PhD. In particular I would like to acknowledge Boris Veith at the Institut für Solarenergieforschung Hameln (ISFH), and Emanuele Cornagliotti at the Interuniversity Microelectronics Centre (IMEC) for their fruitful collaboration. Numerous other friends and colleagues at IMEC helped to make my stay there a highly enjoyable and profitable one.

I have made many friends during the course of my PhD, both at ANU and beyond. My fellow PhD students shared the ups and downs, and helped to keep me sane. I would particularly like to acknowledge Arnold McKinley and Chog Barugkin, with whom I shared many good times. More generally, I would like to acknowledge the many members of the solar research community at ANU, who made it such a rich and enjoyable place to work for four years. I have been privileged to be able to spend my time in such fine company. Our lunchtime conversations were often profound, and always entertaining.

Special thanks go to my girlfriend Melde for her patience and support, especially during the final months of writing, when it looked like I'd never get there, and for helping to spur me on towards the finish line.

Finally I must thank my parents, to whom I owe a debt greater than I can ever repay, for their constant love and support throughout my life.

Abstract

High-efficiency crystalline silicon solar cells must suppress recombination at their *p*-type surfaces. Thin-film, amorphous aluminium oxide (Al_2O_3) has been shown to provide very effective passivation of such surfaces, assisted by its negative fixed charge. However, many details of Al_2O_3 passivation remain poorly understood. Furthermore, conventional means of depositing passivating Al_2O_3 are too slow or too expensive to be suitable for high-volume commercial production.

This thesis addresses these issues in three ways: 1) by contributing to a deeper understanding of semiconductor–dielectric interfaces and semiconductor surface recombination mechanisms in general, 2) by investigating the properties of Al_2O_3 as a passivating dielectric for silicon surfaces, and 3) by demonstrating the viability of APCVD as a high-throughput, industrially compatible deposition method for Al_2O_3, enabling its application to commercial solar cells.

Using Al_2O_3 as a test case, it is shown how a novel analysis of the extended conductance method can be used to i) distinguish the separate contributions to the interface state distribution at a semiconductor-dielectric interface, and ii) determine their capture cross-sections for both minority and majority carriers. Furthermore, the direct link between these measured interface state properties and the recombination rate at the semiconductor surface is experimentally demonstrated by showing that the former can be used to accurately predict the latter.

Investigations of the surface passivation properties of Al_2O_3 reveal a remarkably consistent picture. It is shown that the properties of the Si–Al_2O_3 interface states are essentially independent of the Al_2O_3 deposition conditions and technique. The interface properties are found to be independent of the surface dopant concentration at boron- and phosphorus-doped surfaces, while recombination is shown to be only weakly dependent on surface orientation and morphology as a result of the remarkable orientation-independence of the Si–Al_2O_3 interface state properties. Meanwhile, the chemical origin of the charge at the Si–Al_2O_3 interface is elucidated by correlating FTIR and electrical measurements.

APCVD is clearly shown—for the first time—to be capable of depositing Al_2O_3 films with exceptional surface passivation properties, comparable to the best results achieved using other deposition techniques. In the best case, interface state densities as low as $5 \times 10^{10}\,\mathrm{eV^{-1}\,cm^{-2}}$ at midgap, and negative fixed charge concentrations of $3.3 \times 10^{12}\,\mathrm{cm^{-2}}$ are measured, resulting in a saturation current density of $7\,\mathrm{fA\,cm^{-2}}$ on undiffused p-type surfaces. The APCVD films are shown to be thermally stable under standard solar cell processing conditions and are demonstrated in large-area solar cells with peak efficiencies of 21.3 %. These results demonstrate the viability of APCVD Al_2O_3 as a surface passivation layer for industrial silicon solar cells.

Contents

List of Abbreviations

AC	Alternating current
ALD	Atomic layer deposition
ANU	Australian National University
APCVD	Atmospheric pressure chemical vapour deposition
ATI	Aluminium tri-isopropoxide
ATSB	Aluminium-tri-(*sec*-butoxide)
C–V	Capacitance–voltage
CVD	Chemical vapour deposition
Cz	Czochralski
DLTS	Deep level transient spectroscopy
DMAI	Dimethylaluminium isopropoxide
DRM	Depletion region modulation
ECV	Electrochemical capacitance–voltage
EOT	Equivalent oxide thickness–voltage
ESR	Electron spin resonance
FTIR	Fourier transform infrared spectroscopy
FZ	Float-zone
IMEC	Interuniversity Microelectronics Centre
ISFH	Institut für Solarenergieforschung Hameln
MOCVD	Metal-organic chemical vapour deposition
MIS	Metal–insulator–semiconductor
NMR	Nuclear magnetic resonance
PECVD	Plasma-enhanced chemical vapour deposition
PCD	Photoconductance decay
PL	Photoluminescence
RCA	Radio Corporation of America
RTA	Rapid thermal annealing
SRH	Shockley–Read–Hall

PV	Photovoltaic
QSS-PL	Quasi-steady-state photoluminescence
TEA	Triethylaluminium
TEDA-TSB	Triethyldialuminium-tri-(*sec*-butoxide)
TMA	Trimethylaluminium
TMAH	Tetramethylammonium hydroxide

List of Symbols

A	Area
C	Capacitance
C_D	Depletion layer capacitance
C_{hf}	High frequency capacitance
C_I	Inversion layer capacitance
C_i	Insulator capacitance
C_{it}	Interface state capacitance
C_{lf}	Low frequency capacitance
C_m	Measured capacitance
C_{mp}	Measured parallel capacitance
C_{ms}	Measured series capacitance
C_p	Parallel capacitance
$\langle C_p \rangle$	Corrected parallel capacitance
C_s	Semiconductor capacitance
c_n	Electron capture coefficient
c_p	Hole capture coefficient
D_{it}	Interface state density
$D_{it,midgap}$	Midgap interface state density
$D_{it,peak}$	Peak density of interface state distribution
D_p	Diffusion coefficient for holes
E	Energy
E_c	Energy of conduction band edge
E_F	Fermi energy
E_{Fn}	Quasi Fermi energy for electrons
E_{Fp}	Quasi Fermi energy for holes
E_g	Bandgap energy
E_i	Intrinsic Fermi energy
E_t	Defect state energy

E_v	Energy of valence band edge
FF	Fill factor
f	Frequency
f_t	Interface state Fermi occupation function
G_{eff}	Effective Gummel number
G_{mp}	Measured parallel conductance
G_p	Parallel conductance
$\langle G_p \rangle$	Corrected parallel conductance
I_d	Displacement current
I_s	Static current
J_0	Saturation current density
J_{0s}	Surface saturation current density
J_{sc}	Short circuit current density
k	Extinction coefficient
L	Series inductance
N_A	Acceptor dopant concentration
N_b	Bulk dopant concentration
N_c	Effective density of states in the conduction band
N_D	Donor dopant concentration
N_{dop}	Dopant concentration
N_{it}	Interface state density per area
N_s	Surface dopant concentration
N_v	Effective density of states in the valence band
n	Refractive index
n	Free electron concentration
n_0	Equilibrium electron concentration
n_1	SRH electron emission term
n_d	Electron concentration at the edge of the quasi-neutral region
n_i	Intrinsic carrier concentration
n_{ie}	Effective intrinsic carrier concentration
n_s	Surface electron concentration
$P(\psi_s)$	Probability density function for surface potential
p	Hole concentration
p_0	Equilibrium hole concentration
p_1	SRH hole emission term
p_d	Hole concentration at the edge of the quasi-neutral region
p_s	Surface hole concentration

Q_f	Insulator fixed charge density
Q_g	Gate charge density
Q_{it}	Interface state charge density
$Q_{it,FB}$	Interface state charge density at flatbands
Q_s	Semiconductor charge density
Q_{tot}	Total density of insulator and interface state charge
$Q_{tot,FB}$	Total density of insulator and interface state charge at flatbands
q	Fundamental charge
R_{ms}	Measured series resistance
R_{ns}	Electron capture resistance
R_{ps}	Hole capture resistance
R_s	Series resistance
R_{sheet}	Sheet resistance
SD	Standard deviation of interface state distribution
S_{eff}	Effective surface recombination velocity
S_{n0}	Fundamental surface recombination velocity of electrons
S_{p0}	Fundamental surface recombination velocity of holes
T	Temperature
T_{dep}	Deposition temperature
t	Time
t_i	Insulator thickness
U_s	Surface recombination rate
$U_{s,total}$	Total surface recombination rate
U_{SRH}	Bulk Shockley–Read–Hall recombination rate
U_{total}	Total recombination rate
V_{fb}	Flatband voltage
V_g	Gate voltage
V_{g0}	Gate voltage for zero interface state density
V_{oc}	Open circuit voltage
iV_{oc}	Implied open circuit voltage
v_{th}	Thermal velocity
W	Wafer thickness
W_{ms}	Metal-semiconductor work-function difference
w_D	Depletion region width
x_c	Location of insulator charge centroid
x_j	Junction depth
Δn	Average excess carrier concentration

Δn_d	Excess carrier concentration at the edge of the quasi-neutral region
ϵ_0	Vacuum permittivity
ϵ_i	Insulator permittivity
ϵ_r	Relative permittivity
ϵ_s	Semiconductor permittivity
η	Energy conversion efficiency
$\rho(x)$	Net charge density
σ_n	Electron capture cross-section
σ_p	Hole capture cross-section
σ_s	Standard deviation of surface potential
τ_{eff}	Effective excess carrier lifetime
τ_{int}	Intrinsic bulk carrier lifetime
τ_s	Surface carrier lifetime
τ_{SRH}	Bulk Shockley–Read–Hall carrier lifetime
$\phi(x)$	Semiconductor potential
ϕ_b	Semiconductor bulk potential
ϕ_m	Metal work function
ϕ_s	Semiconductor work function
ψ_s	Semiconductor surface potential relative to the bulk
$\bar{\psi}_s$	Mean semiconductor surface potential
ω	Angular frequency

Chapter 1

Introduction

> *I would like to start by emphasizing the importance of surfaces. It is at a surface where many of our most interesting and useful phenomena occur. We live for example on the surface of a planet. It is at a surface where the catalysis of chemical reactions occur. It is essentially at a surface of a plant that sunlight is converted to a sugar. In electronics, most if not all active circuit elements involve non-equilibrium phenomena occurring at surfaces. Much of biology is concerned with reactions at a surface.*
>
> — Walter H. Brattain
> SURFACE PROPERTIES OF SEMICONDUCTORS

The surface of a semiconductor is a site of great importance to the operation of devices based on this class of materials. The abrupt structural and material discontinuity represented by the surface results in the presence of numerous structural imperfections, or defects, which greatly facilitate charge-carrier recombination. The presence of such surface recombination is highly detrimental to the performance of many semiconductor devices, and in particular of photovoltaic devices (solar cells). Fig. 1.1 shows efficiency vs recombination at the rear surface for a typical high-efficiency commercial solar cell design, illustrating how increasing recombination significantly reduces cell efficiency. The effective suppression of surface recombination, referred to as surface "passivation" is thus essential to the realisation of high-efficiency photovoltaic devices.

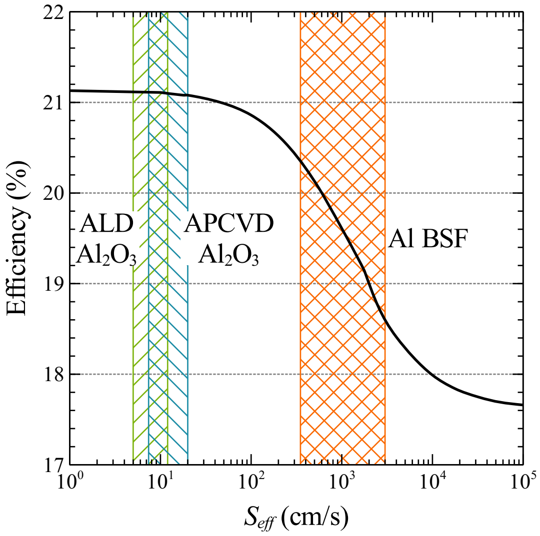

Figure 1.1: Energy conversion efficiency of a typical high-efficiency Czochralski (Cz)-Si solar cell (1 Ω cm p-type base, 160 µm thick, bulk lifetime of 300 µs, negligible front surface recombination) calculated using the device simulation software PC1D as a function of the rear surface recombination velocity S_{eff}. Representative ranges of S_{eff} on a 1 Ω cm p-type surface for atomic layer deposition (ALD) and atmospheric pressure chemical vapour deposition (APCVD) Al_2O_3 and for a conventional Al-alloyed "back surface field" (BSF) [1]–[7] are shown (literature values are adjusted to the relevant substrate dopant concentration according to Equation (2.35)).

1.1 Characterisation of surface passivation

While the basic principles and relationships underlying surface recombination are well understood, it is difficult to apply these principles in practice because of insufficient knowledge concerning the properties of actual semiconductor–dielectric interfaces. This is fundamentally due to the fact that the semiconductor–dielectric interface is characterised by a high degree of complexity, resulting from its disordered state. Multiple potential defect configurations exist, and these give rise to electronic states (interface states) with widely varying properties, modified in each individual case by local variations in bonding and chemical environment. Measured properties represent an integration of the individual interface state responses, smeared out by local variation in surface carrier concentrations. The task of disentangling the properties of each state from the gross signals accessible to experiment is therefore a highly challenging one.

Significant progress has nevertheless been made over decades of intensive work, particularly on the interface between silicon and thermal silicon dioxide (SiO_2). The overall energetic distribution of the interface states, and their apparent capture cross-sections, which describe their recombination effectiveness, have been measured for Si–SiO_2 interfaces prepared in a wide variety of ways [8], and to a lesser extent for other material systems. In a few cases, it has even been possible to assign particular sub-components of the interface state distribution to certain physical defects via the use of techniques such as electron spin resonance (ESR) in conjunction with electrical measurements [9]. Substantial efforts have also been made to understand the role of the interface in surface recombination, particularly for photovoltaic applications [10]–[12].

Despite this, significant gaps in understanding remain. Even for the Si–SiO_2 interface, the properties of the interface states are only partially understood. In almost all cases capture cross-sections have been measured only over limited and non-overlapping energy ranges for each type of carrier, due to limitations of the approximate analysis standardly employed [8]. In addition, capture cross-sections reported by different authors, and by the same authors for differently prepared samples, vary over orders of magnitude [10]. This points to an underlying complexity of the interface which must be resolved to permit a full understanding. There has also been little or no consideration of how the apparent capture cross-sections measured by experiment relate to those of the individual interface states present.

Consequently, unknown capture cross-sections must frequently be guessed at or extrapolated from other measurements, and the use of modelling to relate interface properties to surface recombination generally requires the use of multiple free variables. The state of understanding is worse for dielectric layers other than SiO_2, and semiconductors other than silicon, which have received less attention. This incomplete knowledge has led to numerous misunderstandings, and a resulting incapacity to fully understand the role of the interface in solar cells.

This thesis improves the current understanding of semiconductor–dielectric interfaces by showing how application of the extended conductance method to determine both majority and minority carrier capture cross-sections over a wider energy range, combined with a novel analysis based on an appreciation of the distinction between real and apparent capture cross-sections, allows a more complete determination of the interface state properties, and even permits the contributions of individual species of states to be distinguished. Furthermore, it is shown that the resulting knowledge of the interface properties allows these properties to be related directly to measured recombination via physical theory, without the use of free variables. This generally applicable methodology will be demonstrated here for the Si–Al_2O_3 interface as an exemplary test case that is highly relevant to photovoltaic devices.

1.2 Al_2O_3 as a passivating dielectric

Thin film, amorphous Al_2O_3 possesses some remarkable properties that make it well-suited to passivating silicon surfaces in photovoltaic devices. It is a wide-bandgap material, with little or no absorption in the visible range. It may be deposited by various methods at moderate temperatures, well below those required for thermal oxidation. It is capable of forming a high quality interface with silicon, with a low density of interface states. Most distinctively, it possesses a large, stable negative charge that makes it ideally suited to passivate highly and lowly doped *p*-type silicon surfaces.

It is this ability to effectively passivate *p*-type surfaces that has generated so much recent interest in Al_2O_3 for photovoltaic applications. Conventional silicon nitride (SiN_x) passivation layers are not well-suited to this role, because their positive charge makes them susceptible to parasitic shunting on undiffused *p*-type surfaces [13], and induces depletion at diffused *p*-type surfaces that significantly increases surface recombination [14]. Al_2O_3 thus has applications both as a replacement for the Al-alloyed "back surface field" at the rear of conventional *p*-type silicon cells (which, as shown in Fig. 1.1, increasingly limits efficiency), and as an enabling passivation layer for the boron-diffused $p+$ region in new high-efficiency cells based on *n*-type material, with its desirable material properties [15].

The first investigation of thin film Al_2O_3 as a material for electronic device applications was reported by Aboaf [16] in 1967. The Al_2O_3 in question was deposited by an APCVD process using aluminium tri-isopropoxide (ATI) as a chemical precursor. It was reported that unlike SiO_2, which was well known to increase the *n*-type character of a surface (i.e. induce a negative surface charge due to its positive fixed charge), Al_2O_3 applied to Si or Ge surfaces could, for certain deposition conditions, have the opposite effect, producing a strongly *p*-type surface regardless of the substrate type. This was the first evidence of Al_2O_3's large negative fixed charge.

While this negative charge was considered useful for some electronic device applications, interest in Al_2O_3 as a possible replacement for SiO_2 was stimulated mainly by its higher dielectric constant, effectiveness as a diffusion barrier for ionic

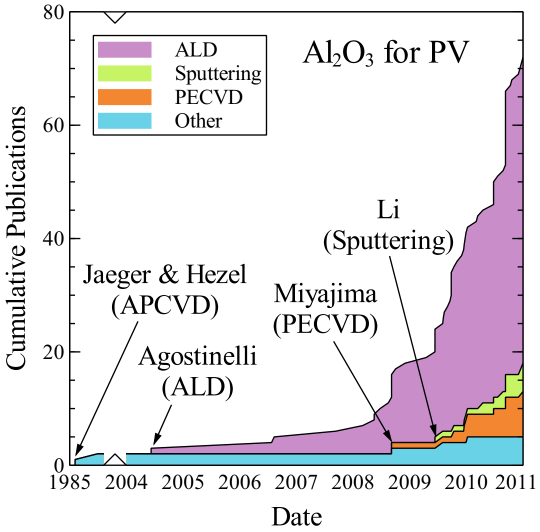

Figure 1.2: Cumulative count of scientific publications relating primarily to Al_2O_3 for surface passivation of photovoltaic devices, divided by the deposition method employed, up to the beginning of 2011. Publications in which multiple deposition methods are investigated are counted more than once.

impurities, better radiation resistance, and the possibility of low temperature deposition by various methods [17]–[21]. Subsequent investigations of the Si–Al_2O_3 interface revealed a high-quality interface, with a low density of interface states [17], [20], [22].

The first investigation of Al_2O_3 as a passivation layer for photovoltaic applications was reported by Jaeger and Hezel [23], [24] in the late 1980s. Deposition was again performed by APCVD with ATI as precursor, following Aboaf [16]. The results were promising, but were not followed up at the time, as attention shifted to SiN_x from plasma-enhanced chemical vapour deposition (PECVD), which was better suited to passivating the phosphorus-diffused front-side of conventional p-type cells. Interest revived in the mid 2000s as the need for a passivation material for p-type surfaces became apparent, with reports by Agostinelli *et al.* [25], [26] and Hoex *et al.* [27] highlighting the excellent passivation achievable using Al_2O_3 from ALD. Subsequent years saw an explosion of studies on Al_2O_3 for photovoltaic applications, as illustrated in Fig. 1.2.

As a result, many features of Al_2O_3 as a passivation layer are now much better understood. A review of work up to that point was provided by Dingemans and Kessels [28] in 2012. Al_2O_3 has been shown to provide excellent passivation both of p- and n-type undiffused surfaces [25]–[27], and of p-type diffused surfaces [29], while passivation of *n*-type diffused surfaces is significantly poorer [30]. Indeed, the quality of surface passivation achievable with Al_2O_3 on some surfaces is such that it has recently necessitated a reassessment of the intrinsic limits to carrier lifetime in silicon [31]. Various deposition methods have been shown to be capable of depositing high quality Al_2O_3 passivation layers, including both chemical and physical vapour deposition techniques [23]–[27], [32]–[38].

Interface state densities are typically in the range of 10^{11}–$10^{12}\,\mathrm{eV^{-1}\,cm^{-2}}$ at midgap [32], [33], [35], [39]–[53], while exceptional films may have interface state densities below $10^{11}\,\mathrm{eV^{-1}\,cm^{-2}}$ [24], [42], [44], [49]. Measurements of the interface state capture cross-sections have also been performed [47], [48], [54]. Concentrations of negative fixed charge as high as $10^{13}\,\mathrm{cm^{-2}}$ have been reported [26], [55], but more typically are found in the range of 1–$5 \times 10^{12}\,\mathrm{cm^{-2}}$ [24], [26], [32]–[35], [37], [42], [43], [45]–[47], [49]–[54], [56], [57], depending on the deposition method and post-deposition heat treatments. Various evidence suggests the charge is located within a very short distance of the Si–Al_2O_3 interface [43], [58]–[60]. Some thermal step at temperatures above ~400 °C is generally required to "activate" the passivation of films deposited at lower temperatures [33], [41], [61]–[64].

On the practical side, significant work has been devoted to examining the thermal stability of Al_2O_3 passivation, due to the need for compatibility with the high-temperature step in standard screen-printed metallization [45], [46], [53], [57], [65]–[74]. It has also been shown that excellent passivation performance may be retained even for very thin Al_2O_3 layers of 1 nm or less, at least when Al_2O_3 forms part of a larger dielectric stack [62], [75]. In addition Al_2O_3 passivation layers have been demonstrated successfully in a number of high-efficiency device structures [46], [69], [71], [76]–[81].

However, despite this recent work, significant gaps in knowledge and understanding remain. Incomplete knowledge of the interface state properties prevents a comprehensive understanding of the recombination mechanisms, and hinders the application of device modelling to solar cells featuring Al_2O_3 passivation. This deficiency is remedied in Chapter 4, where the properties of the dominant recombination-active state are determined by the extended conductance method, while the use of these properties to predict surface recombination under various conditions is demonstrated particularly in Chapters 4 and 7.

Evidence from various techniques suggests that a thin (on the order of several monolayers [43]) SiO_x interlayer is commonly present between the Si substrate and the bulk Al_2O_3 film [27], [28], [43], [58], [82]–[85]. It has been speculated by a number of authors that this is the reason for the excellent chemical passivation provided by Al_2O_3 [41], [55], and that the Si–Al_2O_3 interface is thus essentially similar to that of thermal SiO_2 [28], [47], [54], [86]. The results of Chapter 8 show that this assumption is unwarranted, and that the interface properties are quite distinct from those of SiO_2.

Although Al_2O_3 has been shown to provide excellent passivation of p-type diffused surfaces, little attempt has been made to understand the influence of the surface dopant concentration on surface recombination and (potentially) on the interface properties themselves. Behaviour on n-type surfaces is even less well understood, with the reason for the injection dependence of surface recombination observed at undiffused n-type surfaces remaining the subject of debate. Chapter 7 addresses these questions, showing that the interface properties are independent of the dopant concentration, and that two-dimensional transport-mediated recombination may account for the latter effect.

Similarly, the influence of surface orientation and morphology on Al_2O_3 interface properties and passivation performance has received little systematic attention, despite being known to be important for other dielectrics. In Chapter 8 it is shown that not only is recombination at the Si–Al_2O_3 interface only weakly dependent on these properties, but also more remarkably that the interface state properties are entirely independent of surface orientation.

Finally, while the concentration of fixed charge is known, its chemical origins remain unresolved, which limits the ability to understand its variation with processing conditions. On the basis of correlated FTIR and capacitance–voltage (C–V) measurements, Chapter 9 provides strong evidence for tetrahedrally coordinated AlO_4 in the near-interfacial region as the origin of the charge.

1.3 Industrial application of Al_2O_3

Much recent work on Al_2O_3 for surface passivation has utilised ALD, either thermal or plasma-assisted, as a deposition method, with trimethylaluminium (TMA) as the chemical precursor. However, for industrial applications in photovoltaics, conventional ALD is generally regarded as too slow to be economically viable [28], [87]. Consequently, significant attention in recent years has focussed on alternative high-throughput deposition methods for Al_2O_3.

Naturally, various attempts to adapt the proven ALD process for such applications have been made (all based on the thermal variant of this technique). These include large-scale batch ALD, and two separate approaches to spatial

ALD, where the reaction half-cycles are separated in space rather than in time [71], [88]–[91]. PECVD, already used for $\mathrm{SiN_x}$ deposition, and hence familiar to the photovoltaic industry, has also received significant attention [34]–[36]. Reactive sputtering, which saw some use in very early work on $\mathrm{Al_2O_3}$, is a dark horse, being significantly different in principle to the other methods, and hence having unique advantages and drawbacks [37], [38]. $\mathrm{Al_2O_3}$ films deposited by all of these methods have been shown to be capable of providing excellent passivation in recent years. Various other deposition techniques, including sol-gel [92]–[94] and screen-printed pastes [95], [96], have also been investigated, though so far with less impressive results.

Given such interest in low-cost, high-throughput deposition techniques for $\mathrm{Al_2O_3}$, surprisingly little attention has been paid to what would seem an obvious candidate, namely APCVD. This technique possesses a number of inherent advantages which make it particularly suited for such a role. Deposition occurs at atmospheric pressure under ambient conditions, using simple thermal activation at moderate temperatures. Therefore, no load-lock system, vacuum pump, or plasma is required. Deposition is continuous, rather than self-limiting, allowing in-line operation with only a single deposition zone. A wider range of precursors can be used than for ALD, many at lower cost than TMA. The use of non-pyrophoric (non-explosive) precursors in particular significantly reduces costs associated with shipping, storage, and handling of such chemicals. All of these factors contribute to a low cost of ownership for APCVD $\mathrm{Al_2O_3}$.

APCVD was used both in the earliest work on $\mathrm{Al_2O_3}$ for electronic applications, by Aboaf [16], and in the first work to apply the material to photovoltaic applications, that of Jaeger and Hezel [23], [24]. As noted previously, the results of the latter work, though not followed up at the time, were quite encouraging. Hezel and Jaeger [24] reported a low midgap interface defect density of $8 \times 10^{10}\,\mathrm{eV^{-1}\,cm^{-2}}$ and a large fixed charge of $-3.2 \times 10^{12}\,\mathrm{cm^{-2}}$. They also measured a surface generation velocity S_0 of $210\,\mathrm{cm\,s^{-1}}$ by the pulsed metal–insulator–semiconductor (MIS) capacitor method.

The latter result has usually been misunderstood and hence misrepresented in the more recent literature, where the S_0 value reported by [24] has been conflated with the more familiar S_{eff} [25], [35], [37]. The latter includes the effect of charge-assisted passivation, while the former does not, being measured under conditions of free-carrier depletion. By misleadingly reporting the S_0 value measured by [24] as though it were an S_{eff}, this result, and by association the quality of APCVD $\mathrm{Al_2O_3}$ passivation in general, have been made to appear significantly worse in comparison with those of other techniques.

In this thesis the suitability of APCVD as a deposition method for surface-passivating Al_2O_3 is investigated. Two different chemical presursors are examined, each offering clear advantages over currently widely-used TMA due to non-pyrophoricity and lower cost. It will be demonstrated that in fact APCVD is capable of depositing Al_2O_3 layers with excellent passivation performance, with interface state density, charge concentration, and surface recombination rate comparable to the best values achieved by other deposition techniques. This passivation performance is shown to lead to an efficiency of 21.3 % in initial experiments incorporating such films into large-area solar cells. APCVD is therefore demonstrated to be an excellent candidate for low-cost deposition of Al_2O_3 passivation layers for photovoltaic applications.

1.4 Outline of this work

Thus, this thesis extends the ability to characterise semiconductor–dielectric interfaces, applies that extension to characterise the Si–Al_2O_3 interface, and shows that APCVD is a viable deposition method for surface-passivating Al_2O_3. Its structure is divided as follows. Chapter 2 reviews the physical theory relevant to surface recombination, while Chapter 3 describes the Al_2O_3 deposition method and the experimental techniques employed in sample preparation and characterisation. The first experimental results are presented in Chapter 4, with an exploration of the electrical properties of the Si–Al_2O_3 interface. Chapter 5 discusses the influence of deposition parameters on passivation performance of APCVD Al_2O_3, and establishes a baseline deposition process. Chapter 6 investigates the thermal stability of the surface passivation properties with respect to both a conventional fast-firing process and a rapid thermal anneal (RTA). Chapter 7 examines the influence of the surface dopant concentration on recombination for both p- and n-type surfaces, while Chapter 8 investigates the influence of surface orientation and texturing. Chapter 9 explores the relationship between the Al_2O_3 bulk properties and those of the interface. Finally, Chapter 10 summarises the major conclusions and presents the first results for solar cells passivated by the APCVD Al_2O_3 films developed in this work.

Chapter 2

Surface Recombination Theory

> *If it is true that every theory must be based upon observed facts, it is equally true that facts cannot be observed without the guidance of some theory. Without such guidance, our facts would be desultory and fruitless; we could not retain them: for the most part we could not even perceive them.*
>
> — Isidore Auguste Marie François Xavier Comte
> THE POSITIVE PHILOSOPHY

In order to provide a theoretical background for subsequent experimental chapters, we begin in this chapter with a review of the physical theory relevant to semiconductor surface recombination. We start with a discussion of the mechanisms of surface recombination and passivation, and review the conceptual picture of the semiconductor–dielectric interface. We proceed to the definition of the relevant energies and potentials, before describing the calculation of the surface carrier concentrations in the presence of charge-induced band-bending. We then introduce the equations describing recombination at the semiconductor surface, and discuss some simplifying cases. Finally we describe how the experimental parameters commonly used to characterise surface recombination relate to the physical properties of the interface.

Familiarity with basic semiconductor physics is assumed, as necessarily only brief and partial coverage of such topics is provided here. Many excellent texts on this subject exist (see for example [8], [97]–[99]). For a more extensive discussion of surface recombination theory (albeit covering somewhat different ground) see the work of Aberle [100].

2.1 The semiconductor surface

At the surface of a semiconductor, the atomic lattice is abruptly interrupted. Surface atoms lack neighbours to bind to, and are left with unsatisfied “dangling” bonds (unpaired outer-shell electrons). These dangling bonds introduce electronic energy levels inside the normally forbidden semiconductor bandgap, referred to as surface or interface states.[1] Such states greatly enhance electron–hole recombination at the surface by acting as stepping stones for charge carrier transitions between the conduction and valence bands.

The reduction of surface recombination is referred to as surface passivation. Since each recombination event at the surface requires, in addition to an interface state, precisely one electron and one hole, the two fundamental approaches to passivation are

1. to reduce the number of interface states, or
2. to reduce the concentration of one or other carrier at the surface.

The first of these approaches, usually referred to as “chemical” passivation, is generally accomplished by the formation of a thin layer of a wide-bandgap material on the semiconductor surface, such that most previously dangling bonds are chemically bound to atoms within this layer. The material in question may be a dielectric (e.g. SiO_2, SiN_x, Al_2O_3), or it may be another semiconductor, or even the same semiconductor in a different structural form (e.g. amorphous Si on a crystalline Si surface). Additional dangling bonds may often be passivated by hydrogen atoms, either sourced from within the passivating layer itself or externally via a hydrogen anneal. By this means, interface state density may be reduced to extremely low levels[2], though not entirely eliminated.

The second approach, of reducing the concentration of one type of carrier at the surface, may be accomplished in several different ways. Firstly, the surface concentration of one carrier may be reduced by the application of a field to the surface that repels that type of carrier. This field may be the result of an externally applied bias in a MIS structure, or of inbuilt stable charges within a passivating dielectric layer or stack. Passivation effected in this way may be referred to as “field-effect” or “charge-assisted” passivation.

---

[1] In the case of a bare surface the interface in question is between the semiconductor and the surrounding ambient.

[2] Concentrations as low as a few $10^9\,\mathrm{eV^{-1}\,cm^{-2}}$ have been reported for Si–SiO_2 [101], compared to surface bond densities on the order of $10^{14}\,\mathrm{cm^{-2}}$.

Alternatively, such a reduction of the surface carrier concentration may be achieved by the formation of a heavily doped region at the semiconductor surface, which suppresses the concentration of one carrier type due to the change in chemical potential. Such a doped region may be formed by the introduction of dopant atoms (most commonly B, P, and Al in silicon) via thermal diffusion, ion implantation, or alloying. The most well-known example of this effect is the so-called "back-surface field"[3], or high–low junction, commonly formed by alloying of Al at the rear of conventional *p*-type silicon solar cells during the high-temperature contact firing step.

Finally, the concentration of minority carriers at the surface may be suppressed by reducing the minority carrier mobility in the near-surface region of the semiconductor, such that the surface concentration becomes transport-limited. This mechanism is significant, for example, in heavily doped diffused regions, where it operates in conjunction with the doping mechanism described above to reduce the minority carrier concentration at the surface.

The two basic approaches to surface passivation described above are not mutually exclusive, and indeed are typically employed in combination to minimise surface recombination in actual devices. For example, conventional *p*-type silicon solar cells feature a phosphorus-diffused $n+$ region on their front surface, which apart from performing a charge-separation role, also acts to suppress the surface hole concentration. Outside of the contacted regions, this surface is also passivated by a dielectric layer (PECVD $\mathrm{SiN_x}$), which both reduces the interface state concentration and contains positive fixed charges which induce further charge-assisted passivation. It is the recombination at such semiconductor–dielectric interfaces that we shall be concerned with here.

The use of dielectric surface passivation was first reported by Atalla *et al.* [103] in 1959, who discovered that the formation of a thermally grown $\mathrm{SiO_2}$ layer greatly reduced the concentration of electronic states at the silicon surface. An enormous amount of work on understanding the electrical properties of silicon–dielectric interfaces, especially that of $\mathrm{SiO_2}$, was performed during the following decades, primarily motivated by applications in microelectronics. This work resulted in the emergence of a well-established conceptual picture of such interfaces, along with a standard nomenclature describing them.

Important general results of this work are that:

---

[3] Although widespread in use, this term is a significant historical misnomer, as clearly explained by [102]. In reality the passivation effect involved has little to do with any field.

- Defects at the disordered semiconductor–dielectric interface, unlike those in the well-ordered crystalline bulk, give rise to an energetic continuum of states distributed throughout the bandgap, due to the influence of small variations in the chemical environment of each defect, and the existence of multiple species of states.

- Such states may be donor- or acceptor-like (the former are positively charged when empty, and neutral when occupied by an electron, while the latter are neutral when empty and negatively charged when occupied).

- For typical concentrations, these states are non-interacting (because their spatial separation makes electron transitions extremely unlikely).[4]

- Additional permanently charged states, known as "fixed charges", are typically present in the dielectric near the interface. These do not exchange charge with the semiconductor and are not recombination-active. However, they do contribute to charge-assisted surface passivation.

2.2 Definition of energies and potentials

Preliminary to a discussion of the equations describing recombination, it is necessary to define the terms that we will be using for the various energies and potentials involved. Fig. 2.1 shows the band diagram of a p-type silicon surface under non-equilibrium conditions, with the surface in accumulation. E_c and E_v are the energies of the conduction and valence band edges respectively, with the bandgap energy $E_g = E_c - E_v$. E_{Fn} and E_{Fp} are the energies of the quasi-Fermi-levels for electrons and holes, defined such that

$$n = N_c F_{1/2}\left(\frac{E_{Fn} - E_c}{kT}\right) , \tag{2.1}$$

$$p = N_v F_{1/2}\left(-\frac{E_{Fp} - E_v}{kT}\right) , \tag{2.2}$$

where n and p are the free electron and hole concentrations, N_c and N_v are the effective densities of states in the conduction and valence bands, k is the Boltzmann constant, and T is the temperature in Kelvin. $F_j(\eta)$ is the Fermi–Dirac

---

[4] A partial exception to this are so-called "amphoteric" defects, where a single physical defect contributes two energy levels within the semiconductor bandgap. A well-known example is the so-called $\mathrm{P_b}$ defect at the Si–$\mathrm{SiO_2}$ interface [9].

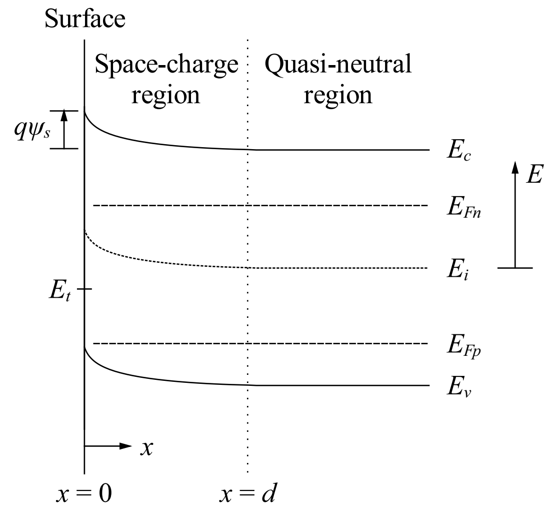

Figure 2.1: Band diagram of the (p-type) silicon surface under non-equilibrium conditions, and with non-zero surface band-bending (accumulation), showing definitions of relevant energies and potentials.

integral of the jth order, defined by

$$F_j(\eta) = \frac{1}{\Gamma(j+1)} \int_0^{\infty} \frac{\varepsilon^j}{1 + \exp(\varepsilon - \eta)}\, d\varepsilon\,, \tag{2.3}$$

which must generally be solved numerically. However, excellent analytical approximations for (2.3) are available [104], [105] and readily implemented in numerical software.

The intrinsic Fermi energy E_i is defined as the energy for which $n = p = n_i$ when $E_{Fn} = E_{Fp} = E_i$, where n_i is the intrinsic carrier concentration. For carrier concentrations much less than the relevant density of states, Equations (2.1) and (2.2) may be approximated by their nondegenerate (Boltzmann) forms:

$$n = N_c \exp\left(\frac{E_{Fn} - E_c}{kT}\right) = n_i \exp\left(\frac{E_{Fn} - E_i}{kT}\right), \text{for } n \ll N_c\,, \tag{2.4}$$

$$p = N_v \exp\left(-\frac{E_{Fp} - E_v}{kT}\right) = n_i \exp\left(-\frac{E_{Fp} - E_i}{kT}\right), \text{for } p \ll N_v\,, \tag{2.5}$$

In this work we make use of the values of E_g and N_c recommended by Green [106] for crystalline silicon. The value of N_v, which is known with less confidence [106], is calculated to be consistent with these values and with the value for n_i of Misiakos and Tsamakis [107].

2.3 Surface charge and band-bending

The presence of external net charge in an overlying dielectric layer or gate contact, or trapped in interface states, induces a compensating net charge in the semiconductor, distributed over a spatially extended region near the surface. This "space-charge region" may take the form of either an accumulation layer, inversion layer, or depletion region, depending on whether the dominant contribution to the charge comes from majority free carriers, minority free carriers, or uncompensated ionised dopant atoms respectively. It appears in the band diagram of Fig. 2.1 as a bending of the semiconductor energy bands near the surface. The extent of this band-bending is described by the surface potential ψ_s, which is positive for downward band-bending towards the surface. Further from the surface, approximate charge neutrality prevails, and the semiconductor is said to be in a quasi-neutral state. The boundary between the quasi-neutral and space-charge regions is located at a distance d from the surface.

Charge neutrality requires that the total net charge in the space-charge region, Q_s, precisely balance the total external charge Q_{tot}, such that $Q_s + Q_{tot} = 0$. Most commonly, Q_{tot} may include contributions from insulator fixed charge Q_f, interface trapped charge Q_{it}, and charge in the gate contact Q_g. The latter is absent in many photovoltaic test structures and devices, which lack a gate contact, while Q_{it} is typically negligible at well-passivated surfaces, so that Q_{tot} is dominated by Q_f.

Typically, we know Q_{tot} and hence Q_s (usually from C–V measurements), and wish to determine the surface carrier concentrations p_s and n_s. In order to determine the extent of band-bending, and hence the surface carrier concentrations, we must start from the carrier concentrations at the edge of the quasi-neutral region. In non-equilibrium, we have

$$n_d = n_{0d} + \Delta n_d \,, \tag{2.6}$$

$$p_d = p_{0d} + \Delta n_d \,, \tag{2.7}$$

where n_0 and p_0 are the equilibrium concentrations of electrons and holes respectively, and Δn is the excess carrier concentration. The subscript d indicates that these parameters are referenced to the edge of the quasi-neutral region.

n_0 and p_0 may be calculated from (2.1) and (2.2) together with the equilibrium condition ($E_{Fn} = E_{Fp}$) and the requirement of charge neutrality:

$$n_0 + N_A = p_0 + N_D \,, \tag{2.8}$$

where N_D and N_A are the active donor and acceptor concentrations respectively. For a uniformly doped sample with surface recombination that is not very large, Δn_d is simply equal to its average bulk value, Δn, which is typically known directly from experiment. In other cases, such as when a diffused surface dopant profile is present, Δn_d must first be calculated separately. In the general case, this requires a numerical solution of the coupled semiconductor equations over the surface dopant profile, taking into account local variation of the carrier mobility, recombination, and bandgap narrowing, as described by [108]–[110]. Given n_d and p_d, the corresponding values of E_{Fn} and E_{Fp} may then be calculated from (2.1) and (2.2).

Having determined E_{Fn} and E_{Fp} in the quasi-neutral region, we need an expression relating the semiconductor charge Q_s to the surface potential ψ_s. This requires a solution of Poisson's equation in one dimension. For Fermi–Dirac statistics we obtain [111]

$$\begin{aligned} Q_s = (2kT\epsilon_s)^{1/2}\Bigg\{ & N_c\left[F_{3/2}\left(\frac{E_{Fn}-E_c+q\psi_s}{kT}\right)-F_{3/2}\left(\frac{E_{Fn}-E_c}{kT}\right)\right]+ \\ & N_v\left[F_{3/2}\left(\frac{E_v-E_{Fp}-q\psi_s}{kT}\right)-F_{3/2}\left(\frac{E_v-E_{Fp}}{kT}\right)\right]+ \\ & (N_A-N_D)\left(\frac{q}{kT}\psi_s\right)\Bigg\}^{1/2}. \end{aligned} \tag{2.9}$$

Under nondegenerate conditions this may be approximated by

$$\begin{aligned} Q_s = (2kT\epsilon_s)^{1/2}\Bigg\{ & N_c\left[\exp\left(\frac{E_{Fn}-E_c+q\psi_s}{kT}\right)-\exp\left(\frac{E_{Fn}-E_c}{kT}\right)\right]+ \\ & N_v\left[\exp\left(\frac{E_v-E_{Fp}-q\psi_s}{kT}\right)-\exp\left(\frac{E_v-E_{Fp}}{kT}\right)\right]+ \\ & (N_A-N_D)\left(\frac{q}{kT}\psi_s\right)\Bigg\}^{1/2}. \end{aligned} \tag{2.10}$$

Given Q_s, Equations (2.9) or (2.10) must be solved iteratively to determine ψ_s, in the manner described by [112]. The surface carrier concentrations may then be calculated using either (2.1) and (2.2), or (2.4) and (2.5), as appropriate.

Finally, we note that Equation (2.10) is equivalent to

$$Q_s = (2kT\epsilon_s)^{1/2}\{n_s - n_d + p_s - p_d + (N_A-N_D)\left[(kT/q)^{-1}\psi_s\right]\}^{1/2}. \tag{2.11}$$

For large Q_s, the n_s and p_s terms in (2.11) dominate [113], so that at a strongly p-type surface we have

$$p_s = Q_s^2(2kT\epsilon_s)^{-1}, \tag{2.12}$$

i.e. the majority surface carrier concentration is simply proportional to Q_s^2. This useful result will be employed later to provide a simple analytical expression for surface recombination at charge-passivated surfaces.

2.4 Recombination through defect states

The net rate of excess carrier recombination arising from non-interacting single-level states in the semiconductor bandgap is described by the well-known Shockley–Read–Hall (SRH) statistics [114], [115]. For a single state located at energy E_t, the recombination rate U_{SRH} is given by

$$U_{SRH} = \frac{pn - n_i^2}{c_p^{-1}\big(n + n_1\big) + c_n^{-1}\big(p + p_1\big)} \,, \tag{2.13}$$

where c_n and c_p are the capture coefficients for electrons and holes, and n_1 and p_1 are the equilibrium electron and hole concentrations for the case where $E_{Fn} = E_{Fp} = E_t$, given by

$$n_1 = N_c F_{1/2}\left((E_t - E_c)/kT\right) \,, \tag{2.14}$$

$$p_1 = N_v F_{1/2}\left(-(E_t - E_v)/kT\right) \,. \tag{2.15}$$

These last terms account for re-emission of trapped carriers, which occurs in competition with recombination, and have the effect of reducing the recombinative effectiveness of states located close to the band edges. For states not very near the band edges, n_1 and p_1 may be approximated by their nondegenerate forms, and $F_{1/2}$ in (2.14) and (2.15) may be replaced by an exponential term.

The numerator in Equation (2.13) $(pn - n_i^2)$ describes the displacement of the carrier concentrations from thermal equilibrium, which is the driving force for net recombination or generation (the latter occurring for $pn < n_i^2$).

The capture coefficients describe the capture probability per unit time for a free electron or hole in the vicinity of the state, and may be thought of as relating to the effective cross-sectional area of the potential well formed by the defect, referred to as the capture cross-section, and designated by σ_n and σ_p for electrons and holes respectively. We may write

$$c_n = \sigma_n v_{th} \,, \tag{2.16}$$

where v_{th} is the thermal velocity of the carrier in question (an analogous equation may be written relating c_p to σ_p). As the capture coefficient is both the experimentally determined value and the value relevant to recombination, and the value of v_{th} is somewhat contentious, the concept of capture cross-sections is of limited utility, beyond providing a conceptual aid, and the choice of v_{th} is somewhat arbitrary. However, this mode of representation is widely used in the literature. Since different authors make various assumptions concerning the value of v_{th}, capture cross-section values in the literature should be compared with care.

2.5 Surface recombination

At the semiconductor surface we can write a similar equation to (2.13) for recombination through a single interface state:

$$U_s = \frac{p_s n_s - n_i^2}{c_p^{-1}\big(n_s + n_1\big) + c_n^{-1}\big(p_s + p_1\big)} \, , \tag{2.17}$$

where the subscript s denotes that these properties relate to the surface.

The total recombination rate is found by summing the contributions of the individual states. At the surface this involves an integration over energy, due to the energetic continuum of interface states. Integrating (2.17) over energy E for all interface states within the semiconductor bandgap yields

$$U_s = \int_{E_v}^{E_c} D_{it} \frac{p_s n_s - n_i^2}{c_p^{-1}\big(n_s + n_1\big) + c_n^{-1}\big(p_s + p_1\big)} \, dE \, , \tag{2.18}$$

where D_{it} is the areal density of interface states as a function of energy. Note that besides D_{it}, c_p, c_n, n_1, and p_1 are also functions of energy, though we have omitted this dependence from (2.18) for the sake of brevity.

In Equation (2.18), we have assumed that all surface states at a given energy have the same c_n and c_p. In general however, this is unlikely to be the case. Instead, multiple types of surface state (arising from distinct chemical sites) with overlapping energy distributions and distinct capture properties are likely to be present. We must then calculate $U_{s,total}$ as the sum of contributions due to each distribution:

$$U_{s,total} = \sum_{i=1}^{n} U_{s,i} \, . \tag{2.19}$$

Limiting cases

It is worthwhile to consider some limiting cases under which Equation (2.18) may be simplified. Such cases occur frequently in practice and aid considerably in exposing the functional dependencies involved.

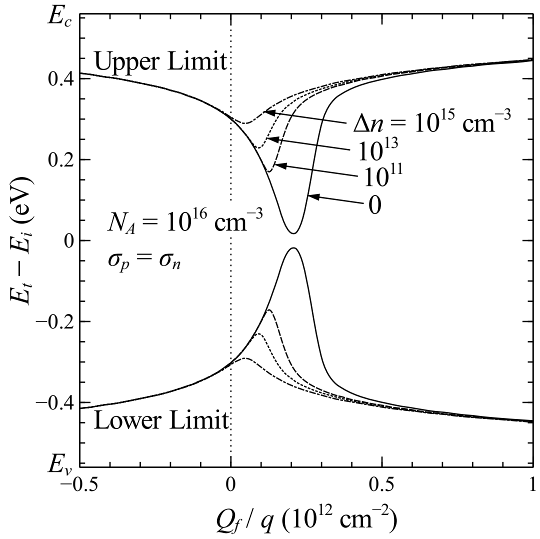

Figure 2.2: Bandgap energy range over which interface state recombination is greater than 90 % of the midgap value, as a function of insulator fixed charge Q_f and with bulk excess carrier concentration Δn as a parameter. We assume $N_A = 10^{16}\,\mathrm{cm}^{-3}$ and $\sigma_p = \sigma_n$.

The first point to note is that p_1 and n_1 may frequently be neglected for interface states not very close to the band edge, since they are insignificant compared to either p_s or n_s. This will be the case when either 1) the excess carrier concentration Δn is large, or 2) the surface is in strong accumulation or inversion, such that p_s or n_s is large, regardless of Δn.

Illustrating this case, Fig. 2.2 shows the bandgap energy range over which interface state recombination efficiency is greater than 90 % of its midgap value, as a function of surface charge and of excess carrier concentration. A bulk acceptor concentration $N_A = 10^{16}\,\mathrm{cm}^{-3}$ and equal capture cross-sections for electrons and holes are assumed (the effect of increasing dopant concentration is to stretch out the curves on the Q_f/q axis). When the surface is in depletion, the recombination efficiency of interface states not near midgap is strongly reduced due to competing re-emission of trapped carriers. However, this effect is substantially suppressed when the bulk excess carrier concentration is significant, as under illumination. In accumulation or strong inversion, emission processes are important only for states located near the band edges, regardless of bulk injection.

For the case shown in Fig. 2.2, interface states in the middle 0.7 eV or more of the bandgap contribute equally to recombination for $Q_f/q > 2.5 \times 10^{11}\,\mathrm{cm}^{-2}$ or $Q_f/q < -1 \times 10^{11}\,\mathrm{cm}^{-2}$, even at a low injection level of $\Delta n = 10^{11}\,\mathrm{cm}^{-3}$. These charge magnitudes are significantly smaller than those typically encountered at silicon–dielectric interfaces, even in the case of SiO_2, which is usually considered to possess a rather low charge. Additionally, interface states located closer to the band edges are generally found to possess rather low capture cross-sections [8], so that they are unimportant for recombination regardless of band-bending. Consequently, the neglect of p_1 and n_1 is frequently justified in determining surface recombination.

Secondly, in many cases of interest the concentration of one or other carrier will be dominant at the surface, such that recombination is limited by the rate of minority carrier capture. Taking the case of a strongly p-type surface ($c_p p_s \gg c_n n_s$), and neglecting p_1 and n_1 for the reasons described above, Equation (2.18) reduces to

$$U_s = \frac{p_s n_s - n_i^2}{p_s} \int_{E_v}^{E_c} D_{it} c_n \, dE \tag{2.20}$$

The integral in (2.20) now contains all the terms relating to the interface state properties, and no others. It therefore encapsulates the *chemical* passivation of the interface. Noting that the integral has units of velocity, we may define a fundamental surface recombination velocity of electrons S_{n0}, given by

$$S_{n0} = \int_{E_v}^{E_c} D_{it} c_n dE \, . \tag{2.21}$$

The conditions relating to Equation (2.20) will hold for all p-type surfaces and most undiffused n-type surfaces passivated by a negatively charged dielectric such as Al_2O_3. An analogous expression for U_s in terms of S_{p0} may be derived for strongly n-type surfaces.

S_{eff} and J_{0s}

Because the surface carrier concentrations p_s and n_s are generally not known, it is common to describe surface recombination in terms of an effective surface recombination velocity S_{eff}, defined with respect to the excess (non-equilibrium) carrier concentration Δn_d at the edge of the quasi-neutral region of the semiconductor,

$$S_{eff} \equiv \frac{U_s}{\Delta n_d} \, . \tag{2.22}$$

From (2.20)–(2.22), S_{eff} is related to S_{n0} via

$$S_{eff} = S_{n0} \frac{p_s n_s - n_i^2}{p_s \Delta n_d} \approx S_{n0} \frac{n_s}{\Delta n_d} \, , \tag{2.23}$$

where the latter expression applies when the surface carrier concentration is far from thermal equilibrium ($p_s n_s \gg n_i^2$). For surfaces not in inversion, i.e. where the surface minority carriers are the same as those in the near-surface quasi-neutral region, we can make the further substitution $\Delta n_d \approx n_d$. Note that it is not necessary to include bandgap narrowing in the calculation of n_s and p_s in (2.23), so long as this effect is approximately constant over the surface space-charge profile induced by Q_f.

Making the substitution $p_s n_s \approx (N_s + \Delta n_d)\Delta n_d$, (2.23) can be rewritten as

$$S_{eff} = S_{n0}\frac{(N_s + \Delta n_d)}{p_s}\,, \tag{2.24}$$

where we have assumed that the surface dopant concentration N_s is equal to that at the edge of the quasi-neutral region. Using the approximate expression for p_s provided by Equation (2.12) when Q_f is large and the carrier concentrations are nondegenerate, this becomes

$$S_{eff} = S_{n0}\frac{2kT\epsilon_s}{Q_s^2}(N_s + \Delta n_d)\,. \tag{2.25}$$

Equation (2.25) shows that S_{eff} in this case is dependent on both the dopant concentration and the injection level. This limits the usefulness of S_{eff} as a means of characterising surface recombination, as discussed by [113].

As an alternative to S_{eff}, we may instead describe surface recombination in terms of the surface saturation current density J_{0s}, defined by [113]

$$J_{0s} = qU_s\left(\frac{p_s n_s - n_i^2}{n_i^2}\right)^{-1}\,. \tag{2.26}$$

Combining (2.20), (2.21), and (2.26), we find, for a strongly p-type surface,

$$J_{0s} = qS_{n0}p_s^{-1}n_i^2\,. \tag{2.27}$$

Again using the high-charge, nondegenerate approximation for p_s given by (2.12), we obtain

$$J_{0s} = qS_{n0}\frac{2kT\epsilon_s}{Q_s^2}n_i^2\,. \tag{2.28}$$

J_{0s} thus has the merit of being independent of the dopant concentration and injection level when the conditions relating to (2.28) hold, as they do frequently in practice for undiffused surfaces passivated by Al_2O_3.

2.6 Relationship to experimental parameters

Generally, one does not measure surface recombination directly, but rather the effective excess minority carrier lifetime τ_{eff}, typically as a function of the average excess carrier concentration Δn. τ_{eff} is defined by

$$\tau_{eff} \equiv \frac{\Delta n}{U_{total}}\,, \tag{2.29}$$

where U_{total} is the total volumetric recombination rate due to all mechanisms, both in the bulk and at the surface. τ_{eff} can therefore be expressed as the parallel combination of the carrier lifetimes due these various recombination processes. We consider the case of a uniformly doped, undiffused sample. Then

$$\tau_{eff}^{-1} = \tau_{int}^{-1} + \tau_{SRH}^{-1} + \tau_{s}^{-1}\,, \tag{2.30}$$

where τ_{int} is the intrinsic bulk lifetime due to radiative and Auger recombination [31], τ_{SRH} is the extrinsic bulk lifetime due to SRH recombination through bulk defects, and τ_s is the carrier lifetime due to surface recombination. For a symmetrically passivated, undiffused wafer, τ_s is related to U_s by

$$\tau_s = \frac{W}{2}\frac{\Delta n}{U_s}\,. \tag{2.31}$$

where W is the wafer thickness, and U_s refers to the value at each surface. Equation (2.31) assumes that Δn is uniform throughout the width of the wafer, which may not hold if the generation profile is significantly nonuniform, or surface recombination is very large.

Combining Equations (2.22), (2.30), and (2.31), and using the fact that for undiffused surfaces $\Delta n_d = \Delta n$, we arrive at the following expression for S_{eff} in terms of τ_{eff}:

$$S_{eff} = \frac{W}{2}\left(\frac{1}{\tau_{eff}} - \frac{1}{\tau_{int}} - \frac{1}{\tau_{SRH}}\right) \tag{2.32}$$

S_{eff} determined from (2.32) is commonly used to characterise surface recombination at undiffused surfaces, and will be used extensively in the following chapters for this purpose. Since τ_{SRH} is generally unknown, it is usually assumed that $\tau_{SRH}^{-1} = 0$, so that the calculated S_{eff} represents an upper limit.

For diffused surfaces, it is more common to describe the recombination rate in terms of a saturation current density J_0, analogous to the surface saturation current density J_{0s}, but defined with respect to the carrier concentrations at the edge of the diffused region, and including Auger and SRH recombination in the heavily doped diffusion in addition to SRH recombination at the surface. Assuming $\Delta n \gg n_i$, we may write [116]:

$$J_0 = qn_i^2 (N_b + \Delta n)^{-1} \frac{W}{2} \left(\frac{1}{\tau_{eff}} - \frac{1}{\tau_{int}} - \frac{1}{\tau_{SRH}} \right) , \tag{2.33}$$

where N_b is the bulk dopant concentration. The use of J_0 rather than S_{eff} has the advantage that J_0 is independent of Δn at such surfaces, so long as recombination at the surface itself remains limited by minority carrier capture [116]. Equation (2.33) may be used directly to calculate J_0 from τ_{eff} for a given Δn. However, this has the disadvantage that the extracted J_0 includes τ_{SRH}, since this is generally not known independently. Instead, assuming that J_0 is independent of Δn, we may take the derivative of (2.33) with respect to Δn, leading to

$$J_0 = qn_i^2 \frac{W}{2} \frac{d}{d\Delta n} \left(\frac{1}{\tau_{eff}} - \frac{1}{\tau_{int}} - \frac{1}{\tau_{SRH}} \right) . \tag{2.34}$$

J_0 may thus be determined from the linear slope of $\tau_{eff}^{-1} - \tau_{int}^{-1}$ vs Δn [116]. This has the advantage that if the bulk is in high injection ($\Delta n \gg N_b$), τ_{SRH} is independent of Δn, so that the extracted J_0 is unaffected by error due to extrinsic bulk recombination, even if such recombination is significant. Such conditions are readily obtained using high resistivity (lightly doped) substrates.

Although usually applied to characterise recombination at diffused surfaces, J_0 determined from Equations (2.33) or (2.34) is also of use to characterise undiffused surfaces where surface recombination is dominated by minority carrier capture. For an undiffused wafer with uniform doping and injection, $p_s n_s = (N_b + \Delta n)\Delta n$, and therefore $J_0 = J_{0s}$. Thus, when the conditions relating to (2.20) apply, J_0 derived from Equations (2.33) or (2.34) provides an injection-independent means of characterising surface recombination at undiffused surfaces.

Note that the measured quantity in all cases is, in fact, J_0/n_i^2, which is also the quantity relevant to recombination, and is essentially independent of temperature. Consequently, the choice of n_i used to extract J_0 is arbitrary. We present results in terms of J_0 rather than J_0/n_i^2 only because this is the convention. It is however a trivial matter to apply a different value of n_i in order to make the J_0 values comparable with those quoted by other authors using different values of n_i. In all cases in this work we use n_i given by [107] at 300 K ($9.7 \times 10^9\,\mathrm{cm}^{-3}$).

Finally, we note that by comparison of (2.32) and (2.33), S_{eff} is related to J_0 by

$$S_{eff} = J_0 \frac{N_b + \Delta n}{qn_i^2} . \tag{2.35}$$

The methodology developed in this chapter will be employed in Chapters 4–8 to characterise surface recombination experimentally, and to relate it to the physical parameters of the Si–Al_2O_3 interface.

Chapter 3

Al_2O_3 Deposition and Characterisation

> *Toward the effecting of works, all that man can do is to put together or put asunder natural bodies. The rest is done by nature working within.*
>
> — Francis Bacon
> THE NEW ORGANION

In this chapter we describe the experimental techniques used in this work to deposit and characterise the Al_2O_3 films. Deposition of almost all Al_2O_3 films examined in this work was performed by the APCVD method, except in a few cases where Al_2O_3 was deposited by ALD. Therefore we begin in Section 3.1 with a detailed description of the APCVD deposition technique and the APCVD system used to deposit the Al_2O_3 passivation layers, including a discussion of the various options for the chemical precursor. The details of the more established ALD process are given briefly in Section 3.2, where we also describe the general procedures used for sample preparation. Finally, in Section 3.3 we describe the principal experimental techniques employed to characterise the samples.

3.1 Al_2O_3 deposition by APCVD

APCVD is a versatile process that can be used to deposit many different materials. As a chemical vapour deposition (CVD) method, deposition is based on the *chemical* reaction of one or more precursor molecules in the *vapour* phase.

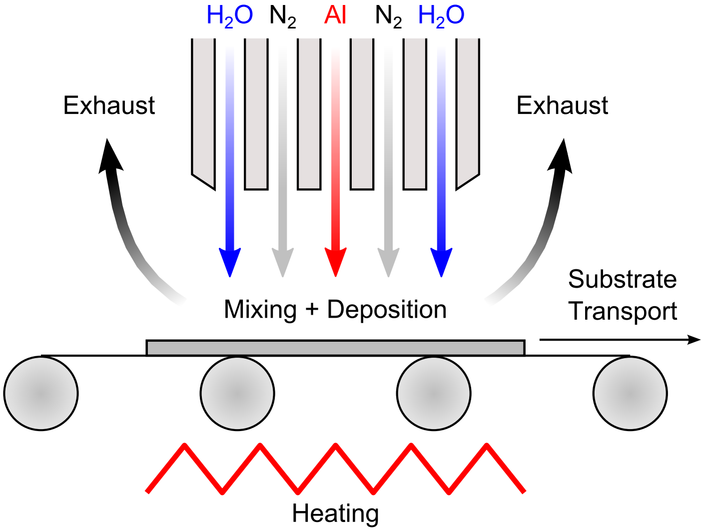

Figure 3.1: Schematic illustration of the APCVD Al_2O_3 deposition system used in this work, showing the configuration of the various input gas flows (Al precursor, H_2O or O_2 reactant, and separator N_2).

The deposition reaction occurs at the substrate surface, or nearby, and generally requires an external source of energy. For APCVD that energy is purely thermal, coming from the temperature of the substrate (PECVD, on the other hand, supplements this thermal energy with energy from an ionised plasma). Importantly, the entire process takes place at *atmospheric* pressure.

The deposition reaction may be based on one or more of several mechanisms, including pyrolysis (thermal dissociation), hydrolysis (reaction with water), oxidation, nitridation, or reduction. The reaction may involve a single, or two or more reactant species (common secondary species include H_2O, O_2, CO_2, and NH_3). The primary reactant, or precursor, is often a metal-organic molecule. In this case the process may also be referred to as metal-organic chemical vapour deposition (MOCVD).

3.1.1 Deposition system

The APCVD system used for Al_2O_3 thin film deposition in this work was an in-line APCVD reactor manufactured by Schmid Thermal Systems Inc. (formerly SierraTherm Production Furnaces Inc., Watsonville, California, USA). The system in question was a former pilot line tool previously used at the Australian National University (ANU) primarily to deposit titanium dioxide (TiO_2). It was modified by the manufacturer as a prototype system for Al_2O_3 deposition.

In this system, substrates are transported on a continuously moving conveyor belt. A multi-zone, resistive heating system is used to preheat the belt and the substrates prior to film deposition. Deposition occurs in a deposition chamber isolated by nitrogen curtains from the surrounding ambient. The precursor, and any reactants, are delivered to the substrate by separate nitrogen carrier gas flows via injector slots positioned above the substrate, and oriented laterally with respect to the direction of travel of the belt. These injector slots are precision-machined in order to provide uniform distribution of gas flows and hence a uniform deposition rate across the substrate. The use of intermediate separator nitrogen flows limits mixing of the precursor and reactant flows prior to delivery to the substrate (the latter can result in parasitic gas-phase reactions that limit deposition efficiency). Fig. 3.1 shows a schematic illustration of the deposition system.

Delivery of the liquid Al precursor is achieved via precision-metered liquid injection into a heated carrier N_2 flow. The maximum rate of delivery is limited by the vapour pressure of the precursor and the temperature of the delivery lines. Both H_2O and O_2 are available as reactants, with the former delivered by an N_2 bubbler system. Additional dilution nitrogen is used to maintain constant total gas flow rates through the reactant slots independently of the reactant flow rate.

3.1.2 Process parameters

The characteristics of the APCVD process, and the properties of the resulting Al_2O_3 films, depend fundamentally on 1) the precursor/reactant chemistry, 2) the rate of arrival of precursor and reactant molecules at the substrate surface, and 3) the temperature of the surface, where the latter two factors may be a function of time. The chemistry of the reaction may be directly controlled through the choice of precursor and reactant species (albeit constrained by the properties of available chemical species). However, the latter two factors may only be influenced indirectly through the manipulation of experimentally accessible process parameters.

For the system used in this work, these parameters are, principally, the precursor and reactant flow rates, the set-point temperature profile, and the belt speed. The relationship between these experimentally accessible parameters and the fundamental characteristics of the deposition process is somewhat complex. For example, the rate of arrival of precursor and reactant molecules at the substrate surface depends not only on the input flow rates, but on the gas flow dynamics in the deposition chamber, as well as the extent of parasitic gas-phase reactions, which in turn depend on the gas temperature and precursor/reactant chemistry. Similarly, the substrate temperature depends not only on the set-point temperature profile and the belt speed, but also on the flow rate and temperature of gases in the deposition zone.

The influence of these process parameters on the properties of the resulting Al_2O_3 films will be explored in the following chapters, particularly in Chapter 5.

3.1.3 Chemical precursors

A wide variety of chemical species can be used as precursors for Al_2O_3 deposition by CVD techniques. The general requirements are that they must contain Al, be deliverable in the vapour phase, and be able to react at a substrate surface under accessible conditions of pressure and temperature. These compounds may be broadly divided into a number of categories and sub-categories, depending on the structure and composition of the chemical groups (ligands) bonded to the Al atom or atoms. Most broadly there is a division between inorganic and metal-organic precursors, the former including the halides (e.g. $AlCl_3$) and hydrides (the Al hydride AlH_3 is not used for CVD, but the silicon hydride SiH_4 is). Within the category of metal-organic compounds, a division can be made between alkyl (e.g. $Al(CH_3)_3$), alkoxide (e.g. $Al(OC_2H_5)_3$), and mixed alkyl-alkoxide compounds (e.g. dimethylaluminium isopropoxide (DMAI)), as well as more complex structures such as the β-diketonates (e.g. aluminium acetylacetonate ($Al(acac)_3$)).

This wide variation of precursor composition and structure leads to a wide range of physical and chemical properties. Important properties for CVD applications include the phase state at room temperature, the boiling point or vapour pressure, and whether or not the material is pyrophoric (explosively reactive in air). Most Al precursors are moisture-sensitive, some violently so, such that handling must be performed in a dry atmosphere. Table 3.1 summarizes key properties of selected Al precursors, while Fig. 3.2 presents vapour pressure data taken from the literature. Fig. 3.3 shows price data for various precursors.

Most research and development work to date on CVD and ALD of Al_2O_3 for surface passivation has utilised TMA as the aluminium precursor. This material has been favoured primarily because of its high vapour pressure, a requirement for use in ALD. However, it has the disadvantage of being pyrophoric, which greatly complicates handling and safety. Also, it is relatively expensive even in lower purity (so-called “solar grade”) form, such that its cost as a consumable would be a significant portion of the cost of ownership of an Al_2O_3 deposition

Table 3.1: Properties of selected Al chemical precursors.

Common Abbreviation	Abbreviated Chemical Formula	Molecular Weight ($\mathrm{g\,mol^{-1}}$ of Al)	State at RT	Pyrophoric?	O:Al Ratio	Melting Point (°C)	Boiling Point at 5 Torr (°C)
$AlCl_3$	$AlCl_3$	133.34	Solid	No	0	190	115.7
TMA	$AlMe_3$	72.09	Liquid	Yes	0	15.2	15.2 (7 Torr)
DMAI	$AlMe_2(O^iPr)$	116.14	Liquid	No	1		54.2
TEDA-TSB	$Al_2Et_3(O^sBu)_3$	180.25	Liquid	No	1.5		~142
ATI	$Al(O^iPr)_3$	204.25	Solid	No	3	118.5	141.1
ATSB	$Al(O^sBu)_3$	246.33	Liquid	No	3		166.8

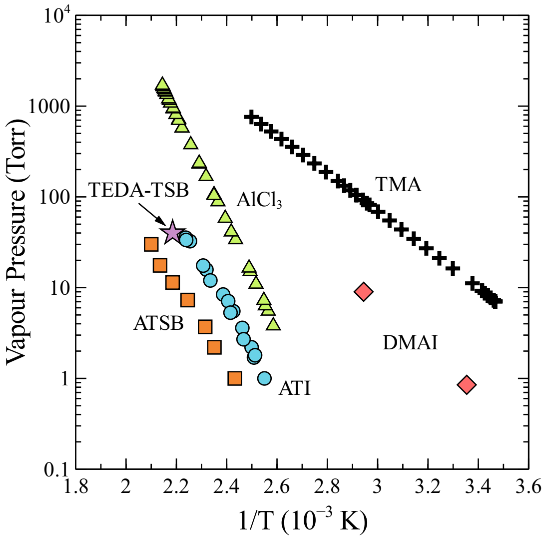

Figure 3.2: Vapour pressure data taken from the literature [117], [121]–[128] for selected Al precursors.

system.

Because of these issues, it is desirable to replace TMA with a safer, less expensive precursor. Table 3.1 lists the properties of several candidates. DMAI has been suggested [117] as a non-pyrophoric alternative to TMA with a relatively high vapour pressure still suitable for ALD, but unfortunately this material is fundamentally more expensive even than TMA, since its synthesis typically proceeds *via* TMA [118]. Jaeger and Hezel [23], [24] in the earliest experiments in surface passivation with Al_2O_3 used ATI as a precursor in an APCVD process. ATI is inexpensive, but forms a solid at room temperature, which complicates handling. More critically, on heating or during prolonged storage it freely interconverts between several isomeric forms with substantially different vapour pressures, resulting in an aging process that limits batch-to-batch deposition repeatability [119]. Another commonly used and inexpensive precursor for CVD of Al_2O_3 is the metal-halide aluminium chloride ($AlCl_3$). However this too is solid at room temperature, requires high deposition temperatures (typically between 700 and 1000 °C [120]), and produces corrosive HCl as a by-product of the deposition reaction.

A strong potential candidate as a replacement for TMA is the alkyl-alkoxide triethyldialuminium-tri-(*sec*-butoxide) (TEDA-TSB), which combines a number of favourable properties for CVD applications. It has a moderate vapour pressure, is non-pyrophoric, and forms a clear, low viscosity liquid at room temperature. It

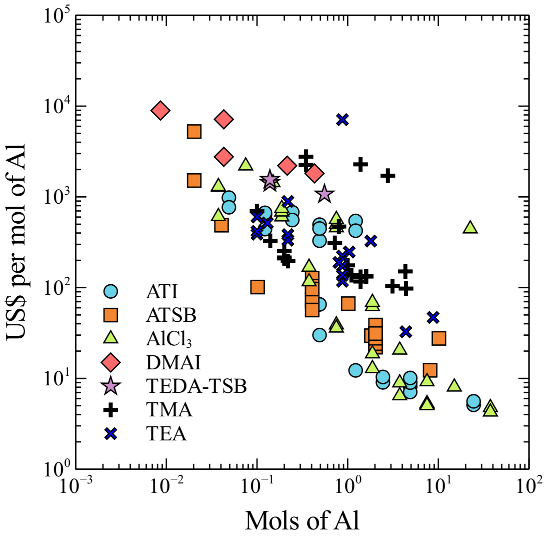

Figure 3.3: Retail price in US$ per mol of Al vs quantity in mols of Al for selected Al precursors, taken from the online catalogues of various suppliers. The data are for products of various purity, which accounts for some of the price variation.

is easily synthesised from equimolar quantities of triethylaluminium (TEA) and aluminium-tri-(*sec*-butoxide) (ATSB), both of which are less expensive to produce than TMA, the latter significantly so. Its synthesis and use as a precursor for CVD of Al_2O_3 has previously been demonstrated by Gordon *et al.* [128]. In this thesis, TEDA-TSB is employed as the primary precursor for APCVD of Al_2O_3. The material in question was produced commercially by Strem Chemicals Inc.

While TEDA-TSB is potentially cheaper than TMA in large-scale production, the cost advantage is not likely to be more than a factor of about a third at most. Consequently we also investigate ATSB (98 % pure, Strem Chemicals Inc.) as an alternative low-cost precursor. Like TEDA-TSB, ATSB is a liquid at room temperature, and non-pyrophoric. It is widely used as a rheology modifier in inks, and as a catalyst in the synthesis of a wide range of organic compounds. It is one of the least expensive of the available aluminium precursors, with a cost around a third that of TMA of comparable purity and quantity (calculated in terms of dollars per mol of Al). Its use in atmospheric- and low-pressure CVD of Al_2O_3 for non-passivation purposes has previously been demonstrated by Haanappel *et al.* [127], [129]–[131].

An interesting feature of ATSB is its O:Al ratio of 3:1, well above the 3:2 ratio of stoichiometric Al_2O_3. This means that it is possible for Al_2O_3 deposition to occur without the presence of additional oxygen-containing reactants such as

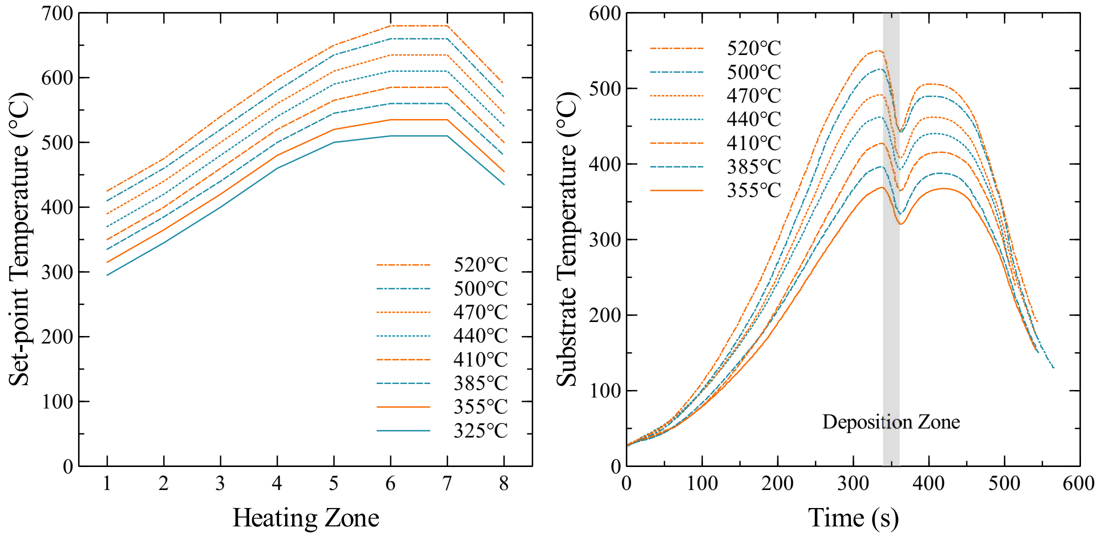

(a) **(b)**

Figure 3.4: a) Set-point temperature, and b) measured substrate temperature for the various APCVD temperature profiles used in this work. Deposition occurs in heating zone 7. Belt speed was 12 inches/min. Labelled temperature values represent the nominal deposition temperature referred to elsewhere in this work.

O_2 or H_2O. This allows considerable simplification of the CVD vapour delivery system, which otherwise must deliver the reactants in separate streams to the substrate while avoiding gas-phase intermixing.

The principal drawback of ATSB is its relatively low vapour pressure (see Table 3.1 and Fig. 3.2) which limits the rate at which the precursor can be delivered to the substrate, and therefore the deposition rate. This drawback can be overcome by several means, including 1) raising the temperature of the delivery lines, 2) increasing the flow rate of the carrier gas, and 3) using multiple delivery systems in series, to achieve the desired deposition rate. We will show that the ability of ATSB to act as a single-source precursor serendipitously facilitates the use of such solutions.

3.1.4 Temperature profiles

The APCVD deposition system used in this work features a series of heating zones to heat the substrate prior to deposition. In this work, eight different set-point temperature profiles were used to achieve different deposition temperatures for the Al_2O_3 films. Fig. 3.4a shows the temperature setpoints for each profile.

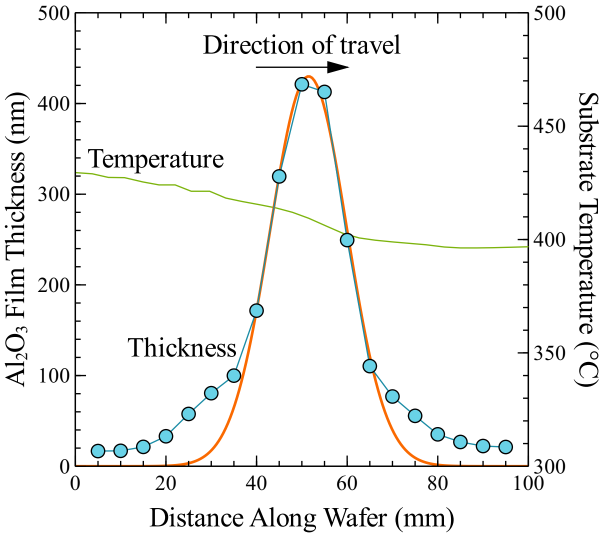

Figure 3.5: Static deposition profile for the APCVD system used in this work. Al_2O_3 film thickness is shown (symbols) as a function of position (in the direction of travel) on a polished silicon substrate. The belt was stopped for 50 s with the wafer directly under the injector. Deposition was continuous during substrate drive-in and drive-out (belt speed 12 inches/min), which accounts for the deposition near the wafer edges. A Gaussian fit to the main peak is shown. The corresponding substrate temperature for the 410 °C profile with a 12 inches/min belt speed is also shown.

The corresponding substrate temperature profiles were determined using a silicon wafer substrate with an attached thermocouple, where the latter was connected to an automated data recorder. Fig. 3.4b shows the resulting temperature profiles (the profile for the lowest temperature setting was not measured and is hence not shown). The profiles are shown as a function of time for a belt speed of 12 inches/min. The sudden dip in temperature that appears in the deposition zone is due to contact with the reactant carrier gas flows, which are heated to a substantially lower temperature. The extent of this drop is overestimated by the data in Fig. 3.4b due to poor contact between the thermocouple and substrate. When the thermocouple was more securely bonded to the substrate with thermal cement, the measured dip was much shallower (35 °C compared to 69 °C without the cement). The other parts of the profile were not affected by this difference.

Fig. 3.5 shows that most deposition occurs close to the centre of the deposition zone, where precursor flow is at maximum (substrate directly under the injector head). This corresponds to a substrate temperature roughly in the middle of the range measured across the deposition zone. In Fig. 3.4, each profile is labelled with a nominal temperature. This temperature represents a best estimate of the substrate temperature at the point when the deposition rate is at maximum, taking into account the overestimation of the temperature dip in Fig. 3.4b just mentioned. The value for the lowest temperature profile is extrapolated from the relative set-point temperatures. These values are those referred to in subsequent experimental chapters.

It can be seen that the profiles include some time at elevated temperatures after deposition. It is likely that this has some influence on the "as-deposited" properties of the Al_2O_3 films, as discussed in subsequent chapters.

3.2 Sample preparation

This section describes the general sample preparation sequence employed in this work. Details relating to specific experiments are given in the following chapters. All samples were fabricated on mono-crystalline (float-zone (FZ) or Cz) silicon wafer substrates, either boron or phosphorous doped, with various resistivities. Wafers supplied as-cut by the manufacturer (without chemical or mechanical surface polishing) were given a surface-damage-removal etch in either an HF:HNO_3 or tetramethylammonium hydroxide (TMAH) solution. A standard Radio Corporation of America (RCA) cleaning sequence (RCA1, HF, RCA2, HF) was used to remove metallic and organic surface contaminants for all samples prior to further processing. The final step in this sequence (a dip in dilute HF followed by a rinse in deionised water) was performed immediately prior to Al_2O_3 deposition.

In addition to the APCVD Al_2O_3 deposition system described in Section 3.1, some Al_2O_3 films were deposited by thermal ALD from TMA and H_2O using a Beneq TFS 200 reactor. These films were used as a benchmark for the films deposited by APCVD. Post-deposition annealing of both APCVD and ALD films was performed in a quartz tube furnace, typically at a temperature of 425 °C in N_2.

Two main types of sample structure were employed in this work. Firstly, symmetrically processed, full-area passivated wafers were prepared for photoconductance and photoluminescence (PL) carrier lifetime measurements. For these, Al_2O_3 was deposited first on the front, illuminated side, then on the rear. The second common type of structure were MIS capacitors for C–V and parallel conductance measurements. These received an Al_2O_3 deposition on the front side only, followed by thermal evaporation of $\sim$100 nm of Al through a shadow mask to form roughly circular gate contacts (∅ ≈ 700 µm). GaIn eutectic paste was applied manually to form an ohmic contact to the bare silicon rear surface.

3.3 Characterisation

This section describes the experimental techniques most commonly employed to characterise the properties of the Al_2O_3 samples. Details of additional characterisation techniques employed in particular experiments are given in the relevant chapters.

Al_2O_3 film thickness was generally determined from normal-incidence spectral reflectance measured between 199 and 1100 nm using a Filmetrics F20 thin film measurement system. Measurements were performed on co-processed films deposited on mirror-polished silicon substrates. Film thickness was determined by fitting the measured spectra with a single layer model using the optical constants determined in Section 9.3.

Injection-dependent effective excess carrier lifetime τ_{eff} was measured using a Sinton Instruments WCT-120 photoconductance tool. In this system, excess carriers are generated using a flash lamp, and the resulting excess conductance is monitored as a function of time by an inductively coupled coil located underneath the sample. For samples with high carrier lifetimes ($\tau_{eff} \gtrsim 100\,\mu s$) a short-duration flash was generally used, and the lifetime was determined using the transient analysis [116], since this requires no assumptions about the optical properties of the sample. For samples with lower lifetimes, or for lifetime measurements at higher injection levels, a flash of longer duration was employed to produce quasi-steady-state conditions, and the generalised analysis described by [132] was used to extract the lifetime. The optical constant required for this analysis was determined either from spectral reflectance measurements as described in [133], or by comparison with transient measurements at lower injection levels. Values of τ_{eff} presented in this work are taken at $\Delta n = 10^{15}\,cm^{-3}$ where not otherwise specified. Surface recombination parameters were extracted from τ_{eff} as described in Section 2.6.

In addition to photoconductance measurements, calibrated PL lifetime imaging was performed using a BT Imaging LIS-R1 system. This method was used to evaluate the spatial uniformity of the surface passivation, and to detect the presence of handling damage and surface contamination. Fig. 3.6 shows a typical example of a calibrated PL lifetime image of a silicon wafer passivated by

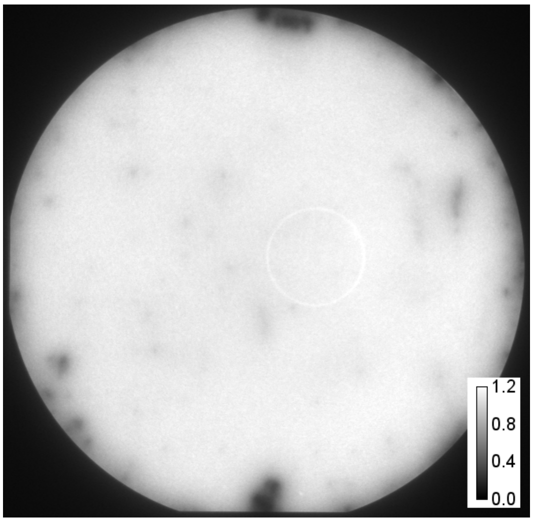

Figure 3.6: Typical calibrated PL lifetime image of a 4 inch silicon wafer (1 Ω cm *p*-type) passivated on both sides with APCVD Al_2O_3. The scale shows lifetime in ms. The photoconductance coil can clearly be seen, as well as low-lifetime regions corresponding to post-passivation labelling and handling.

APCVD Al_2O_3, showing the high degree of spatial uniformity achievable by this technique.

High-frequency alternating current (AC) C–V measurements were performed using an HP 4284A precision LCR meter at a frequency of 1 MHz using an AC signal voltage of 30 mV. Measurements of the AC parallel conductance for the determination of capture cross-sections via the conductance method were performed at frequencies between 20 Hz and 1 MHz using the same system. Quasi-static C–V measurements were performed via the linear voltage ramp method using an HP 4140B picoammeter/dc voltage source, with voltage sweep rates of 0.01–0.1 $\mathrm{V\,s^{-1}}$. Both high-frequency and quasi-static C–V measurements were generally performed using a voltage sweep from inversion to accumulation. Measurements were performed in the dark to avoid non-equilibrium generation of carriers in the sample by illumination. A light positioned above the chuck was controlled remotely and used for temporary illumination of the sample prior to the measurement sweep, while the sample was held at a bias in strong inversion, in order to rapidly generate minority carriers for the inversion layer. The illumination was then removed, and the device capacitance was allowed to stabilise before beginning the voltage sweep. For both C–V and conductance measurements the MIS samples were mounted on a temperature-controlled chuck, which was generally maintained at a temperature of either 23 or 25 °C, unless otherwise mentioned. Gate contact areas were determined by optical microscopy.

Initial electrical investigations of the Si–Al_2O_3 MIS test structures revealed excellent dielectric characteristics, with clear inversion behaviour, minimal frequency dispersion throughout the measured bias range, negligible hysteresis, and minimal leakage current. With some exceptions (notably for films deposited at the lowest temperatures), this high dielectric quality generally prevailed for the Al_2O_3 films examined in this work, permitting a detailed investigation of the electrical properties of the Si–Al_2O_3 interface. The details of the C–V analysis are given in Appendix A, and those of the conductance method in Appendix B.

Chapter 4

Electrical Properties of the Si$-$Al$_2$O$_3$ Interface

> *Unity of plan everywhere lies hidden under the mask: of diversity of structure—the complex is everywhere evolved out of the simple.*
>
> — Thomas Henry Huxley
> A LOBSTER; OR, THE STUDY OF ZOOLOGY

The effectiveness of silicon surface passivation by Al$_2$O$_3$ is fundamentally determined by the properties of the various electronic states present at the Si–Al$_2$O$_3$ interface. By better understanding these properties, we gain a deeper understanding of the physical processes underlying observed surface recombination. Furthermore, we gain a powerful predictive tool which allows us to anticipate the behaviour of the surface under arbitrary conditions.

In this chapter experimental evidence regarding the electrical properties of the Si–Al$_2$O$_3$ interface is presented and discussed. These properties include the density of fixed charges in the dielectric, the energetic distribution of interface states, and the capture cross-sections of these states for electrons and holes. C–V measurements are used to investigate the first and second of these, while the conductance method is employed to cast light on the second and third. Critically, we make use of the full MIS equivalent circuit model, including minority carrier transitions, to derive information regarding minority as well as majority carrier capture properties. The former are rarely evaluated, but turn out to be crucial to explaining recombination at the Si–Al$_2$O$_3$ interface. It is shown that this interface is characterised by a distinctive set of electrical properties, which mark it as fundamentally distinct from other silicon–dielectic interfaces, in particular from Si–SiO_2, to which it is often compared. The available evidence suggests that these characteristics are largely independent of the method used to form the Al_2O_3 film.

It is shown that apparent complexities in the energy dependence of the interface properties emerge from a relatively simple underlying physical picture. At least three interface state species with distinct properties are found to be present. The most important of these from the point of view of surface passivation is a donor-like state located just below midgap. This state dominates recombination when electrons are the minority carrier, which is usually the case due to the large negative charge of Al_2O_3. It is demonstrated that surface recombination rates predicted from the properties of this state are in excellent agreement with measured values.

4.1 Interface state distribution

As discussed in Section 2.1, defect states at a semiconductor–dielectric interface generally form a continuum of energy levels within the semiconductor bandgap. This continuum is made up of separate contributions from different species of states with different properties. The available evidence suggests that each of these sub-distributions may be approximately described by a Gaussian function centred around a certain energy [9], [134]. The energy levels of the states associated with such defects in principle depend on the local chemical environment of each defect. Consequently it is expected that the distribution of interface states at the Si–Al_2O_3 interface will, for example, be distinct from that of Si–SiO_2, even if the major interface states arise from silicon dangling bonds in both cases.[1]

Measurements of the energetic distribution of the Si–Al_2O_3 interface states have been reported by a number of authors [39], [40], [43], [45], [46], [48]–[50], [52], [53], [91], [135]–[140]. However, relatively little consideration has been given to the significance of this distribution to a fundamental understanding of the interface properties, and little attempt has been made to compare and contrast it with the interface state distributions exhibited by other silicon–dielectric systems. In this section the Si–Al_2O_3 interface state distribution is presented, and its

---

[1] This remains so despite the likely presence of a thin SiO_x interlayer at the Si–Al_2O_3 interface (see Sections 1.2 and 9.1.3), as demonstrated in Chapter 8.

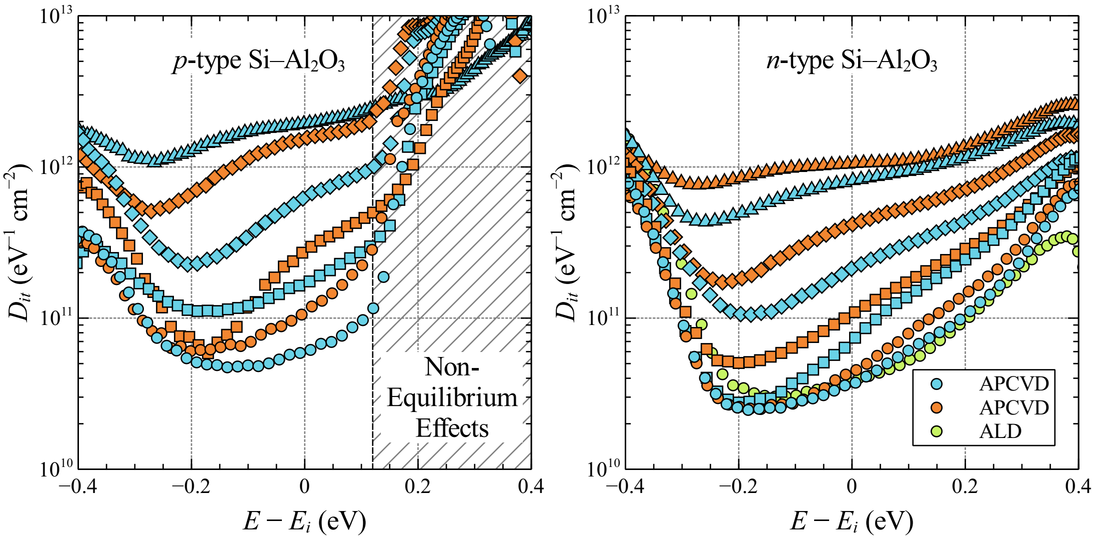

(a) (b)

Figure 4.1: Interface state density D_{it} as a function of energy in the bandgap for various Al_2O_3 films on Si. The data have been selected to show the behaviour of $D_{it}(E)$ over a wide range of concentrations and to illustrate some of the possible variations in the shape of the distribution.

characteristic features and modes of variation are described and discussed. Such an exposition will provide a foundation for later, more detailed discussion of the interface state properties.

Fig. 4.1 shows $D_{it}(E)$ determined for p- and n-type surfaces passivated by various Al_2O_3 films. The films were deposited using APCVD with a variety of deposition conditions, reactants, and post-deposition treatments, and have been selected to show the behaviour of $D_{it}(E)$ over a wide range of concentrations, and to illustrate some of the possible variations in the shape of the distribution. Data for Al_2O_3 deposited by thermal ALD is also shown for comparison.

From Fig. 4.1 it can be seen that the Si–Al_2O_3 interface state distribution is not symmetric in the silicon bandgap. Rather, in all cases it possesses a minimum in the lower half of the bandgap. This minimum is located near $E_i - 0.18$ eV for surfaces with low values of D_{it}, and generally shifts to lower energies as D_{it} increases. On either side of the minimum, D_{it} increases monotonically towards the band edges. When viewed on a log scale, the increase of D_{it} through the middle part of the bandgap towards E_c generally appears to occur in three distinct stages: first a relatively rapid increase above the minimum up to a point just below midgap, then a more gradual rise, approaching a plateau in some cases, to about 0.2 eV above midgap, and finally another sharp climb towards the band edge, which is observed to continue with a more or less constant slope (i.e. an exponential behaviour) over the energy range in which the measurement is accurate. This complex energy dependence suggests the existence of multiple contributions to the distribution in this range. The density of states at all energies above the minimum varies substantially between different samples, which suggests that these states are largely extrinsic. In contrast, the density of states in that part of the distribution nearest the valence band appears to be practically independent of sample processing, suggesting that these states may be intrinsic, possibly band-tail states.

While D_{it} is observed to increase towards both band edges within the energy range accessible to experiment, the extent of this increase is relatively slight. Indeed for samples with midgap D_{it} in the range of $10^{12}\,\mathrm{eV}^{-1}\,\mathrm{cm}^{-2}$, D_{it} at midgap may be higher than that near the valence band in the measurable part of the distribution. It would be a gross oversimplification simply to refer to the distribution as “U-shaped”, as is sometimes done. This would be to ignore the most interesting and pertinent features of the data (the distribution of states in the middle part of the gap) in favour of those elements that are most superficial, most uncertain, and least relevant to recombination.

Measurements by other authors using the most reliable methods (quasi-static C–V measurements) of Si–Al_2O_3 interfaces formed by a variety of other techniques (spray pyrolysis, thermal and plasma-enhanced ALD, and PECVD) [39], [40], [43], [46], [48], [49], [52], [53], [91], [136], [137], [140] agree well with the shape of the distributions shown here. This suggests that the observed characteristics are a general feature of the Si–Al_2O_3 interface, independent of the means used to form the film. Fig. 4.1b shows the extremely close match between the lowest $D_{it}(E)$ distribution shown for APCVD Al_2O_3, and that measured for thermal ALD Al_2O_3. In both cases the value of D_{it} at midgap is in the range of $3\text{–}4 \times 10^{10}\,\mathrm{eV}^{-1}\,\mathrm{cm}^{-2}$, which is remarkably low, on par with the best values reported elsewhere in the literature for Al_2O_3 [42], [44], [49]. This shows that, contrary to common preconceptions, APCVD is capable of producing Si–Al_2O_3 interfaces of a quality every bit as good as that achieved by ALD or other techniques.

For p-type surfaces passivated by Al_2O_3, D_{it} could not in most cases be measured accurately at energies of about 0.12 eV or more above midgap. This is due to a non-equilibrium behaviour of the inversion layer charge that occurs for these substrates. When sweeping the voltage from inversion to accumulation, this manifests as an apparent shift in the onset of strong inversion to lower voltages, and in some cases the presence of a pronounced peak in the quasi-static capacitance in weak inversion. When sweeping from accumulation to inversion, it results in partial deep depletion of the silicon surface and a consequent dip in the apparent quasi-static capacitance. The result in either case is a significant error in the value of D_{it} extracted from the C–V curve in weak inversion, either an overestimation (for a sweep from inversion), or underestimation (for a sweep from accumulation). The onset of this non-equilibrium behaviour can be shifted to more positive voltages either by reducing the voltage sweep rate, or by increasing the measurement temperature. However, even at the lowest practical sweep rates (5 to $10\,\mathrm{mV\,s^{-1}}$), the effect remains significant at room temperature. The same effect has been reported to occur for p- and n-type Si–SiO$_2$ MIS structures at low temperature, with high lifetime substrates, or under illumination [141], and has been explained as being due to the inability of minority carrier generation and recombination processes to maintain an equilibrium concentration of inversion layer charge. This explains why the effect is not observed for n-type surfaces passivated by Al$_2$O$_3$, since for these surfaces the inversion layer charge under the gate is coupled to that in the external inversion layer induced by the negative charge in the film beyond the gate contact area. It can therefore more easily maintain equilibrium with the voltage signal, in the manner discussed by [142].

It is notable that D_{it} measured for p-type substrates is consistently higher than that for n-type substrates with the same processing. It is not entirely clear whether this difference is real, or whether it is a measurement artifact. On the side of it being real the following evidence can be cited: 1) D_{it} measured by the conductance method at midgap was also found to be higher for p-type than for n-type samples with the same Al$_2$O$_3$ film (compare Figs. 4.5 and 4.6), and 2) J_0 at undiffused n-type surfaces is found to be consistently lower than that of undiffused p-type surfaces passivated by the same film (see Chapter 7), while J_0 should be identical if D_{it} and Q_{tot} are the same (for large Q_{tot}).

On the other hand, it is shown in Section 8.2 that the apparent D_{it} depends, at least in some cases, on the direction of the voltage sweep used to measure the C–V curves. The use of the same sweep direction generally results in good agreement of D_{it} for p- and n-type samples in that case. Data measured using both sweep directions are not available in majority of cases, because such sweeps were not routinely recorded, which makes testing this hypothesis more difficult. However, in cases when such data is available, its use does not always result in a significant difference in apparent D_{it}, or significantly better agreement between p and n-type data. The balance of the evidence therefore appears to be on the side of there being a real difference in D_{it} between p- and n-type surfaces. The reasons for this could perhaps relate to different surface carrier concentrations during the initial stages of deposition. However, we should remain cautious on this question.

In summary, it is concluded that the Si–Al$_2$O$_3$ interface states form a characteristically asymmetric distribution with a minimum in the lower part of the bandgap. The shape of this distribution varies relatively little between films processed under different conditions or deposited by different techniques, pointing to the fundamental similarity of the different interfaces. The apparent density of interface states is consistently found to be somewhat higher at p-type surfaces than at n-type, though there is reason for caution in interpreting this as a true difference in D_{it}.

4.2 Capture cross-sections

Besides density and energetic distribution, the other important properties that characterise the interface states are their capture cross-sections for electrons and holes. Two methods are generally used for the determination of the capture cross-sections of interface states, both of which employ the same MIS structures used for C–V measurements. These are 1) measurements of the small-signal parallel conductance as a function of frequency, generally referred to as the conductance method, 2) measurements of pulsed-voltage time-domain capacitance transients as a function of temperature, known as deep-level transient spectroscopy (DLTS). The former technique is used in this work. The use of the conductance method to determine interface state properties was first described by Nicollian and Goetzberger [143], [144], and the method has subsequently been applied by numerous authors to various interfaces, especially Si–SiO$_2$. A comprehensive exposition of the method and a review of work up to that point was given by Nicollian and Brews [8].

4.2.1 The conductance method

The principle of the conductance method is based on the measurement of the MIS parallel conductance G_p, which is a measure of the energy loss due to non-equilibrium charge transfer between interface states and the semiconductor. Such energy loss occurs when interface states are in partial equilibrium with Fermi level variations in the semiconductor induced by the applied AC voltage signal. Charge transfer between the semiconductor and states above or below the Fermi level results in an energy loss that is measured as a conductance. When measured as a function of angular frequency ω, the normalised interface state conductance $\langle G_p \rangle / \omega$ forms a peak centred on the frequency of maximum energy loss. The peak frequency is related to the capture cross-section of the interface states, while the area under the peak is proportional to the density of these states.

The conductance method is particularly powerful because the measured quantity, the MIS parallel conductance G_p, generally relates directly and solely to the interface states. This is not the case for capacitance-based methods, where the measured capacitance contains contributions from the semiconductor and dielectric which must be separated from that of the interface states. As a result, the conductance method is capable of accurately measuring extremely small interface state densities, on the order of $10^9\,\mathrm{eV}^{-1}\,\mathrm{cm}^{-2}$ [8].

A significant source of uncertainty in the conductance method is that the surface carrier concentration is not measured directly, but must be calculated from the surface potential determined from a C–V measurement or some other method. Because the dependence of the surface concentration on the surface potential is exponential, the extracted capture cross-sections are very sensitive to error in the surface potential. As a result, such measurements can never be more accurate than about a factor of two.

In analysing conductance measurement data, it is usual to make the simplifying assumption that minority carrier capture and emission processes may be neglected. This allows a considerable simplification of the analysis, which is why this approach has long been the conventional one [8]. However, it restricts the energy range over which the method is valid to that in which majority carrier processes are dominant. In practice, this means that σ_p can be determined in the lower part of the bandgap, and σ_n in the upper part of the bandgap, from measurements of p-type and n-type samples respectively. Furthermore, neither σ_p nor σ_n may be determined accurately close to midgap, where minority and majority carrier concentrations are comparable.

In order to use the measured capture cross-sections to model surface recombination, it is therefore necessary to make some assumption concerning the values of σ_p and σ_n over the energy range in which they were not measured (i.e. the greater part of the bandgap). This is typically done by extrapolating the measured values in some way [10], [11], [47], [145]–[147]. Such an approach leads to large uncertainties, being capable of producing vastly different results depending on the functional dependence chosen for the extrapolated values.

Still more crude is an approach taken by some authors of extrapolating the measured σ_p and σ_n to midgap, and treating the resulting capture cross-section ratio as characteristic of recombination at the interface in question. It ought to be remembered that under typical levels of illumination, and especially when the surface charge is significant, interface states across the greater part of the bandgap contribute equally to recombination, not merely those at midgap, and the value of both capture cross-sections must therefore be known over the same range.

A major problem for approaches based on measuring only majority carrier capture cross-sections is that interface states tend to be donor-like in the lower half of the bandgap and acceptor-like in the upper half. Consequently, the minority carrier capture cross-sections tend to be larger than those for majority carriers in both halves of the bandgap. Since recombination will be dominated by the states with the largest capture cross-sections, it will usually be these (unmeasured) minority carrier capture cross-sections that determine the recombination rate.

The limitations imposed by neglecting minority carrier capture can be overcome by considering the complete small-signal MIS equivalent circuit, including minority carrier processes. This approach was first demonstrated by Cooper and Schwartz [148] for the Si–SiO_2 interface in 1974, but apart from the work presented here, some of which was previously published in [33], it appears only to have been applied by [149] (to the Ge–SiO_2 interface). The likely reason for this is that the resulting equations are significantly more complex, and must be solved numerically, which complicates analysis. However, modern computing power makes this a feasible task even for large datasets. The ensuing advantages are considerable. With this approach it is possible to determine both minority and majority capture cross-sections at the same energy over an energy range from near flatbands, through depletion, midgap, and weak inversion, from measurements on a single sample. Consequently, this is the approach adopted in this work. The relevant theory and equations are described in Appendix B.

4.2.2 Previous work

Several authors have reported measurements of the capture properties of the Si–Al_2O_3 interface states. Already in 1969, Tanaka and Iwauchi [22] evaluated σ_n of reactively sputtered Si–Al_2O_3 structures by the conductance method, finding $\sigma_n = 1.5 \times 10^{-14}\,\mathrm{cm}^2$ in the upper part of the bandgap.[2] Saint-Cast *et al.* [54] assessed capture cross-sections of PECVD Al_2O_3 interfaces using the DLTS technique. The resulting capture cross-section values were strongly energy-dependent, increasing to values on the order of $\sigma_p = \sim 1 \times 10^{-17}\,\mathrm{cm}^2$ and $\sigma_n = \sim 1 \times 10^{-14}\,\mathrm{cm}^2$ towards the centre of the bandgap. In contrast Werner *et al.* [47] determined σ_p and σ_n of plasma-assisted ALD Al_2O_3 interfaces using the conductance method, finding an energy-independent $\sigma_p = \sim 1.5 \times 10^{-16}\,\mathrm{cm}^2$ in the lower half of the bandgap, while σ_n in the upper half of the bandgap was found to increase somewhat with energy towards midgap, varying between $\sim 5 \times 10^{-16}\,\mathrm{cm}^2$ to $\sim 2.5 \times 10^{-15}\,\mathrm{cm}^2$ in the measured range.[3]

All of these preceding works limited their analysis to majority carrier capture, and were therefore only able to determine σ_p and σ_n in the lower and upper parts of the bandgap respectively, where majority carrier capture was dominant for either p-type or n-type substrates. In the following sections we describe the results of conductance measurements of the Si–Al_2O_3 interface in which both minority and majority capture cross-sections are determined over a significantly wider energy range.

4.2.3 Real and apparent capture cross-sections

Before considering measurements of the capture cross-sections of the Si–Al_2O_3 interface states, it will be useful to make a distinction between real and apparent capture cross-sections, and to illustrate some of the ways in which the latter may differ from the former in misleading ways.

In extracting capture cross-section values from measured conductance or DLTS data it is usually implicitly assumed that a) all states at a given energy have the same σ_n and σ_p (i.e. only a single species of interface states is present), and b) D_{it}, σ_n, and σ_p are approximately independent of energy over the range probed by the conductance measurement AC signal or by the DLTS bias pulse (where this range is broadened by the Fermi occupation function at finite temperatures and by surface potential fluctuations). These assumptions significantly simplify

---

[2] Note that Tanaka and Iwauchi [22] used the tunnelling model of [150] to account for frequency dispersion, rather than the surface potential fluctuation model of [144] used here and in most recent works, resulting in a systematically larger value for σ_n. The value of σ_n corresponding to the measurements of [22] is reassessed in Fig. 4.7

[3] Each of the preceding authors used different values of v_{th} in extracting σ_p and σ_n, either $2 \times 10^7\,\mathrm{cm\,s}^{-1}$ [22], $5 \times 10^7\,\mathrm{cm\,s}^{-1}$ [54], or $1 \times 10^7\,\mathrm{cm\,s}^{-1}$ [47]. The values mentioned in the text have been normalised to $v_{th} = 2 \times 10^7\,\mathrm{cm\,s}^{-1}$.

the analysis and therefore are routinely employed in practice. We will call the values of σ_n and σ_p extracted under such assumptions the "apparent" values.

Unfortunately, these assumptions are often invalid. Interface defect states are not in general distributed uniformly with energy across the semiconductor bandgap, but exist as statistically broadened energy distributions centred around certain characteristic peak energies [9], [151]. Furthermore, the generally observed existence of a continuum of interface states throughout the bandgap implies that these separate distributions (due to different interface state species) are likely to overlap over at least some part of the energy range. The apparent values of σ_n and σ_p will deviate systematically from the true values whenever the energy dependence of D_{it}, σ_n, or σ_p is significant, or when interface states with different σ_n or σ_p are present in the energy range probed by the measurement. Because the relevant measurement techniques in fact probe states spanning a significant range of energies (on the order of several kT/q to either side of the mean surface potential), the resulting errors can be quite significant.

The equations presented in Appendix B allow $\langle G_p \rangle/\omega$ to be calculated as a function of frequency f and average surface potential for arbitrary combinations of defect states with arbitrary $D_{it}(E)$, $\sigma_p(E)$, and $\sigma_n(E)$ dependences. Surface potential fluctuations are described by the normalised standard deviation of surface potential σ_s. The corresponding apparent σ_p and σ_n may then be calculated by fitting such modelled $\langle G_p \rangle/\omega$ vs f curves with the same equations, assuming a single defect type at each energy, with energy independent D_{it}, σ_p, and σ_n.

Fig. 4.2 shows the divergence between the apparent and real values of $D_{it}(E)$, $\sigma_p(E)$, and $\sigma_n(E)$, due to energy dependence in $D_{it}(E)$ only, for a single Gaussian interface state distribution with energy-independent capture cross-sections. The apparent values of $\sigma_p(E)$, $\sigma_n(E)$, and $\sigma_s(E)$ only approach their input values in the energy range where $D_{it}(E)$ is a slowly varying function of energy. Outside of this range, the apparent values deviate systematically from the inputs due to the energy dependence of $D_{it}(E)$. The apparent $D_{it}(E)$ is simply broadened relative to the input function by the effects of thermal broadening and surface potential fluctuations, which limit the ability of the technique to resolve fine features in the $D_{it}(E)$ distribution.

At some threshold energy in inversion the deviation of σ_p, σ_n becomes exponential with respect to energy. This occurs when the minority carrier capture resistance becomes small enough that the states are effectively coupled together via the inversion layer and respond as an ensemble with a single time constant. At this point the shape of the conductance peak becomes independent of σ_p, σ_n,

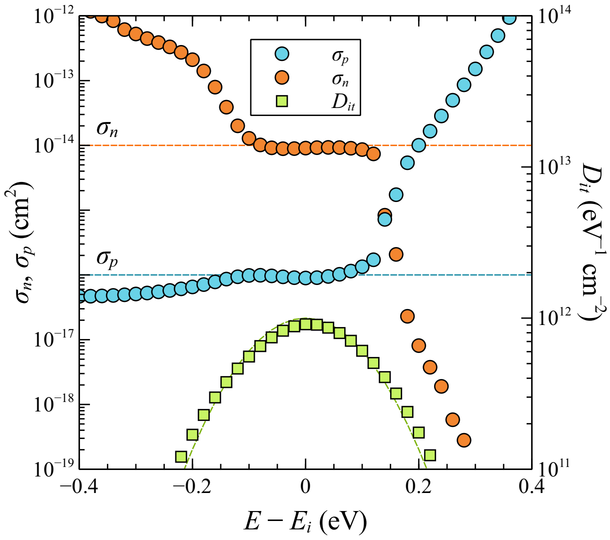

Figure 4.2: Apparent σ_p, σ_n, and D_{it} vs energy for a single Gaussian distribution of interface states with energy-independent capture cross-sections. The input values of σ_p, σ_n, and D_{it} are shown as dashed lines. $\sigma_s = 3$.

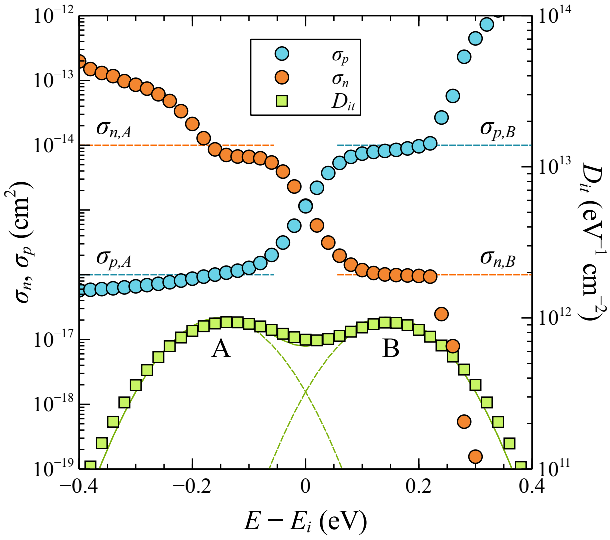

Figure 4.3: Apparent σ_p, σ_n, and D_{it} vs energy for two overlapping Gaussian distributions of interface states (labelled A and B) with different energy-independent capture cross-sections. The input values of σ_p, σ_n, and D_{it} for each distribution are shown as dashed lines. $\sigma_s = 3$.

and σ_s, while the peak frequency depends on both σ_p and σ_s. There is therefore too little information to determine any parameter except D_{it}. The energy at which this threshold occurs shifts to higher energies as σ_n decreases.

The dependence of the apparent interface state properties on energy becomes more complex when a second distribution of interface states with different properties is added to the model. Fig. 4.3 shows the apparent properties that result from the addition of a second distribution of interface states with different capture cross-sections from the first, where the properties of the first defect are unchanged from the previous example except for its location in the bandgap. In this case the apparent capture cross-sections only approach the true values in the range where one or other of the distributions is dominant. In the range where the distributions overlap, the apparent capture cross-sections exhibit a pronounced energy dependence as they transition between those of the two states.

Note that even in this transition region, excellent fits to the simulated $\langle G_p \rangle/\omega$ vs f data are achieved with a model that includes only a single type of interface state. This is because the contributions of the two states frequently merge into a single peak that could have been produced by a single type of state. Consequently in this and many other cases it is difficult or impossible to distinguish the presence of more than one type of interface state merely from the measured $\langle G_p \rangle/\omega$ vs f characteristics at a given voltage. It is therefore rather from the energy dependence of the apparent properties that we must infer the presence of multiple types of states.

The distinction between real and apparent interface state properties is often not appreciated by experimenters. It is common practice to accept the apparent values of σ_n and σ_p at face value, even when this results in obvious inconsistencies between the assumptions of the analysis and its results, because the apparent D_{it}, σ_n, or σ_p are, in fact, strongly varying functions of energy. The preceding discussion and simulation results make clear that a strong energy dependence of the apparent σ_n and σ_p does not necessarily imply any energy dependence of the real values, but may result from the energy dependence of D_{it}, or from a change in the relative concentrations of two or more interface state species with different energy-independent capture cross-sections. This may create a highly misleading picture of the energy dependence of interface properties, which is exacerbated when these spurious energy dependences are used to extrapolate σ_n and σ_p outside the measured energy range (for examples of this practice see [11], [145]–[147]).

A final important distinction needs to be made between "apparent" and "effective" capture cross-sections. It should be stressed that the apparent capture cross-sections are not "effective" values from the point of view of recombination. That is, the recombination rate calculated from the apparent values does not in general equal the recombination rate that would be calculated from the true values (in fact it may differ by orders of magnitude). The direct use of apparent capture cross-sections to calculate recombination may therefore be a source of significant error.

4.2.4 Determination of σ_p and σ_n

Determination of minority carrier capture cross-sections is sensitive to the shape of the conductance peak at low frequencies, where the measured signal is weakest and therefore most susceptible to noise and calibration errors. In order to minimise such errors, measurements were performed on Si–Al_2O_3 MIS structures with a relatively large density of interface states. Since the conductance contribution of the interface states is proportional to D_{it}, this results in a greater signal-to-noise ratio which allows more accurate measurements at low frequencies. The samples were selected from those described in Section 5.1. The Al_2O_3 films were deposited at 410 °C with an H_2O carrier flow rate 0.25 SLPM. These samples were chosen because, despite their larger D_{it}, they also exhibited negligible hysteresis or leakage currents, which would have interfered with the accurate determination of the capture cross-sections.

The assumption that the capture cross-sections determined for these high-D_{it} samples are also characteristic of well-passivated Si–Al_2O_3 interfaces is supported by the following evidence. Firstly, the shape of the $D_{it}(E)$ distributions is fundamentally similar to that of the samples with low D_{it} (see Section 4.1), which suggests that the same species of defects are present in both cases. Secondly, subsequent measurements of the capture cross-sections performed on samples with over an order of magnitude lower D_{it} (Section 8.2), although not generally allowing for the confident extraction of the minority carrier capture cross-sections, resulted in values of the majority capture cross-sections in excellent agreement with those determined here. We conclude, therefore, that the values of σ_p and σ_n determined for such high-D_{it} samples may be taken as characteristic of Si–Al_2O_3 interfaces in general.

Measurements of the parallel conductance G_p and capacitance C_p were performed as a function of frequency between 20 Hz and 1 MHz at various gate voltages in depletion and weak inversion for both p- and n-type MIS structures. Electron and hole capture coefficients (c_n and c_p) were determined by fitting the frequency-dependent normalised parallel conductance $\langle G_p \rangle / \omega$ at each voltage with the equivalent circuit model described in Appendix B, using a non-linear

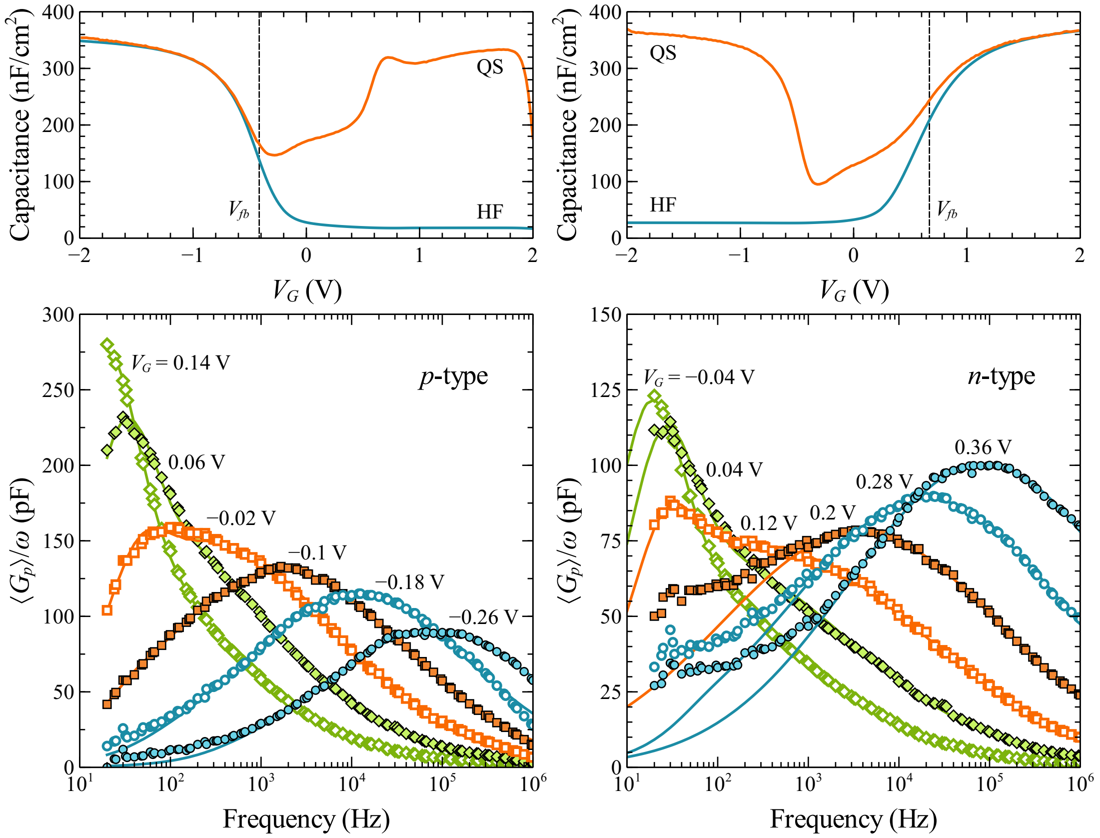

(a) (b)

Figure 4.4: Examples of measured $\langle G_p\rangle/\omega$ versus frequency data (symbols) for a) p-type and b) n-type Si–Al_2O_3–Al MIS structures at 23 °C, and modelled fits (lines) used to extract the data of Figs. 4.5 and 4.6. The corresponding high-frequency and quasi-static C–V curves are also shown.

least-squares fitting procedure based on the Levenberg–Marquadt algorithm. A selection of the resulting fits are shown in Fig. 4.4. The surface potential ψ_s was calculated from the quasi-static C–V curve using the method of [152], as described in Appendix A. Electron and hole capture cross-sections σ_n and σ_p were calculated from the determined capture coefficients via (2.16) with $v_{th} = 2 \times 10^7\,\mathrm{cm\,s^{-1}}$.

p-type structures

Fig. 4.5 shows the extracted values of σ_n and σ_p for a p-type substrate, together with D_{it} determined from the same measurements and from the quasi-static capacitance. The minority carrier capture cross-section σ_n is determined over a

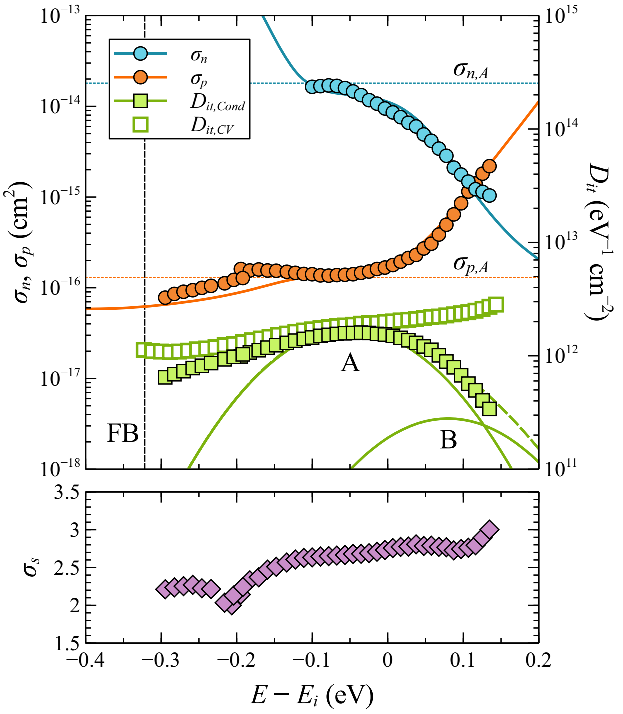

Figure 4.5: Apparent electron (σ_n) and hole (σ_p) capture cross-sections and corresponding interface defect distribution (D_{it}) and standard deviation of the surface potential σ_s as a function of energy measured from E_i, determined by the conductance method for a p-type Al_2O_3 MIS structure. The data were extracted from the data shown in Fig. 4.4a and other similar measurements. D_{it} determined from a quasi-static C–V measurement of the same sample is also shown for comparison. Solid lines show the proposed two-defect distribution used to account for the measured data, and the resulting simulated apparent capture cross-section values. Dotted lines show the energy independent capture cross-sections of the primary defect distribution used in the model.

smaller range than σ_p because σ_n does not significantly affect the measured conductance when the surface potential is far from E_i. It can be seen that σ_p is relatively independent of energy over a significant range below midgap, and that where σ_n is measured it is inversely related to σ_p, appearing to plateau in a similar range.

By comparison with the simulation results discussed above, the apparent change in $\sigma_n(E)$ and $\sigma_p(E)$ above midgap is likely to be due to the change in relative concentrations of two species of interface state with different capture cross-sections. Conversely the relative independence of $\sigma_n(E)$ and $\sigma_p(E)$ with respect to energy just below midgap suggests that one defect species is dominant

Table 4.1: Properties of the interface state distributions used to fit the apparent interface properties in Fig. 4.5.

Parameter	State A	State B
σ_p (cm^{-2})	1.3×10^{-16}	1×10^{-16}
σ_n (cm^{-2})	1.8×10^{-14}	2×10^{-14}
$E_t - E_v$ (eV)	0.51	0.64
SD (eV)	0.09	0.07
$D_{it,peak}/D_{it,midgap}$	0.8	0.13

in this range. We therefore assume that the values of $\sigma_n \approx 1.8 \times 10^{-14}\,\mathrm{cm}^2$ and $\sigma_p \approx 1.3 \times 10^{-16}\,\mathrm{cm}^2$ measured in this range represent the actual values for this (probably donor-like) state.

In order to account for the measured $\sigma_n(E)$ and $\sigma_p(E)$ distributions, such a state must dominate the overall $D_{it}(E)$ distribution just below midgap, while making up a decreasing fraction above midgap. To meet these requirements we have previously [33] posited a Gaussian distribution of states centered just below midgap, with a peak close to the measured D_{it} in that region, in addition to a smaller secondary distribution centered just above midgap, as shown in Fig. 4.5. Energy-independent capture cross-sections are assumed for both states. The distributions are described by

$$D_{it}(E) = D_{it,peak} \exp\left(\frac{(E - E_t)^2}{2SD^2}\right) , \tag{4.1}$$

where E_t is the peak energy and SD the standard deviation of the interface state distribution. The relevant parameters for the two distributions are summarised in Table 4.1. In Fig. 4.5 we also plot the apparent capture cross-section values calculated from these distributions. As with the data of Figs. 4.2 and 4.3, these are determined by calculating $\langle G_p \rangle / \omega$ due to the combination of the two defects, and subsequently fitting this in the same way as the experimental data using a single apparent defect. It can be seen that the results are in excellent agreement with the measured values.

The parameters assigned to state B in Table 4.1 and Fig. 4.5 (including the position and shape of its distribution) are not expected to be the true values of this state. There are in fact multiple sets of parameter values for state B that would result in a good fit to the measured apparent data. This state is included in Fig. 4.5 only to illustrate that the observed energy dependence of

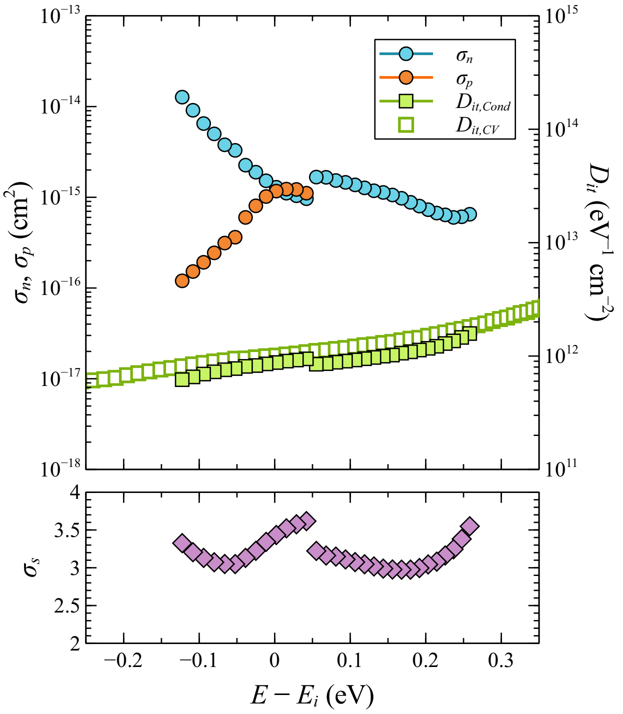

Figure 4.6: Apparent electron (σ_p) and hole (σ_n) capture cross-sections and corresponding interface defect distribution (D_{it}) and standard deviation of the surface potential σ_s as a function of energy measured from E_i, determined by the conductance method for a n-type Al_2O_3 MIS structure. The data were extracted from the data shown in Fig. 4.4b and other similar measurements. D_{it} determined from a quasi-static C–V measurement of the same sample is also shown for comparison.

the apparent σ_n and σ_p can be accounted for by the presence of a second state. Its exact parameters are relatively unimportant, because a) the determination of parameters for state A is not strongly dependent on those assumed for state B, and b) recombination in most situations of interest will be dominated by state A due to its higher σ_n. It will be shown in the following sections that the fit shown in Fig. 4.5 is indeed somewhat naïve, in that it takes the apparent σ_n, σ_p, and D_{it} in the upper part of the bandgap at face value. Nevertheless, the general picture of two species of interface states near the centre of the bandgap, and the specific properties of state A, will be seen to remain valid.

n-type structures

Fig. 4.6 shows apparent σ_n, σ_p, and D_{it} determined in the same way for an n-type MIS structure. The apparent σ_n in depletion is higher than σ_p for the p-type

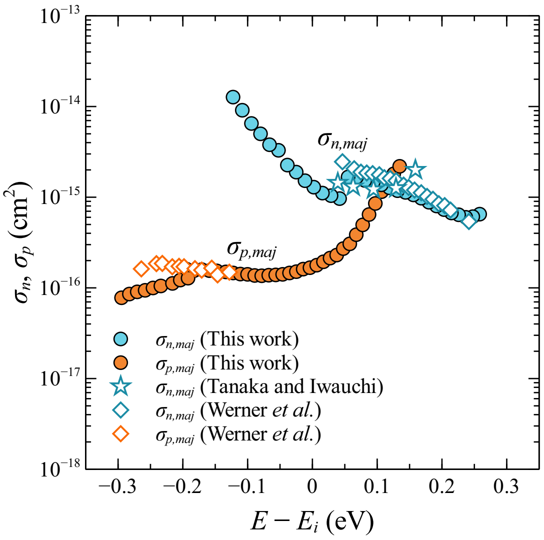

Figure 4.7: Comparison of apparent σ_p and σ_n determined in this work for majority carriers at the Si–Al$_2$O$_3$ interface to those reported by Tanaka and Iwauchi [22] and Werner *et al.* [47].

structure, on the order of $10^{-15}\,\mathrm{cm}^2$, and increases somewhat towards midgap. There is no obvious plateau in σ_n to indicate that a single state is dominant in the examined range, and σ_p is sufficiently low relative to σ_n that it cannot be assessed with confidence from the data. As shown in Fig. 4.4b, the measured $\langle G_p \rangle/\omega$ vs f at most energies in depletion cannot be accounted for by a single type of state, because a distinct rise in $\langle G_p \rangle/\omega$ (it is difficult to identify a clear peak) occurs at low frequencies. Though not commented on by the authors, a similar feature appears to be present in the data of [47]. Assuming this feature is not an artifact, it appears to show the existence of a type of state with very low σ_n. In such cases, the fit to extract the apparent values shown in Fig. 4.6 was performed only to the larger peak.

Near midgap and in weak inversion, it again becomes possible to adequately fit the data over the whole frequency range with a single apparent state. Consequently there is some discontinuity in the apparent parameters at this point. The apparent σ_p just above midgap is on the same order as σ_n. However, the significant increase in apparent σ_s in this range is indicative of the continued presence of two or more types of state, so the apparent value must be interpreted with caution. Below midgap, the apparent σ_n and σ_p significantly increase and decrease respectively, appearing to approach values consistent with those measured for the p-type sample below midgap.

It is not straightforward to interpret the apparent data for n-type surfaces. It appears that at least three types of state contribute significantly to the conductance signal in the upper part of the bandgap. One of these is presumably that identified just below midgap on the basis of the p-type data, and labelled as state A. Determination of the properties of the remaining states may be assisted by measurements of n-type samples at higher and lower temperatures, as well as analysis of variations in the energy dependence of D_{it} between differently processed samples. For the time being we merely note that σ_n of the states in the upper part of the bandgap is significantly lower than that of state A, so that these states will be relatively ineffective as recombination centres when holes are the majority carrier at the surface, as in most cases of interest for Al_2O_3. It is possible, however, that some of these states are those responsible for the recombination observed at diffused n-type surfaces passivated by Al_2O_3 (Section 7.3).

Comparison to literature data

Fig. 4.7 compares the values of σ_p and σ_n determined as majority capture cross-sections in this work to those reported by Tanaka and Iwauchi [22] for reactively sputtered Al_2O_3 and by Werner *et al.* [47] for plasma-assisted ALD Al_2O_3, where these have been adjusted to $v_{th} = 2 \times 10^7\,\mathrm{cm\,s^{-1}}$. The data of [22], which were originally extracted using the tunnelling model of Preier [150], were reassessed from the measured $\langle G_p \rangle / \omega$ peaks using the more conventional surface potential fluctuations model of Nicollian and Goetzberger [144], [8], together with the surface carrier concentrations given by [22]. The surface potential was recalculated to be consistent with these concentrations and with modern values for n_i [107].

While these previous works did not determine capture cross-sections for minority carriers, the agreement between the majority carrier values is extraordinary. It should be recalled that capture cross-sections reported for the more heavily studied Si–SiO_2 interface commonly vary by orders of magnitude between different experimenters, and even between differently prepared samples measured by the same experimenter. That such close agreement is found between these several sets of values, determined by different studies using significantly different Al_2O_3 deposition techniques, is therefore quite remarkable. It is further strong evidence that the nature of the Si–Al_2O_3 interface is independent of the method used to deposit the film. It should also be noted that the data of Tanaka and Iwauchi [22] were measured on a $\langle 111 \rangle$ silicon surface. This is consistent with our own results in Chapter 8 which show that the Al_2O_3-passivated $\langle 100 \rangle$ and $\langle 111 \rangle$ silicon surfaces are electrically indistinguishable.

4.2.5 Information from temperature-dependent measurements

In Fig. 4.5, the value of D_{it} determined by the conductance method is systematically lower than that determined from the quasi-static capacitance, diverging particularly at energies above E_i. In depletion, such divergence is readily explained. Since each state responds individually to the AC voltage signal according to its time constant for majority carrier capture and emission, interface states with capture time constants well outside (above or below) the measured frequency range will not be detected by the conductance method. On the other hand, such states, unless their capture rate is extremely low, will be detected by the quasi-static capacitance method. This may account for the lower D_{it} determined by the conductance method toward the valence band edge.

However, the increasing underestimation of total D_{it} by the conductance method at energies above E_i appears at first more difficult to explain. In the simple picture of the MIS equivalent circuit in inversion, the interface states are expected to be coupled together to the inversion layer node via their negligible capture resistance for electrons (R_{ns}), and therefore to respond to the AC signal as an ensemble characterised by a single time constant (determined by their average capture cross-section for majority carriers) [8], [144], [148]. In this case the measured conductance peak ought to represent the total concentration of interface states, regardless of their individual capture properties.

The reason for this apparent discrepancy is due to two factors. The first is that the assumption that R_{ns} is negligible for all states in weak inversion is not true in this case, either because σ_n of some of these states is extremely small, or merely because of the significant contribution of states at lower energies (with higher R_{ns}) to $\langle G_p \rangle/\omega$ due to surface potential fluctuations. This results in a $\langle G_p \rangle/\omega$ peak shape that deviates significantly from single-time-constant behaviour. The second factor is the finite frequency range of the measurement. As the surface potential moves into weak inversion, and the majority carrier concentration is reduced, the $\langle G_p \rangle/\omega(f)$ peak shifts to lower frequencies, so that in weak inversion only a part of the curve above the peak can be measured. Because the peak shape remains complex (i.e. a function of $D_{it}(E)$, σ_p, σ_n, and σ_s), fits to only this upper part of the curve will result in apparent parameters that differ from those that would be determined from the complete curve, if it could be measured, producing in this

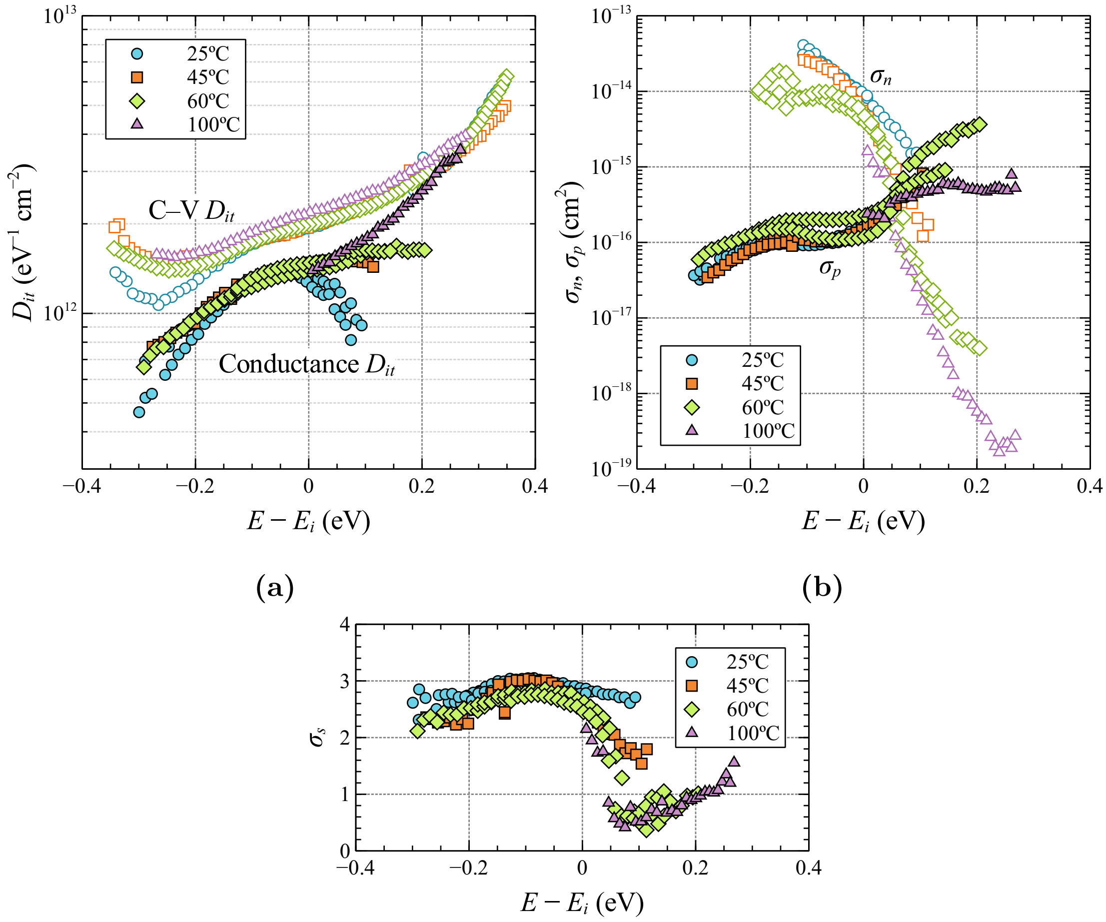

(a) **(b)**

(c)

Figure 4.8: Apparent Si–Al$_2$O$_3$ interface state properties determined from the conductance method for a p-type substrate at various temperatures. In some cases two separate sets of measurements were performed at a given temperature. The different figures show a) D_{it}, b) σ_p and σ_n, and c) σ_s, as a function of energy. D_{it} determined by the quasi-static C–V method is also shown for comparison.

case a spuriously low apparent D_{it}.

This can be demonstrated by performing the same measurements at higher temperatures, as shown in Fig. 4.8. This results in a shift of the $\langle G_p \rangle / \omega$ peak to higher frequencies, due to the increased surface carrier concentrations. Consequently, a larger portion of the $\langle G_p \rangle / \omega$ peak may be measured in weak inversion, and the apparent values of D_{it}, σ_p, σ_n, and σ_s approach those that would be determined from a fit of the complete peak. As a result, the apparent D_{it} shown in Fig. 4.8a increasingly approaches the value determined from C–V measurements as temperature increases, until at 100 °C the two are almost perfectly matching

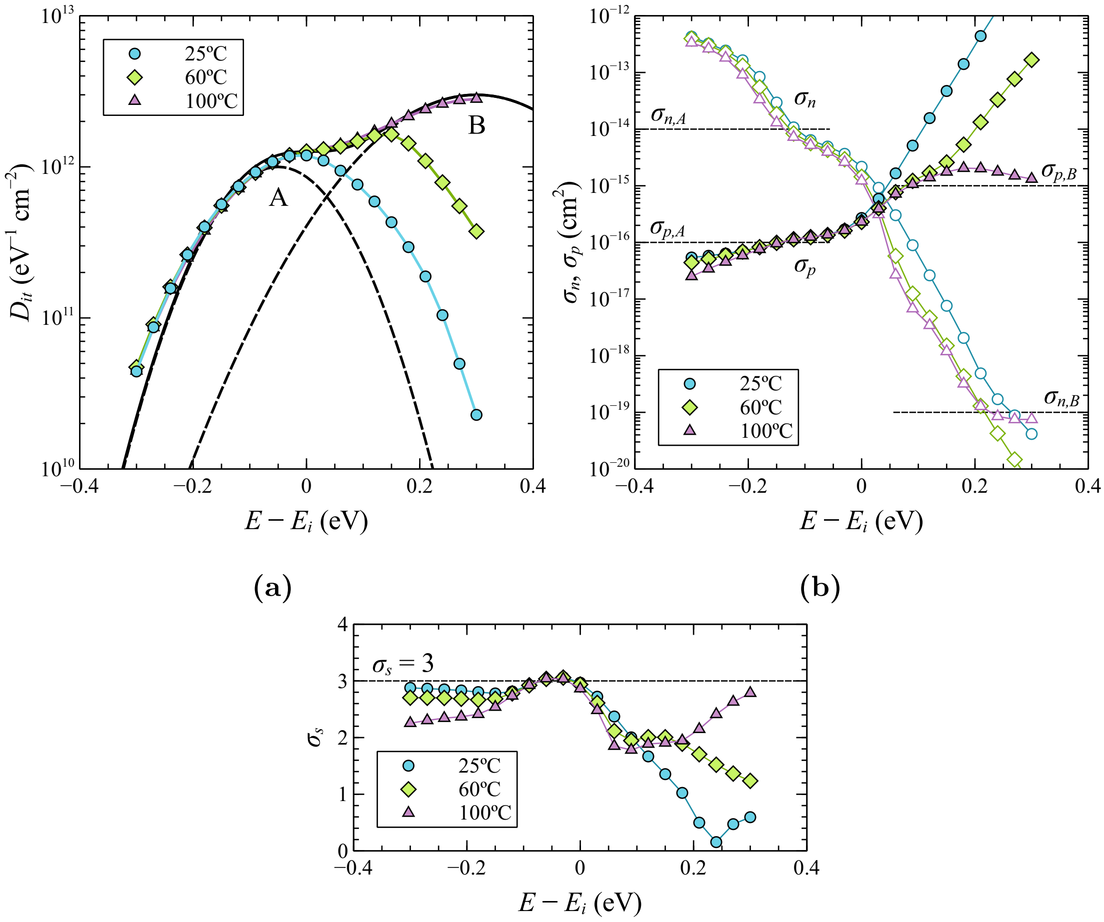

(a) **(b)**

(c)

Figure 4.9: Modelled apparent interface state properties as determined by the conductance method for a p-type substrate at various temperatures. The modelled interface includes two overlapping interface state distributions as shown in a), designated A and B. The states in each distribution have energy-independent capture cross-sections $\sigma_{p,A}$, $\sigma_{n,A}$, $\sigma_{p,B}$, and $\sigma_{n,B}$. These are shown as dashed lines in b). $\sigma_s = 3$. $\langle G_p \rangle / \omega$ data was modelled between 20 Hz and 1 MHz and fit over the same range to extract the apparent values.

at the onset of strong inversion.

The strong energy and temperature dependence of the apparent capture cross-sections, and even of σ_s, shown in Fig. 4.8, appears at first glance to suggest an underlying physical picture characterised by a rather high degree of complexity. In fact this apparent complexity can be shown to emerge in a straightforward manner from a small number of relatively simple components. Fig. 4.9 shows simulated apparent interface parameters as a function of energy and temperature for two Gaussian distributions of states with constant capture cross-sections. The properties of these distributions have been chosen to approximate the measured apparent values. Fitting of the simulated data was performed over the same frequency range as for the measurements (20 Hz to 1 MHz). The simulated data of Fig. 4.9 demonstrates a similar dependence on energy and temperature as observed for the experimental data of Fig. 4.8. In particular, a similar reduction of the apparent D_{it} at lower temperatures is seen in the upper part of the bandgap.

Despite this fairly good agreement, we ought to be cautious in assigning capture cross-sections to the interface states in the upper part of the bandgap. Data measured in inversion are more difficult to interpret, and preliminary investigations suggest that similar apparent capture cross-sections may be produced by a variety of combinations of $\sigma_{p,B}$ and $\sigma_{n,B}$. Measurements on n-type surfaces suggest a significantly higher value of $\sigma_{n,B}$ is required than that used in Fig. 4.8. There is also evidence that more than two types of interface states are present in this energy range, and would need to be considered in a fully successful model.

Determination of the physical parameters underlying measured conductance data represents a fairly complex case of mathematical inversion. Further work will need to be done to establish the best set of parameters to describe the entire Si–Al_2O_3 interface state spectrum. Nevertheless, it is clear that the fundamental approach adopted here—of treating the apparent values as arising from a small number of distinct interface state distributions with energy-independent properties—provides a sound basis for explaining the observed phenomena. For the time being we take the model shown in Fig. 4.5 and Table 4.1 as constituting a good initial description of the interface state most important to recombination. In the following section we compare this model to surface recombination measurements taken from a range of experiments. This model is also used in subsequent chapters to compare measurements of interface properties and surface recombination.

4.3 Comparison of model and experiment

In principle, the interface state model established in Section 4.2 and summarised in Table 4.1 can be used to calculate the surface recombination velocity via the physical theory described in Chapter 2, given values for $D_{it,midgap}$ and Q_{tot}. This requires an iterative solution of the surface potential in order to determine the surface carrier concentrations, as described in Section 2.3. S_{eff} may then be

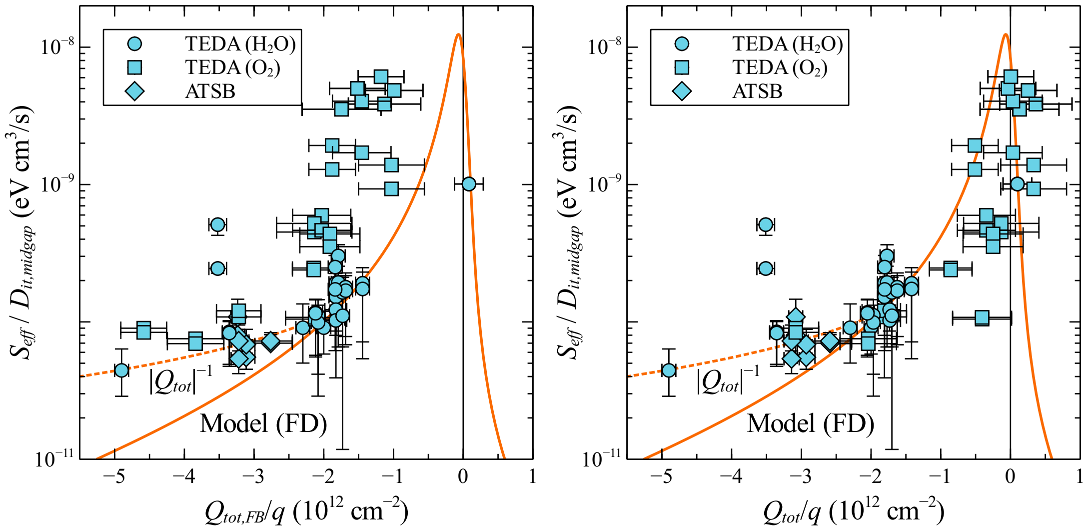

(a) **(b)**

Figure 4.10: Measured (symbols) and modelled (solid lines) S_{eff} at $\Delta n = 10^{15}\,\mathrm{cm}^{-3}$ for a $0.8\,\Omega\,\mathrm{cm}$ p-type substrate, normalized to $D_{it,midgap}$, versus total charge Q_{tot}, where Q_{tot} is evaluated either a) at flatbands (for a p- or n-type MIS structure), or b) under open-circuit, illuminated conditions. Horizontal error bars indicate uncertainty in Q_{tot} due to interface trapped charge Q_{it}. Vertical error bars show upper and lower limits of S_{eff} due to uncertainty in τ_{int}. Dotted lines show a $|Q_{tot}|^{-1}$ dependence, which empirically describes the data at large $|Q_{tot}|$.

calculated from Equation (2.18) or one of its approximations as described in Section 2.5, using the interface state parameters given for State A in Table 4.1.

Chapters 5 and 6 include results from a number of experiments in which S_{eff}, D_{it}, and Q_{tot} are determined for the same Al$_2$O$_3$ films. This allows a comparison of the S_{eff} calculated as just described from the interface properties to that determined from photoconductance measurements. In order to show this comparison across a large data set, we normalise the measured S_{eff} to $D_{it,midgap}$, using the fact that $S_{eff} \propto D_{it}$ from (2.18) and (2.22), and plot the normalised values as a function of Q_{tot}. We thereby isolate the influence of Q_{tot} on S_{eff}.

Fig. 4.10 shows normalised S_{eff} vs Q_{tot}. S_{eff} data are for p-type $\langle 100 \rangle$ FZ-Si wafers passivated with APCVD Al$_2$O$_3$ films deposited either from TEDA-TSB (H$_2$O or O$_2$ reactants), or from ATSB. Most data are for $0.8\,\Omega\,\mathrm{cm}$ substrates, while some are for $1\,\Omega\,\mathrm{cm}$ substrates. S_{eff} of the latter is adjusted to the doping level of the $0.8\,\Omega\,\mathrm{cm}$ samples, using the fact that for large $|Q_{tot}|$ ($|Q_{tot}| > 10^{12}\,\mathrm{cm}^{-3}$ for all such samples), $S_{eff} \propto (N_A + \Delta n)$ (see Equation (2.25)).

The values of Q_{tot} in Fig. 4.10a were evaluated from C–V measurements at flatbands ($Q_{tot,FB}$). This is the value usually quoted. In principle, we ought rather to consider the value of Q_{tot} under the conditions prevailing during the photoconductance measurement (i.e., open-circuit, non-zero injection, fixed doping). This value is generally not the same as $Q_{tot,FB}$, since the latter value includes $Q_{it,FB}$, the value of Q_{it} determined at flatbands, while Q_{it} generally is a function of surface potential. $Q_{it,FB}$ (and hence $Q_{tot,FB}$) naturally also depends significantly on the substrate doping type for the C–V measurement, being more negative for n-type substrates.

Under equilibrium conditions, the difference between Q_{it} and $Q_{it,FB}$ can in principle be assessed directly from C–V measurements, since these provide Q_{tot} as a function of surface potential. However, under non-equilibrium conditions, the occupancy of the interface states is no longer determined simply by the Fermi distribution, but depends on the dynamic properties of the interface states (their capture cross-sections), which are generally not known. Rather than attempt to resolve this difficulty, we have chosen to evaluate the non-equilibrium Q_{tot} from the measured $D_{it}(E)$ assuming that the occupancy of the interface states is simply determined by the majority carrier quasi-Fermi-level.

Fig. 4.10b shows normalised S_{eff} vs Q_{tot} where Q_{tot} is evaluated under non-equilibrium ($\Delta n = 10^{15}\,\mathrm{cm}^{-3}$) open-circuit conditions, and at a doping level corresponding to that of the photoconductance samples. The choice of where to evaluate Q_{tot} has a significant effect for samples with large D_{it}, which also tend to be those with the highest S_{eff}, even after normalising to D_{it}. This is especially the case where $Q_{tot,FB}$ was evaluated on n-type MIS structures, since the difference between Q_{it} and $Q_{it,FB}$ is greater in this case.

When plotted against the appropriate value of Q_{tot}, the data clearly follows a trend of decreasing S_{eff} with increasing (negative) Q_{tot}, as expected. The theoretical dependence predicted using Fermi–Dirac statistics, together with the interface state parameters for state A given in Table 4.1, is also shown. There is excellent quantitative agreement, especially in the range of $|Q_{tot}|/q = 1\text{–}2.5 \times 10^{12}\,\mathrm{cm}^{-2}$, which includes the most reliable data. We emphasise that the modelled curve is not a fit to the data, but is calculated directly from the measured interface properties, without any free parameters. Considering this, the quality of the agreement observed in Fig. 4.10b is remarkable.

For $|Q_{tot}|/q < 1 \times 10^{12}\,\mathrm{cm}^{-2}$, there is significant scatter in the data. This scatter can be attributed both to the significant uncertainty applying to Q_{tot} for all data in this range (due to the fact that D_{it} of these samples tends to be quite large), and secondly to the more pronounced dependence of S_{eff} on Q_{tot} as Q_{tot} approaches zero. It is therefore difficult to draw firm conclusions regarding the agreement or disagreement of the data and model in this range. However, the fact that the maximum measured S_{eff} is nevertheless very similar to the modelled peak value is encouraging. Note that the inclusion of surface potential fluctuations in the model is expected to lower the predicted peak value somewhat, which may improve the agreement. For significant $|Q_{tot}|$ the effect of such fluctuations should to be minimal, due to free carrier screening.

For large $|Q_{tot}|$, and assuming Boltzmann statistics, S_{eff} is expected to follow a $|Q_{tot}|^{-2}$ dependence as described by Equation (2.25). Under Fermi–Dirac statistics the rate of decrease of S_{eff} is even faster. In fact the data suggest that S_{eff} decreases more slowly with increasing $|Q_{tot}|$ than predicted by such theory, particularly for $|Q_{tot}|/q > 2 \times 10^{12}\,\text{cm}^{-2}$. This is consistent with previous studies which show a saturation of surface recombination with increasing surface charge under various experimental conditions [11], [153]–[157]. Empirically, the data in the range of $|Q_{tot}|/q > 2 \times 10^{12}\,\text{cm}^{-2}$ is better described by a $|Q_{tot}|^{-1}$ dependence (shown as a dotted line in the figure) than by the $|Q_{tot}|^{-2}$ dependence predicted by classical statistics. The reason for this discrepancy is likely to be related to the distribution of free charge near the semiconductor surface, which differs from that expected from Boltzmann or even Fermi–Dirac statistics due to charge quantisation effects at high surface fields.

It should be noted that the model shown in Fig. 4.10 is only expected to be valid for negative Q_{tot}. This is because it includes only a single donor-like state ($\sigma_n > \sigma_p$) that dominates recombination when holes are the majority carrier at the surface, but is an inefficient recombination centre when electrons are the majority carrier. This is the reason for the steep decrease in the modelled S_{eff} for positive Q_{tot}. Different interface states with larger σ_p are expected to dominate recombination in this regime, and would need to be included in a truly comprehensive model. The presence of such states will be inferred from recombination measurements of heavily phosphorus-doped surfaces in Chapter 7.

4.4 Conclusions

Investigations of the electrical properties of the Si–Al_2O_3 interface provide a remarkably consistent picture. The energetic distribution of interface states is asymmetric, with a minimum in the lower part of the gap. The shape of this distribution varies relatively little between Al_2O_3 films deposited in various ways, and may therefore be regarded as characteristic of the materials system. In addition, excellent agreement is found between the apparent majority carrier capture cross-sections determined here and those reported by previous authors, despite the use of significantly different deposition methods, which further highlights the general nature of the obtained results.

Capture cross-section measurements reveal the presence of a donor-like interface state ($\sigma_n > \sigma_p$) which dominates the distribution just below midgap, and allow its properties to be determined to a high degree of confidence. Due to its large σ_n, this state is expected to dominate recombination at Al_2O_3-passivated silicon surfaces where electrons are the minority carrier, which is the case in most situations of interest because of the negative charge of Al_2O_3. Finally, it is shown that the derived Si–Al_2O_3 interface state model may indeed be used to accurately predict the recombination rate at Al_2O_3-passivated silicon surfaces from measurements of D_{it} and Q_{tot}, thus providing a link between the measured interface parameters and passivation performance.

Chapter 5

Influence of Deposition Parameters

> *Before anything else, preparation is the key to success.*
>
> — Alexander Graham Bell

While the general nature of the electronic states present at the Si–Al_2O_3 interface appears remarkably insensitive to processing, the concentrations of these states, and hence the passivation properties of the interface, depend sensitively on the conditions under which this interface is formed, and therefore on the parameters of the deposition process in question. As described in Chapter 3, for APCVD the main deposition parameters which may be adjusted are the substrate temperature, the relative concentrations of the aluminium precursor and any additional reactants, and the precursor species itself. The following sections will describe the influence of each of these parameters in turn. The main results are presented in terms of τ_{eff} and S_{eff}. Values for D_{it} and Q_{tot} are also presented when available.

5.1 Substrate temperature

The temperature of the silicon substrate during the deposition reaction (designated T_{dep}) provides the energy available for the various chemical reactions involved in the deposition process, and as such it strongly influences the bulk and interfacial structure and properties of the resulting Al_2O_3 films. The influence on bulk properties will be described in Chapter 9. Here it is shown how the deposition temperature influences the Si–Al_2O_3 interface structure and associated

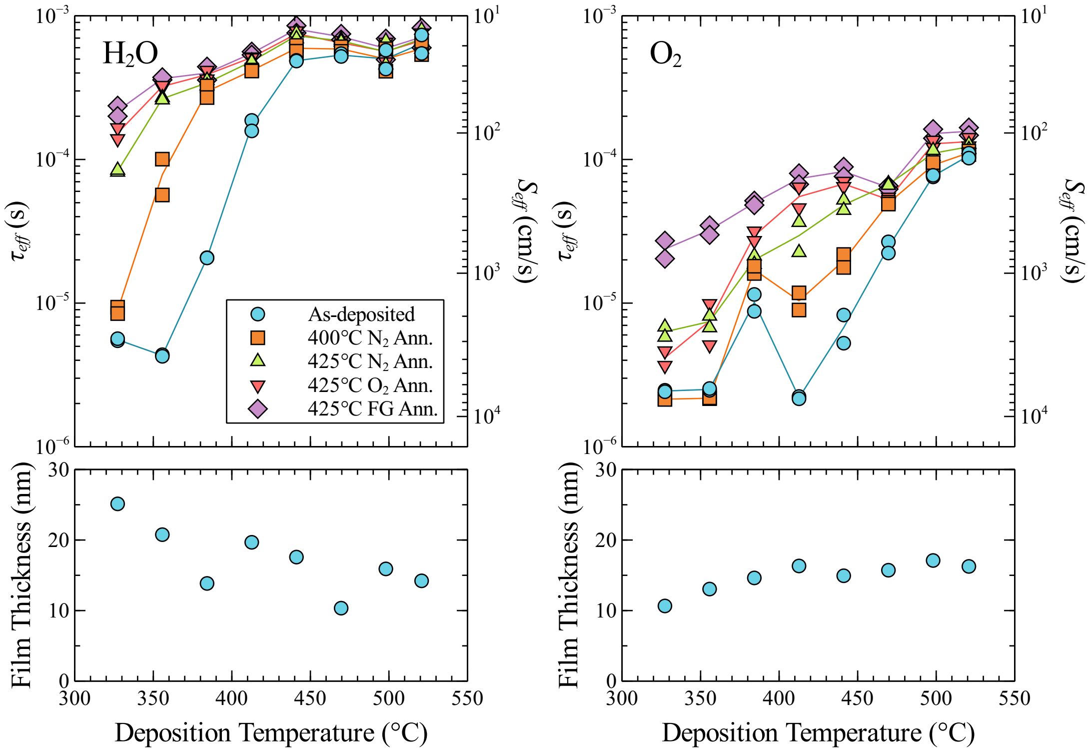

(a) **(b)**

Figure 5.1: τ_{eff} and S_{eff} as a function of deposition temperature for APCVD Al_2O_3 deposited from TEDA-TSB and either a) H_2O or b) O_2, as-deposited, and after various successive anneals. The thickness of the as-deposited films is also shown. TEDA-TSB flow was $1\,\mu L\,s^{-1}$, H_2O carrier flow was 0.25 SLPM, and O_2 flow was 0.7 SLPM. Substrates were 325 µm thick, 0.8 Ω cm *p*-type ⟨100⟩ FZ-Si.

passivation properties.

The influence of deposition temperature on the passivation properties of Al_2O_3 was investigated for films deposited from TEDA-TSB, with either H_2O or O_2 as co-reactants. The temperature profiles shown in Fig. 3.4 were used, resulting in values of T_{dep} ranging from 325 °C to 520 °C. For the case of H_2O as co-reactant the results were presented previously in [33].

5.1.1 H_2O

The passivation quality of films deposited from TEDA-TSB and H_2O improves significantly with increasing deposition temperature. Fig. 5.1a shows that τ_{eff} increases and S_{eff} decreases with increasing T_{dep}, up to a temperature of ∼440 °C. S_{eff} is approximately independent of T_{dep} for $T_{dep} \geq$ ∼440 °C, and quite low, at between 16 and 27 cm/s for a 0.8 Ω cm p-type substrate. Subsequent annealing reduces S_{eff} for all samples, particularly those with lower T_{dep}, reducing but not eliminating the dependence on T_{dep}. A minimum S_{eff} of 13 cm s^{-1} is reached at T_{dep} values of ~440 °C and ~520 °C.

This value of $S_{eff} = 13\,\mathrm{cm\,s^{-1}}$ represents an excellent degree of surface passivation, and is comparable to the best values reported for Al_2O_3 from thermal and spatial ALD (both 5 cm s^{-1}) and PECVD (6 cm s^{-1}) for less heavily doped 1.3 Ω cm p-type samples [87], and much better than the value of 55 cm s reported for sputtered films on the same 0.8 Ω cm substrates [37] For comparison, S_{eff} values of 7 cm s^{-1} and 14 cm s^{-1} (reassessed using the intrinsic lifetime model of [31]) have been reported as exemplary values for "alnealed" SiO_2 and PECVD SiN_x respectively on 1 Ω cm p-type substrates [158], [159]. It should be recalled that, from Equation (2.25), S_{eff} is expected to scale proportionally with $N_A + \Delta n$. We note also that significantly lower values of S_{eff} for APCVD Al_2O_3 films are reported in Chapter 6 (as low as 3 cm s^{-1} on 1.35 Ω cm p-type substrates).

Examination of Fig. 5.2 reveals that the decrease in S_{eff} with increasing T_{dep} can be attributed both to a decrease in D_{it} and to an increase in negative Q_{tot} for the as-deposited films. Both D_{it} and Q_{tot} saturate for $T_{dep} \geq$ ~440 °C, in accordance with the lifetime data, with $D_{it} \approx 1.4 \times 10^{11}\,\mathrm{eV^{-1}\,cm^{-2}}$ and $Q_{tot} \approx -2 \times 10^{12}\,\mathrm{cm^{-2}}$. After annealing, D_{it} is reduced for all T_{dep}, while the magnitude of negative Q_{tot} increases strongly at low T_{dep}, but remains relatively unchanged for $T_{dep} \geq$ ~440 °C.

5.1.2 O_2

For the Al_2O_3 films deposited from TEDA-TSB and O_2, the dependence of passivation level on temperature is qualitatively similar to the case for H_2O as reactant, in that S_{eff} decreases with increasing T_{dep} (Fig. 5.1b). S_{eff} also generally decreases following annealing. However, the apparent onset of saturation in S_{eff} is shifted to higher T_{dep} compared to the case for H_2O, occurring only for $T_{dep} >$ ~500 °C. S_{eff} is also significantly higher than for the H_2O samples throughout the whole range of T_{dep}, reaching a minimum value of ~140 cm s^{-1} at $T_{dep} =$ ~520 °C for the as-deposited films, close to a factor of 10 higher than the value of ~16 cm s^{-1} achieved by the H_2O films deposited at the same temperature.

Annealing again reduces S_{eff} for all samples. The anneal in forming gas appears to have a particularly pronounced effect in the case of these films, particularly for low T_{dep}, which may indicate that lack of interfacial hydrogen is

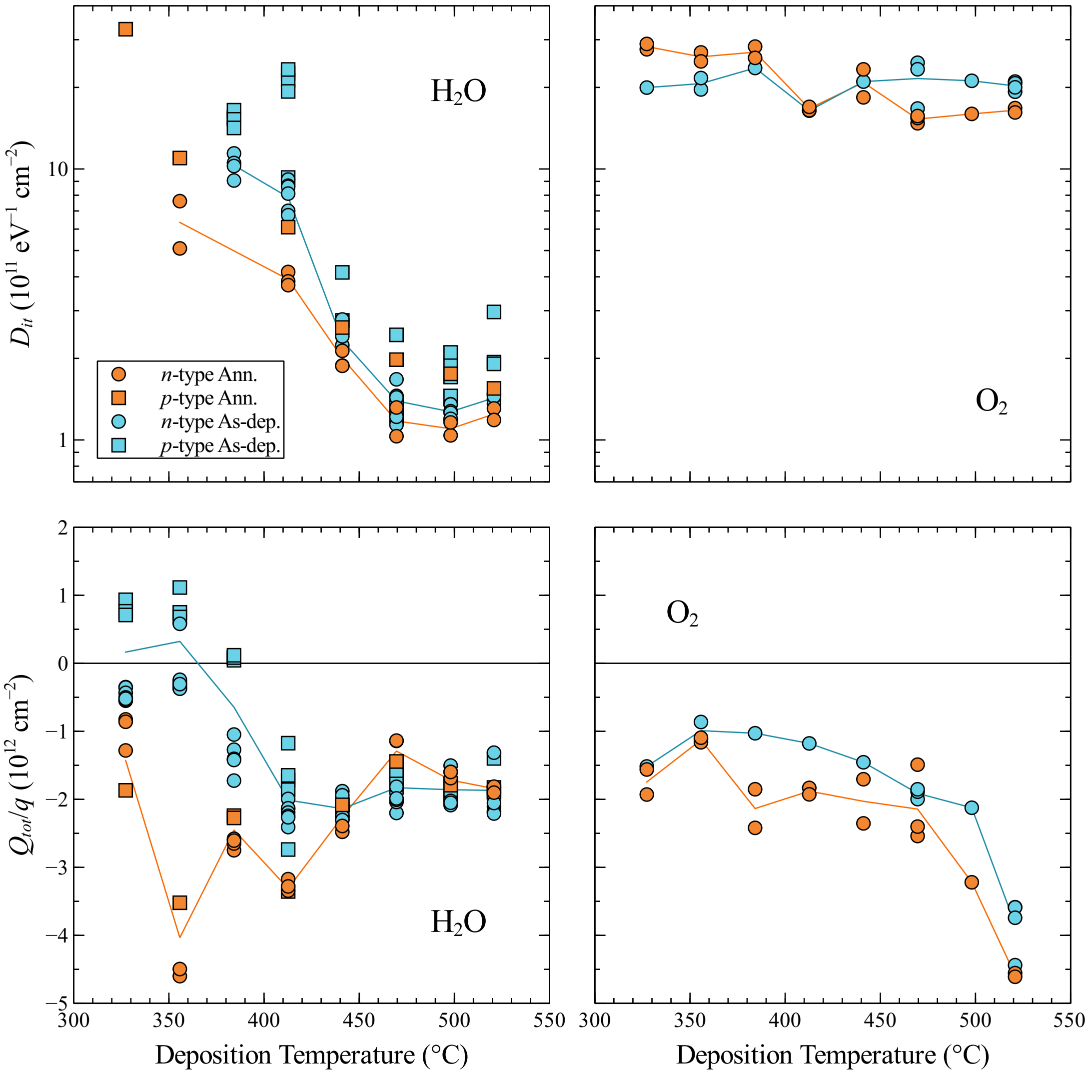

Figure 5.2: D_{it} (at midgap) and Q_{tot} as a function of deposition temperature for APCVD Al_2O_3 deposited from TEDA-TSB and either H_2O or O_2, as-deposited, and after annealing in N_2 at 400 °C for 30 min. Al_2O_3 deposition conditions were identical to those of the lifetime samples in Fig. 5.1.

limiting the passivation quality. After annealing, S_{eff} of the best films is reduced to slightly below 100 cm s^{-1}, which remains too high for high-efficiency devices.

Examination of D_{it} and Q_{tot} of the films deposited with O_2 reveals a qualitatively different behaviour to that of those deposited with H_2O. D_{it} appears to be essentially independent of T_{dep} for the as-deposited films, and relatively high at $\sim 2 \times 10^{12}$ eV^{-1} cm^{-2}, while an increasing negative Q_{tot} accounts for the decrease in S_{eff} with increasing T_{dep}. After annealing, D_{it} is reduced slightly for higher T_{dep}, but actually increases for lower T_{dep}, resulting in the appearance of a slight dependence of D_{it} on T_{dep}. The increase in D_{it} at low T_{dep} after annealing is consistent with the slight increase in S_{eff} observed for the corresponding lifetime samples.

The magnitude of Q_{tot} increases after annealing for all values of T_{dep}. This appears to account for a large part of the observed decrease in S_{eff}, especially for samples with T_{dep} in the middle of the examined range, for which the change in D_{it} is negligible. Contrary to the case for H_2O, films deposited with O_2 as reactant exhibit the largest values of Q_{tot} at high T_{dep}, both before and after annealing, and Q_{tot} does not appear to saturate within the examined range, increasing rapidly from approximately $-2 \times 10^{12}\,\text{cm}^{-2}$ at temperatures below ~440 °C to $-4.6 \times 10^{12}\,\text{cm}^{-2}$ at the highest examined T_{dep} of ~520 °C.

The reason for the much higher defect density (D_{it}) at the O_2-derived interface is not immediately apparent. It might be thought that these films lack the hydrogen provided by H_2O, but the Al precursor (TEDA-TSB) itself contains hydrogen, and certainly significant hydrogen is present in the bulk films (see Section 9.1). We may hypothesise that the activation energy of the chemical reaction that leads to a lowly defected interface structure is significantly higher for the case of TEDA-TSB + O_2 than for TEDA-TSB + H_2O, so that a higher substrate temperature, beyond the examined range, is required for this reaction to occur at a sufficient rate in the absence of other energy sources.

In general, regardless of the chemistry of the deposition reaction, it is apparent that higher deposition temperatures promote the formation of a high quality (low D_{it}) Si–Al_2O_3 interface, at least within the examined temperature range.[1] Conversely, the dependence of charge on temperature appears to be more complex, especially following subsequent thermal treatments, which may result in the location of the passivation optimum at some intermediate temperature.

5.2 Reactant concentration

During the Al_2O_3 deposition reaction, various oxygen-containing reactants (i.e. H_2O, O_2, O_3, or CO_2) provide the necessary building blocks for the formation of chemical bonds (Al–O and Si–O) at the interface and in the bulk of the film.[2]

---

[1] On the other hand, extended exposure to even higher temperatures may have a detrimental effect on D_{it}, as shown in Chapter 6.

[2] This may not be the case if the aluminium precursor itself contains sufficient oxygen for the deposition reaction, which is generally the case for aluminium alkoxide compounds such as e.g. ATSB. See Section 5.3.

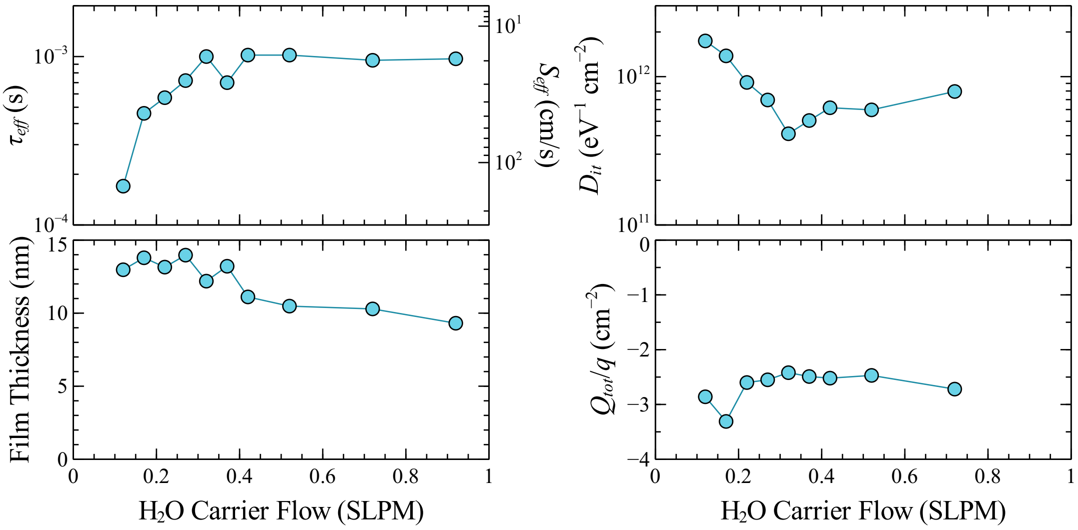

Figure 5.3: τ_{eff}, S_{eff}, film thickness, D_{it}, and Q_{tot} as a function of H_2O reactant concentration during Al_2O_3 deposition from TEDA-TSB. Deposition temperature was ~440 °C and TEDA-TSB flow was $1\,\mu L\,s^{-1}$. Lifetime substrates were ~500 µm thick, 1 Ω cm p-type ⟨100⟩ FZ-Si. C–V measurements were performed on co-deposited thickness monitor samples (2.6 Ω cm p-type ⟨100⟩ polished FZ-Si) which were not cleaned prior to deposition: D_{it} and Q_{tot} values should therefore be taken only as being indicative of the qualitative trends at a clean surface.

The Si–Al_2O_3 interfacial structure and resulting passivation properties may thus be strongly influenced by the supply of these reactant species, which is determined in part by their concentration in the vicinity of the substrate surface. This concentration can be controlled by changing the flow rate of the reactant to the APCVD system deposition zone. The following sections discuss the influence of H_2O and O_2 concentration on the passivation properties of Al_2O_3 films deposited from TEDA-TSB.

5.2.1 H_2O

The influence of H_2O reactant concentration on the surface passivation properties of Al_2O_3 films deposited from TEDA-TSB and H_2O was investigated by varying the volumetric flow of carrier nitrogen through the H_2O bubbler during Al_2O_3 deposition for various Al_2O_3-passivated lifetime samples. The total flow of gases through the reactant slot of the injector head was maintained at 3 SLPM by varying the flow of dilution nitrogen in turn, thereby preserving consistent flow dynamics within the deposition zone.

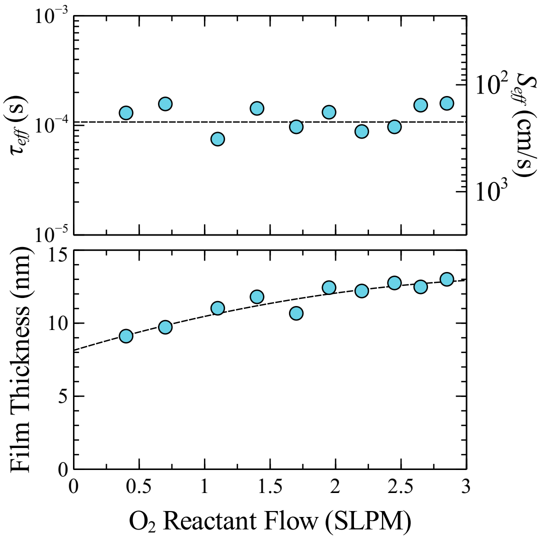

Figure 5.4: τ_{eff}, S_{eff}, and film thickness as a function of O_2 reactant concentration during Al_2O_3 deposition from TEDA-TSB. Deposition temperature was ~520 °C and TEDA-TSB flow was $1\,\mu L\,s^{-1}$. Lifetime substrates were ~500 µm thick, 1 Ω cm *p*-type ⟨100⟩ FZ-Si.

The H_2O reactant concentration has a strong effect on the passivation properties of Al_2O_3 films deposited from TEDA-TSB. As shown in Fig. 5.3a, S_{eff} decreases with increasing H_2O reactant flow, until it saturates at higher flow rates. Presumably, this saturation occurs when the relevant surface reactions are no longer limited by the supply of H_2O. However, the deposition rate also decreases somewhat with increasing H_2O concentration (Fig. 5.3b), probably due to parasitic gas-phase reactions between H_2O and precursor molecules. Figs. 5.3c and 5.3d show that the improved passivation may be attributed to a decrease in D_{it} with increasing H_2O concentration, rather than any change in Q_{tot}, which appears to be approximately independent of the reactant concentration.

5.2.2 O_2

In contrast to the case of H_2O, the dependence of Al_2O_3 passivation quality on O_2 concentration, when O_2 is used in place of H_2O as the reactant, is much less pronounced. Indeed, no significant dependence of surface passivation quality on O_2 concentration could be observed for O_2 flow rates ranging from 0.4 SLPM to 2.85 SLPM (Fig. 5.4a). On the other hand, a significant dependence of film thickness *was* observed, with film thickness increasing with O_2 concentration (Fig. 5.4b).

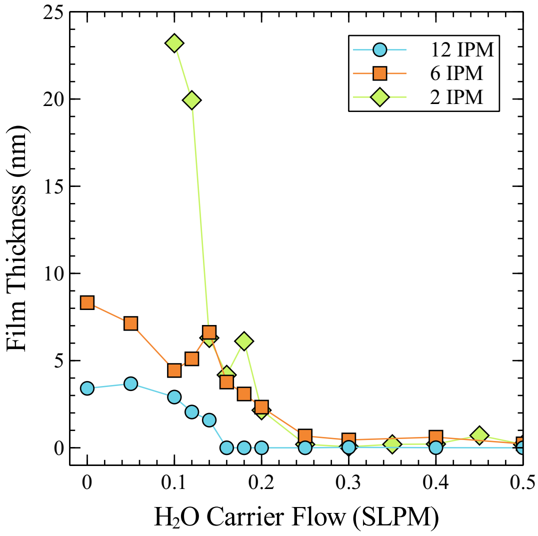

Figure 5.5: a) Film thickness vs volumetric flow rate of H_2O carrier nitrogen for Al_2O_3 deposited from ATSB, with belt speed (in inches per minute) as a parameter. H_2O bubbler temperature was 40 °C. The set-point temperature profile was the same at all belt speeds, and would result in a deposition temperature of ~440 °C at a belt speed of 12 inches/min. ATSB flow was $0.3\,\mu L\,s^{-1}$.

This may indicate that the deposition reaction at the silicon surface is not limited by the supply of oxygen, i.e. it is still surface-limited, rather than diffusion-limited, even at ~520 °C, while the bulk deposition reaction (with a presumably lower activation energy) *is* diffusion-limited to some extent.

5.3 Chemical precursor

As discussed in Section 3.1.3, a wide variety of potential chemical precursors for CVD of Al_2O_3 exist. The use of a different precursor can offer advantages in terms of cost, ease of handling, deposition rate, or other factors, but may also alter the passivation properties of the resulting films and the dependence of these properties on deposition conditions.

ATSB was selected as an interesting candidate for investigation as an alternative to TEDA-TSB or TMA. ATSB is inexpensive, liquid at room temperature, and non-pyrophoric. Its primary disadvantage is a relatively low vapour pressure, which limits the rate at which it can be delivered to the substrate, and hence the deposition rate. However, this can be overcome to some extent by increasing delivery line temperatures, and for thin passivation layers it is not a major issue.

An interesting property of ATSB, as a metal alkoxide compound, is its O:Al ratio of 3, well above the ratio of 1.5 of stoichiometric Al_2O_3. This opens up the possibility of performing Al_2O_3 deposition from ATSB without additional oxidising reactants, which has the potential to substantially simplify the deposition process and equipment.

Deposition experiments were performed in which TEDA-TSB was replaced by ATSB as the aluminium precursor, either without additional reactants, or together with H_2O or O_2. Deposition was achieved in all cases, but the presence of H_2O at the concentrations usually used together with TEDA-TSB was found to strongly suppress the deposition rate (Fig. 5.5), probably due to increasing parasitic gas-phase reactions as H_2O concentration is increased. A similar effect was observed by [131].

Because the film thickness resulting from a single deposition at the standard belt speed is quite low, multiple sequential depositions were performed in order to develop thicker films and investigate the importance of film thickness to passivation effectiveness. Film thickness was found to increase linearly with the number of deposition steps (Fig. 5.6a), with the deposition rate highest when no additional reactants were present. By comparison, the presence of O_2 was found to decrease the deposition rate slightly, though to a far lesser extent than H_2O.

The passivation performance of Al_2O_3 films deposited from ATSB improves with increasing film thickness (Fig. 5.6b), but does not appear to otherwise be influenced by the presence of O_2 or H_2O in the reactant gas flow. S_{eff} reaches a minimum value of $\sim 18\,\mathrm{cm\,s^{-1}}$ for the thickest film on a $1.1\,\Omega\,\mathrm{cm}$ p-type substrate. This represents an excellent level of surface passivation sufficient for high-efficiency devices (see Fig. 1.1). It is likely that further improvements in S_{eff} could be achieved by optimising the deposition temperature and by applying a post-deposition anneal. The passivation of the thinner films is also likely to be improved by their incorporation in a dielectric stack, as observed for very thin ALD Al_2O_3 films [62], [75].

Fig. 5.7 shows that the decrease in S_{eff} with increasing film thickness can be attributed almost entirely to a decrease in D_{it}, since Q_f remains practically constant. The small increase in total negative charge Q_{tot} (Fig. 5.7) is very likely accounted for by the reduction of positive Q_{it} as D_{it} is reduced. The interface quality of the thickest films is fairly good, with a moderately low D_{it} of $\sim 3 \times 10^{11}\,\mathrm{eV^{-1}\,cm^{-2}}$, and a large negative Q_{tot} of $-3.2 \times 10^{12}\,\mathrm{cm^{-2}}$. This value of Q_{tot} is significantly higher than that of films deposited from TEDA-TSB at the same temperature (Fig. 5.2), which compensates the higher D_{it}.

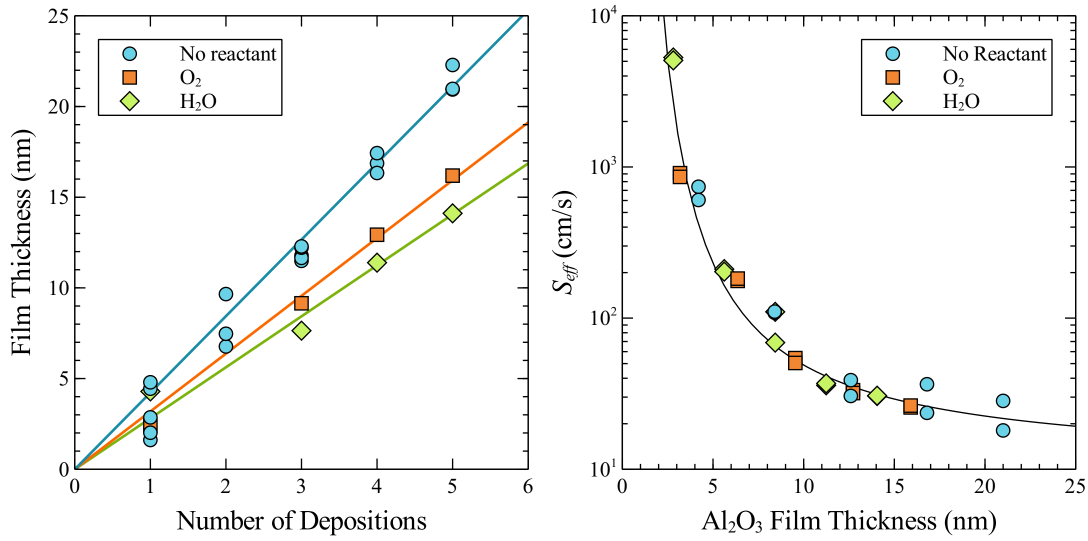

(a) (b)

Figure 5.6: a) Film thickness vs number of depositions, and b) S_{eff} vs film thickness, for Al_2O_3 deposited from ATSB either alone or with O_2 or H_2O as coreactants. Deposition temperature was ∼440 °C, ATSB flow was $0.3\,\mu L\,s^{-1}$, H_2O carrier flow was 0.12 SLPM, and O_2 flow was 0.7 SLPM. Lifetime substrates were 500 µm thick, 1.1 Ω cm *p*-type ⟨100⟩ FZ-Si. No separate post-deposition anneal was performed.

The characteristics of the Al_2O_3 deposition process from ATSB, in terms of the dependence of the interface quality on reactant type and concentration, are fundamentally different to the case of TEDA-TSB. In the latter case, the use of O_2 as reactant results in a poor interface quality, with high D_{it}, while the use of H_2O greatly reduces D_{it} at higher deposition temperatures, resulting in a high quality interface. For ATSB, a high-quality interface may be formed by deposition without additional reactants, or with O_2, while the presence of H_2O does not appear to enhance interface quality, but does strongly reduce the deposition rate. This contrasting behaviour highlights the sensitivity of the interface properties to the chemistry of the deposition reaction. Different chemical precursors may thus be more or less suited to synthesising interfaces with a low defect density.

5.4 Conclusions

In general, higher deposition temperatures tend to result in Al_2O_3 films with better passivation properties, at least within the examined temperature range.

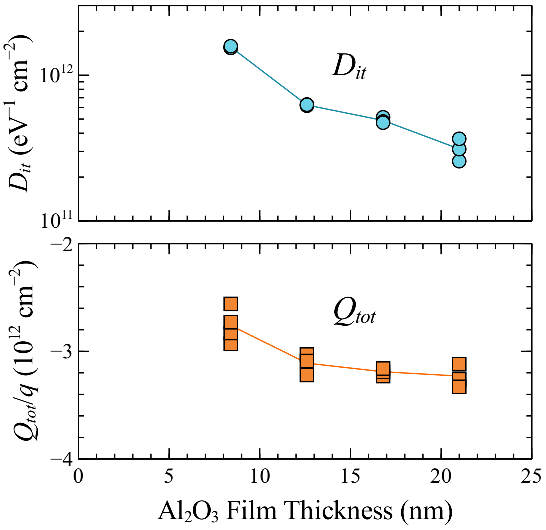

Figure 5.7: D_{it} and Q_{tot} vs film thickness for Al_2O_3 deposited from ATSB without additional reactants. Deposition conditions were the same as those of Fig. 5.6b. Substrates were 2.5 Ω cm *p*-type ⟨100⟩ FZ-Si

.

Different aluminium precursors exhibit qualitatively different behaviour in terms of the quality of the Si–Al_2O_3 interface resulting from their reaction with various oxidants. For TEDA-TSB, the use of H_2O as reactant results in much better passivation than that achieved with O_2, and passivation improves with increasing H_2O concentration. For ATSB, a high-quality interface may be formed without the presence of additional reactants, although low vapour pressure limits the deposition rate.

APCVD Al_2O_3 films deposited with both precursors were shown to be capable of providing excellent surface passivation, comparable with that reported for Al_2O_3 from other deposition techniques, and consistent with the requirements of high-efficiency silicon solar cells (see Fig. 1.1). The reason for this excellent passivation was found to be a very low interface state density D_{it} approaching $1 \times 10^{11}\,\mathrm{eV^{-1}\,cm^{-2}}$ combined with a large negative fixed charge Q_f of around $2 \times 10^{12}\,\mathrm{cm^{-2}}$. In Chapter 6 it will be shown that optimised post-deposition thermal processing may be used to reduce D_{it} and increase Q_f of APCVD Al_2O_3 still further, resulting in an exceptionally high level of surface passivation.

Based on the results presented in this chapter, a baseline deposition process using TEDA-TSB and H_2O as reactants, with the parameters specified in Table 5.1, was selected for use in subsequent experiments. These deposition conditions are those generally used in the experimental results presented in subsequent chapters,

Table 5.1: Parameters of the baseline Al_2O_3 deposition process.

Process Parameter	Value	Units
Deposition temperature	440	°C
Belt speed	12	IPM
TEDA-TSB flow	1	$\mu L\,s^{-1}$
H_2O carrier flow	0.5	SLPM
H_2O bubbler temperature	40	°C

except where otherwise noted, and typically result in an Al_2O_3 film thickness of $\sim$12 nm.

Chapter 6

Effect of Post-Deposition Thermal Processing

If you can't stand the heat, get out of the kitchen.

— Harry S. Truman

The quality of surface passivation provided by Al_2O_3 depends not only on the deposition conditions, but also on subsequent thermal processing. Indeed for Al_2O_3 films deposited at lower temperatures, some thermal treatment is generally required to "activate" the passivation. This step most commonly takes the form of an anneal performed at a temperature of 400–500 °C, typically in an N_2 ambient. In Chapter 5 it was shown that the APCVD Al_2O_3 films examined here also benefit from such an anneal, though those deposited at temperatures already above the annealing temperature benefit to a much lesser extent.

The effect of thermal processing at significantly higher temperatures appears to be more complex. The motivation for studying such effects comes primarily from the need to integrate Al_2O_3 passivation layers into solar cells featuring industry-standard screen-printed metallisation, which require a high-temperature contact-"firing" step subsequent to passivation. Several authors have reported that the surface passivation provided by both plasma-assisted and thermal ALD Al_2O_3 degrades substantially following a firing step [65], [67], [68], [70], and that this degradation can be mitigated by the addition of a PECVD SiN_x capping layer [45], [67], [68], [70]. Conversely, it has been reported by other authors that plasma-assisted ALD and PECVD Al_2O_3 films are relatively firing-stable, that their passivation suffers only minor degradation, and that a SiN_x capping layer has no effect on stability [44], [46], [66]. It appears that, as with other film characteristics, the deposition method and conditions may exert a significant influence on the thermal stability of the passivation.

In this chapter we examine the influence of high-temperature thermal processing on the passivation properties of the APCVD Al_2O_3 films described in Chapter 5. We first investigate the extent of compatibility with a standard industrial firing process. Both *p*- and *n*-type silicon substrates are considered, as well as boron-diffused planar surfaces, and we examine the influence of film thickness and a SiN_x capping layer. We then attempt to evaluate the influence of temperature in a more controlled manner using rapid thermal annealing. It will be shown that, while extended high-temperature processing can be detrimental to passivation, high-temperature thermal processing of shorter duration can be beneficial for passivation quality. Indeed, the use of a short high-temperature step, in combination with optimised deposition conditions, allows APCVD Al_2O_3 films to achieve a passivation quality rivalling the very best reported.[1]

6.1 Firing

Experimental investigations of the firing stability of the APCVD Al_2O_3 films were performed in collaboration with the Institut für Solarenergieforschung Hameln (ISFH). The results were previously published in [53].

Experimental method

Symmetrical lifetime structures were prepared on 1.35 Ω cm *p*-type and 1.2 Ω cm *n*-type, ⟨100⟩, 300 µm thick, 5 inch semi-square FZ Si wafers, and on boron-diffused 100 Ω cm *p*-type, ⟨100⟩, 435 µm thick, 4 inch FZ Si wafers. The latter received an $HF:HNO_3$ damage etch, while the former were electrochemically polished by the manufacturer. All received an RCA clean, with a final HF dip and DI water rinse performed immediately prior to Al_2O_3 deposition. Boron diffusions were performed in a quartz tube furnace at 900, 950, and 1000 °C from

---

[1] Several authors have reported significant blistering of Al_2O_3 or Al_2O_3/SiN_x stacks during high-temperature processing, particularly for thicker layers [44], [45], [69], [71]–[73], [160]. However, no conclusive correlation between visible blistering and changes in surface passivation has been reported. The evidence strongly suggests that blistering is at best an accompanying phenomenon of depassivation, and not its cause, except perhaps in extreme cases. More often it bears no relation to passivation at all. In this work we are concerned primarily with changes in surface passivation, and therefore we do not examine blistering in detail.

a liquid BBr_3 source, with sheet resistance measured by four-point probe prior to film deposition. The electrically active dopant profiles were measured by the electrochemical capacitance–voltage (ECV) method once processing and characterisation of the samples was complete. MIS structures for C–V measurements were prepared on $1\,\Omega\,\mathrm{cm}$ p-type, $\langle 100\rangle$, 480 µm thick, 4 inch FZ Si wafers. These received an HF:HNO_3 damage etch prior to the RCA clean and HF dip. Additional symmetrical lifetime structures were prepared on the same substrates for comparison. The MIS structures were contacted ohmically at the rear with GaIn paste, with gate contacts formed by thermal evaporation of Al dots ($\varnothing \approx 700\,\mu\mathrm{m}$). Metallization occurred after firing.

The Al_2O_3 films were deposited from TEDA-TSB and water vapour at a substrate temperature of ∼440 °C. An initial layer of ∼10 nm was deposited for all samples in order to ensure identical initial interface properties. Some samples subsequently received a second deposition of either 20 or 100 nm, resulting in total Al_2O_3 film thicknesses of approximately 10, 30 and 110 nm. This second deposition was performed at a lower belt speed and set-point temperature in order to produce a thicker film with a similar deposition temperature profile. The samples did not receive a separate post-deposition anneal. Some samples additionally received a 100 nm thick capping layer of PECVD SiN_x (Roth & Rau SiNA) with a refractive index $n = 2.05$ at 632 nm. The same film has previously been shown to improve firing stability when used as a capping layer for ALD Al_2O_3 films [70]. The 5 inch semi-square wafers were divided into $4 \times 4\,\mathrm{cm}^2$ pieces for lifetime measurements and firing, while the 4 inch undiffused wafers were quartered.

Firing was performed in an industrial infrared conveyor-belt furnace (Centrotherm Contact Firing Furnace DO-FF-8.600-300). A firing profile with a peak set-point temperature of 910 °C and belt speed of $5.9\,\mathrm{m\,min^{-1}}$ was used for most of the samples. In a few cases a slower profile with a peak set-point of 860 °C and a belt speed of $3\,\mathrm{m\,min^{-1}}$ was used instead. These profiles represent typical firing profiles used in the production of screen-printed solar cells, and are respectively the same as the “fast” and “slow” profiles used in [70]. Both profiles result in a similar peak wafer temperature of ∼810 °C, with approximately 6 and 12 s above 600 °C, respectively. Samples were characterised before and after firing, and again after illumination with a halogen lamp at $\sim 20\,\mathrm{mW\,cm^{-2}}$ for approximately 10 min.

Measurements of the saturation current density J_0 of the boron-diffused samples were performed under quasi-steady-state illumination using the generalised photoconductance analysis. The optical constant was determined from spectral reflectance and transmission measurements of the samples combined with knowledge of the flash spectrum and external quantum efficiency of the reference cell, in the manner of [133]. J_0 was extracted from the measured τ_{eff} via (2.34). The value of the derivative in (2.34) was calculated locally using a quadratic fit over five data points, and averaged over the range where it showed the least variation with Δn, which was generally for Δn between 1 and $2 \times 10^{16}\,\mathrm{cm}^{-3}$. Quasi-static and high-frequency (1 MHz) C–V measurements were performed at 25 °C.

Firing stability

Fig. 6.1 shows lifetime as-deposited, after firing (with the “fast” profile), and after firing and illumination, for p- and n-type samples with various thicknesses of Al_2O_3, with and without a SiN_x capping layer. Lifetimes of p-type samples generally dropped significantly after firing, but recovered above their initial values after a short period of illumination, as discussed below. Conversely, lifetimes of n-type samples occasionally fell, but in many cases increased after firing, and usually fell very slightly after illumination. Fig. 6.2 shows the injection dependence of the lifetime at each stage for several representative samples. In principle, the negative charge of Al_2O_3 could be expected to result in surface recombination velocities that are independent of the excess carrier concentration in low injection for p-type substrates, but significantly injection-dependent for n-type substrates (see Section 7.3). However other recombination mechanisms and measurement artefacts may also influence the effective lifetime. The significant dip in the lifetime of the p-type samples in low injection is likely due to bulk SRH recombination, while the apparent lack of an injection dependence in the lifetimes of the n-type samples is probably due to a depletion region modulation effect. Both dependencies are also observed for the same type of substrates passivated with plasma-assisted ALD Al_2O_3 layers [161].

Effect of Al_2O_3 film thickness and SiN_x capping layer

Although there was some amount of sample-to-sample variation in lifetime due to differences in film deposition conditions and handling damage, there appears to be little systematic influence of the Al_2O_3 film thickness on the thermal stability of the passivation. Indeed it is notable that even for samples that were known to have suffered significant handling damage before firing, the firing step actually tended to reduce or eliminate the lifetime disparity with other samples (data not

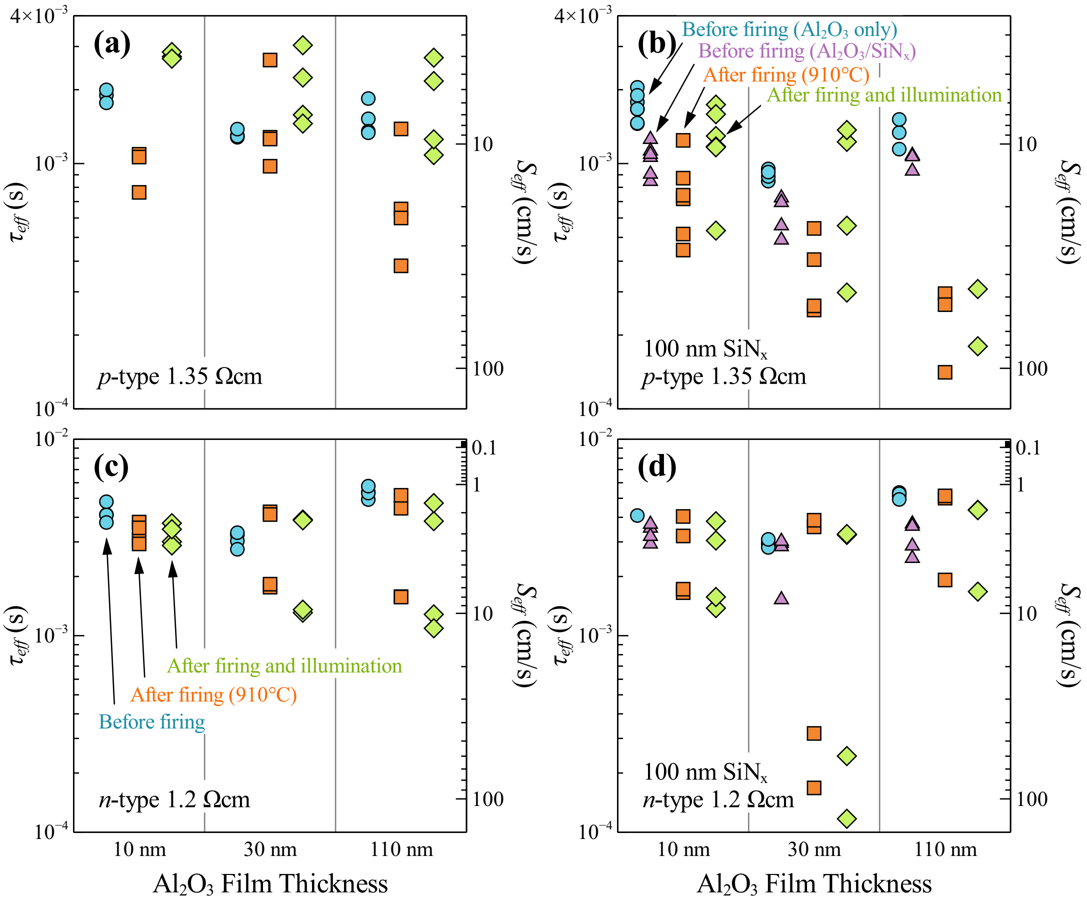

Figure 6.1: τ_{eff} and S_{eff} at $\Delta n = 10^{15}\,\mathrm{cm}^{-3}$, before and after firing, and after firing and illumination, for Al_2O_3 films of 10, 30, and 110 nm thickness, on *p*-type Si substrates a) without and b) with a SiN_x capping layer, and on *n*-type Si substrates c) without and d) with a SiN_x capping layer.

shown). There are two notable exceptions to this generally observed thickness independence. Firstly, the slightly lower initial lifetimes for the 30 nm Al_2O_3 films of Fig. 6.1b, c and d, which are reflected in lower post-firing lifetimes at least in the case of the *p*-type sample (Fig. 6.1b), are believed to be a result of the fact that these samples had their initial films stripped and re-deposited due to problems with the initial deposition. Secondly, the very low post-firing lifetime of the *p*-type sample with 110 nm thick SiN_x-capped film in Fig. 6.1b was observed to be correlated with significant blistering, which was minimal or non-existent on the other samples.

The addition of a SiN_x capping layer resulted in an initial reduction of lifetime for all samples, although the lifetime remained high. Firing stability appeared to

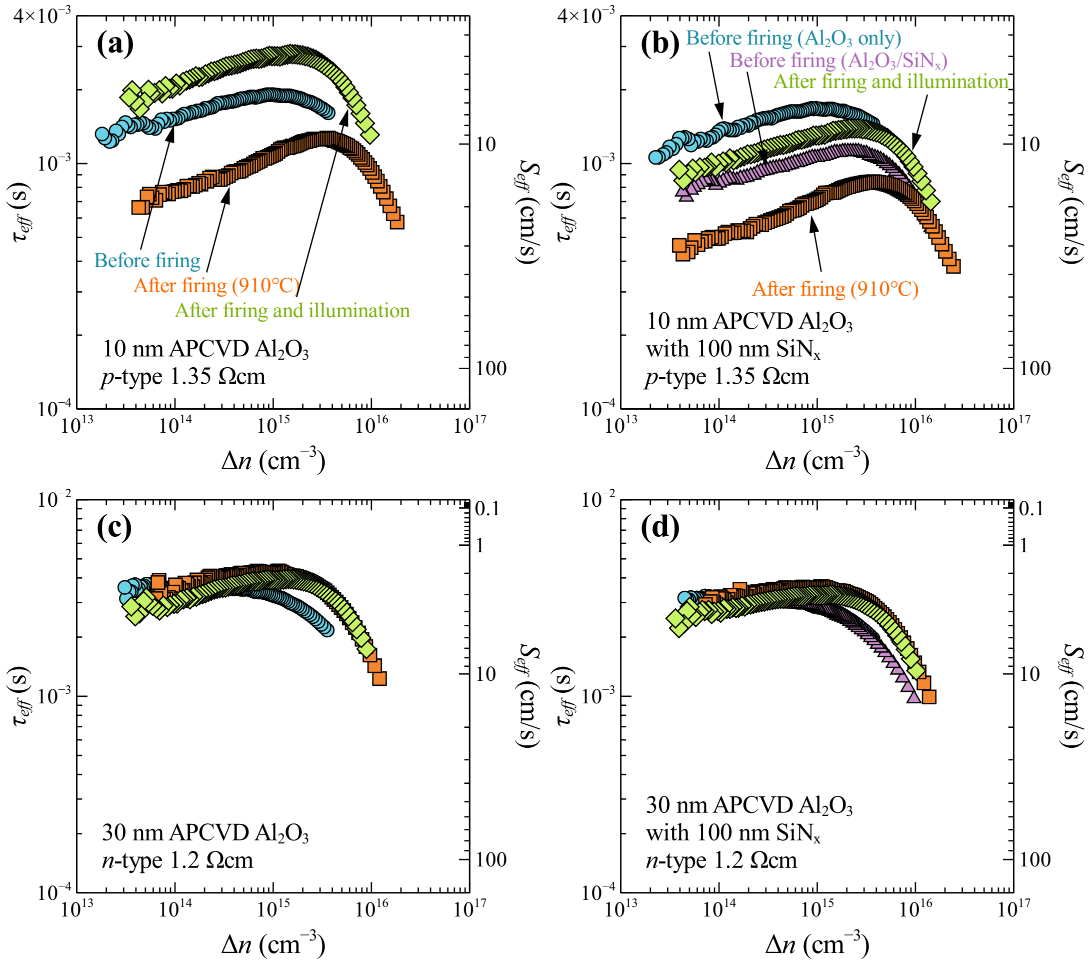

Figure 6.2: τ_{eff} as a function of Δn, both before and after firing, and after firing and illumination, for selected samples from Fig. 6.1.

be unaffected by the presence of the capping layer, with the SiN_x-capped samples exhibiting similar relative lifetime changes upon firing and illumination to those with single Al_2O_3 layers. Overall, the SiN_x capping layer neither helped nor significantly hindered the thermal stability of the Al_2O_3 passivation.

Effect of post-firing illumination

As noted above, it was found that for the p-type samples of Fig. 6.1, a short period of illumination resulted in a dramatic recovery of the post-firing lifetime to values above even the as-deposited values. Conversely, in n-type samples, post-firing illumination tended to reduce the lifetime very slightly from post-firing levels. This lifetime recovery effect for p-type samples under illumination has been reported previously for plasma-assisted ALD Al_2O_3 films on the same substrates after firing [70]. A similar effect with the same trends for *p*- and *n*-type samples has also been reported for SiO_x/SiN_x stacks [162]. It is clear that the effect is not related to bulk contamination by iron [163], because the lifetime increase occurs more or less uniformly across the whole injection range (Fig. 6.2). However, as noted below, the effect was not observed for samples prepared on other *p*-type substrates, both diffused and undiffused, so that we cannot rule out some influence of the substrate. Samples stored in the dark and remeasured 5 months after the initial firing and illumination showed lifetimes that had fallen by only 20–30 % of the difference between pre- and post-illumination values, indicating that the time constants involved in lifetime decay after illumination are much longer than those of the initial improvement. No significant change in lifetime under illumination was observed for the samples prior to firing.

Presuming that the effect represents a real change in the surface passivation, we should note that the level of illumination used is less than that to which cells would be exposed in the field, and that illumination on a single side appears to be sufficient to activate the recovery on both sides of the sample. Therefore, even rear-side Al_2O_3 passivation would likely be fully restored by illumination during device operation, without the need for additional processing steps. This indicates that the recovery is related to the increased carrier concentration under illumination, and not to the energy of the incident photons, since high energy photons will only be absorbed close to the illuminated surface.

Boron diffused surfaces

The passivation provided by the Al_2O_3 films on planar boron-diffused surfaces was also found to be firing stable. Fig. 6.3a shows the measured J_0 as a function of sheet resistance for the boron-diffused samples passivated with ~10 nm of Al_2O_3, both as-deposited, after firing with the "fast" profile, and after post-firing illumination. The inset shows the electrically active dopant profiles of the three diffusions, as measured by ECV. Fig. 6.3b graphically shows the J_0 extraction from the inverse lifetime via (2.34) for several representative samples. It can be seen that the data is quite linear, and therefore we can be confident in the accuracy of the extracted values. J_0 decreased somewhat in all cases after firing, indicating a slight improvement of the surface passivation. Conversely, post-firing illumination was found to have only a minor effect on J_0. This behavior contrasts with that of the undiffused *p*-type samples of Figs. 6.1a and b, which exhibited a reduced lifetime after firing, with a substantial increase following illumination.

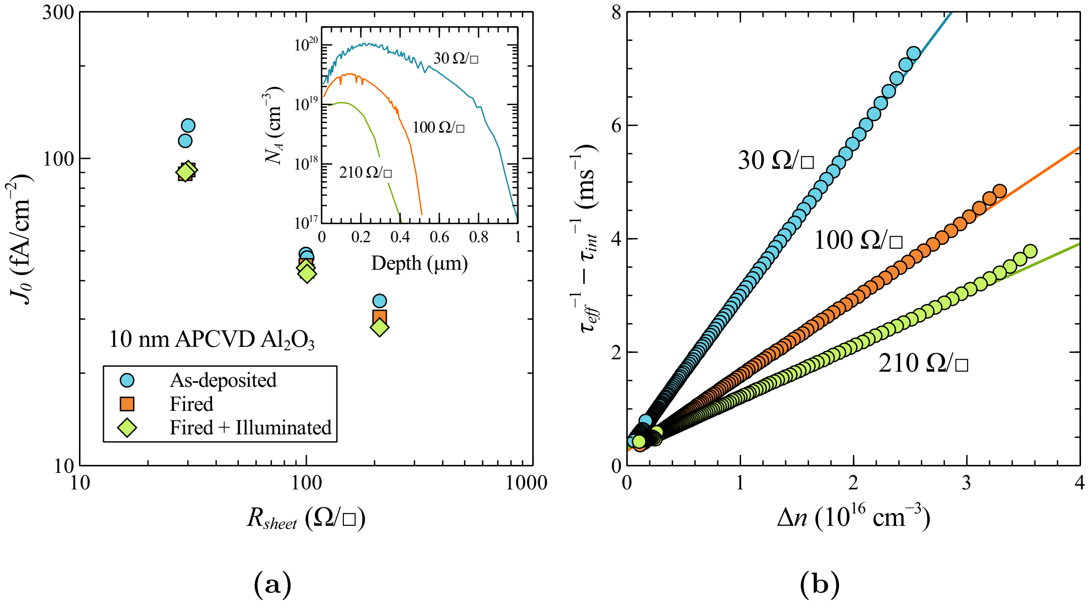

Figure 6.3: a) Saturation current density J_0 of boron-diffused samples passivated with ~10 nm Al_2O_3 as a function of the sheet resistivity of the diffusion R_{sheet}. Values are shown for the films both as-deposited, after firing with the "fast" profile, and again after illumination. The inset shows the active doping profiles of the diffusions determined by ECV measurements. b) Inverse τ_{eff}, corrected for bulk recombination, vs excess carrier density Δn, for several of the samples of Fig. 6.3a after illumination, showing the linear fits used to extract J_0 via (2.34).

J_0 values of 89, 42 and 28 fA cm^{-2} were measured on diffusions of 30, 100, and 210 Ω □$^{-1}$ respectively (with active surface dopant concentrations of 2×10^{19}, 1.3×10^{19}, and 9×10^{18} cm^{-3}) after firing.

Interface defect density and insulator charge

To investigate the physical mechanisms behind the changes in surface passivation observed after firing, C–V measurements were performed on *p*-type MIS structures with ~10 nm thick Al_2O_3 films, both as-deposited and after firing with either the "fast" or "slow" firing profiles. Corresponding lifetime samples were prepared on the same substrates for comparison, and fired together with the C–V samples. Note that these substrates differ from those of the *p*-type samples of Fig. 6.1. Fig. 6.4 shows the midgap interface defect density D_{it} and insulator fixed charge Q_f measured over a number of locations on each sample, while Table 6.1 summarizes the average values, and also shows S_{eff} measured on the corresponding lifetime samples. Fig. 6.5 shows the injection-dependent lifetime data for one

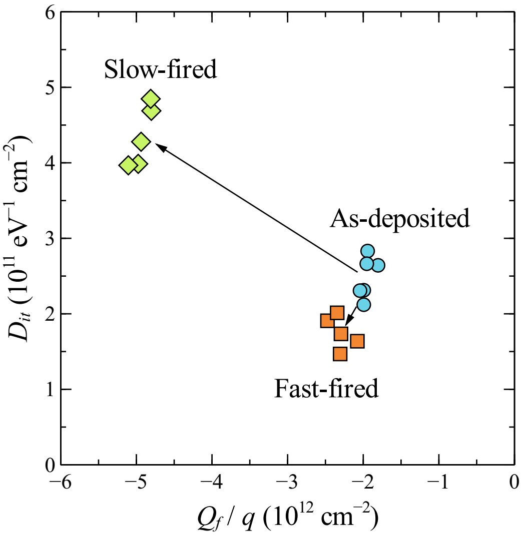

Figure 6.4: Midgap interface defect density D_{it} vs insulator fixed charge density Q_f/q for APCVD Al_2O_3 films as-deposited, and after firing with either the "fast" or "slow" firing profiles.

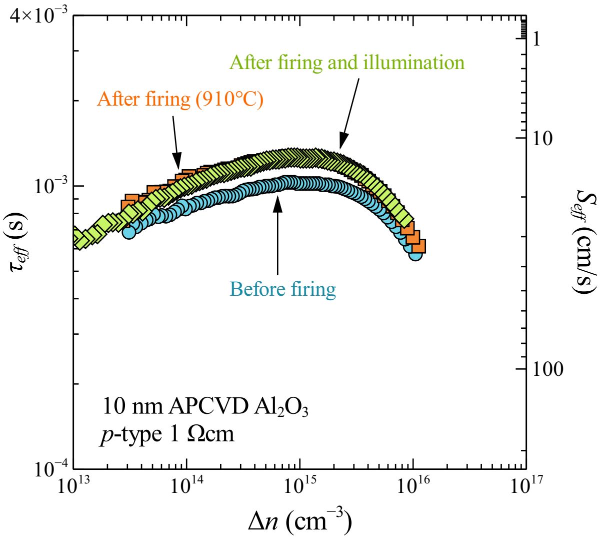

Figure 6.5: Effective excess carrier lifetime τ_{eff} as a function of excess carrier concentration Δn, both before and after firing, and after firing and illumination, for a lifetime sample fabricated on the same 1 Ω cm p-type wafers used for the C–V measurements, and fired using the "fast" profile.

of the fast-fired samples.

Firing the films with the "fast" profile resulted in a reduction of the average midgap D_{it} from 2.5 to 1.75×10^{11} eV^{-1} cm^{-2}, while the negative insulator fixed

Table 6.1: Average midgap D_{it} and Q_f derived from the data of Fig. 6.4, compared to S_{eff} measured on lifetime samples fabricated on the same $1\,\Omega\,\mathrm{cm}$ p-type substrates, for ~10 nm APCVD Al_2O_3 films as-deposited, and after firing with either the "fast" or "slow" profile. The value of S_{eff} predicted from this measured D_{it} and Q_f using the defect model of Chapter 4 is also shown.

Condition	D_{it} ($\mathrm{eV^{-1}\,cm^{-2}}$)	Q_f/q ($\mathrm{cm^{-2}}$)	Modelled S_{eff} ($\mathrm{cm\,s^{-1}}$)	Measured S_{eff} ($\mathrm{cm\,s^{-1}}$)
As-deposited	2.5×10^{11}	-2.0×10^{12}	21.9	17.8
Fast-fired	1.8×10^{11}	-2.3×10^{12}	11.7	12.8
Slow-fired	4.4×10^{11}	-4.9×10^{12}	6.4	15.3

charge Q_f/q increased slightly from -1.95 to $-2.3 \times 10^{12}\,\mathrm{cm^{-2}}$. This is consistent with the post-firing decrease in S_{eff} observed for the corresponding lifetime samples (Table 6.1), though it contrasts with the reduction in post-firing lifetime observed for most of the samples in Fig 6.1a prior to illumination. Firing with the "slow" profile resulted in a substantial increase in both D_{it} and Q_f/q to average values of $4.35 \times 10^{11}\,\mathrm{eV^{-1}\,cm^{-2}}$ and $-4.9 \times 10^{12}\,\mathrm{cm^{-2}}$ respectively. While the apparent measured Q_f includes interface trapped charge Q_{it}, which scales with D_{it}, this is unlikely to be greater than about $-1.5 \times 10^{11}\,\mathrm{cm^{-2}}$ in this case, and will almost certainly be positive, so that it cannot account for the increase in Q_f. The corresponding lifetime data show that the net result is a slight decrease in S_{eff} compared to the as-deposited films, with the increase in charge slightly overcompensating the increase in D_{it}.

Fig. 6.6a shows example C–V data for films as-deposited, and after firing with the fast and slow profiles. The increase of negative insulator fixed charge with firing can clearly be seen in the shift of the C–V curves to the right. Fig. 6.6b shows the corresponding interface defect energy distributions D_{it} calculated from the same data. The shape of the distribution is virtually unchanged after both firing steps, indicating that defect passivation or depassivation during firing does not significantly alter the relative concentration of different defect species at the interface.

Table 6.1 also shows S_{eff} calculated from the average measured D_{it} and Q_f values (also Table 6.1) with the Al_2O_3 interface model of Chapter 4. It can be seen that there is good quantitative agreement between the modeled and measured values of the surface recombination velocity for the as-deposited and

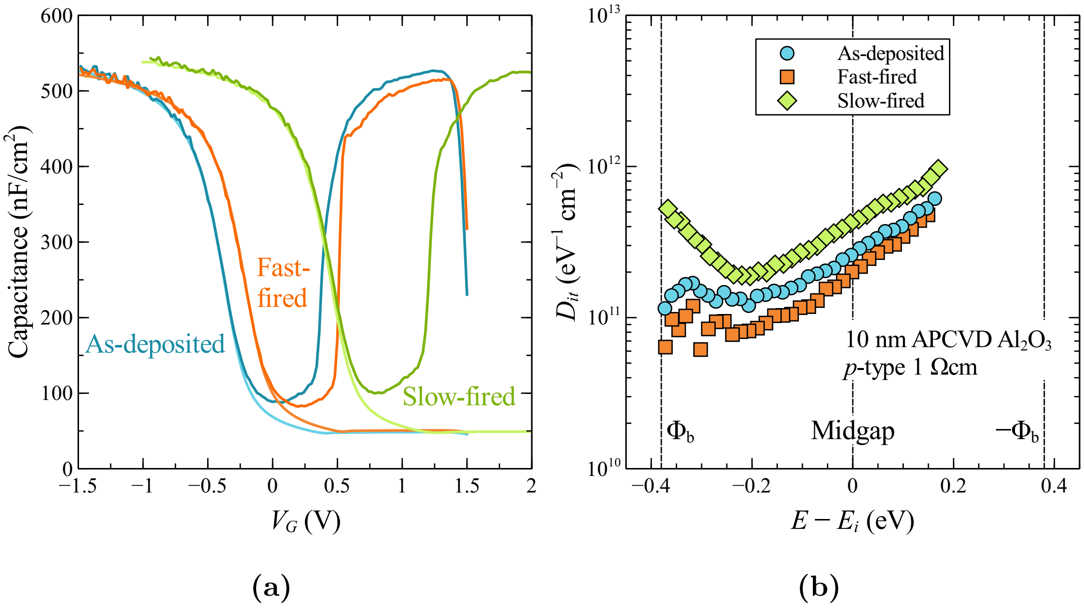

(a) **(b)**

Figure 6.6: a) Representative high frequency and quasi-static capacitance-voltage data, and b) corresponding interface defect density $D_{it}(E)$ as a function of energy with respect to midgap, for ∼10 nm APCVD Al_2O_3 as-deposited, and after firing with either the "fast" and "slow" firing profiles.

fast-fired samples, when Q_f/q is around $2 \times 10^{12}\,\mathrm{cm}^{-2}$, but the strength of the charge-assisted passivation due to the higher charge of the slow-fired films is significantly overestimated by the Boltzmann carrier statistics, consistent with the results of Section 4.3. The higher values of S_{eff} for these samples compared to the 1.35 Ω cm samples shown in Figs. 6.1 and 6.2 are only partly explained by the difference in dopant density. The additional difference may be due to a higher D_{it} as a result of the rougher surfaces of the 1 Ω cm samples, or due to differences between the actual bulk lifetime of the samples and the empirical parameterization of [31]. In neither case are our conclusions significantly affected.

Effect of post-firing illumination on C–V characteristics

Several attempts were made to probe the previously observed illumination recovery effect via C–V measurements. MIS samples were measured before and after several minutes of illumination with a halogen lamp at 50 W (illumination occurred with the ∼100 nm thick Al gate contacts in place, but the diffusion length in these samples should be greater than the diameter of the contacts, and the effect appears to be induced by the carrier concentration rather than the photon energy). No significant change in $D_{it}(E)$ or Q_f was observed after illumination.

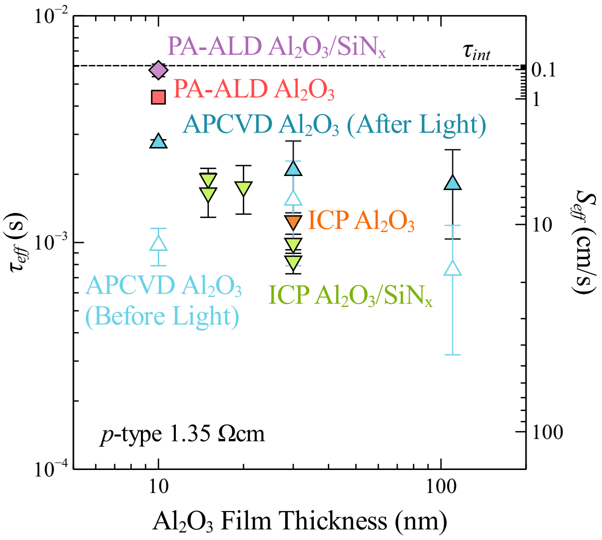

Figure 6.7: Comparison of post-firing lifetimes for Al_2O_3 films and Al_2O_3/SiN_x stacks deposited by various methods. All samples were fabricated on the same 300 µm thick, 1.35 Ω cm p-type samples, and fired with the same "fast" firing profile. Data points show average values and error bars the standard deviation derived from multiple samples. The intrinsic bulk lifetime according to the parameterisation of [31] is indicated by the dotted line. Data for the plasma-assisted ALD and inductively coupled plasma (ICP) PECVD samples are from [46].

The high frequency capacitance at zero bias was also monitored prior to and immediately after the removal of illumination. If charge injection under illumination were creating additional insulator charge, the C–V curves would shift along the voltage axis and the capacitance at a given gate bias would increase or decrease accordingly. However, no such change in the capacitance was observed.

The lack of response of the MIS samples to illumination is consistent with the behaviour of the lifetime samples on the same substrates. These exhibited only a very small increase in τ_{eff} after illumination, which could be entirely attributed to the presence of a small concentration of iron in the silicon bulk (from the difference in pre- and post-illumination injection-dependence of τ_{eff}). Coupled with the similar behaviour of the boron-diffused samples with respect to firing and illumination, this suggests that the behaviour observed for the p-type samples of Fig. 6.1 and 6.2 might be a substrate-dependent effect, rather than an intrinsic property of the films. This is unexpected, and indeed the use of different substrates for the MIS measurements, which revealed this dependence, was based on the opposite assumption.

Comparison to other deposition methods

Fig. 6.7 compares post-firing lifetimes as a function of film thickness for Al_2O_3 single layers and Al_2O_3/SiN_x stacks deposited by several different methods, including plasma-assisted ALD and inductively coupled plasma (ICP) PECVD [46], as well as the APCVD results reported here. Error bars show the standard deviation of measurements for multiple samples. The comparison is direct because both the substrates and the firing conditions are identical. It can be seen that the APCVD films perform well relative to those deposited by other techniques, with generally higher lifetimes than for the ICP PECVD films, at least after illumination, and not far below the state-of-the-art plasma-assisted ALD films, which in any case are not suitable for high throughput applications because of their low deposition rate. All of the films provide a level of surface passivation sufficiently high that it would not limit the efficiency of a typical industrial high-efficiency cell (see Fig. 1.1).

Summary

Al_2O_3 films deposited by APCVD have been shown to provide excellent, stable surface passivation under a typical high-temperature fast-firing step, as used in the metallization of screen-printed silicon solar cells. Passivation generally showed minor changes for n-type samples and improved for p-type samples and boron-diffused planar samples following firing and illumination. Final lifetimes were generally sufficiently high that they would not limit solar cell efficiency. Initial degradation after firing, and recovery under illumination, was observed for some p-type substrates, but not others, suggesting a substrate dependence of the effect. No systematic dependence on the Al_2O_3 film thickness, or on the presence or absence of a SiN_x capping layer, was observed. C–V measurements showed that short firing times resulted in an initial reduction of interface defect density D_{it} and a small increase in insulator charge Q_f, while longer firing times led to substantial increases in both D_{it} and Q_f. These results demonstrate the suitability of APCVD Al_2O_3 for integration into devices undergoing rapid high-temperature thermal processing.

6.2 Rapid thermal annealing

The results of Section 6.1 show that a short high-temperature contact-firing step in a belt furnace can either reduce or increase D_{it}, and may result in either small or large changes in Q_f, depending on the duration of such treatment. It is clear then that the response of the interface properties to such high temperature steps is a complex one that is likely to include both temperature and time dependencies. It is also clear that by carefully tuning the post-thermal treatment, we can expect to further optimise the passivation properties of the films.

Experimental method

In order to more systematically investigate the influence of short high-temperature treatments on passivation, a commercial RTA system using infrared lamps was used to heat samples with well controlled temperature profiles. Symmetrical lifetime structures were prepared on ∼480 µm thick, 1 Ω cm p-type ⟨100⟩ FZ-Si wafers, with Al_2O_3 passivation layers deposited at various temperatures. These then received an RTA with a 40 °C s^{-1} ramp rate and a 1 s peak at temperatures of between 500 and 900 °C in an N_2 ambient. In some cases a standard furnace anneal at 425 °C was performed prior to the RTA step.

Lifetime measurements were performed immediately following Al_2O_3 deposition and after each subsequent heat treatment. Analysis of the data is complicated by the fact that contamination of the wafer bulk was also found to occur during the RTA step. This is apparent from the fact that the resulting τ_{eff} exhibits a pronounced dip in low injection, characteristic of a SRH recombination process. This reduced lifetime also remains after stripping the original film and repassivating the surface, and is observed for wafers given an RTA prior to Al_2O_3 deposition. The magnitude of this lifetime reduction was found to increase with increasing RTA temperature, generally being negligible at temperatures of 550 °C or below.

Comparison of $\tau_{eff}(\Delta n)$ before and after the application of strong illumination revealed that bulk iron contamination was definitely present, although neither interstitial iron (Fe_i) or iron-boron pairs (FeB) are sufficient to explain all of the observed injection dependence, when using the parameters of [163], [164]. Nevertheless, it was found that the post-illumination lifetime data for all samples could be accurately modelled by assuming surface recombination described by a constant J_0 (i.e. Equation (2.20) is valid) and two bulk defects: one with the characteristics of interstitial iron (Fe_i) [163], [164], and one with a σ_n/σ_p ratio of 2.5. The resulting effective lifetime is described by the following equation:

$$\tau_{eff}^{-1} = \frac{J_0}{qW(N_A + \Delta n)} + \tau_{int}^{-1} + \tau_{SRH,Fe_i}^{-1} + \tau_{SRH,2}^{-1}\,, \tag{6.1}$$

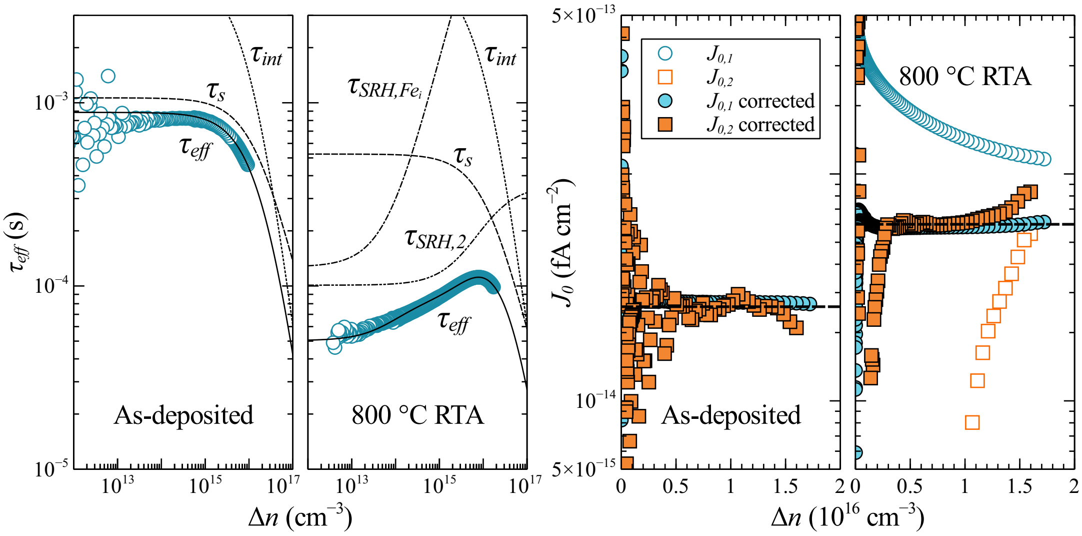

(a) **(b)**

Figure 6.8: a) τ_{eff} and b) J_0 as a function of Δn for an Al_2O_3-passivated sample ($T_{dep} = 410\,°C$, no anneal) before and after RTA at 800 °C. The various contributions to τ_{eff} in Equation (6.1) are shown, along with J_0 calculated from both Equation (2.33) ($J_{0,1}$) and Equation (2.34) ($J_{0,2}$). Prior to RTA, τ_{eff} is well-described by Equation (6.1) without the SRH terms, and $J_{0,1}$ and $J_{0,2}$ agree closely without the need for any corrections. After RTA, significant bulk contamination is present, and $J_{0,1}$ and $J_{0,2}$ diverge. The bulk SRH components are determined such that good agreement is achieved between $J_{0,1}$ and $J_{0,2}$ calculated from the corrected τ_{eff}. Dashed lines show the extracted J_0 values in each case.

where τ_{SRH,Fe_i} and $\tau_{SRH,2}$ account for bulk SRH recombination via interstitial iron (Fe_i) defects and the second unidentified defect, respectively.

Fig. 6.8 illustrates the process of J_0 extraction via (6.1). For the samples measured prior to RTA, and for those measured after RTA at the two lowest peak temperatures (500 and 550 °C), excellent agreement between the data and Equation (6.1) was obtained while neglecting the SRH terms, indicating negligible bulk contamination in these samples. Excellent agreement between J_0 calculated by Equations (2.33) and (2.34) was also obtained for these samples. For the other samples, J_0 was calculated by adjusting the concentration of the two bulk defect types in order to give good agreement both between Equation (6.1) and the measured τ_{eff}, and also between J_0 calculated from Equations (2.33) and (2.34). Fig. 6.9 shows the extracted bulk defect concentrations as a function of RTA peak temperature, assuming $\sigma_p = 1 \times 10^{-15}\,\mathrm{cm}^2$ for the second defect.

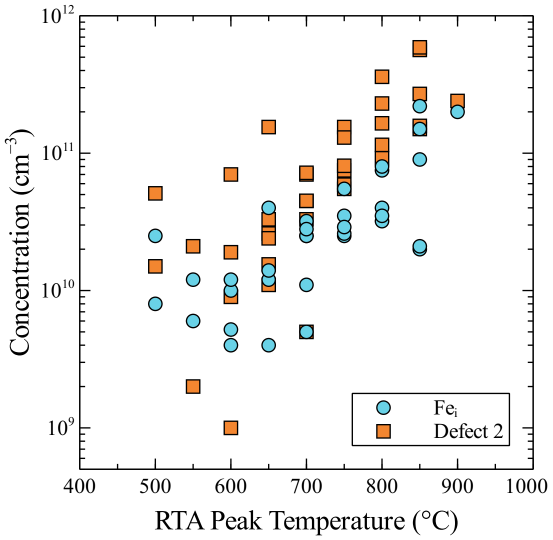

Figure 6.9: Bulk concentration of $\mathrm{Fe_i}$ and the second, unidentified defect as a function of RTA peak temperature, as determined during J_0 extraction using Equation (6.1). $\sigma_p = 1 \times 10^{-15}\,\mathrm{cm}^2$ is assumed for the second defect.

Despite some scatter, there is a clear trend of increasing bulk defect concentration with increasing RTA temperature, which is likely associated with the diffusion of metallic contaminants.

J_0 results

Fig. 6.10 shows J_0 extracted in this way for each sample set as a function of the peak RTA temperature. A number of trends are apparent. For films deposited at temperatures of 325 and 355 °C, J_0 as-deposited is rather high, but improves substantially upon RTA. An optimum RTA temperature exists within the examined range, and this shifts to lower temperatures as deposition temperature increases. For the films deposited at 385 °C, J_0 as-deposited is quite variable, because the deposition temperature is in the transition region where substantial changes in interface quality occur. J_0 after RTA is generally substantially reduced, except in the case of RTA temperatures greater than 800 °C, and displays much less random variation, increasing with RTA temperature. As the deposition temperature increases further to 410 °C, the as-deposited J_0 stabilises at a significantly lower level, while the RTA temperature above which J_0 increases rather than decreases after RTA is reduced to between 600 and 650 °C. The use of a standard anneal prior to RTA initially reduces J_0, but results in somewhat higher J_0 after RTA. At a deposition temperature of 440 °C, J_0 is no longer significantly reduced by

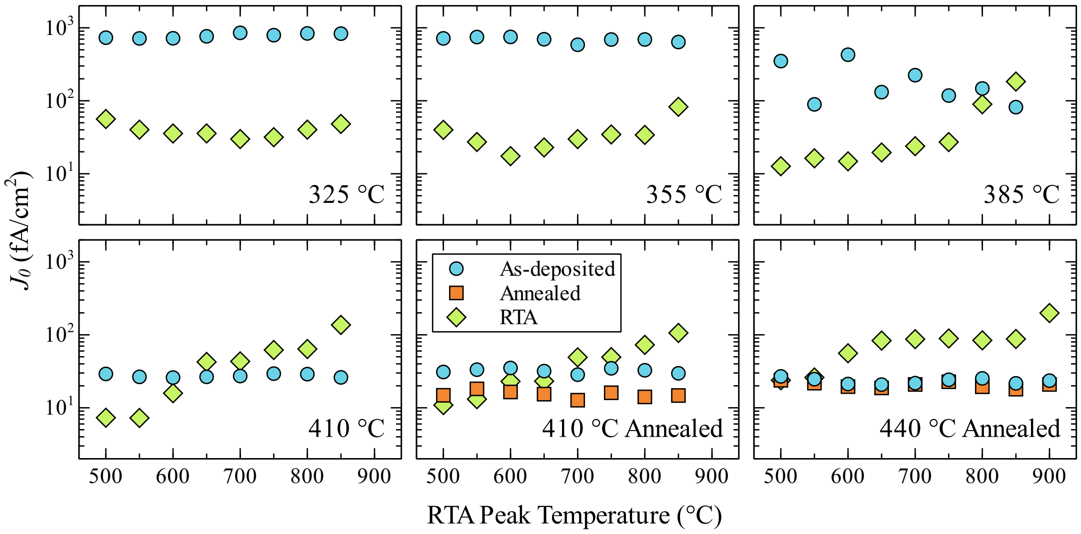

Figure 6.10: J_0 as a function of RTA peak temperature for Al_2O_3 films deposited at various temperatures (indicated in each subfigure) on undiffused p-type surfaces, with or without an intermediate anneal at 425 °C in N_2. Values are shown for the films as-deposited, after annealing (if applicable), and after RTA. TEDA-TSB flow was 1 µL s^{-1}, and H_2O carrier flow was 0.4 SLPM. Substrates were ~480 µm thick, 1 Ω cm p-type ⟨100⟩ FZ-Si.

annealing, and is significantly increased by RTA at temperatures of 600 °C or above.

Fig. 6.11a shows post-RTA J_0 in the form of a contour map, as a function of both Al_2O_3 deposition temperature and RTA peak temperature. Fig. 6.11a shows clearly that the optimum Al_2O_3 deposition temperature (in terms of minimising J_0) depends strongly on the post-deposition thermal processing to be applied. For RTA peak temperatures between 500 and 600 °C, the optimum deposition temperature occurs at ~410 °C. As RTA peak temperature increases, the optimum deposition temperature decreases, falling to ~350 °C at an RTA peak temperature of 800 °C.

Al_2O_3 films deposited at higher temperatures display excellent passivation following low-temperature RTA heat treatment, but their passivation quality degrades substantially at higher temperatures. Conversely, films deposited at lower temperatures require moderate heat treatment to reach their minimum J_0 values, which are not as low as those of higher temperature films, but maintain their passivation quality over a broader and higher range of RTA temperatures. This difference in thermal stability may be related to the greater hydrogen content of

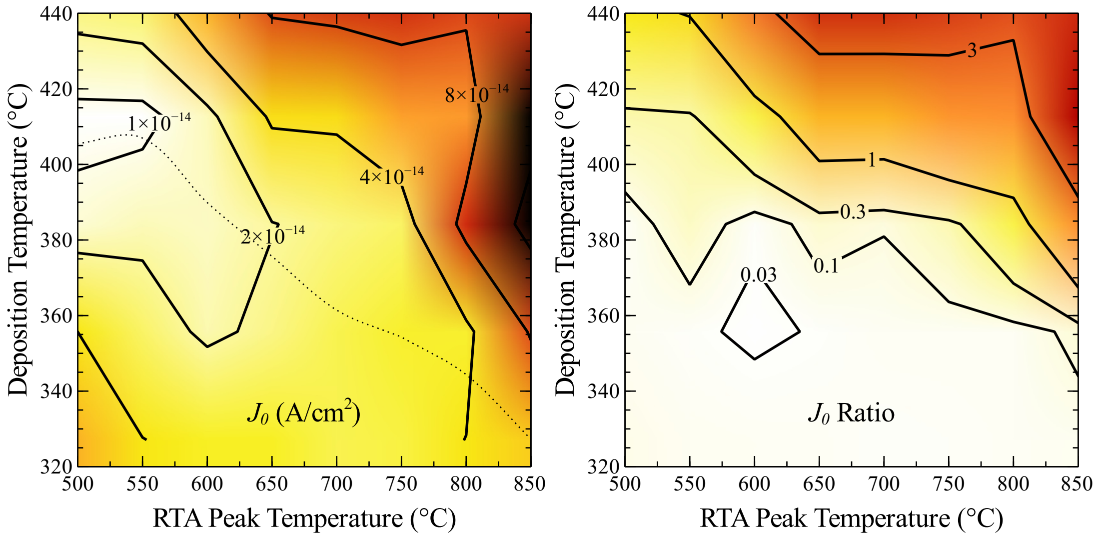

(a) (b)

Figure 6.11: Contour maps of a) post-RTA J_0 and b) the ratio of post-RTA and as-deposited J_0, as a function of RTA peak temperature and Al_2O_3 deposition temperature, derived from the data of Fig. 6.10. The dotted line shows the deposition temperature corresponding to the minimum value of post-RTA J_0 at a given RTA peak temperature

the low-temperature films (Section 9.1), or perhaps more generally to the greater thermal budget required for the structural transitions involved in passivation and depassivation of the surface.

Fig. 6.11a provides information about the optimisation of the absolute value of J_0. This is all that must be considered from a purely practical, device optimisation perspective. However, from a physical perspective it is also of interest to examine the *relative* changes in J_0 (and hence in interface properties) after RTA treatment. Hence Fig. 6.11b provides a similar contour map, this time showing the *ratio* of post-RTA and as-deposited J_0. From Fig. 6.11b it is clear that the relative change in J_0 following RTA depends strongly on the Al_2O_3 deposition temperature T_{dep}. At low T_{dep}, J_0 is strongly reduced following RTA, while for high T_{dep}, J_0 may be increased by RTA treatment, especially as RTA temperature increases.

The J_0 of 7 fA cm^{-2} observed for the optimum deposition and annealing conditions (~410 °C deposition temperature, 500 or 550 °C RTA peak temperature) is exceptionally low, and prompts an investigation of the interface properties of these films. C–V measurements of identically prepared MIS structures (Fig. 6.12) reveal that after RTA, D_{it} is reduced by a factor of two, from 11×10^{10} eV^{-1} cm^{-2}

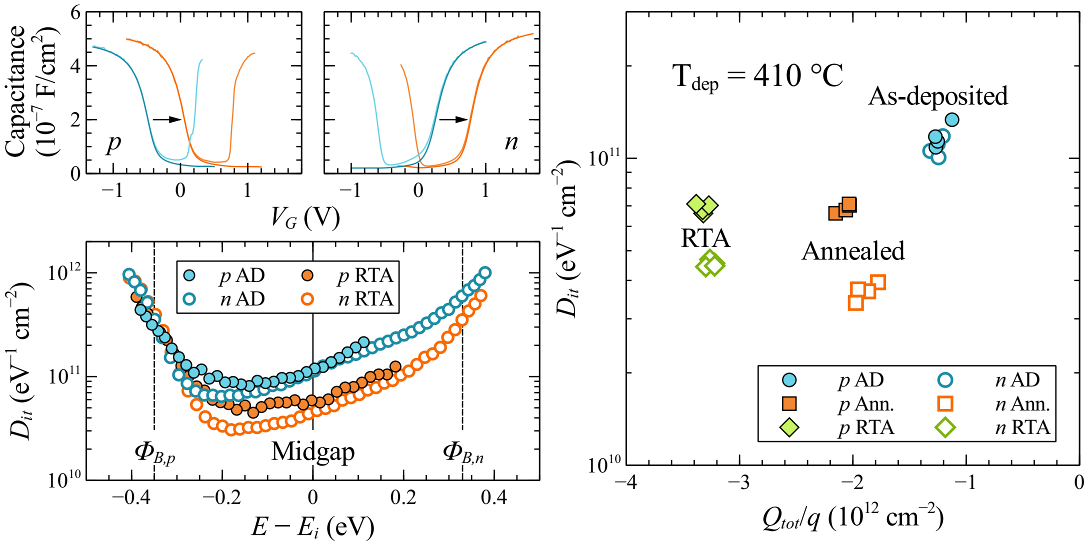

(a) (b)

Figure 6.12: a) Typical C–V characteristics and resulting D_{it} distribution for Al_2O_3 deposited on p- and n-type substrates at ∼410 °C, as-deposited and after RTA at 500 °C. b) Midgap D_{it} vs Q_{tot} determined from multiple such measurements at different points on the same samples, both as-deposited, and after either annealing at 425 °C in N_2, or RTA at 500 °C.

to $\sim 5 \times 10^{10}\,\text{eV}^{-1}\,\text{cm}^{-2}$. A similar reduction of D_{it} occurs upon extended (30 minutes) annealing at 425 °C in N_2. However, while the longer, lower temperature anneal results in an increase in negative Q_{tot} to $-2.0 \times 10^{12}\,\text{cm}^{-2}$ from its as-deposited value of $-1.2 \times 10^{12}\,\text{cm}^{-2}$, the RTA results in a significantly larger increase, to $Q_{tot} = -3.3 \times 10^{12}\,\text{cm}^{-2}$. This combination of remarkably low D_{it} and large Q_{tot} accounts for the exceptionally low J_0 of surfaces passivated by these films.

Discussion

Given the results presented in Fig. 6.4, it appears that not only peak temperature, but also time must be considered. On the other hand, peak temperature clearly plays an important role, given the much smaller increase in charge observed after extended annealing at 425 °C compared to that obtained by a brief 500 °C RTA (Fig. 6.12). This suggests that the concept of activation energies will be more useful than that of a simple ”thermal budget” in understanding thermally-induced changes in surface passivation for such films.

In Section 6.1, Al_2O_3 passivation was observed to improve following a conventional fast-firing step in a belt furnace with peak substrate temperature over 800 °C. Conversely, a much shorter RTA step at a similar temperature was found to result in a significant deterioration of passivation quality for the same films. The reason for this apparent discrepancy may be related to the different heating methods employed by the two processes, which in the case of RTA involves high-intensity illumination of the substrate by infrared lamps. Such illumination has previously been linked to surface passivation degradation observed for SiO_2-passivated surfaces during RTA [165]. It is therefore possible that the observed degradation is related to the presence of illumination rather than being a purely thermal process. Further work will be needed to clarify this question.

Summary

Systematic investigation of the effects of post-deposition heat treatment by RTA on Al_2O_3 surface passivation reveals a number of trends. J_0 post-RTA may either increase or decrease depending on the Al_2O_3 deposition temperature and the RTA peak temperature. Post-RTA J_0 generally increases with increasing RTA peak temperatures. The optimum deposition temperature depends on the post-deposition thermal processing to be applied. Films deposited at lower temperatures provide worse passivation after low temperature heat treatment, but maintain this passivation better at higher RTA temperatures. An exceptionally low J_0 of 7 fA cm^{-2}, due to a combination of very low D_{it} and unusually high Q_f, is achieved by the use of a short 500–550 °C RTA combined with optimised deposition conditions.

6.3 Conclusions

The effect of high-temperature post-deposition thermal processing on the surface passivation provided by APCVD Al_2O_3 has been examined using both a conventional contact-firing furnace, and an RTA system. Significantly, passivation is shown to remain stable or even improve following a standard contact-firing step, as used in conventional screen-printed metallisation, independently of film thickness or the presence of a SiN_x capping layer. Q_{tot} was found to increase monotonically with increasing firing time, while D_{it} first decreased then increased above the initial level. Investigations using RTA over a wide range of temperatures show that the final passivation effectiveness depends both on the initial deposition temperature and on the temperature and duration of post-deposition thermal processing, so that the two should be optimised in parallel. The combined optimisation of deposition conditions and post-deposition RTA temperature are shown to result in outstanding passivation quality, comparable to the best results reported for Al_2O_3 deposited by other methods.

Chapter 7

Effect of Surface Dopant Concentration

It is vain to do with more what can be done with less.

— William of Ockham
Summa Totius Logicae

The effectiveness of Al_2O_3 surface passivation depends not only on the processing history of the film, but also on the properties of the semiconductor surface on which it is deposited. In this chapter we examine the influence of surface dopant type and concentration on the recombination rate at Al_2O_3-passivated surfaces. Both boron- and phosphorus-doped surfaces are considered, with surface dopant concentrations in the range of 10^{15} to $10^{20}\,\mathrm{cm}^{-3}$. The injection dependence of recombination at lightly doped n-type surfaces is also discussed. We shall show that the observed dependencies are well described by physical theory and consistent with the interface state model of Chapter 4. Critically, interface properties appear to be independent of dopant concentration. The existence of an additional defect state which dominates recombination at phosphorus-diffused surfaces is inferred. Finally, we demonstrate that recombination at Al_2O_3-passivated surfaces of both types is minimised by the omission of a heavily doped region.

7.1 Introduction

The intentional introduction of bulk dopant impurities into semiconductor materials in order to modify their electronic properties, whether during the crystallisation process or subsequently by diffusion or ion implantation, is a crucial element in the fabrication of practically all working semiconductor devices. The surface of a typical silicon solar cell contains both n- and p-type regions, usually doped by phosphorus and boron respectively. The surface dopant concentration N_s in these regions may range over many orders of magnitude. The type and concentration of dopant atoms at the surface may influence the effectiveness of surface passivation in two ways. Firstly, it influences the concentration of free charge carriers at the surface, which directly affects the rate of recombination through interface defects via Equation (2.18). Secondly, the presence of large concentrations of dopant atoms may possibly induce additional recombination-active defects and charges at the silicon–dielectric interface, changing the physical properties of the interface. The latter effect has been reported or implied by several authors for the interface between Si and thermally grown SiO_2 [166]–[168].

In order to predict the performance of photovoltaic devices incorporating Al_2O_3 passivation layers, it is necessary to know the recombination rate at the Si–Al_2O_3 interface as a function of N_s. In principle, this can be calculated from physical theory via Equation (2.18) together with a solution of the surface band-bending problem as described in Section 2.3, given knowledge of the interface state properties and Q_{tot}. However in practice such an approach has previously been subject to large uncertainties. Even for the classical Si–SiO_2 interface—by far the most extensively characterised semiconductor–dielectric system—there remains both a lack of data on minority carrier capture coefficients and considerable variation in the measured majority capture coefficients of the interface states [10], some of which may be process-related, and some related to measurement uncertainty. Furthermore, the reported dependence of interface properties on N_s for the Si–SiO_2 interface naturally complicates any modelling based on these parameters.

Therefore, a common approach for device simulation purposes has been to make use of empirical parameterisations of S_{eff} derived from measurements of multiple samples with N_s spanning the range of interest [169]–[175]. However, this approach has serious drawbacks. It limits knowledge of S_{eff} to the range of N_s accessible by experiment and requires that new parameterisations be derived whenever the properties of the passivation layer are changed, which entails extensive tedious experimental work. More importantly, it provides no physical insight into the doping dependence of S_{eff}.

In this chapter the effect of the surface dopant concentration on the effectiveness of Al_2O_3 passivation is investigated for both p-type (boron-doped) and n-type (phosphorus-doped) surfaces. In both cases we show that the dependence of interface recombination on N_s can be accurately described over a wide range by physical theory combined with interface parameters that are independent of N_s and consistent with values measured independently by the C–V and conduction methods (Section 4.2). The work presented in Section 7.2 on boron-doped surfaces has previously been published [52].

7.2 Boron-doped surfaces

As discussed in Section 1.2, Al_2O_3 is of most interest for application to p-type surfaces, owing to the negative polarity of its charge. In particular, the application of Al_2O_3 to heavily doped $p+$ regions, usually formed by diffusion, is of significant interest because Al_2O_3 is able to passivate these surfaces far more effectively than existing passivation layers like SiN_x [13], [14].

While a number of authors have reported Al_2O_3 passivation of boron-diffused silicon surfaces spanning a range of N_s [29], [57], [176]–[179], the purpose of these works has primarily been to demonstrate the effectiveness of the passivation of such surfaces, rather than to gain a quantitative physical understanding of the passivation mechanisms.

In this section, we determine S_{eff} as a function of N_s for Al_2O_3-passivated boron-doped surfaces via two independent methods: (1) from photoconductance-based measurements of carrier recombination on diffused and undiffused substrates with a range of Ns, and (2) from measurements of the Si–Al_2O_3 interface state density D_{it} and insulator fixed charge Q_f for MIS structures at a single moderate dopant density. We show that the latter approach, in conjunction with the values for the Si–Al_2O_3 interface state properties measured in Section 4.2, permits very accurate quantitative prediction of S_{eff} over a wide range of N_s. Furthermore, we demonstrate that the fundamental surface recombination velocity of electrons, S_{n0}, which is the energy-integrated product of D_{it} and the electron capture coefficient c_n, is independent of the surface boron concentration within the examined range.

We conclude, therefore, that unlike what has been reported for Si–SiO_2, the Si–Al_2O_3 interface properties are independent of the surface boron concentration. For a given set of deposition and annealing conditions, it is therefore possible to predict the recombination rate at any boron-doped silicon surface (diffused or undiffused) passivated with Al_2O_3 by using the Si–Al_2O_3 interface properties measured on a moderately doped Si wafer, rather than needing to measure this

Table 7.1: Properties of the boron diffusion profiles prepared in this work. Depth refers to the distance from the surface at which the boron concentration is equal to $10^{17}\,\mathrm{cm}^{-3}$.

Diffusion Temp. (°C)	Drive-in Time (min)	Sheet Resistance (Ω/□)	Surface Boron Concentration (cm^{-3})	Peak Boron Concentration (cm^{-3})	Depth (µm)
1000	0	26.75	2.8×10^{19}	1.1×10^{20}	0.92
	30	27.5	5.2×10^{19}	5.4×10^{19}	1.67
	90	29.5	3.3×10^{19}	3.3×10^{19}	2.27
	180	31.25	2.5×10^{19}	2.5×10^{19}	2.75
950	0	74.25	2.5×10^{19}	4.7×10^{19}	0.46
	30	69.75	2.3×10^{19}	2.3×10^{19}	1.24
	90	70.0	1.5×10^{19}	1.5×10^{19}	1.76
	180	69.0	1.2×10^{19}	1.2×10^{19}	2.27
900	0	186.75	7.0×10^{18}	1.8×10^{19}	0.36
	30	158.5	7.5×10^{18}	7.5×10^{18}	0.98
	90	146.0	5.5×10^{18}	5.5×10^{18}	1.37
	180	139.5	4.0×10^{18}	4.0×10^{18}	1.77

directly. The combination of S_{n0} and Q_f is shown to provide an efficient doping- and injection-independent parameterisation of the passivation properties of this interface, superior to S_{eff}.

Sample preparation

To provide samples with a range of high N_s, boron-diffused symmetrical $p+/p/p+$ structures were prepared on ~480 µm thick, high resistivity ($> 100\,\Omega\,\mathrm{cm}$) p-type(B-doped) ⟨100⟩ FZ-Si wafers. These received a surface-damage etch in an HF:HNO_3 solution, followed by an RCA clean and dilute HF dip. Boron diffusions were performed in a quartz tube furnace from a BBr_3 source. Three separate diffusions with different deposition temperatures of 900, 950, and 1000 °C were performed on different sets of samples. The diffusion parameters and resulting sheet resistances measured by four-point probe are given in Table 7.1.

After diffusion, the wafers were stripped of borosilicate glass by immersion in dilute HF until hydrophobic. They were then RCA cleaned and subjected to

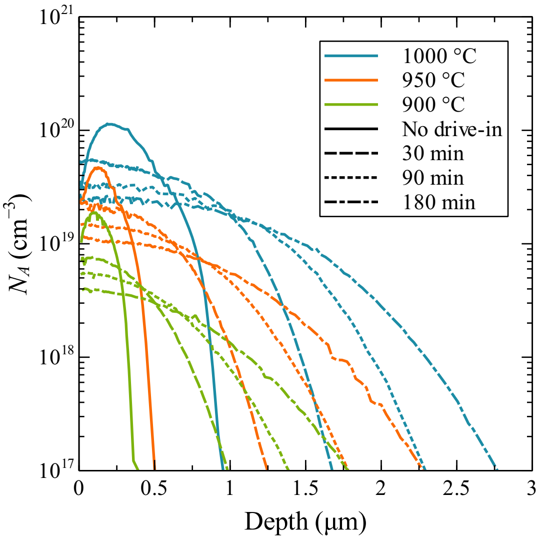

Figure 7.1: Acceptor concentration profiles measured by the ECV method for the boron diffusions used in this work. Three different diffusion temperatures and three different post-diffusion drive-in annealing times were used to achieve a broad range of surface concentrations.

different drive-in anneals in an N_2 ambient at 1100 °C for either 30, 90, or 180 min. The drive-in step redistributes the diffused boron into the wafer, resulting in a stretch-out of the dopant profile and providing a broad range of N_s. One sample from each of the three diffusion sets did not receive a drive-in. The resulting dopant profiles were measured by a WEP Wafer Profiler CVP21 tool using the ECV method. The surface concentrations were extrapolated from quadratic fits of the near-surface data.

Fig. 7.1 shows the resulting measured boron concentration profiles, while Table 7.1 summarises their key properties. The different diffusion and drive-in steps resulted in a wide spread in surface concentration and profile depth, with N_s ranging from 4.0×10^{18} to 5.2×10^{19} cm^{-3}. For the samples which did not receive a drive-in, the profile peak occurs away from the surface due to the oxide acting as a sink for near-surface boron during the oxidation stage of the diffusion. Because of the resulting steep near-surface profiles there is consequently somewhat greater uncertainty in the extrapolated values of N_s for these samples.

Following the diffusion, drive-in, and an RCA clean, the samples were passivated with Al_2O_3 and characterised. Two deposition methods were sequentially examined: APCVD and thermal ALD. Samples were first passivated by APCVD Al_2O_3, then this layer was removed in HF, and the samples were again RCA cleaned and repassivated with Al_2O_3 using thermal ALD. The APCVD films were characterised both in the as-deposited and annealed state, while the ALD films are known to be unstable as-deposited, and were therefore annealed immediately after deposition.

The APCVD Al_2O_3 films were deposited using the baseline deposition parameters given in Table 5.1. The thickness of the films was ~12 nm, as determined by spectral reflectance measurements on co-deposited polished samples as described in Section 3.3. Thermal ALD Al_2O_3 films were deposited in a Beneq TFS 200 reactor from TMA and H_2O at a substrate temperature of 200 °C. These had a thickness of 20 nm. Annealing of both APCVD and ALD films was performed in a quartz tube furnace at 425 °C for 30 min in an N_2 ambient.

In order to extend the range of examined N_s, additional lifetime samples were prepared on various undiffused, boron-doped $\langle 100 \rangle$ FZ-Si substrates with bulk resistivity ranging from 1.6 to $0.5\,\Omega\,\mathrm{cm}$, corresponding to boron concentrations of 0.9–$3.3 \times 10^{16}\,\mathrm{cm}^{-3}$. Like the diffused samples these received a surface-damage etch in HF:HNO_3, followed by an RCA clean and HF dip before Al_2O_3 deposition.

Photoconductance measurements: experimental details and results

The effective excess carrier lifetime τ_{eff} of the symmetrically passivated lifetime structures, both diffused and undiffused, was measured as a function of the average bulk excess carrier density Δn as described in Section 3.3. For the undiffused samples a short flash illumination was used and τ_{eff} vs Δn was extracted from the resulting photoconductance decay. For these samples, S_{eff} was calculated directly from the measured value of τ_{eff} at $\Delta n = 10^{15}\,\mathrm{cm}^{-3}$, according to Equation (2.32), assuming negligible bulk SRH recombination. For the most lightly doped samples ($N_s = 9.2 \times 10^{15}\,\mathrm{cm}^{-3}$) the bulk lifetime was observed to be significantly degraded due to iron contamination, rendering the latter assumption invalid. Therefore for these samples S_{eff} was instead extracted from the slope of the inverse lifetime in high injection via Equations (2.34) and (2.35), where the lifetime was measured after strong illumination to dissociate the iron-boron pairs.

Photoconductance measurements of the diffused samples were performed using quasi-steady-state illumination with the generalised analysis. The optical constant required to calculate the generation rate was determined from reflectance and transmission measurements of the passivated samples, together with the measured lamp spectrum and quantum efficiency of the reference cell, as described

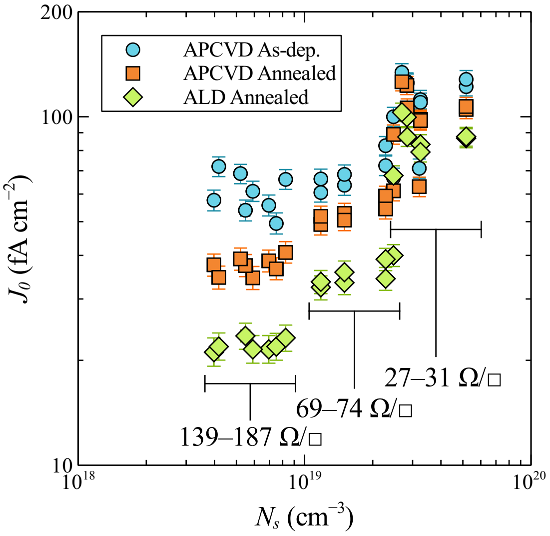

Figure 7.2: Measured recombination current density J_0 vs. surface boron concentration N_s for the diffusion profiles of Fig. 7.1 passivated with Al_2O_3 deposited either by APCVD (as-deposited and annealed), or thermal ALD (annealed only). Error bars show uncertainty due to error in the substrate thickness and the optical constant.

in [133]. It was confirmed that the use of this optical constant resulted in good agreement (within ±2%) between lifetime values determined from the illuminated part of the measurement before the cutoff of the flash, and those determined from the unilluminated transient tail measured after the cutoff.

For the diffused samples, J_0 was extracted from $\tau_{eff}(\Delta n)$ via Equation (2.34). The value of the derivative in (2.34) was extracted using a linear fit over the range of $\Delta n = 8$ to $12 \times 10^{15}\,\text{cm}^{-3}$. This range was chosen as that for which the local value of the derivative showed the least variation with Δn for all samples.

Fig. 7.2 plots the resulting J_0 values as a function of N_s. It also gives ranges for the sheet resistance of the diffusions. The figure shows that J_0 increases roughly monotonically with N_s for each type of Al_2O_3. This trend is caused by an increase in Auger recombination as the silicon becomes more heavily doped. While S_{eff} also increases with N_s, as will be seen, the contribution of surface recombination to J_0 remains essentially independent of doping in this range, due to the fact that the surface minority carrier concentration also decreases with increasing N_s in roughly inverse proportion to S_{eff}, as we have shown elsewhere [113]. The J_0 data for the samples that did not receive a drive-in lie on a slightly different trend, because the peak dopant concentration for these samples (which strongly influences the Auger recombination component of J_0) is greater than N_s.

Fig. 7.2 also shows that the as-deposited APCVD samples have the highest J_0 and therefore provide the poorest passivation. The J_0 of these APCVD samples decreases once they are annealed, and their magnitudes correspond to very good surface passivation. For example, for the lightest B diffusion, the J_0 is just $35\,\mathrm{fA\,cm^{-2}}$. This level of passivation is of particular interest to solar cell manufacturers due to the low-cost nature of APCVD [32]. The J_0 of annealed thermal ALD samples is lower still with a J_0 of $20\,\mathrm{fA\,cm^{-2}}$ on the lightest B diffusions. The J_0 values for these samples are in good agreement with the few previously reported passivation results for Al_2O_3 from thermal ALD on boron-diffused surfaces [49], [180], despite significantly different post-deposition thermal processing. Even lower values of J_0, down to less than $10\,\mathrm{fA\,cm^{-2}}$, have been reported for Al_2O_3 from plasma-assisted ALD and PECVD [29], [49], [57], [176], [178], [179].

Determination of S_{eff} from J_0 data

The J_0 extracted via (2.34) includes contributions from Auger recombination in the heavily doped p+ region and SRH recombination through interface states at the silicon surface. To evaluate the surface passivation provided by the Al_2O_3 films, it is therefore necessary to extract the contribution due to surface recombination. This extraction is performed by numerical simulation of the measured dopant profiles, as described in [110], to determine the surface recombination velocity S_{eff}, which then allows a comparison of the passivation to that attained on undiffused samples.

For such highly doped semiconductor regions, doping-induced bandgap narrowing becomes significant and must be included in the analysis. For this purpose we used the recent empirical parameterisation of [181], which is based on a large self-consistent dataset, and makes use of the most up-to-date values for the physical parameters. We use the Fermi-Dirac variant of this parameterisation together with Fermi–Dirac carrier statistics. While this parameterisation was derived for phosphorus rather than boron-doped silicon, previous work has shown that the bandgap narrowing data for both dopants agrees quite closely [182].

Auger recombination in the diffused region was, as in the bulk, calculated using the model of Richter *et al.* [31]. This model gives slightly lower values for the Auger recombination at high dopant concentrations than the widely used model of Dziewior and Schmid [183], and substantially lower than that of Kerr and Cuevas [184], which was not optimised to fit the data at higher dopant

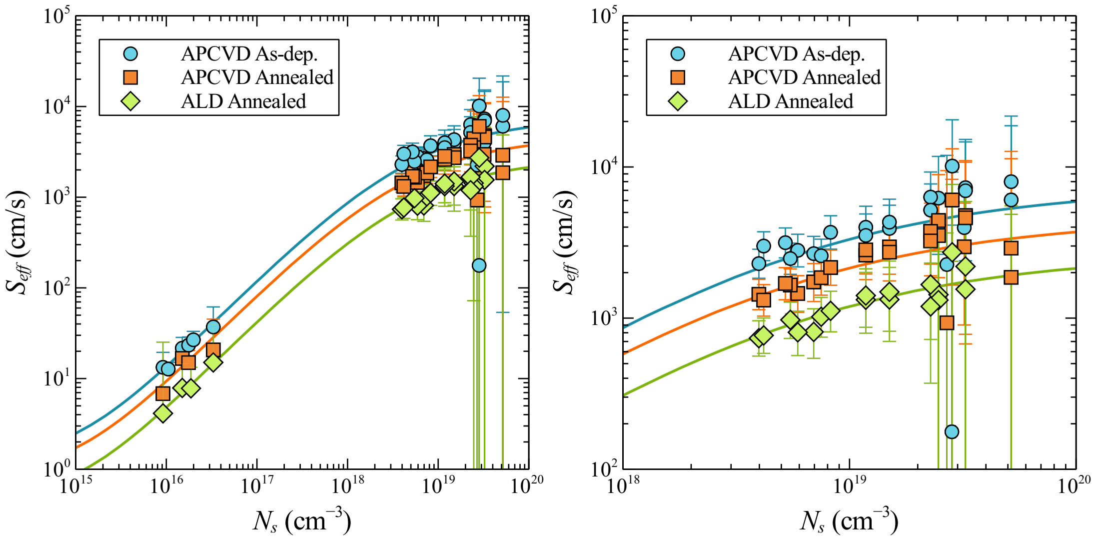

(a) (b)

Figure 7.3: Effective surface recombination velocity S_{eff} as a function of surface boron concentration N_s, for a) both bulk-doped and diffused surfaces, and b) diffused surfaces only. Data for diffused surfaces is extracted from the data of Figs. 7.1 and 7.2. Lines show values calculated from the measured D_{it} and Q_{tot}, using the interface state model of Section 4.2

concentrations. It is likely that the use of the model of [184] in the analysis of some previous measurements of Al_2O_3-passivated boron-diffused surfaces [57] resulted in a significant underestimation of the extracted S_{eff}.

Fig. 7.3 plots S_{eff} against N_s, where the symbols show the results of the photoconductance measurements, and the lines show the results of simulations based on experimental measurements of the interface properties (as described below). Fig. 7.3b contains just the diffused samples, and Fig. 7.3a contains both the diffused and undiffused samples. There is a clear trend of increasing S_{eff} with increasing N_s in all cases.

Note that the same samples shown in Fig. 7.3b were also passivated with APCVD films deposited at a slightly higher deposition temperature (490 °C) (data not shown). In this case they exhibited S_{eff} values very similar to those of the annealed APCVD data shown, both as-deposited and after annealing. This is consistent with the observation in Section 5.1 that at higher deposition temperatures both D_{it} and Q_{tot} saturate and are not significantly affected by post-deposition annealing. The data is not included here to avoid cluttering the figure.

Error bars for the diffused samples in Fig. 7.3 show the combined error

Table 7.2: Si–Al_2O_3 interface properties determined by C–V measurements of undiffused boron-doped samples: total insulator charge Q_{tot}, midgap interface state density D_{it}, and corresponding fundamental surface recombination velocity of electrons, $S_{n0,A}$, calculated from (7.4).

Passivation Layer	Q_{tot}/q ($10^{12}\,\mathrm{cm}^{-2}$)	$D_{it,midgap}$ ($10^{11}\,\mathrm{cm}^{-2}\,\mathrm{eV}^{-1}$)	$S_{n0,A}$ ($10^{3}\,\mathrm{cm\,s}^{-1}$)
APCVD As-dep.	1.65	1.65	10.7
APCVD Annealed	1.55	1.00	6.5
T-ALD Annealed	1.67	0.60	3.9

due to the stated uncertainty in the bandgap narrowing parameterisation of [181], together with the error in J_0 shown in Fig. 7.2. For the samples with $N_s > 2 \times 10^{19}\,\mathrm{cm}^{-3}$ there is large scatter in the data. For such heavily doped surfaces, Auger recombination in the diffused region dominates J_0, making the extraction of S_{eff} subject to significant relative uncertainty. This occurs both because Auger recombination increases with higher doping, and also because surface recombination is reduced due to suppression of the surface minority carrier concentration at higher N_s. This uncertainty is compounded by uncertainty in the minority carrier concentration due to the onset of significant bandgap narrowing, and is reflected in the significantly larger error bars for this data. Note that the assumption of higher bandgap narrowing corresponds to lower extracted S_{eff}, and vice versa. Error bars for the undiffused samples show the upper limit of S_{eff} assuming an infinite bulk lifetime.

The clear increase in S_{eff} with N_s misleadingly suggests that the physical interface properties themselves are changing with doping. This might, for example, have been caused by a decrease in negative charge Q_{tot} or an increase of interface states D_{it}. It is next shown, however, that neither Q_{tot} nor D_{it} depends on N_s, and that instead, the increase of S_{eff} with N_s is simply a consequence of the definition of S_{eff}.

C–V measurements: experimental details and results

Conventional C–V measurements of D_{it} are difficult on highly doped surfaces because the interface state capacitance appears in parallel with a very large substrate capacitance, making it challenging to extract D_{it} accurately, especially when D_{it} is small. The large voltages required to drive the surface from inversion

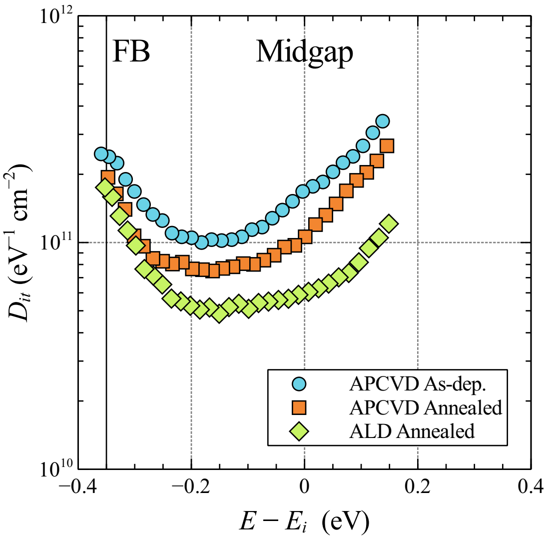

Figure 7.4: Interface state density D_{it} as a function of energy E with respect to midgap, determined from C–V measurements for each of the Al_2O_3 films. Note that the values shown here are taken from representative single measurements, while the average midgap D_{it} values in Table 7.2 are taken from multiple such measurements.

to accumulation can also lead to dielectric breakdown, making low frequency measurements impossible due to high leakage currents through the film. C–V measurements were therefore performed only on moderately doped undiffused substrates, and $S_{eff}(N_s)$ was calculated assuming that the measured values of D_{it} and Q_{tot} were independent of N_s. This assumption is subsequently justified by comparison with S_{eff} determined from the photoconductance measurements.

The MIS structures for C–V measurements were prepared on $2.7\,\Omega\,\text{cm}$ ($N_A = 5.2 \times 10^{15}\,\text{cm}^{-3}$) boron-doped $\langle 100 \rangle$ polished Si substrates, which received an RCA clean and HF dip prior to Al_2O_3 deposition. C–V measurements were performed at multiple points on each sample in the manner described in Section 3.3. Representative extracted $D_{it}(E)$ profiles for each of the films are presented in Fig. 7.4, while averaged extracted values of Q_{tot} and D_{it} at midgap are presented in Table 7.2. All three films have similar Q_{tot}, being distinguished principally by differences in D_{it}.

Note that while the C–V data for the APCVD films was measured using the standard voltage sweep from inversion to accumulation, the data for the ALD films was measured using a voltage sweep in the opposite direction. This is because it was found that for these films the apparent D_{it} showed a substantial dependence on the sweep direction, with a voltage sweep in the standard direction resulting in an apparent D_{it} that was substantially larger than that of even the as-deposited APCVD films. As it cannot be the case that the recombination-active interface state density is greater for the ALD films, we suspect that these additional apparent interface states represent recombination-ineffective charge states, perhaps slow traps associated with the slight hysteresis in the C–V characteristics also observed for these films but which is not present for the APCVD films. Hence, for the ALD films, we use the C–V data resulting from the accumulation to inversion voltage sweep, which results in a lower and more plausible value for D_{it}. Care was taken to use sufficiently slow (0.01 and 0.02 V/s) voltage sweeps, such that thermal equilibrium would be maintained through the midgap region for this measurement.

Determination of S_{eff} from C–V data

The negative Q_{tot} of the Al_2O_3 films (Table 7.2) results in accumulation of majority carriers at the p-type surfaces under consideration. Under these conditions (and when not very close to thermal equilibrium), S_{eff} is related to D_{it} and Q_{tot} by (see Section 2.5)

$$S_{eff} = S_{n0}\frac{n_s}{n_d}\,, \tag{7.1}$$

where

$$S_{n0} = \int_{E_v}^{E_c} D_{it}c_n \, dE\,. \tag{7.2}$$

S_{n0} is the fundamental surface recombination velocity of electrons,[1] and n_s/n_d is the ratio of the electron concentration at the surface to that at the edge of the quasi-neutral region in the semiconductor. This ratio is a function of Q_{tot}, and generally must be calculated numerically.

The measured midgap D_{it} can be used in conjunction with the experimentally based Si–Al_2O_3 interface state model of Section 4.2 to calculate S_{n0} via (7.2). In this model, which was derived from measurements of the Si–Al_2O_3 interface state

---

[1] Note that some authors use S_{n0} or S_{p0} to refer to what is essentially an effective surface recombination velocity including the influence of charge, identical to our S_{eff}. This is because they make the implicit assumption that $Q_{tot} = 0$, so that $S_{eff} = S_{n0}$ or S_{p0} from (7.1). It should also be noted that S_{n0} and S_{p0} do not bear a simple relation to the parameter S_0 measured at depleted surfaces in the absence of illumination [167], [185] (for example via the pulsed MIS capacitor technique [186]) since in the latter case the emission-related terms in (2.18) become significant and only defects near the middle of the bandgap effectively contribute to recombination or generation.

properties using the conductance method, the dominant recombination-active defect for surfaces where holes are the majority carrier is described by a Gaussian distribution of states centered just below midgap with energy-independent c_n and c_p. The integral of this distribution with respect to energy is easily calculated to be

$$\int_{E_v}^{E_c} D_{it}\, dE = 0.18 \times D_{it,midgap}\,, \tag{7.3}$$

expressed in terms of D_{it} measured at midgap. We will designate the properties of this defect with the subscript A in anticipation of the following section on phosphorus-doped surfaces, for which other defects become important. Assuming the conditions relating to (7.2) hold (as they do in our case), $S_{n0,A}$ is then given by

$$S_{n0,A} = c_n \int_{E_v}^{E_c} D_{it}\, dE = 6.5 \times 10^{-8} \times D_{it,midgap}\,, \tag{7.4}$$

where $S_{n0,A}$ is in units of $\mathrm{cm\,s^{-1}}$ and $D_{it,midgap}$ is in units of $\mathrm{cm^{-2}\,eV^{-1}}$. The values of $S_{n0,A}$ calculated from (7.4) are summarised in Table 7.2.

The surface electron concentration n_s was calculated from the surface dopant density N_s and insulator fixed charge Q_{tot} of Table 7.2 using Fermi-Dirac statistics together with an iterative solution of the silicon surface potential, as described in Section 2.3. For this purpose we treat the dopant concentration as constant across the width of the surface charge profile, and equal to the measured N_s of the diffused samples. This should be a reasonable approximation, even for the steeper dopant profiles, since the width of the surface charge profile in accumulation for such high N_s is only on the order of 10 nm or less.

$S_{eff}(N_s)$ calculated from the measured D_{it} and Q_{tot} via (7.1)–(7.4) for each of the passivation layers are shown as solid curves in Fig. 7.3. These lines agree very well—both in terms of trends and absolute values—with the symbols that were independently determined from the photoconductance measurements. The agreement is remarkable considering that both S_{eff} and N_s span several orders of magnitude.

The calculation of S_{eff} from the measured interface properties (i.e. from the C–V measurements on undiffused Si) was predicated on the assumption that these properties were independent of the surface boron concentration N_s. The excellent agreement in S_{eff} over such a wide range of N_s is strong evidence that this assumption is indeed valid.

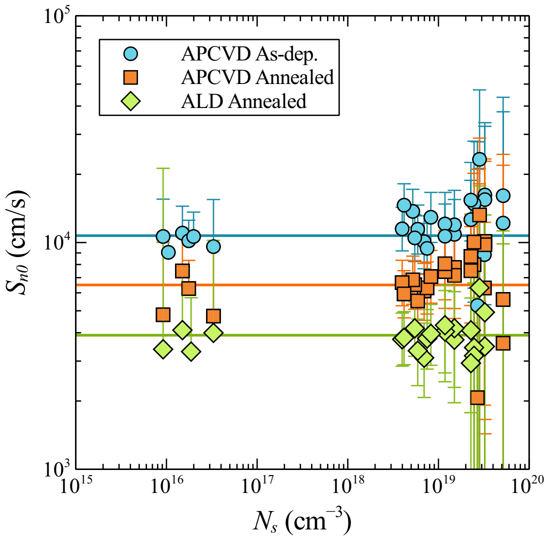

Figure 7.5: The fundamental surface recombination velocity of electrons, S_{n0}, extracted from the data of Fig. 7.3 via (7.1). Lines show S_{n0} calculated from the measured interface state density D_{it} via (7.4).

Determination of S_{n0}

The large variation of S_{eff} with N_s highlights the limitations of this parameter as a means of describing surface passivation, as discussed in Chapter 2. It is useful to present the surface recombination rate in terms of S_{eff} because this parameter is easily determined and it includes the influence of both charge-assisted and chemical surface passivation. It is also often used to describe surface recombination and is hence familiar to many readers. However, because S_{eff} depends on both Q_{tot} and N_s, it can only provide a complete description of the interface passivation properties when quoted together with these parameters. It is not very meaningful to directly compare S_{eff} values measured for substrates with different N_s, as is commonly done.

In contrast, Q_{tot} and S_{n0} or S_{p0} in combination constitute a complete description of the interface properties (so long as the assumptions pertaining to (2.20) apply) and do not possess an intrinsic dependence on N_s. That is, a dependence on N_s would only arise via a dependence of the physical properties of the interface (Q_{tot}, D_{it}, c_n and/or c_p) on the dopant concentration.

To reinforce this point, it is worthwhile to analyze the data of Fig. 7.3 to extract S_{n0}, using the relation defined in (7.1). This decouples the effect of Q_{tot} from S_{eff}, leaving a term which depends only on the concentration of interface states and their effectiveness as recombination centers. Fig. 7.5 presents the resulting S_{n0} values, with lines of constant S_{n0} indicating the values of $S_{n0,A}$ calculated from the measured D_{it} of Table 7.2 via (7.4). It is clear that, despite experimental scatter, the data is indeed well described by a constant value of S_{n0}, highlighting the advantage of the use of this parameter (or S_{p0}) in conjunction with Q_{tot} as a means to describe the effectiveness of a given surface passivation. This conclusion holds at least up to $N_s = {\sim}3 \times 10^{19}\,\mathrm{cm}^{-3}$, above which point the experimental uncertainty becomes too large to draw any reliable conclusions, although the lines of constant S_{n0} remain within the error bounds for all the data.

The uncertainty in S_{n0} at high N_s derives from the increasing importance and eventual dominance of Auger recombination in the heavily doped region, relative to surface recombination. At high N_s any error in the Auger recombination model would contribute significantly to error in the extraction of S_{eff} and S_{n0}. This is compounded by uncertainty in the bandgap narrowing model, and hence in the minority carrier concentration, both in the bulk and at the surface. The qualitative effect of using a different bandgap narrowing model in the extraction of S_{eff}, and hence S_{n0}, can be seen in the extent of the error bars for the diffused samples. For $N_s < 2\text{–}3 \times 10^{19}\,\mathrm{cm}^{-3}$, where Auger recombination is less important, the conclusion that S_{n0} is independent of N_s is relatively insensitive to changes in bandgap narrowing, though the agreement with the data of the undiffused samples at lower N_s is affected. At higher N_s, the slope of apparent S_{n0} vs N_s becomes very sensitive to the bandgap narrowing and Auger models. If significantly lower bandgap narrowing were assumed, the extracted S_{n0} would increase strongly with N_s above this point, while for significantly higher bandgap narrowing the extracted S_{n0} would decrease sharply and even assume (unphysical) negative values at high N_s.

The S_{n0} values presented in Fig. 7.5 and Table 7.2 are similar to the value of ${\sim}1 \times 10^4\,\mathrm{cm\,s^{-1}}$ determined by Ma *et al.* [177] for PECVD $\mathrm{Al_2O_3/SiN_x}$ stacks on boron-diffused planar surfaces. The agreement is partly coincidental, since Ma *et al.* used the Auger model of Kerr and Cuevas [184], and also made use of simulated dopant profiles with higher N_s than those measured by ECV. These two factors would have respectively acted to decrease and increase the apparent surface recombination velocity, and may have effectively compensated each other in the calculation of S_{n0}. The values are therefore not directly comparable, but nevertheless they are clearly of the same order of magnitude.

The fact that S_{n0} appears to be constant for the examined passivation layers could conceivably be exploited in order to provide improved determinations of the other important processes occurring at high dopant concentrations: Auger recombination and bandgap narrowing. A constant S_{eff} (equal to the thermal velocity) is already often assumed in the extraction of bandgap narrowing from measurements of J_0 on metal-coated diffused surfaces [170], [171], [181]. The ability to make a similar assumption for passivated surfaces could effectively provide multiple coupled equations for a given diffusion profile, possibly even allowing both Auger recombination and bandgap narrowing to be determined simultaneously from the same dataset. The practicality of such a procedure would of course depend on the repeatability of the passivation process.

The value of S_{n0} determined here for boron-doped surfaces is properly assigned to the interface state distribution labelled A in Section 4.2. In the second part of this chapter, on phosphorus-doped surfaces, we will refer to this parameter as $S_{n0,A}$ in order to distinguish it from S_{n0} of a second defect state, designated B, that becomes important on such surfaces.

Conclusions

We conclude that, in contrast to what has been reported for thermal SiO_2 [166]–[168], D_{it}, c_n, and Q_f at the boron-doped Si–Al_2O_3 interface are independent of the surface boron concentration N_s over a range of at least $9 \times 10^{15}\,\mathrm{cm}^{-3}$ to $3 \times 10^{19}\,\mathrm{cm}^{-3}$. Furthermore, the recombination rate at this interface can be determined with a high degree of accuracy over the same range, given only knowledge of the total insulator charge Q_{tot} and the fundamental surface recombination velocity of electrons, S_{n0}, measured at any N_s. The latter can be determined either from the measured interface state density D_{it} via (7.4), or from measurements of the excess carrier recombination lifetime via (2.32) and (7.1) when Q_{tot} is known. The practical implications of this finding for device simulation and modeling are significant, in that it obviates the need to experimentally assess surface recombination as a function of N_s whenever the properties of the film are changed, for example as a result of changing deposition conditions. Most importantly, it provides valuable physical insight into the mechanisms of surface passivation.

7.3 Phosphorus-doped surfaces

The passivation properties of Al_2O_3 on n-type silicon surfaces, while not entirely neglected, have received less attention than those on p-type surfaces. This is understandable given that the distinguishing feature of Al_2O_3, its large negative charge, is detrimental for passivation of heavily doped n-type surfaces, and can lead to increased recombination in low injection for more lightly doped n-type surfaces, while existing alternatives such as SiN_x, with its positive charge, do not suffer such difficulties. However, a complete understanding of Al_2O_3 passivation properties demands the study of its performance on both types of surface. Moreover, for certain cell architectures there may be practical considerations that make it desirable for Al_2O_3 to simultaneously passivate highly doped n- and p-type surfaces.

In this section we describe and discuss measurements of Al_2O_3-passivated n-type surfaces, both undiffused and diffused. We show that Al_2O_3 is capable of providing excellent passivation of undiffused n-type surfaces, and good passivation of diffused n-type surfaces over a certain range of N_s. The increased recombination often observed in low injection for undiffused n-type surfaces is attributed to two-dimensional transport phenomena, and a simple analytical model is proposed to describe these effects. Finally, we conclude that a second, acceptor-like interface state is required to explain recombination at diffused n-type surfaces, and we determine the properties of this state.

7.3.1 Undiffused surfaces

A number of authors have demonstrated excellent passivation of undiffused Al_2O_3-passivated n-type Si at low to moderate doping levels [27], [28], [32], [38], [55], [61]. This is consistent with the fact that the negative Q_{tot} of Al_2O_3 is expected to induce strong inversion of such surfaces, so that surface recombination is limited by the surface electron concentration in accordance with (2.20) in the same way as for p-type surfaces. However, in many cases τ_{eff} of Al_2O_3-passivated n-type Si is observed to be significantly injection-dependent in low injection, decreasing with decreasing Δn [31], [32], [55], [61], [161], [187], [188]. In some cases τ_{eff} is observed to decrease continually over five or more decades of Δn [31]. A similar effect is observed for p-type Si passivated by positively charged SiN_x or SiO_2 [11], [12], [158], [159], [189]–[191], suggesting that it is related to the presence of the inversion layer.

Al_2O_3 from APCVD is able to provide similarly excellent levels of passivation for n-type surfaces. Fig. 7.6 shows injection-dependent excess carrier lifetime measured on undiffused n-type (P-doped) $\langle 100 \rangle$ Cz and FZ-Si wafers of various resistivity passivated with APCVD Al_2O_3, both before and after annealing. The values of τ_{eff} shown in Fig. 7.6 represent excellent levels of surface passivation. As shown by the figure, the lifetimes of both the $1.6\,\Omega\,\mathrm{cm}$ and $0.11\,\Omega\,\mathrm{cm}$ samples

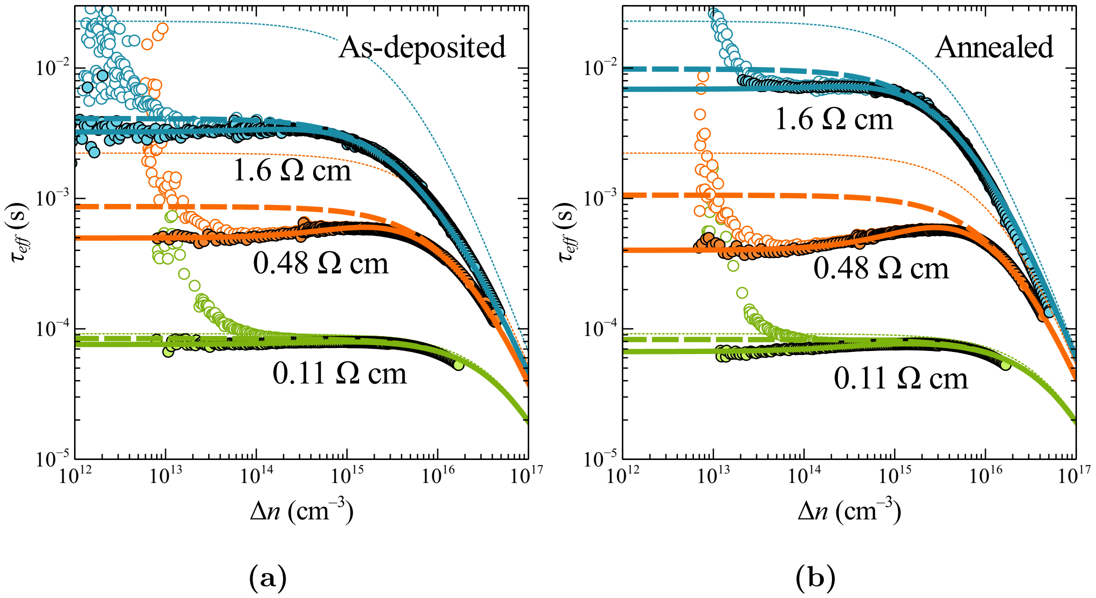

(a) **(b)**

Figure 7.6: Lifetime injection dependence for undiffused n-type (P-doped) Si passivated by APCVD Al_2O_3, both a) as-deposited, or b) annealed. Data is shown before (open symbols) and after (closed symbols) correction for depletion region modulation (DRM) effects. Solid lines show fits including transport-mediated recombination at localised high-recombination features, using the model described in Equations (7.5)–(7.10), while dashed lines show the projected lifetime in the absence of this recombination. Thin dotted lines show the intrinsic bulk lifetime according to [31].

approach close to the intrinsic limits determined by [31].

All samples exhibited an apparent increase in τ_{eff} at low Δn, consistent with the presence of DRM effects, which are expected for samples in which a surface inversion layer is present [192], [193]. The DRM model described in [193] was used to correct the data for this effect. After correction, data for all samples displayed a more-or-less flat dependence on Δn at the lowest measured injection levels, with in most cases a slight increase in τ_{eff} with increasing Δn near the transition between low and high injection.

Despite this slight injection dependence, the lifetime for all samples shown in Fig. 7.6 remains high over the measured injection range. The steeper decrease of τ_{eff} in low injection reported in some cases for n-type wafers passivated by Al_2O_3 is *not* observed for these samples. Fig. 7.6 therefore demonstrates that it is possible to achieve excellent passivation of undiffused n-type surfaces over a wide range of dopant concentrations and injection levels using Al_2O_3.

On the injection dependence of τ_{eff} at inverted surfaces

The reason for the pronounced injection dependence of τ_{eff} observed for many Al_2O_3 surfaces in low injection, and present to a lesser extent in the data of Fig. 7.6, is not obvious from conventional theory. Early explanations for this effect attributed it to the presence of SRH surface recombination limited by both carrier types [12], [189]. However, this requires either extreme asymmetry of capture coefficients, or very low insulator charge densities, both of which are inconsistent with experiment. A number of subsequent explanations have revolved around recombination in the depletion region formed by the inversion layer [11], [147], [154], [190], [194], [195]. For this recombination to be of the necessary magnitude to explain the observed τ_{eff} dependence, the carrier lifetime in the depletion region must be significantly lower than in the bulk of the wafer [147], [190], [194]–[196]. Consequently, it is supposed that there exists a highly defected region of low lifetime near the silicon surface [147], [190], [194]–[196] (a "surface damage region" in recent parlance [147], [195], [196]). The assumption of a surface damage region allows sufficient degrees of freedom to reproduce just about any injection dependence of τ_{eff}, but physical evidence for the existence of a highly defected region near the surface is scant, and the apparently universal nature of the observed effect is inconsistent with its attribution to damage caused by particular processing techniques.

More convincingly, it has been shown that two-dimensional carrier transport effects are able to account for the experimental observations [161], [188], [191], [197]. Essentially the inversion layer (or diffused junction) acts as a lateral conductive pathway that allows bulk minority carriers (in this case holes) to reach high-recombination regions in the device, such as unpassivated edges or localised surface damage features. The resulting recombination is injection-dependent because the transport mechanism acts as an approximately injection-independent resistive pathway for recombination, appearing in parallel with the injection-dependent capture resistance of the interface defects. At low injection levels it acts as a shunt, dominating recombination, while surface recombination becomes increasingly important as Δn increases. The two-dimensional nature of this mechanism means that it is easily verified experimentally by varying sample geometry, or through the use of PL imaging, as shown convincingly by [161], [188], [191], [197]. The attribution of the low injection lifetime dependence to transport-limited edge recombination can for instance explain the injection-independent lifetime observed in low injection for the extremely high-resistivity n-type wafers

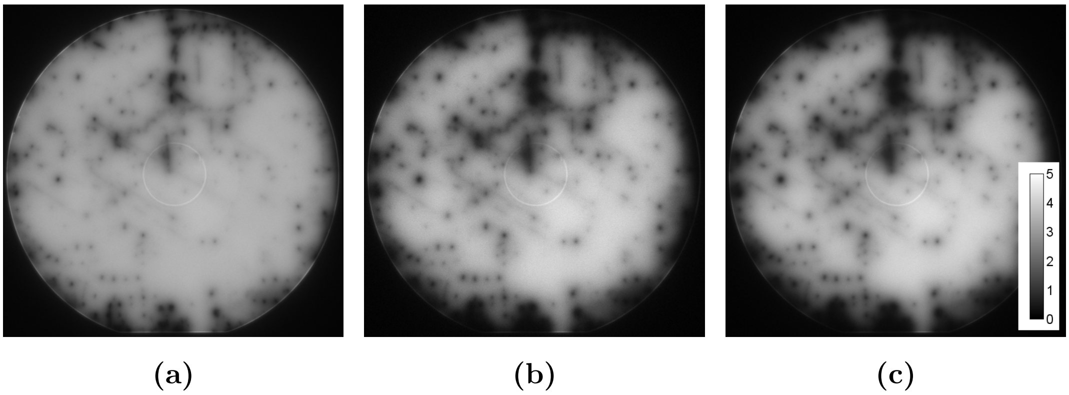

(a) (b) (c)

Figure 7.7: Calibrated PL lifetime images of a 4 inch 1.6 Ω cm n-type wafer passivated by as-deposited Al_2O_3, at injection levels of a) $10^{15}\,\text{cm}^{-3}$, b) $10^{14}\,\text{cm}^{-3}$, and c) $10^{13}\,\text{cm}^{-3}$. The position of the coil, visible at the centre of the wafer, corresponds to the location of the photoconductance decay (PCD) lifetime measurement of Fig.7.6. The scale shows lifetime in ms and is the same for all images.

measured by [55] using quasi-steady-state photoluminescence (QSS-PL), since edge recombination for these samples would be limited by majority carrier transport through the highly resistive bulk.

For the relatively slight injection dependence observed in Fig. 7.6, a satisfactory fit can be achieved using a bulk SRH recombination term. However, it appears unlikely that this is the true cause, since the magnitude of this recombination component increases following annealing in all cases, while bulk lifetime is not expected to vary as a result of such relatively low-temperature processing. On the other hand, the injection dependence of τ_{eff} shown in Fig. 7.6 can be explained by a model that includes lateral carrier transport by the inversion layer in combination with a spatially non-uniform surface passivation featuring localised regions of high surface recombination, similar to that described by [191]. In this case recombination through local surface states occurs in competition with transport of carriers to nearby high-recombination regions.

PL imaging provides direct experimental evidence of the presence of such regions and their increasing influence at low injection levels. Fig. 7.7 shows calibrated PL lifetime images of the as-deposited 1.6 Ω cm sample shown in Fig. 7.6a, taken at injection levels of $\Delta n = 10^{15}$, 10^{14}, and $10^{13}\,\text{cm}^{-3}$. It can be seen that in addition to a generally highly uniform background lifetime, there are a significant number of low-lifetime features, many point-like, and some more like scratches. Such features are often observed for lifetime samples fabricated even in cleanroom environments, and may be attributed either to surface contamination or to

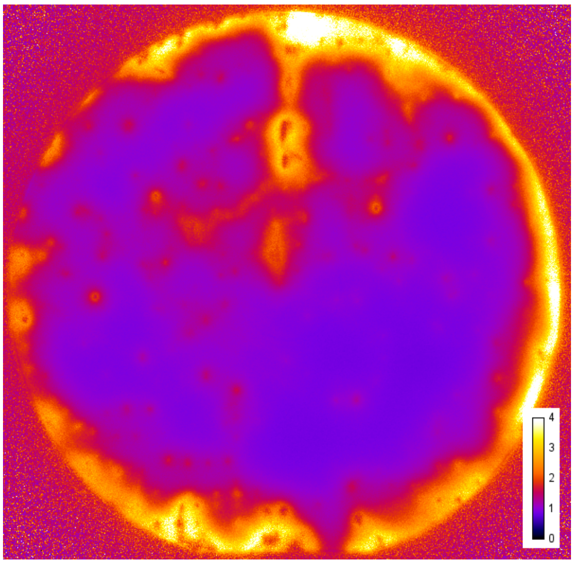

Figure 7.8: Ratio of τ_{eff} measured at $\Delta n = 10^{15}\,\mathrm{cm}^{-3}$ to that at $\Delta n = 10^{13}\,\mathrm{cm}^{-3}$, calculated from the PL images shown in Fig. 7.7.

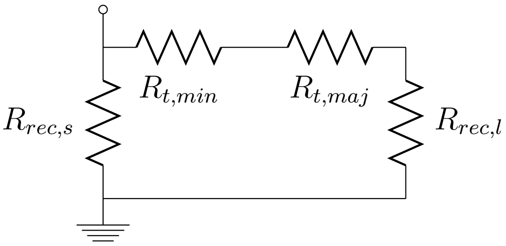

Figure 7.9: Simple lumped equivalent circuit model for the effective surface recombination resistance including transport-mediated recombination at localised high-recombination regions.

damage of the passivation layer during post-deposition handling. As the injection level decreases from 10^{15} to $10^{13}\,\mathrm{cm}^{-3}$, the background lifetime increases slightly, in accordance with the expected injection dependence of S_{eff}. However, the area affected by the low lifetime features also expands, showing that transport-mediated recombination at these features is increasingly dominant. Fig. 7.8 shows the ratio of τ_{eff} at 10^{15} and $10^{13}\,\mathrm{cm}^{-3}$, showing clearly how τ_{eff} in regions near high-recombination features decreases with decreasing Δn.

Previous authors have used circuit simulations [191], [197] and numerical device modelling [161], [197] to model the influence of transport-mediated recombination at edges and other high-recombination features on measured τ_{eff}. We choose instead to use a simple analytical model for this purpose. In this model we make use of the concept of recombination resistances introduced by Shockley and Read [114]. In this conception, the recombination rate may be viewed as analogous to a current, and the separation of the quasi-Fermi levels to a driving voltage. This equivalence is used in deriving the contribution of interface states to the equivalent circuit of the MIS capacitor, as described in Appendix B. By exploiting this equivalence here we are able to consider recombination and transport effects on an equal footing and in an intuitive manner.

In the proposed model the total effective surface recombination rate is described by the current flowing through a resistive network, in which $R_{rec,s}$, the surface recombination resistance, appears in parallel with the resistive path made up of the transport resistances for minority and majority carriers, $R_{t,min}$ and $R_{t,maj}$, and the recombination resistance of the localised high-recombination region $R_{rec,l}$ (Fig. 7.9). The total resistance of the network is thus given by

$$R_{rec,total}^{-1} = R_{rec,s}^{-1} + (R_{t,min} + R_{t,maj} + R_{rec,l})^{-1} \, . \tag{7.5}$$

Since the surface is in strong inversion, $R_{rec,s}$ is simply given by the capture resistance for electrons [114]

$$R_{rec,s} = (kT/q^2)S_{n0}^{-1}n_s^{-1} = (kT/q)J_0^{-1}n_i^2(N_D + \Delta n)^{-1}\Delta n^{-1} \, . \tag{7.6}$$

Assuming that recombination in the localised high-recombination region is also limited by the supply of electrons, its recombination resistance is similarly given by

$$R_{rec,l} = (kT/q^2)S_{n0,l}^{-1}n_s^{-1} = (kT/q)J_{0,l}^{-1}n_i^2(N_D + \Delta n)^{-1}\Delta n^{-1} \, . \tag{7.7}$$

The lateral transport resistance for bulk minority carriers (holes) in the inversion layer can be calculated as

$$R_{t,min} = A_l R_{sheet} = A_l |Q_{tot}|^{-1} \mu_{min,inv}^{-1} \, , \tag{7.8}$$

where A_l is an area factor that depends on the geometry of the sample and the relative distribution of the high recombination regions, and $\mu_{min,inv}$ is the average mobility of bulk minority carriers in the inversion layer. Similarly the lateral transport resistance for majority carriers (electrons) in the bulk of the wafer is given by

$$R_{t,maj} = 2A_l q^{-1}(N_D + \Delta n)^{-1}\mu_{maj,bulk}^{-1} W^{-1} \, , \tag{7.9}$$

where $\mu_{maj,bulk}$ is the mobility of majority carriers in the bulk of the wafer. The factor of 2 enters because of the assumption of a symmetrically passivated sample,

Table 7.3: Fitting parameters J_0, $J_{0,l}$, and A_l, used with Equations (7.5)–(7.10) to fit the lifetime data of Al_2O_3-passivated n-type samples in Fig. 7.6.

	Sample	J_0 (fA cm^{-2})	$J_{0,l}$ (fA cm^{-2})	A_l (cm^2)
As-deposited	1.6 Ω cm	11.9	3.9	8.0×10^{-2}
	0.48 Ω cm	11.6	14.1	1.4×10^{-3}
	0.11 Ω cm	2.8	4.0	1.4×10^{-3}
Annealed	1.6 Ω cm	3.5	2.6	6.8×10^{-2}
	0.48 Ω cm	8.1	25.5	6.6×10^{-4}
	0.11 Ω cm	3.4	8.7	1.0×10^{-3}

so that only half the thickness of the bulk can contribute to conduction. Finally S_{eff} is simply related to $R_{rec,total}$ by

$$S_{eff} = (kT/q^2)R_{rec,total}^{-1}\Delta n^{-1}\,. \tag{7.10}$$

Injection dependence arises because of the different injection dependences of the capture and transport resistances. At low Δn, the transport resistance is much smaller than either of the capture resistances, and S_{eff} will be limited by the parallel combination of the capture resistances, resulting in a constant τ_{eff}. As Δn increases, this capture resistance decreases, and the recombination current becomes transport-limited, so that τ_{eff} increases. Eventually, the transport mechanism is shunted by the decreasing $R_{rec,s}$, and τ_{eff} resumes its normal behaviour. For surfaces where an inversion layer is not present (e.g. for p-type surfaces passivated by Al_2O_3), $R_{t,min}$ will be very large, and S_{eff} will be independent of Δn in low injection, as observed experimentally. Equations (7.5)–(7.10) can also be used to describe transport-limited edge recombination, simply by setting $J_{0,l} = J_{0,edge}$, and A_l to a value on the order of the sample area. Note that the resistances in the model are intended as lumped parameters that approximate the behaviour of a potentially complex spatial distribution of localised high-recombination regions within and around the measurement area. Analogous versions of Equations (7.5)–(7.10) apply to p-type samples passivated by a positively charged dielectric.

Fits to the data of Fig. 7.6 using Equations (7.5)–(7.10) were performed by setting N_D and Q_{tot} to measured values and treating J_0, $J_{0,l}$, and A_l as fitting parameters. These fits are shown as solid lines in Fig. 7.6 and the values of the fitting parameters are given in Table 7.3. In all cases the model is able to satisfactorily describe the measured injection dependence of τ_{eff}, with the values of the fit parameters indicating an increase in the concentration of high-recombination regions following annealing (reducing A_l), which could arise from additional handling damage or from contamination during the anneal. We conclude that the observed injection-dependence is almost certainly caused by transport-mediated recombination at such regions.

7.3.2 Diffused surfaces

Heavily doped n-type surfaces, whether prepared by diffusion or other methods, represent the most challenging application for Al_2O_3 surface passivation. This is because the large negative charge present at the Si–Al_2O_3 interface—normally its greatest asset where surface passivation is concerned—becomes a liability at such surfaces. Unlike the situation at most undiffused n-type surfaces, typical densities of Q_{tot} are insufficient to strongly invert even lightly diffused n-type surfaces. Instead, the negative Q_{tot} merely induces weak depletion of the surface electron concentration, while significantly increasing the concentration of minority holes, and therefore the rate of surface recombination. Thus, Al_2O_3 has to fight an uphill battle to effectively passivate such surfaces, and the Al_2O_3 films that are most effective on p-type surfaces because of their large negative charge may not be those best suited for the job of passivating n-type surfaces.

Two previous studies have examined Al_2O_3 passivation of phosphorus-diffused surfaces in detail. The first, by Hoex *et al.* [30], used plasma-assisted ALD as the deposition method. They reported reasonably good passivation of moderately doped diffusions, with ~60 fA cm^{-2} for an R_{sheet} of ~125 Ω □$^{-1}$, but an increasingly poor passivation of lighter diffusions in the range of 100 to 200 Ω □$^{-1}$, before a significant improvement in passivation for the lightest diffusion (R_{sheet} = 318 Ω □$^{-1}$), attributed to inversion of the lightly doped surface. It was also noted that the inverse lifetime for the more lightly doped surfaces was non-linear, so that J_0 could not be extracted via Equation (2.34).

In contrast, Duttagupta *et al.* [178], using PECVD Al_2O_3/SiN_x stacks, reported significantly lower J_0 values for a wide range of n-type diffusions, with a very low $J_0 = 12$ fA cm^{-2} for an R_{sheet} of 165 Ω □$^{-1}$. The significant difference between these results and those of [30] was attributed to the lower negative charge of the PECVD films, in the range of ($1–2 \times 10^{12}$ cm^{-2}). However, the values reported by [178] need to be treated with caution. In the first place, [178] used

$n_i = 8.6 \times 10^9\,\mathrm{cm^{-3}}$ in Equation (2.34) rather than the $n_i = 9.65 \times 10^9\,\mathrm{cm^{-3}}$ used by [30] or $n_i = 9.70 \times 10^9\,\mathrm{cm^{-3}}$ used in this work, so the direct comparison made in Fig. 5 of [178] to the results of [30] is invalid. The J_0 values of [178] should therefore be multiplied by a factor of $\sim$1.3 when comparing to the values reported here or in [30]. The use of the intrinsic lifetime parameterisation of [184] by both [30] and [178] rather than the more recent parameterisation of [31] also results in an extracted J_0 lower by several $\mathrm{fA\,cm^{-2}}$, which is significant for well-passivated surfaces.

Besides these systematic influences, which are fairly easily accounted for, at least some of the J_0 extractions shown in Fig. 3 of [178] appear to be of dubious validity, because the inverse lifetime in fact appears significantly non-linear, suggesting that bulk SRH recombination is present. Because [178] used lower resistivity wafers with $N_A \approx 2 \times 10^{15}\,\mathrm{cm^{-3}}$, the bulk cannot be assumed to be in high injection in the range used for J_0 extraction, and consequently τ_{SRH} cannot be ignored. The effect of such bulk SRH recombination will be to decrease the apparent J_0 determined by Equation (2.34).

Consequently, we believe the J_0 values reported by [178] to be significantly underestimated. Our own results, reported below, are more consistent with those of [30].

Experimental details

In order to examine Al_2O_3 surface passivation of highly doped n-type surfaces, phosphorus-diffused $n{+}/n/n{+}$ structures were prepared on 410–465 µm thick, high resistivity ($> 100\,\Omega\,\mathrm{cm}$) n-type (P-doped) planar ⟨100⟩ FZ-Si wafers. These received a surface-damage etch in an HF:HNO_3 solution, followed by an RCA clean and dilute HF dip. Phosphorus diffusions were performed from a liquid $POCl_3$ source in a tube furnace at either 760, 790, or 820 °C for 25 min.

Following diffusion, the wafers were stripped of phosphosilicate glass by immersion in dilute HF until hydrophobic. Some of the samples were then RCA cleaned and subjected to different drive-in anneals in an N_2 ambient at 900 or 1000 °C for either 30, 60, 120, or 220 min. As with the boron-diffused samples of Section 7.2, these drive-ins were intended to redistribute the dopant atoms into the wafer, reducing the concentration at the surface. Other samples received no drive-in, but instead were given a short etch in HF:HNO_3 solution for 5, 10, 20, or 30 s, in order to remove a small part of the diffused region, again reducing the surface dopant concentration. Still other samples received neither a drive-in

Table 7.4: Properties of the phosphorus diffusion profiles prepared in this work. Depth refers to the distance from the surface at which the phosphorus concentration is equal to $10^{17}\,\mathrm{cm}^{-3}$. Asterisks (*) indicate that N_s and depth of the profile were not measured directly, but calculated from the sheet resistance as described in the text.

Diffusion Temp. (°C)	Drive-in/Etch	Sheet Resistance (Ω/□)	Surface Phos. Concentration (cm^{-3})	Depth (µm)
820	None	102.4	-	-
	900 °C, 30 min	34.9	6.6×10^{20}	0.54
	900 °C, 60 min	31.6	5.9×10^{20}	0.69
	900 °C, 120 min	30.2	4.9×10^{20}	0.85
	5 s etch	118.3	5.9×10^{20}	0.32
	10 s etch	127.6	3.7×10^{20}	0.30
	20 s etch	133.4	4.4×10^{20}	0.25
	30 s etch	163.3	3.0×10^{20}	0.23
790	None	229.4	2.5×10^{19}	0.26
	900 °C, 30 min	112.7	9.4×10^{19}	0.39
	900 °C, 60 min	101.6	9.0×10^{19}	0.48
	900 °C, 120 min	94.5	7.8×10^{19}	0.54
760	None	791.0	1.0×10^{19} *	0.15
	900 °C, 30 min	757.1	9.3×10^{18} *	0.17
	900 °C, 60 min	680.2	7.1×10^{18} *	0.22
	900 °C, 120 min	563.9	4.5×10^{18} *	0.33
	1000 °C, 30 min	580.0	4.8×10^{18}	0.35
	1000 °C, 60 min	508.3	3.6×10^{18} *	0.41
	1000 °C, 120 min	446.0	2.7×10^{18} *	0.54
	1000 °C, 220 min	392.1	2.0×10^{18} *	0.69

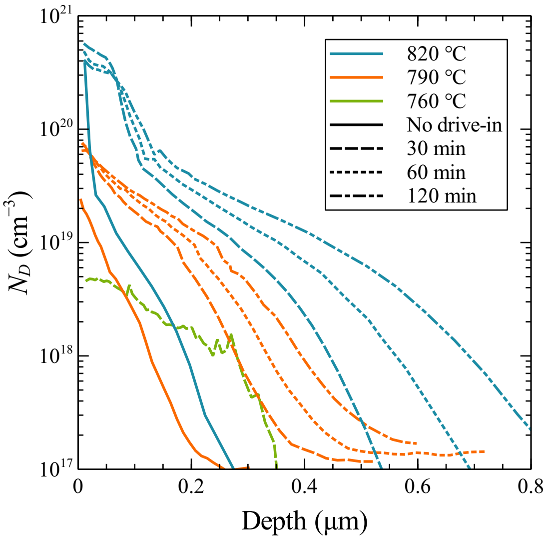

Figure 7.10: Active donor concentration profiles measured by the ECV method for a selection of the phosphorus diffusions used in this work. The drive in of the 760 °C profile shown was performed at 1000 °C, while the other drive-ins were performed at 900 °C.

nor etch, but were left as-diffused. The diffusion parameters and resulting sheet resistances measured by dark conductance are listed in Table 7.4.

Dopant profiles measured on selected samples by ECV are shown in Fig. 7.10, and values of N_s are given in Table 7.4. Although we do not possess measured dopant profiles for most of the lighter diffusions, we can estimate their likely surface concentration in the following way. We observe that the measured profile of the lightly diffused sample with a 30 min, 1000 °C drive-in is well-described by a Gaussian function over the high-concentration range, as expected for a low-concentration phosphorus profile following a drive-in step [97]. Setting N_s at the measured value, we determine the junction depth x_j of the Gaussian profile that provides the best fit to the measured profile. We then vary N_s and x_j of the Gaussian profile, keeping the total dopant dose constant, in order to match the relative change in calculated R_{sheet} to that of the measured values given in Table 7.4 for each of the dopant profiles. As expected, this results in an increase in x_j and a decrease in N_s with increasing drive-in times and temperature. The resulting profiles are shown in Fig. 7.11

As with the boron-diffused samples of Section 7.2, the phosphorus-diffused samples were passivated sequentially by APCVD and ALD Al_2O_3, with characterisation performed both immediately after deposition and after annealing for

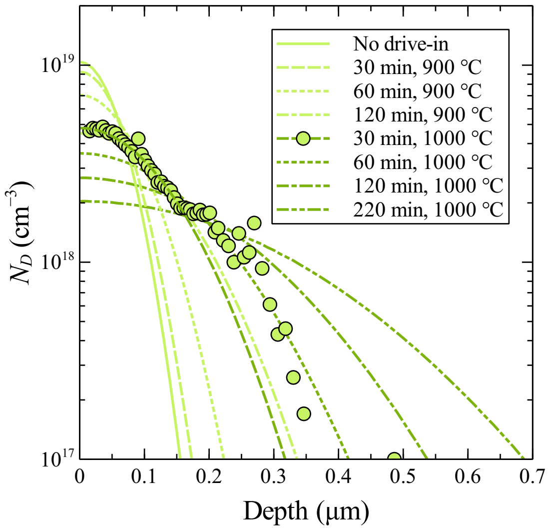

Figure 7.11: Modelled profiles for the unmeasured 760 °C diffusions with various drive-in steps, calculated from the measured sheet resistance as described in the text. Data points show profile data measured by ECV for one of the profiles, which was used to determine the total dopant dose.

the APCVD films, and after annealing only for the ALD films.

J_0 vs implied V_{oc}

The analysis of Al_2O_3 passivation of highly doped n-type Si surfaces is considerably more complicated than for p-type, because the negative charge which is generally present at the Si–Al_2O_3 interface may place the Si surface either in depletion, weak inversion, or strong inversion, depending on the charge density and the concentration of dopants and free carriers. When the surface dopant density is low, as for most undiffused surfaces, the insulator charge is usually sufficient to strongly invert the surface such that $p_s \gg n_s$, resulting in recombination behaviour dominated by S_{n0} in the same manner as described for p-type surfaces in Section 7.2. When the dopant density is very high, the insulator charge is only able to slightly deplete the concentration of majority electrons at the surface, increasing the concentration of minority holes, and thereby increasing surface recombination, which however remains dominated by S_{p0} and may therefore be described by a constant J_0. For intermediate dopant concentrations, however, the ratio of n_s and p_s may be a strong function of injection level, with either one or the other carrier dominating over different ranges of Δn.

Consequently Equation (2.18) cannot always be simplified, and J_0 may be strongly injection-dependent, as previously observed experimentally by [30]. A similar situation occurs at p-type surfaces passivated by positively-charged $\mathrm{SiN_x}$ [14]. Under these circumstances, it is not possible to make use of the slope of $\tau_{eff}^{-1} - \tau_{int}^{-1}$ versus Δn to determine J_0 via Equation (2.34), as usually done. Because of this, some authors have chosen to use an alternative metric such as implied open circuit voltage (iV_{oc}) to characterise surface passivation under such conditions [14], [30], where iV_{oc} is given by

$$iV_{oc} = kT/q \ln\left(\Delta n(N + \Delta n)/n_i^2 + 1\right) \, . \tag{7.11}$$

As iV_{oc} is intrinsically dependent on excess carrier concentration, its value is typically reported at an injection level corresponding to a steady-state illumination level of 1 Sun ($1\,\mathrm{Sun} = 1\,\mathrm{kW\,m^{-2}}$), where the illumination intensity in units of Suns is given by

$$I = J_g/(R_{abs} J_{ph,1Sun}) = (qW\Delta n/\tau_{eff})/(f_{abs} J_{ph,1Sun}) \, , \tag{7.12}$$

and J_g is the generation current, $J_{ph,1Sun}$ is the incident photon current at 1 Sun, and f_{abs} is the fraction of incident photons absorbed by the sample. This approach gets around the inability to use Equation (2.34), but it suffers several disadvantages as a means of characterising surface passivation. The intrinsic injection dependence of iV_{oc} makes direct comparisons of iV_{oc} at different injection levels impossible, even when surface recombination is not injection-dependent. Moreover, reporting iV_{oc} at 1-Sun illumination makes it dependent on both the optical properties of the sample and the bulk lifetime. Consequently, it is difficult to compare values of iV_{oc} between different experiments as a measure of passivation quality.

In all respects J_0 is a superior metric of surface passivation quality, having no intrinsic dependence on injection level or dopant concentration, and being independent of optical properties and bulk recombination. The difficulty in determining J_0 when Equation (2.34) is invalid can be circumvented by using Equation (2.33) directly in its non-derivative form and assuming $\tau_{SRH}^{-1} = 0$. This is the approach taken in this work. The resulting J_0 therefore includes τ_{SRH} (as would iV_{oc}), but we obtain good agreement with J_0 determined from the derivative method in cases where J_0 is independent of injection level, indicating that the contribution from τ_{SRH} in our samples is small. Since J_0 at a single injection level remains an incomplete metric of passivation quality under these conditions, the injection dependence of J_0 is illustrated over a relevant range by presenting J_0 values determined at illumination intensities of 1 and 0.05 Suns. In this case 1 Sun

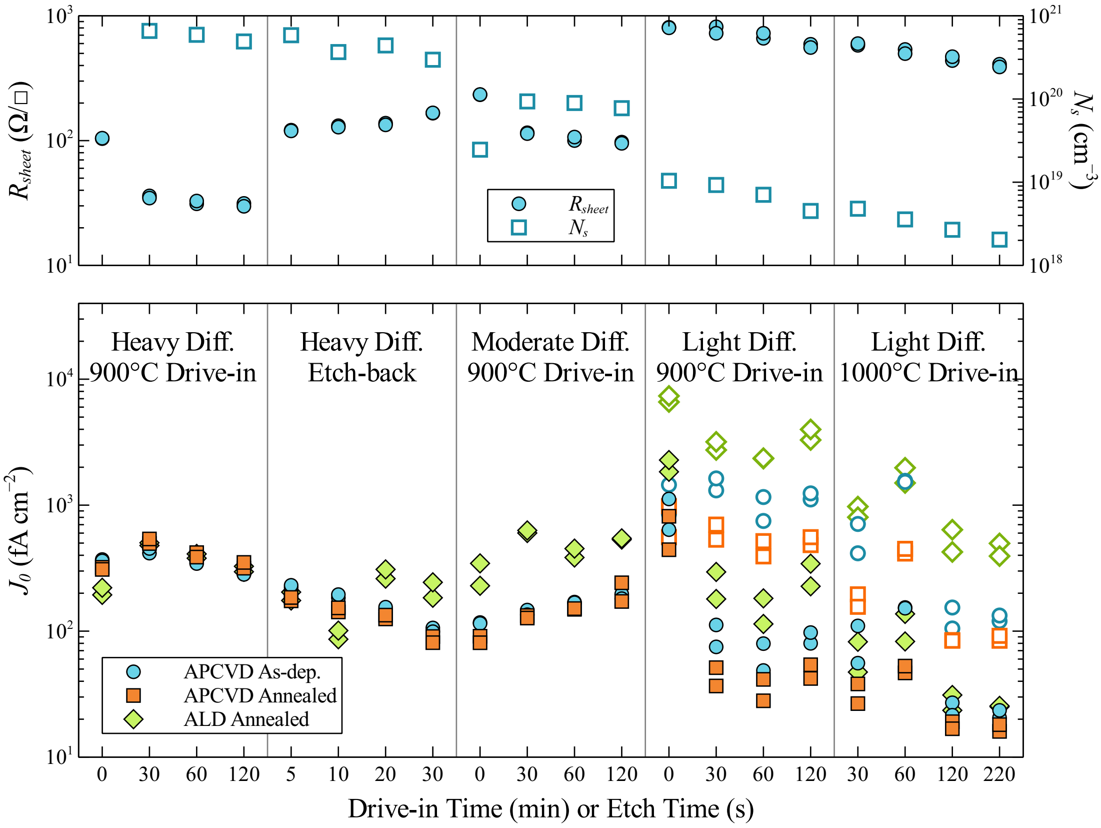

Figure 7.12: J_0 and R_{sheet} of Al_2O_3-passivated phosphorus diffused surfaces as a function of diffusion conditions and post-diffusion drive-in or etch-back time. Where both open and closed symbols are shown, J_0 is significantly injection-dependent. In this case closed symbols show J_0 determined at an illumination intensity of 1 Sun, while open symbols show J_0 determined at 0.05 Suns, where 1 Sun is considered to be equivalent to a generation current of 43.4 mA cm^{-2}. J_0 in this case is determined from τ_{eff} using Equation (2.33) with $\tau_{SRH} = 0$.

is assumed to correspond to a steady-state generation current of 43.4 mA cm^{-2}, corresponding to the integrated photon current of the AM1.5G solar spectrum below 1100 nm. This makes the value of J_0 independent of the optical properties of the sample, but representative of conditions in a high-efficiency device.

J_0 results

Fig. 7.12 shows J_0, R_{sheet}, and N_s as a function of the diffusion conditions and post-diffusion drive-in/etch. Broadly speaking, both surface dopant concentration and Auger recombination in the diffusion reduce as one moves from left to right on the plot, with lighter diffusions, longer drive-in times, and longer etches. The first point to note from Fig. 7.12 is that Al_2O_3 from APCVD is capable of providing good passivation of P-diffused Si surfaces of moderate R_{sheet} in the range of relevance to industrial solar cells. Annealed APCVD films provide J_0 values of 80 to 90 fA cm^{-2} on both etched-back heavy diffusions, and moderate as-diffused profiles, with R_{sheet} values of 163 $\Omega\,\square^{-1}$ and 230 $\Omega\,\square^{-1}$ respectively. These values are close to the best value of ~60 fA cm^{-2} reported by Hoex *et al.* [30] for a ~125 $\Omega\,\square^{-1}$ P diffusions passivated by Al_2O_3 from plasma-assisted ALD.

Similar trends of J_0 across the different profiles are apparent for all of the Al_2O_3 films, indicating that the general passivation behaviour is independent of the deposition method. J_0 in the heaviest diffusions is practically identical for all films, suggesting that J_0 is dominated by recombination in the diffusion (Auger and/or SRH) rather than at the surface. J_0 decreases as the dopant concentration in the diffusion is decreased, due to the reduction of this bulk recombination in the $n+$ region, until it reaches the aforementioned minimum. Beyond this point it increases again, as surface recombination becomes more significant and starts to dominate J_0. For more lightly doped diffused surfaces the ALD films generally provide less effective passivation than the APCVD films in either their as-deposited or annealed state. A possible explanation for this could be that the ALD films contain a higher insulator charge, which is beneficial on p-type surfaces but detrimental here. However, C–V measurements (Table. 7.2) indicate very similar values of Q_f for the two films. Another possibility is that S_{p0} of the ALD passivated surfaces is higher because the density of the defect species responsible for recombination on electron-majority surfaces is higher for the ALD films, despite a comparable or lower midgap D_{it}. This explanation is supported by subsequent analysis.

For the lightest diffusions, J_0 at 1 Sun again improves with decreasing N_s to quite low values of less than 20 fA cm^{-2}. This low J_0 at 1 Sun corresponds to a high iV_{oc} of 709 mV, which is consistent with the high value of iV_{oc} reported by [30] for their lightest diffusion ($R_{sheet} = 318\,\Omega\,\square^{-1}$, $N_s \approx 2 \times 10^{19}\,\mathrm{cm}^{-2}$). However, Fig. 7.12 also shows that J_0 for these lighter diffusions is strongly injection dependent, and that J_0 at 0.05 Suns is approximately an order of magnitude greater than the value at 1 Sun. This injection dependence of J_0 is presumably also the reason for the non-linear inverse lifetime reported by [30] for $R_{sheet} > 150\,\Omega\,\square^{-1}$. The consequence of this for photovoltaic devices is that while V_{oc} may be high, the effective lifetime at the maximum power point will be significantly reduced, even at 1 Sun illumination, leading to a reduction of the fill factor in a similar manner as when significant bulk SRH recombination is present [198].

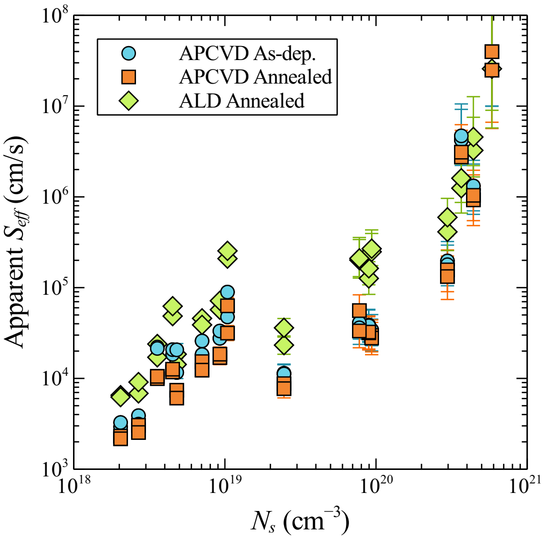

Figure 7.13: Apparent S_{eff} required to provide a match between measured and simulated J_0 at $\Delta n = 10^{15}\,\mathrm{cm}^{-3}$ of Al_2O_3-passivated phosphorus-diffused surfaces, as a function of surface dopant concentration N_s.

Determination of S_{eff} from J_0 data

In order to determine the contribution of surface recombination to J_0, the measured and estimated dopant profiles were simulated in the same way as described in Section 7.2 for the boron diffusions. As before, an apparent S_{eff} was extracted by adjusting S_{eff} to match the simulated and measured J_0 values. The results are shown in Fig. 7.13. In all cases Auger recombination in the diffused region is able to account for only a fraction of the observed J_0. As a result, an increasingly large S_{eff} is required to account for the balance at higher N_s. Indeed for the heaviest diffusions it was not possible to account for the observed J_0 values using only surface recombination, even with values of S_{eff} greater than the thermal velocity.

This mismatch between experiment and theory in the case of heavy phosphorus diffusions has been observed by a number of authors, and has been attributed to SRH recombination activity in the diffused region by otherwise electrically inactive phosphorus [199], [200]. It is possible to account for the observed J_0 values with the inclusion of such recombination in the model. However it is not possible to assess the extent of this recombination independently of recombination at the surface. Therefore we cannot extract S_{eff} in such cases. The fact that such recombination appears to be present casts serious doubt on the reality of the apparent increase of S_{eff} with N_s observed for the other diffused surfaces with

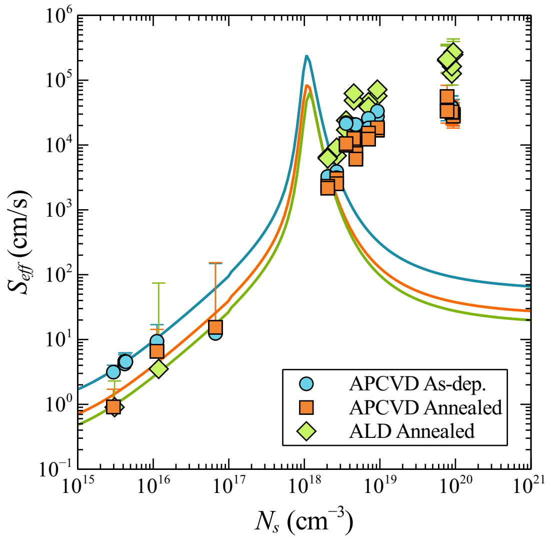

Figure 7.14: S_{eff} vs N_s at $\Delta n = 10^{15}\,\mathrm{cm}^{-3}$ for undiffused ($N_s < 10^{17}\,\mathrm{cm}^{-3}$) and diffused n-type (P-doped) surfaces passivated by Al_2O_3. Lines show modelled S_{eff} using measured values of $D_{it,midgap}$ and Q_{tot} with only the donor-like defect state described in Section 4.2. This state cannot account for the observed recombination at the more heavily doped surfaces.

$N_s > 10^{20}\,\mathrm{cm}^{-3}$, since these were derived from the same initial heavy diffusion. It appears likely that there too the increase in J_0 is primarily a product of SRH recombination in the diffused region. Consequently only the profiles derived from the two lighter diffusions, with $N_s < 10^{20}\,\mathrm{cm}^{-3}$, are considered in subsequent analysis of the surface passivation properties. We also ignore the profiles which did not receive a drive-in, since there is a large uncertainty in N_s for these profiles due to the very steep near-surface dopant profile.

Determination of S_{n0} and S_{p0}

Even considering only the remaining samples, it is apparent that the interface model of Section 4.2 must be extended to account for surface recombination at heavily-doped n-type surfaces. Fig. 7.14 shows S_{eff} vs N_s for both undiffused and diffused phosphorus-doped surfaces, together with the modelled S_{eff} vs N_s dependence, where the latter was calculated in the same way as for the boron-doped surfaces (Section 7.2), but with D_{it} and Q_{tot} taken from C–V measurements for the same films on n-type substrates (Table 7.5). This model includes only a single defect species, with the properties given for “State A” in Table 4.1. Firstly, it is apparent that the model can account for the recombination at undiffused n-

Table 7.5: Si–Al_2O_3 interface properties determined by C–V measurements of phosphorus-doped samples: total insulator charge Q_{tot}, midgap interface state density D_{it}, and corresponding fundamental surface recombination velocity of electrons, $S_{n0,A}$, calculated from (7.4).

Passivation Layer	Q_{tot}/q (10^{12} cm^{-2})	$D_{it,midgap}$ (10^{11} cm^{-2} eV^{-1})	$S_{n0,A}$ (10^3 cm s^{-1})
APCVD As-dep.	1.78	1.20	7.8
APCVD Annealed	1.70	0.50	3.3
T-ALD Annealed	1.75	0.36	2.3

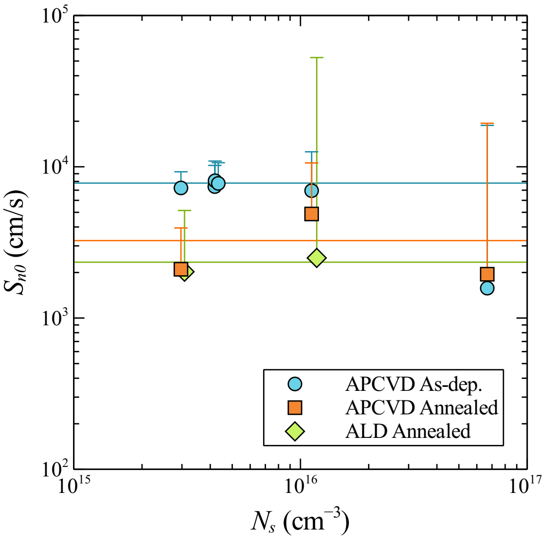

Figure 7.15: S_{n0} extracted from S_{eff} of the undiffused n-type (P-doped) surfaces shown in Fig. 7.14. Lines show S_{n0} predicted from the measured $D_{it,midgap}$ using Equation (7.4) (see Table 7.5).

type surfaces similarly well as for p-type surfaces (Fig. 7.3). S_{n0} can be calculated for such surfaces from S_{eff} in a similar way as described in Section 7.2, using the relationship

$$S_{eff} = S_{n0}\frac{n_s}{\Delta n_d}\,. \tag{7.13}$$

The resulting values of S_{n0} are shown in Fig. 7.15, where they are compared to values predicted from the measured D_{it} using Equation (7.4), with excellent agreement. In all cases they are significantly lower than the values determined for p-type surfaces (Fig. 7.5), which is consistent with the lower D_{it} measured for n-type surfaces (compare Tables 7.2 and 7.5, and see Section 4.1).

On the other hand, it is also apparent that the basic model cannot account for the recombination observed at diffused n-type surfaces. The single donor-like defect state included in this model is an inefficient recombination centre at electron-majority surfaces due to its low capture coefficient for holes. This is the reason for the rapid decrease in simulated recombination as N_s increases. Consequently, the presence of a second species of interface state is necessary to account for recombination at surfaces where ($n_s \gg p_s$). To clearly distinguish the properties of this second state from those of the first, we use the additional subscript "B" when referring to the former, and "A" for the latter. Such a state must have $c_{p,B} \gg c_{n,B}$ (i.e. almost certainly acceptor-like) in order to provide a sufficiently high recombination rate at electron-majority surfaces, while not contributing significantly to recombination at hole-majority surfaces.

$S_{p0,B}$ can be determined directly from S_{eff} of the diffused surfaces with $N_s \approx 1 \times 10^{20}\,\mathrm{cm^{-3}}$, since J_0 for these surfaces is injection-independent, which implies that surface recombination is limited by minority carrier (hole) capture. Consequently S_{p0} is related to S_{eff} by

$$S_{eff} = S_{p0}\frac{p_s}{p_d}\,, \tag{7.14}$$

where p_s and p_d are calculated as described in Section 2.3, using Q_{tot} from Table 7.5. Average values of $S_{p0,B} = 2.2 \times 10^4$, 2.1×10^4, and $1.2 \times 10^5\,\mathrm{cm\,s^{-1}}$ were determined in this way for as-deposited APCVD, annealed APCVD, and annealed ALD films respectively.

The injection dependence of J_0 for the lighter diffusions implies that both $S_{p0,B}$ and $S_{n0,B}$ are important for determining the recombination rate at these surfaces. Such injection dependence occurs when surface recombination transitions from being limited by the concentration of one carrier type to being limited by the other or by both. The exact circumstances under which this occurs therefore depend on the capture cross-section ratio of the relevant interface states, as well as N_s and Q_{tot}.

Additionally, it appears clear from comparison of the measured and modelled injection dependence of recombination that some form of capture time constant dispersion must be included in a truly comprehensive model. To illustrate this, Fig. 7.16 shows measured and modelled S_{eff} vs Δn for the lightly diffused surface with $N_s = 9.3 \times 10^{18}\,\mathrm{cm^{-3}}$ (remembering that S_{eff} here is defined with respect to the edge of the near-surface quasi-neutral region in the diffusion, rather than the silicon bulk). Since these diffusions are sufficiently light to be considered "transparent", S_{eff} can simply be calculated from the measured $J_0(\Delta n)$ using

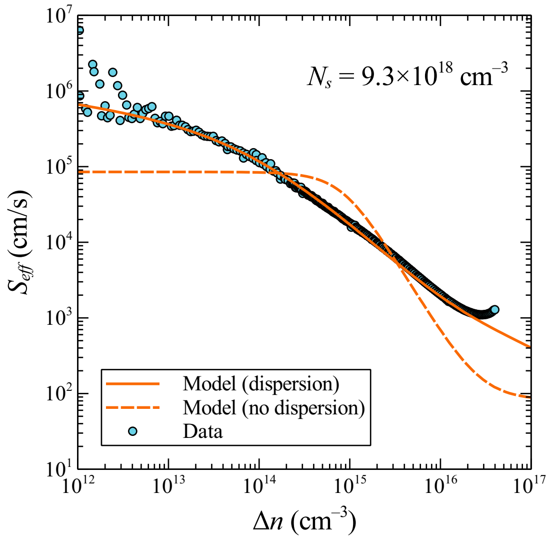

Figure 7.16: Comparison of experimental S_{eff} vs Δn for a lightly doped diffused surface passivated by annealed APCVD Al_2O_3, and modelled values calculated with and without the inclusion of surface potential fluctuations. Parameters of the model are given in Table 7.6.

Table 7.6: Parameters of the modelled fit to injection-dependent S_{eff} shown in Fig. 7.16.

Parameter	Units	Value
Q_{tot}/q	cm^{-2}	-1.7×10^{12}
$S_{p0,B}$	cm s^{-1}	1.4×10^{4}
$S_{n0,B}$	cm s^{-1}	4.5×10^{-2}
$S_{p0,A}$	cm s^{-1}	1.4×10^{1}
$S_{n0,A}$	cm s^{-1}	1.9×10^{3}
σ_s	–	2.4

the analytical expression [109]

$$J_0 = \frac{qn_i^2}{G_{eff}(W) + \dfrac{N_s}{S_{eff}}\dfrac{n_i}{n_{ie,s}}}\,, \tag{7.15}$$

where

$$G_{eff}(x) = \int_0^W \frac{N_D}{D_p}\frac{n_i}{n_{ie}}\,dx\,, \tag{7.16}$$

and x is the distance measured from the bulk into the diffusion, with $x = W$ at the surface.

While both the experimental data and the model in Fig. 7.16 show a similar decrease in S_{eff} with increasing Δn, the slope of this decrease is overestimated by the uniform potential model. This is not something which can be remedied by varying any of the existing model parameters, but is rather an intrinsic limitation of the model and the functional dependencies which it is capable of describing. Note that the modelled S_{eff} is fairly insensitive to the exact energetic distribution of state B, since the significance of the emission terms in (2.17) does not vary strongly with Δn except for states very close to the valence band edge.

In effect, the measured injection dependence of S_{eff} shown in Fig. 7.16 can be described as being broadened relative to the uniform potential model. Such a broadening points to a dispersion of capture time constants at the surface. The most likely origin of this dispersion is the presence of short-range surface potential fluctuations due to the discrete spatial distribution of non-mobile charge states (fixed insulator charges, interface trapped charge, and ionised dopant atoms) in the vicinity of the Si–Al_2O_3 interface. The presence of such fluctuations has been found to be necessary to account for the frequency dispersion invariably observed in MIS measurements of interface state conductance at undiffused surfaces in depletion [8], [144]. It is expected that such fluctuations will also be present to some extent at more heavily doped surfaces, especially under the conditions of depletion obtaining in the present case. In accumulation or strong inversion, on the other hand, surface potential fluctuations should be effectively screened by the large free carrier concentration.

Fig. 7.16 shows that the inclusion of surface potential fluctuations in the modelled S_{eff} can account for the observed broadening with respect to Δn. In this case we have incorporated such fluctuations as a Gaussian distribution of the surface potential ψ_s centred around the mean value $\bar{\psi}_s$, while assuming a uniform potential at the edge of the quasi-neutral region. The probability that the surface potential is ψ_s is

$$P(\psi_s) = (2\pi\sigma_s^2)^{-1/2} \exp\left[-(kT/q)^{-2}\frac{(\psi_s - \bar{\psi}_s)^2}{2\sigma_s^2}\right] , \tag{7.17}$$

where σ_s is the normalised standard deviation of the surface potential. The surface recombination rate including surface potential fluctuations is then given by

$$U_{s,total} = \int_{-\infty}^{\infty} P(\psi_s) U_s\left(n_s, p_s\right) d\psi_s \, . \tag{7.18}$$

The parameters of the fit shown in Fig. 7.16 are given in Table 7.6. It is clear from the quality of this fit that the addition of surface potential fluctua-

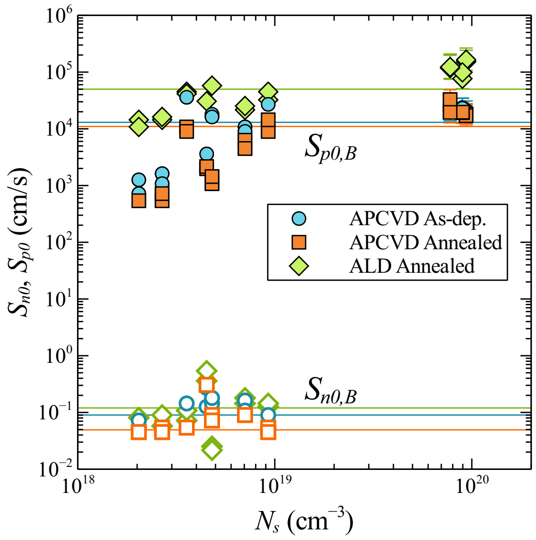

Figure 7.17: Apparent S_{p0} (closed symbols) and S_{n0} (open symbols) extracted from S_{eff} of the P-diffused surfaces shown in Fig. 7.14. Lines denote the proposed values of $S_{p0,B}$ and $S_{n0,B}$.

tions can account very well for the observed injection dependence of S_{eff} for the lightly diffused n-type surfaces. Note that we cannot rule out the possibility that the observed recombination is due to significant contributions by more than one acceptor-like defect species with different capture coefficient ratios. A second or even third defect could be concealed by the broadening of the $S_{eff}(\Delta n)$ curve. This would increase the apparent degree of broadening, but would not produce such broadening in the absence of surface potential fluctuations. S_{eff} for the other lightly doped surfaces displays a similar dependence on Δn, and can be fit similarly well. The resulting values of $S_{p0,B}$ and $S_{n0,B}$ are shown in Fig. 7.17 together with $S_{p0,B}$ determined for the moderately diffused surfaces ($N_s \approx 1 \times 10^{20}\,\text{cm}^{-3}$) from (7.14).

Discussion

In examining Fig. 7.17, it should firstly be noted that for the light diffusions with higher N_s, around $10^{19}\,\text{cm}^{-3}$, $S_{p0,B}$ agrees fairly well with the values determined for the moderately diffused surfaces with $N_s \approx 10^{20}\,\text{cm}^{-3}$. This gives us confidence in the extracted value of $S_{p0,B}$. At lower N_s, $S_{p0,B}$ displays significant systematic variation with N_s. The reasons for this will be discussed later. The second major point to note here is the extremely low value of $S_{n0,B}$, which is more than five orders of magnitude smaller than $S_{p0,B}$. This implies a $c_{n,B}/c_{p,B}$ ratio greater than 10^5 which is significantly larger than the $c_{p,A}/c_{n,A} \approx 140$ of state A. Assuming a density of state B equal to that of state A, implied values for $\sigma_{p,B}$ and $\sigma_{n,B}$ are on the order of $10^{-14}\,\mathrm{cm}^2$ and $10^{-19}\,\mathrm{cm}^2$ respectively.

Nevertheless, the implied low value of $\sigma_{n,B}$ is consistent with observations from conductance measurements of both p- and n-type samples in the energy range just above midgap, which indicate the presence of a defect state with similarly low σ_n (Section 4.2). Such values are very similar to those reported for the $1- \rightleftarrows 2-$ transition of the double acceptor level formed by zinc in silicon [201], [202]. In such a case the low value of σ_n is explained by the low probability of electron capture in a singly-charged, Coulombically repulsive center. Similarly, the relatively large value of σ_p may be attributed to the strong attractive potential for holes formed by the doubly-charged centre. The identification of state B as the $1- \rightleftarrows 2-$ transition of a double acceptor defect appears the most likely explanation for its observed behaviour.

The values of $S_{p0,B}$ determined for the more heavily doped surfaces are significantly larger than the value of $S_{n0,A}$ measured on p-type (Fig. 7.5) and undiffused n-type surfaces (Fig. 7.15). This implies that $c_{p,B}N_{it,B}$ is significantly greater than $c_{n,A}N_{it,A}$. The fact that the ratio $S_{p0,B}/S_{n0,A}$ is different for each passivation layer suggests at least that $N_{it,B}$ at diffused surfaces is different to $N_{it,A}$ at undiffused surfaces. If we assume that the interface defect density is independent of the phosphorus dopant density, as appears to be the case for boron (Section 7.2), this would suggest that state A and B do not simply represent different transitions of a single amphoteric defect species, but that at least two distinct defect species are present and contribute significantly to recombination. It would also indicate that the densities of each defect may vary independently, with $N_{it,B}$ being significantly less affected by the post-deposition anneal than $N_{it,A}$, and significantly larger for the films deposited by ALD than for those deposited by APCVD, in contrast to the case for $N_{it,A}$.

As noted previously, the extracted value of $S_{p0,B}$ deviates systematically from its value on more heavily doped surfaces with decreasing N_s below $\sim 10^{19}\,\mathrm{cm}^{-3}$. If this decrease were due to a dependence of $N_{it,B}$ on N_s, we would expect to observe a similar decrease in $S_{n0,B}$. The fact that $S_{n0,B}$ instead appears remarkably independent of N_s suggests that an alternative explanation is necessary.

The most obvious candidate for such an explanation is the presence of error in the modelled surface minority carrier concentration p_s, used to extract $S_{p0,B}$ from S_{eff}. In fits like that shown in Fig. 7.16, which were used to extract the data of Fig. 7.17, $S_{p0,B}$ is essentially determined from the value of S_{eff} at low

Δn, where $S_{eff} = (p_s/p_d)S_{p0,B}$ in the absence of surface potential fluctuations. $S_{n0,B}$ is then determined from the onset of injection dependence, which depends on the ratio $(p_s S_{p0,B})/(n_s S_{n0,B})$. Consequently, an error in the ratio p_s/p_d due to error in the modelled surface minority carrier concentration p_s would produce a corresponding error in $S_{p0,B}$, but would not affect the extracted value of $S_{n0,B}$, because the extraction of $S_{n0,B}$ depends on the product of p_s and $S_{p0,B}$. This would account for the differing dependence of $S_{p0,B}$ and $S_{n0,B}$ on N_s in Fig. 7.17. An increasing error in p_s at lower N_s could for instance be caused by error in the degree of bandgap narrowing at the surface, which we have assumed to be equal to that at the edge of the quasi-neutral region in the diffusion, but which may differ from that value due to the strong depletion of majority carriers at the surface. Such an error might be expected to increase as the relative extent of depletion increases with decreasing N_s. Consequently we believe the values of $S_{p0,B}$ extracted at higher N_s to be the most reliable.

In principle, surface potential fluctuations should also be accounted for in the extraction of $S_{p0,B}$ for the more heavily diffused surfaces. The inclusion of such fluctuations would tend to decrease the extracted $S_{p0,B}$. However, because S_{eff} of these surfaces is essentially independent of Δn within the measured range, σ_s cannot be determined from the experimental data. It is expected that σ_s will be a function of N_s and Q_{tot}, and that it should be greatest when the surface is strongly depleted, and smallest when the surface carrier concentration is large and the fixed surface charges are effectively screened.

Nicollian and Brews [8] derived the following expression for σ_s due to a random distribution of point charges at the interface, evaluated over a plane parallel to the interface and located at a distance λ into the semiconductor.

$$\sigma_s^2 = \left(\frac{q}{kT}\right)^2 \frac{qQ_{tot}}{4\pi(\epsilon_s + \epsilon_i)^2} \ln\left[1 + \left(\frac{C_\lambda}{C_i + C_s + C_{it}}\right)^2\right], \tag{7.19}$$

where $C_\lambda = (\epsilon_s + \epsilon_i)/\lambda$. Here C_i accounts for screening by charge in the gate of a MIS structure, which is not present in this case, and so can be ignored. Neglecting also C_{it} (which is negligible compared to C_s for such well-passivated surfaces), and taking $\epsilon_i/\epsilon_0 = 9$ from Fig. 9.10a, we calculate σ_s from (7.19) as a function of N_s for different values of λ, and plot it in Fig. 7.18 together with the extracted σ_s of the annealed APCVD samples. Good agreement with both the trend and magnitude of the observed σ_s is obtained for a value of λ on the order of 7.5 Å. This value is an order of magnitude smaller than the value of ~75 Å inferred by [8] from conductance measurements of the Si–SiO$_2$ interface.

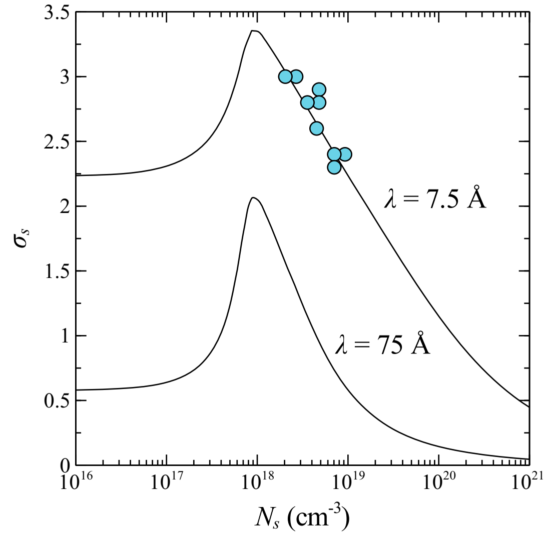

Figure 7.18: Standard deviation of surface potential, σ_s, as a function of N_s. Data points are extracted from injection-dependent lifetime data as described in the text. Lines show values predicted by (7.19) for different values of λ.

According to [8], the value of λ should be approximately equal to the spatial extent of the trapped carrier wave function of the relevant interface states. It is therefore plausible that the low value of λ is related to the very small value of $\sigma_{n,B}$, such that the capture rate is sensitive to surface potential fluctuations occurring over a very short range. In this case, we could expect the measured σ_s to apply only to the calculation of recombination for state B, and perhaps only to the electron capture process, given the much larger value of $\sigma_{p,B}$.

Modelling S_{eff}

If we continue in the assumption that surface potential fluctuations apply equally to the capture processes for both carriers, we can use the modelled σ_s shown in Fig. 7.18 to estimate the influence of surface potential fluctuations on the measured J_0 of the surfaces with $N_s \approx 10^{20}\,\mathrm{cm}^{-2}$. At this dopant concentration, the model shown in Fig. 7.18 predicts $\sigma_s \approx 1$. This would result in a roughly 40 % decrease of the extracted value of $S_{p0,B}$ for these samples, which would result in better agreement with $S_{p0,B}$ determined at lower N_s. On the other hand, as noted above, there seem to be grounds for supposing that the magnitude of surface potential fluctuations relevant to the calculation of $S_{p0,B}$ should be significantly smaller than those shown in Fig. 7.18. It may be that $S_{p0,B}$ instead ought to be adjusted upwards for the more lowly doped surfaces in order to account for the

Table 7.7: Fundamental surface recombination velocities of defects A and B determined from carrier lifetime measurements on n-type surfaces passivated by different Al_2O_3 films. The ratio $S_{p0,B}/S_{n0,B}$ is also shown.

Film	$S_{n0,A}$ ($\mathrm{cm\,s^{-1}}$)	$S_{p0,B}$ ($\mathrm{cm\,s^{-1}}$)	$S_{n0,B}$ ($\mathrm{cm\,s^{-1}}$)	$\frac{S_{p0,B}}{S_{n0,B}}$
APCVD As Dep.	7.8×10^3	1.3×10^4	9×10^{-2}	1.4×10^5
APCVD Annealed	3.3×10^3	1.1×10^4	5×10^{-2}	2.2×10^5
ALD Annealed	2.3×10^3	5×10^4	1.2×10^{-1}	4.2×10^5

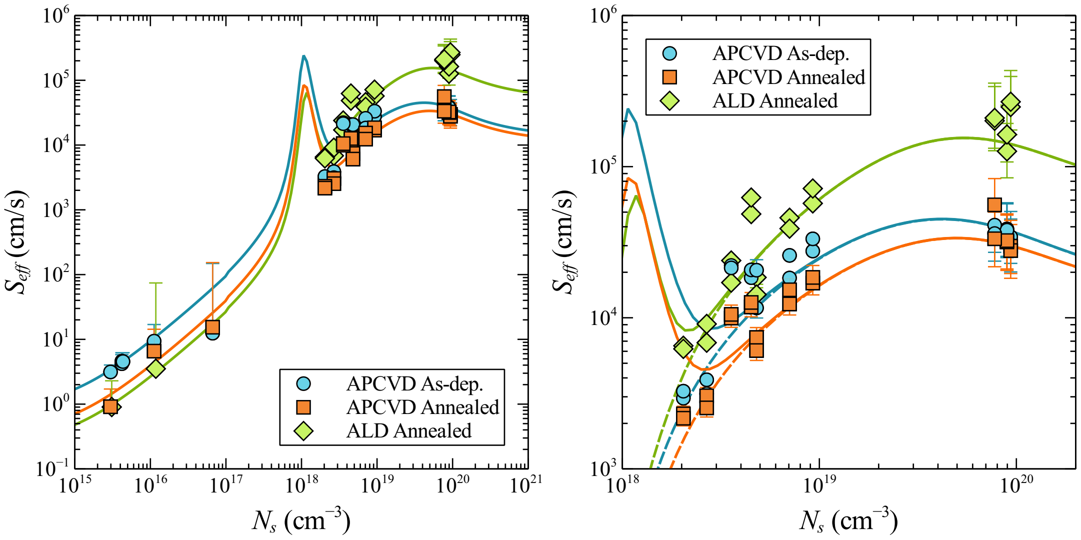

(a) **(b)**

Figure 7.19: Modelled (lines) and measured (data points) S_{eff} vs N_s, as in Fig. 7.14, but with the inclusion of a second, acceptor-like defect state to the modelled S_{eff}, which accounts for the recombination on heavily P-doped surfaces. Solid lines show total modelled recombination, while dashed lines show recombination due to state B only.

existence of potential fluctuations perhaps much smaller than originally assumed for the hole capture process.

We do not attempt to resolve these complexities here. Instead we assume that the extracted surface potential fluctuations apply equally to both capture processes of state B. We then determine values for $S_{p0,B}$ and $S_{n0,B}$ for each film from the data of Fig. 7.17, taking the values determined at higher N_s, adjusted for σ_s as described above, as being the most reliable. These values are listed in

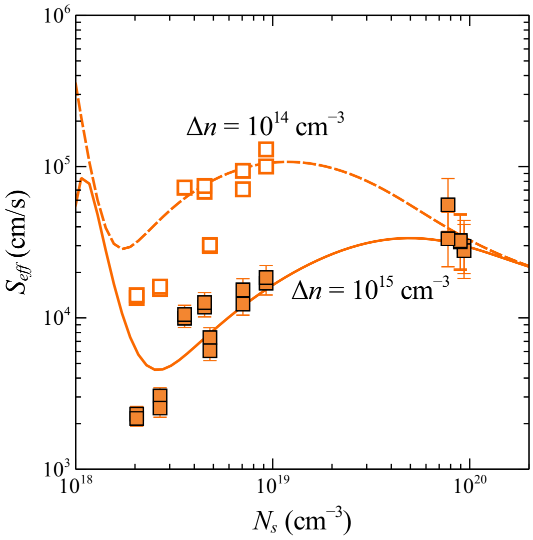

Figure 7.20: Modelled and measured S_{eff} vs N_s at different values of injection level Δn for P-diffused surfaces passivated by annealed APCVD Al_2O_3.

Table 7.7, and shown as lines in Fig. 7.17.

$S_{eff}(N_s)$ evaluated at $\Delta n = 10^{15}\,\text{cm}^{-3}$ using these parameters is plotted against the experimental data in Fig. 7.19. In this evaluation, σ_s is assumed to be given by (7.19) with $\lambda = 7.5\,\text{Å}$ for state B, while surface potential fluctuations for state A are assumed to be negligible. This seems reasonable given the significantly larger neutral capture cross-section of state A, and the fact that recombination through this state is mainly important for undiffused n-type surfaces, where the surface is in strong inversion and surface potential fluctuations are effectively screened. Close fits to measured injection-dependent lifetime were also obtained for state A with $\sigma_s = 0$. The effect of surface potential fluctuations on the capture rate of state A would need to be considered for surfaces with N_s in the range of $\sim 10^{17}$ to $2 \times 10^{18}\,\text{cm}^{-3}$, where the surface is in strong depletion or only weak inversion for typical values of Q_{tot}, and recombination through state A is significant. This would lead to a broadening and smearing out of the sharp peak feature shown in Fig. 7.19. Surface dopant concentrations in this range are rare in practice. We assume Gaussian diffusion profiles with a depth of 0.5 µm. This results in values of G_{eff} from Equation (7.16) similar to those of the measured lightly diffused surfaces in the range of N_s covered by these light diffusions. Outside this range (i.e. where J_0 is independent of Δn) S_{eff} is independent of the profile depth.

To illustrate the influence of the injection level, Fig. 7.20 shows measured and modelled S_{eff} vs Δn at $\Delta n = 10^{14}$ and $10^{15}\,\mathrm{cm}^{-3}$ for the diffused surfaces passivated by annealed APCVD films. From Figs. 7.19 and 7.20 it can be seen that the model provides a good description of the experimentally observed dependence of surface recombination rate on both N_s and Δn, except for diffused surfaces with $N_s < {\sim}3 \times 10^{18}\,\mathrm{cm}^{-3}$, probably because of an overestimation of the modelled p_s at these surfaces, as previously discussed.

Summary

Consistent with previous work, Al_2O_3 is shown to provide excellent passivation of lightly doped n-type surfaces, with $N_s < 10^{17}\,\mathrm{cm}^{-3}$, due to strong inversion of the surface carrier concentrations induced by the negative charge of the films. J_0 values of just over $3\,\mathrm{fA\,cm}^{-2}$ are achieved for annealed APCVD films. It is concluded that the reduction in τ_{eff} often observed for Al_2O_3-passivated n-type surfaces in low injection can be attributed to an increased sensitivity to localised high-recombination surface features due to the lateral minority carrier transport path provided by the inversion layer. Such features must be minimised or avoided to realise the full potential of Al_2O_3 passivation on n-type surfaces, especially at low illumination levels.

It is shown that Al_2O_3 can provide good, though not outstanding surface passivation of n-type diffused Si surfaces with N_s of ${\sim}10^{20}\,\mathrm{cm}^{-3}$ or above, depending on the magnitude of Q_{tot}. For more heavily doped surfaces, J_0 is likely to be dominated by recombination in the diffusion, either Auger or SRH, rather than by surface recombination. For more lightly doped surfaces, J_0 will be highly injection-dependent, decreasing strongly with increasing injection. If such surfaces were incorporated into solar cells they could allow a high V_{oc}, but would limit the fill factor due to increased recombination at the maximum power point.

The passivation performance of Al_2O_3 films on heavily doped n-type surfaces is limited by their negative charge. Better passivation could be achieved by engineering Al_2O_3 films or Al_2O_3-based dielectric stacks with a smaller negative (or even positive) fixed charge, providing that a low interface defect density could be maintained, although this would come at the expense of the film's performance on p-type and lightly doped n-type surfaces.

However, the negative charge is not the only reason for higher recombination at P-diffused surfaces. Another is that the defect states at the Si–Al_2O_3 interface are more effective recombination centres for minority holes than for minority electrons. Measurements of recombination at Al_2O_3-passivated n-type diffused surfaces reveal the existence of an acceptor-like interface state species that dominates recombination on Al_2O_3-passivated surfaces when electrons are the majority carrier. This state, designated state B, possesses a very large hole/electron capture coefficient ratio on the order of 10^5, on the basis of which it is identified as a double acceptor state. This large ratio, combined with the negative charge of the films, is the reason for the strong injection dependence observed for more lightly doped diffused surfaces. S_{p0} of this second state is significantly larger than S_{n0} of state A, and the two appear to vary independently, indicating that the chemical origin of state B is distinct from that of state A. Indeed, the examined ALD films display a higher $S_{p0,B}$ than the APCVD films, even though $S_{n0,A}$ of the same films is lower or comparable. The density of state B is also significantly less affected by the standard anneal in N_2 than that of state A. This suggests that optimisation of deposition and annealing conditions should be performed separately for Al_2O_3 films intended to passivate $n+$ surfaces.

7.4 Consequences for device design

Knowledge of the surface passivation properties of Al_2O_3 as a function of N_s allows us to predict the recombination rate at Al_2O_3-passivated surfaces with arbitrary surface dopant profiles. This ability can be utilised in order to optimise the performance of devices incorporating such surfaces. Surface diffusions have traditionally been considered a contributor to effective surface passivation, through their ability to suppress the minority carrier concentration at the surface. In fact this is true only when surface passivation is relatively poor. Fig. 7.21 shows modelled J_0 for boron and phosphorus diffusions as a function of N_s, for various values of S_{eff}. We have assumed relatively shallow doping profiles described by a Gaussian function, with a junction depth of 0.5 µm, to represent modern screen-print cells. Also shown is J_0 calculated using the $S_{eff}(N_s)$ model described in this chapter for annealed APCVD films.

When surface recombination is negligible, J_0 increases with N_s due to increasing Auger recombination in the diffusion. In contrast, when S_{eff} is very high, increasing N_s is beneficial for reducing J_0, because the reduction in surface recombination due to the resulting suppression of the surface minority carrier concentration outweighs the increase in Auger recombination. If S_{eff} is finite and independent of N_s, J_0 decreases with increasing N_s until Auger recombination becomes a limiting factor, resulting in an optimum value of N_s which minimises

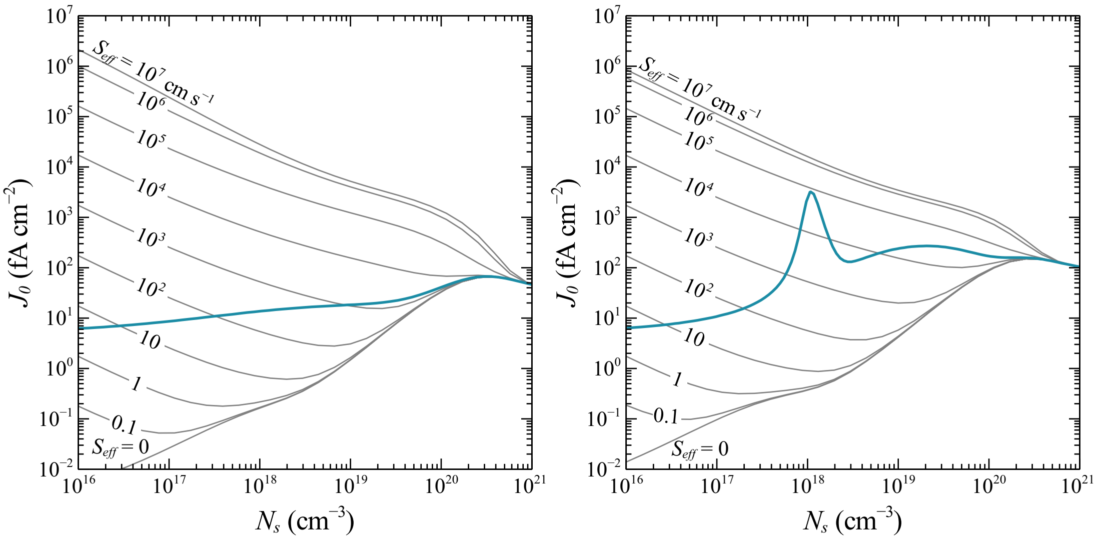

(a) **(b)**

Figure 7.21: Modelled J_0 of a) boron-, and b) phosphorus-diffused Si surfaces as a function of surface dopant concentration N_s, with S_{eff} as a parameter. Profiles are described by a Gaussian function with a junction depth of 0.5 µm (calculated for $N_b = 10^{14}\,\text{cm}^{-3}$). The results are otherwise independent of bulk doping for reasonable values of N_b. Blue lines show the modelled J_0 using S_{eff} calculated from the experimentally-derived Al_2O_3 interface model, assuming $D_{it,midgap} = 5 \times 10^{10}\,\text{eV}^{-1}\,\text{cm}^{-2}$ and $Q_{tot}/q = -1.7 \times 10^{12}\,\text{cm}^{-2}$ as measured for annealed APCVD films, and $S_{p0,B}$ and $S_{n0,B}$ from Table 7.7.

J_0. These trends are well established [100].

However, as shown in this chapter, S_{eff} of the examined Al_2O_3-passivated surfaces is not constant, but generally increases strongly with N_s. As a consequence, the surface component of J_0 is relatively weakly dependent on N_s, and total J_0 is minimised at low N_s. Note that the effect of increasing the profile depth is to increase the minimum and decrease the maximum of the J_0 envelope, while increasing J_0 at the limit of high N_s. A deeper profile therefore accentuates the dependence of J_0 on N_s for Al_2O_3-passivated surfaces.

A diffused surface is therefore not only unnecessary, but actually harmful from the point of view of minimising total recombination, when the surface is passivated with an effective passivation layer such as the examined Al_2O_3 films. The omission of a diffused region, where such a region is not required in order to provide the charge separation necessary to device operation, may therefore have beneficial effects on device performance, while reducing processing complexity.

On the other hand there may be other reasons to include a diffused surface region beneath a passivating layer, such as the need to minimise resistive losses by increasing lateral conductivity and lowering contact resistance, or the need to provide a gettering step for metallic impurities in the bulk. Such considerations must be weighed against the increased recombination losses that result as surface doping is increased.

7.5 Conclusions

In this chapter we have examined Al_2O_3 surface passivation of both boron- and phosphorus-doped Si surfaces as a function of the surface dopant concentration N_s over a broad range. The observed dependence of the surface recombination rates on N_s is well-described by a theoretical model incorporating two dominant defect states, one donor- and one acceptor-like. The former dominates recombination at p-type and undiffused n-type surfaces, while the latter dominates recombination at diffused n-type surfaces. Results for both types of surface suggest that the densities of these states, and of the Al_2O_3 fixed charge Q_f, are independent of N_s. In the case of the donor-like state, excellent agreement is found with the properties of the near-midgap state identified by C–V and conductance measurements in Chapter 4. As a consequence, it is shown that the surface recombination rate at p-type and undiffused n-type surfaces with any N_s can be accurately predicted from Q_{tot} and S_{n0} determined on a single sample, and that C–V measurements can be used for this determination.

Excellent passivation of undiffused n-type surfaces is obtained for a wide range of resistivities and injection levels. The reduction of lifetime in low injection often observed for undiffused n-type surfaces passivated by Al_2O_3 is explained in terms of lateral carrier transport effects, and a simple analytical model is proposed to describe these. It is shown that the greater difficulty of passivating phosphorus-diffused surfaces with Al_2O_3 is due not only to the film's negative charge, but also to the fact that the Si–Al_2O_3 interface states are, on average, more effective recombination centres for holes than for electrons. The injection dependence of J_0 for more lightly doped diffused surfaces is shown to be due to the large asymmetry of capture cross-sections for the dominant acceptor-like defect. The inclusion of surface potential fluctuations is found to be necessary to describe the injection-dependent lifetime for diffused n-type surfaces, but not for p-type or undiffused n-type surfaces.

Finally, on the basis of numerical modelling incorporating the experimentally determined $S_{eff}(N_s)$ dependences, it is shown that total recombination at Al_2O_3-passivated surfaces of both types is minimised by the omission of any diffused region, contrary to the conventional view that diffusions contribute to surface passivation. This allows a simplification of device design where diffused regions are not required for other roles.

Chapter 8

Effect of Surface Orientation and Morphology

> *Look beneath the surface; let not the several quality of a thing nor its worth escape thee.*
>
> — Marcus Aurelius
> MEDITATIONS

Besides the dopant concentration, the major surface properties which may influence passivation quality are crystalline orientation and morphology. At the surface of a silicon wafer, the periodic diamond cubic lattice structure is interrupted, typically along one of the major crystalline planes, leading to $\langle 100 \rangle$, $\langle 110 \rangle$, or $\langle 111 \rangle$ surface orientations. Most mono-crystalline Si solar cells are fabricated on wafers with $\langle 100 \rangle$ surface orientation. However, the front side of these devices is usually textured, and the resulting pyramid structures have $\langle 111 \rangle$-oriented faces. Multi-crystalline devices feature surfaces with a mixture of random orientations. Both the density of silicon atoms in the surface plane and the related density and angle of unsatisfied ("dangling") silicon bonds is different for each orientation, which can result in differences in the electrical properties of the silicon–dielectric interface. The best-known example of this is the interface between Si and thermal SiO_2, for which significant differences in the density and energetic distribution of interface states and the concentration of insulator fixed charge between different surface orientations are well documented [203]–[206]. These differences have for example been shown to result in a five-fold increase in recombination at $\langle 111 \rangle$ compared to $\langle 100 \rangle$ surfaces passivated by thermal SiO_2 [207].

The morphology of the surface—its microscopic structure—may also influence passivation quality. The most obvious effect of morphology on surface recombination is that it directly determines the recombination-active surface area. For instance, an ideal random pyramid textured surface with ⟨111⟩ facets has a surface area $\sqrt{3} = 1.73$ times that of a planar surface [207]. All else being equal, surface recombination is expected to increase in direct proportion to this increase in area. However, non-planar surface morphologies may also influence passivation quality through other mechanisms such as the presence of mechanical stress at the edges and vertices of surface features [207]. The latter mechanism appears to be responsible for significantly increased recombination observed for textured vs planar surfaces passivated by $\mathrm{SiN_x}$ [207].

In this chapter, we evaluate and discuss the effects of surface orientation (⟨100⟩ vs ⟨111⟩) and morphology (planar vs textured) on surface recombination at $\mathrm{Al_2O_3}$-passivated silicon surfaces. We will show that additional recombination at textured surfaces can be attributed mainly, but not entirely, to increased surface area, and that differences in recombination between ⟨100⟩ and ⟨111⟩ surfaces are due solely to different concentrations of insulator fixed charge, which depend on processing conditions. Most remarkably, we show that the concentration and properties of the Si–$\mathrm{Al_2O_3}$ interface states (energetic distribution and capture cross-sections) are entirely independent of surface orientation.

8.1 Recombination at ⟨100⟩, ⟨111⟩, and textured surfaces

Given its importance for device applications, it is somewhat surprising that relatively little systematic work has been performed to assess the impact of either crystalline orientation or surface morphology on the passivation performance of $\mathrm{Al_2O_3}$. The great majority of reported passivation data are for planar ⟨100⟩ surfaces, and although some scattered results on ⟨111⟩ surfaces have been reported, there has generally been no effort to compare these directly to results on ⟨100⟩ surfaces. An exception is the recent work of [49], which examined the surface passivation of $\mathrm{Al_2O_3}$ from ALD, both thermal and plasma-assisted, on diffused and undiffused planar surfaces of ⟨100⟩ and ⟨111⟩ orientation, finding generally slightly worse passivation properties for ⟨111⟩ surfaces. However, no comparison to textured surfaces was made in that work.

A somewhat novel method was adopted by Sio *et al.* [208], who examined

PL lifetime images of mirror-polished multi-crystalline Si surfaces passivated by Al_2O_3 as well as SiN_x and native oxide. This approach allows a wide range of surface orientations to be compared more or less directly using a single sample. They found differences of up to a factor of 2 between surface recombination rates at differently oriented surfaces passivated by Al_2O_3, with the lowest and highest rates found for orientations near ⟨100⟩ and ⟨111⟩ respectively. However, this analysis was based on relatively poorly passivating Al_2O_3 layers from an O_3 ALD process, in order to minimise uncertainty in the extracted surface recombination values due to the low bulk lifetime of multi-crystalline Si. Also, like [49], they did not examine textured surfaces.

Numerous examples of the application of Al_2O_3 to textured surfaces within device structures exist in the literature, but again there are relatively few direct comparisons to planar surfaces. Duttagupta *et al.* [176] measured the passivation quality of PECVD Al_2O_3/SiN_x stacks on boron-diffused textured and planar ⟨100⟩ samples, reporting a textured-to-planar J_0 ratio of 1.5–2. A similar experiment was performed by Richter *et al.* [179] with both Al_2O_3/SiN_x stacks and Al_2O_3 by itself, where the Al_2O_3 was deposited by plasma-assisted ALD. They reported a textured-to-planar J_0 ratio between 1.7 and 2.5. However, neither [176] nor [179] included a comparison to planar ⟨111⟩ surfaces, which leaves the role played by the ⟨111⟩ surface orientation of the textured surface open to speculation.

The only previous study to attempt a systematic investigation of the influence of both orientation and texture on recombination at Al_2O_3-passivated surfaces is that of Baker-Finch [209]. They examined samples with various textured/planar coverage fractions, as well as planar ⟨100⟩ and ⟨111⟩ samples, passivated both by plasma-assisted ALD Al_2O_3, and by PECVD Al_2O_3/SiN_x stacks. Unfortunately, there was significant scatter in the data, which severely limited the confidence of the results. Nevertheless, recombination at ⟨111⟩ surfaces was clearly significantly higher than at ⟨100⟩, while little or no additional recombination was associated with surface features.

In this section, we report measurements of surface recombination at Al_2O_3-passivated, boron-diffused and undiffused surfaces, both planar ⟨100⟩, planar ⟨111⟩, and with a random pyramid texture. This allows us to separate and quantify the various contributions to the different recombination rates observed at planar and textured surfaces. The influence of crystal orientation and surface area may thereby be distinguished from any additional effects. Unlike [209] we are able to obtain clear results in this respect. This work was previously published in [210].

Table 8.1: Substrate properties and J_0 for undiffused planar and textured n-type surfaces passivated by APCVD Al_2O_3, before and after annealing.

Substrate	Resistivity ($\Omega\,$cm)	Thickness (µm)	J_0 As-deposited (fA cm^{-2})	J_0 Annealed (fA cm^{-2})
⟨100⟩	1.5	235	11.4	7.9
⟨111⟩	15	223	16.6	10.9
Textured	2.3	234	31.1	18.4

Experimental details

Boron-diffused symmetrical lifetime structures were prepared on high resistivity ($> 100\,\Omega\,$cm) n-type ⟨100⟩ and ⟨111⟩ FZ silicon wafers, approximately 450 and 325 µm thick respectively. The latter were supplied with a chemical polish by the manufacturer, and were used without additional etching, while the former received either a planar etch in HF:HNO_3 or TMAH solution, or a random pyramid texture in TMAH. All samples received an initial boron diffusion of ~110–120 $\Omega\,\square^{-1}$, with some receiving additional drive-in anneals of 1, 3, or 6 h at 1100 °C in N_2 in order to vary the surface dopant concentration and diffusion profile. Additional undiffused samples were prepared on various n-type substrates (details in Table 8.1) in the same way. All samples were given an RCA clean and HF dip prior to Al_2O_3 deposition.

Results and discussion

Fig. 8.1 shows J_0 values measured on diffused surfaces passivated by as-deposited and annealed Al_2O_3 films. Measurements of the as-deposited films were performed both immediately after deposition and immediately before annealing, approximately 18 hours later. It was found that the surface passivation of all samples, particularly the textured samples, improved significantly over this period under ambient conditions. A similar effect was observed for the annealed samples when remeasured 24 days after annealing. No significant difference in J_0 between planar ⟨100⟩ surfaces prepared by HF:HNO_3 and TMAH etches was observed.

The ratio of J_0 for planar ⟨111⟩ surfaces relative to planar ⟨100⟩ (Fig. 8.2a) was generally in the range of 1.3–1.5 for the as-deposited films on both diffused and undiffused surfaces, decreasing to 1–1.2 after annealing for the diffused surfaces. This suggests either a higher interface defect density or lower fixed charge for the

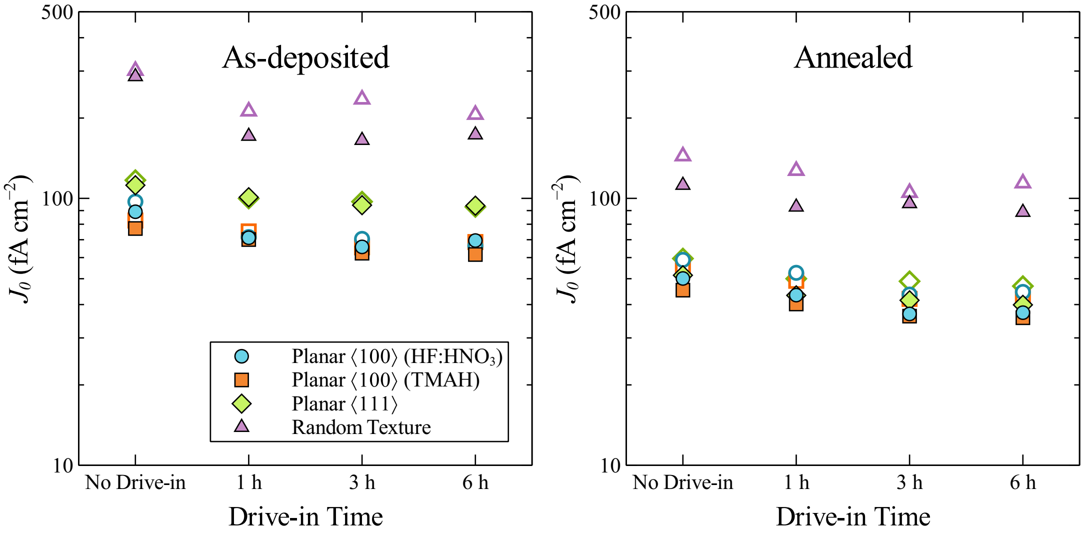

(a) **(b)**

Figure 8.1: J_0 of boron-diffused planar ⟨100⟩, planar ⟨111⟩, and random textured samples with a) as-deposited, and b) annealed Al_2O_3 layers. Values are shown in a) as measured immediately after deposition (open symbols), immediately before annealing (∼18 h later, closed symbols), and in b) immediately after annealing (open symbols), and 24 days after annealing (closed symbols).

⟨111⟩ interface compared to ⟨100⟩, as well as a relative improvement in one or both properties following annealing. The ratio for undiffused surfaces was similar to that of diffused surfaces for the as-deposited films, but did not change significantly after annealing. The reason for this difference is not clear, though we note that the data for undiffused surfaces is based on only a few samples, so not too much weight should be placed on it. We note that while Auger recombination in the diffused region also contributes to J_0, and should be approximately independent of surface orientation, its contribution is small relative to surface recombination for such lightly diffused surfaces.

The ratio of J_0 for textured surfaces relative to planar ⟨111⟩ (Fig. 8.2b) was found to lie between 2.2 and 2.6 for most of the diffused samples. Since this value is higher than the geometric surface area ratio of 1.73 (or possibly 1.66 [211]), this implies the existence of an additional recombination enhancement factor due to the surface structure. A notable exception is the data for the unannealed films measured ∼18 h after deposition, where the J_0 ratio is very close to the geometric ratio. One tentative hypothesis might be that these unannealed films contain significantly more hydrogen, which could perhaps allow for a greater degree of

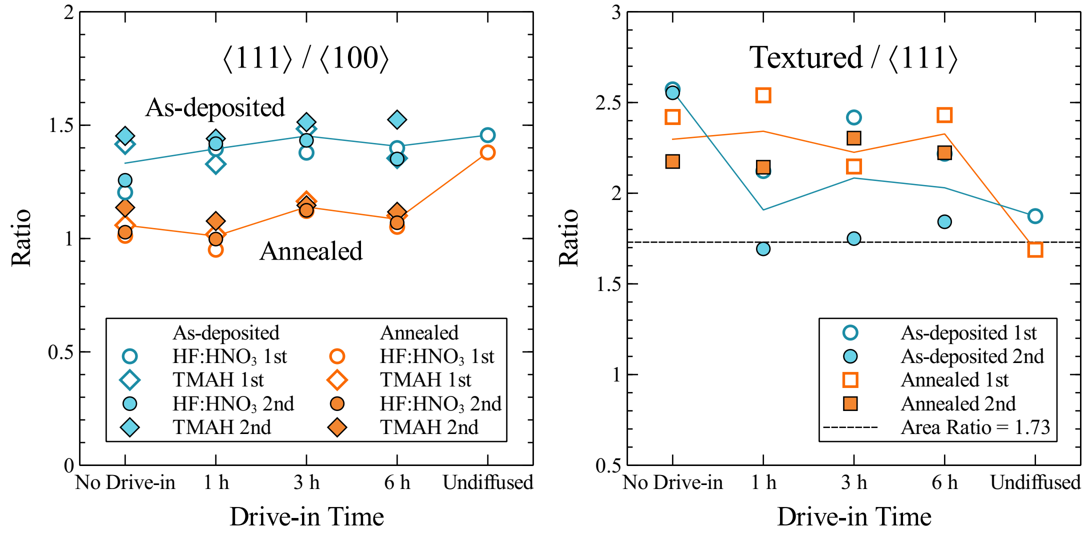

(a) (b)

Figure 8.2: Ratio of J_0 for a) planar $\langle 111 \rangle$ to planar $\langle 100 \rangle$ surfaces, and b) textured to planar $\langle 111 \rangle$ surfaces. Data is shown for both boron-diffused surfaces and undiffused n-type surfaces. Values are shown as measured immediately after deposition (1st), immediately before annealing ($\sim$18 h later) (2nd), immediately after annealing (1st), and 24 days after annealing (2nd). Lines indicate mean values.

lattice relaxation in the vicinity of abrupt surface features, and hence less strain and consequent creation of unsatisfied ("dangling") bonds. In contrast, J_0 ratios for the undiffused surfaces were found to be quite close to the geometric ratio, so that for these samples the increase in J_0 for textured surfaces over planar $\langle 111 \rangle$ can be explained solely by the difference in surface area.

The results presented in Fig. 8.2 are in broad agreement with the previous work of [176] and [179]. Their ranges of 1.5 to 2.0 and 1.7 to 2.5 for the ratio of J_0 at textured and planar $\langle 100 \rangle$ surfaces may be compared with the range of 2.0 to 3.3 measured here. The relatively limited influence of orientation and surface structure on recombination at Al_2O_3-passivated Si surfaces is in marked contrast to the case for SiO_2 and SiN_x. This points to fundamental differences in the structure of the Si–Al_2O_3 interface with respect to those of these other dielectrics. In the following section we shall examine the influence of surface orientation on the detailed electrical properties of this interface.

Table 8.2: Properties of the ⟨100⟩ and ⟨111⟩ substrates used for C–V and conductance measurements. All substrates were single-side polished.

Orientation	Type	Resistivity (Ω cm)	Material
⟨100⟩	p	2.8	FZ
⟨100⟩	n	1.3	FZ
⟨111⟩	p	0.36	Cz
⟨111⟩	n	5.5	Cz

8.2 Electrical properties of the ⟨100⟩ and ⟨111⟩ interfaces

In order to determine the fundamental reasons for differences in recombination at ⟨100⟩ and ⟨111⟩ silicon surfaces passivated by Al_2O_3, we must investigate the fundamental electrical properties of the two interfaces directly. The influence of surface orientation on Si–Al_2O_3 interface properties was previously investigated by [49] for Al_2O_3 deposited by ALD. They reported a consistently larger charge at ⟨100⟩ surfaces compared to ⟨111⟩, but found the interface defect distribution to be relatively independent of orientation. This is consistent with the early report of Duffy and Revesz [20] that the Si–Al_2O_3 interface state density was independent of orientation for ⟨100⟩ and ⟨111⟩ surfaces, in contrast to the case of thermal SiO_2, although no data on the energetic distribution of states was presented by these authors. In this section we will show that Q_{tot} may in fact be higher or lower for ⟨111⟩ surfaces depending on the deposition conditions and post-deposition annealing, while not only the distribution of interface states but also their capture cross-sections are independent of surface orientation.

Experimental details

Si–Al_2O_3–Al MIS structures were prepared in parallel on mirror-polished ⟨100⟩ and ⟨111⟩ FZ Si wafers, both p- and n-type. The relevant substrate properties are given in Table 8.2. Al_2O_3 deposition by APCVD was performed simultaneously for all samples, at either 440 or 410 °C. Some samples received a standard anneal immediately after deposition and prior to metallisation. An effort was made to minimise time between the characterisation of different samples to avoid possible drift of interface properties.

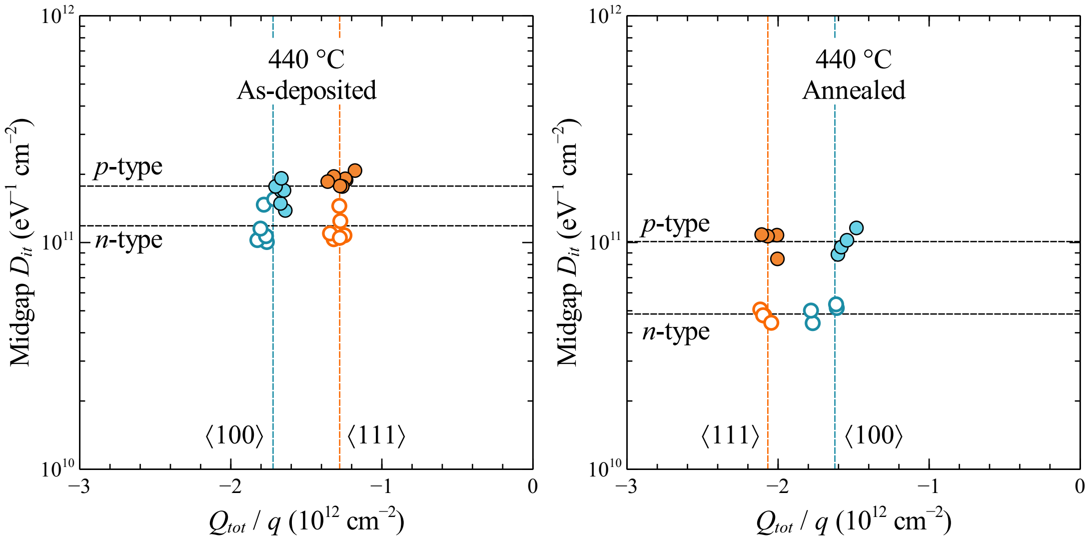

(a) **(b)**

Figure 8.3: D_{it} vs Q_{tot} for p- and n-type ⟨100⟩ and ⟨111⟩ Si surfaces passivated by Al_2O_3 deposited by APCVD at 440 °C, both a) as-deposited, and b) annealed.

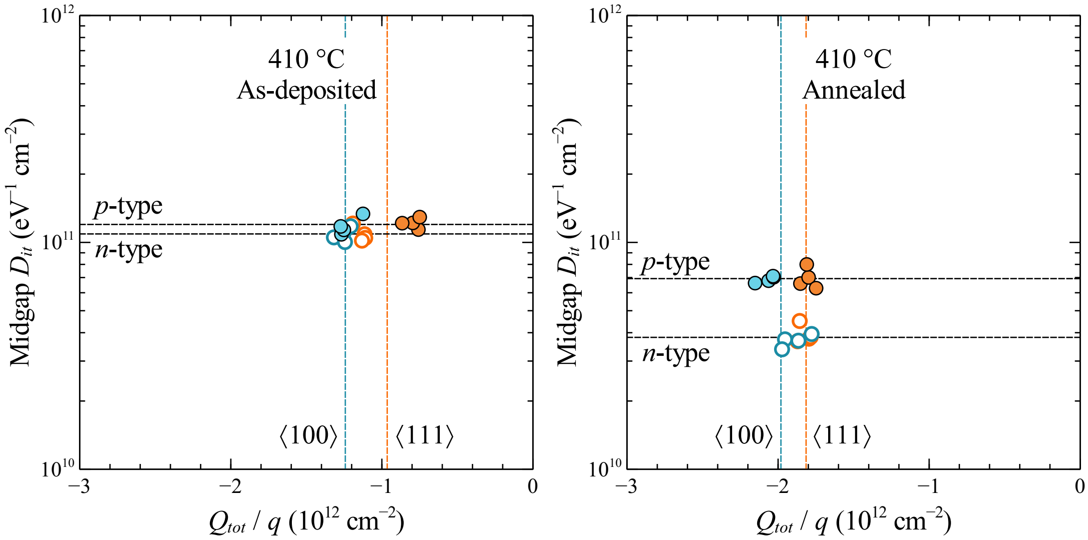

(a) **(b)**

Figure 8.4: D_{it} vs Q_{tot} for p- and n-type ⟨100⟩ and ⟨111⟩ Si surfaces passivated by Al_2O_3 deposited by APCVD at 410 °C, both a) as-deposited, and b) annealed.

Midgap D_{it} and charge

C–V measurements reveal a remarkably consistent picture of the differences and similarities between ⟨100⟩ and ⟨111⟩ Si–Al_2O_3 interface properties. Figs. 8.3 and

8.4 show midgap D_{it} vs Q_{tot} for ⟨100⟩ and ⟨111⟩ samples with $\mathrm{Al_2O_3}$ deposited at two different temperatures, both before and after annealing. It is readily observed that each of these interface properties is generally aligned upon one of two axes depending either on dopant type or orientation. Q_{tot} is independent of doping type but depends on orientation, while D_{it} is independent of orientation, but appears to depend on dopant type. The former dependence is unsurprising, but the latter is unexpected and remarkable.

In calculating Q_{tot}, we have used the value of the Si work function recommended by [212], which differs for ⟨100⟩ and ⟨111⟩ surfaces. This raises the possibility that the values of Q_{tot} determined are subject to different systematic errors. We can nevertheless be certain that Q_{tot} is not identical for ⟨100⟩ and ⟨111⟩ surfaces because of the large increase in $|Q_{tot}|$ observed for ⟨111⟩ but not ⟨100⟩ surfaces after annealing in Fig. 8.3. Prior to annealing, negative Q_{tot}/q is significantly larger for the ⟨100⟩ than for the ⟨111⟩ surface ($-1.7 \times 10^{12}\,\mathrm{cm}^{-2}$ vs $-1.3 \times 10^{12}\,\mathrm{cm}^{-2}$). However, after annealing the order is reversed, with Q_{tot}/q increasing to $-2.1 \times 10^{12}\,\mathrm{cm}^{-2}$ for the ⟨111⟩ surface and decreasing slightly to $-1.6 \times 10^{12}\,\mathrm{cm}^{-2}$ for the ⟨100⟩ surface.

This lower initial charge and its increase following annealing presumably account for the larger value of J_0 observed for ⟨111⟩ surfaces prior to annealing, and the substantial elimination of this difference subsequently, as shown in Fig. 8.2a. The fact that the ⟨111⟩ samples in Fig. 8.2a do not display a J_0 significantly lower than the ⟨100⟩ samples after annealing, as would be expected from their larger Q_{tot}, may be due to variation of the deposition conditions between the two experiments. The significant difference in D_{it} and Q_{tot} for films deposited at a slightly lower temperature (Fig. 8.4) suggests that a small difference in substrate temperature could have a significant effect on the relative recombination rates at ⟨111⟩ and ⟨100⟩ surfaces.

Energy dependence of D_{it}

Examination of the energy dependence of D_{it}, shown in Fig. 8.5, reveals that similarities between ⟨100⟩ and ⟨111⟩ surfaces extend well beyond mere coincidental agreement at midgap. In fact, within the limits of sample-to-sample variability and experimental error, the D_{it} distributions may be stated to be identical. Instead, apparent differences in D_{it} occur between p- and n-type substrates, independent of orientation. These, however, may rather be due to the different voltage sweep directions used in the quasi-static capacitance measurement for p-

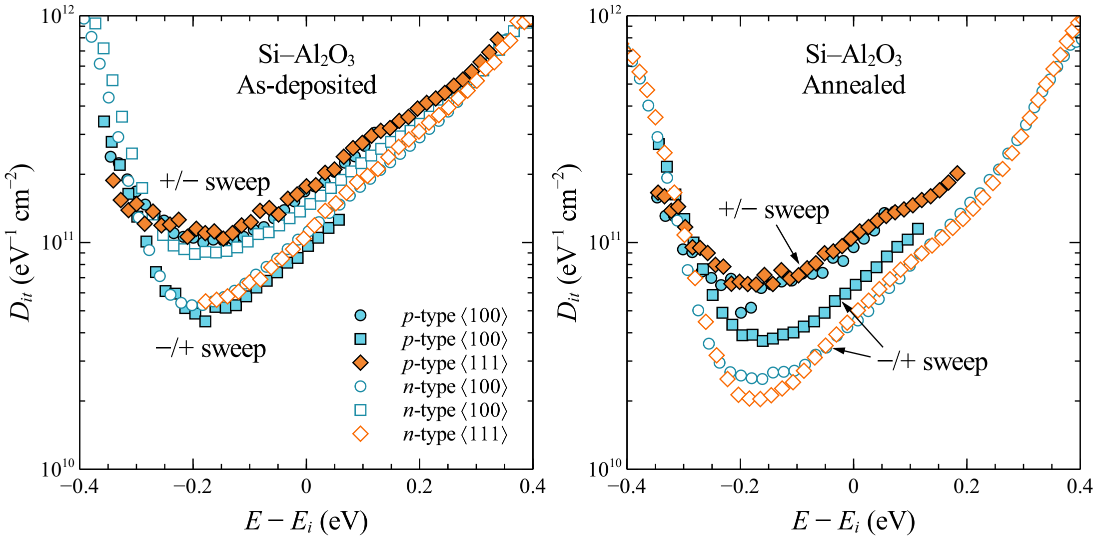

(a) **(b)**

Figure 8.5: D_{it} vs energy for ⟨100⟩ and ⟨111⟩ Si surfaces passivated by Al_2O_3 from APCVD, both a) as-deposited, and b) annealed. Data are shown for both p- and n-type substrates, and for both +/− and −/+ voltage sweeps.

and n-type samples, and not to the substrate type itself. Fig. 8.5 shows that the use of identical voltage sweep directions generally results in much better agreement between D_{it} for p- and n-type samples.

The reason for the apparent dependence of D_{it} on sweep direction is not obvious, though various experiments make clear that it is not simply an artifact of the measurement system. Nor is it entirely clear which of the resulting apparent interface state distributions is to be trusted. The question is not resolved by independent measurements of D_{it} via the conductance method, because D_{it} determined by this method is consistently lower then that determined by sweeps in either direction. One possibility is that the difference between the two distributions is due to the contribution of slow states that are able to maintain equilibrium with the +/− sweep, but not with the −/+ sweep. This would imply a very low capture rate for electrons, but a somewhat larger one (though possibly still small) for holes. Such states would be expected to make a negligible contribution to recombination.

Capture cross-sections

Even if the energetic distribution of interface states is independent of surface orientation, it does not necessarily follow that their capture cross-sections are also

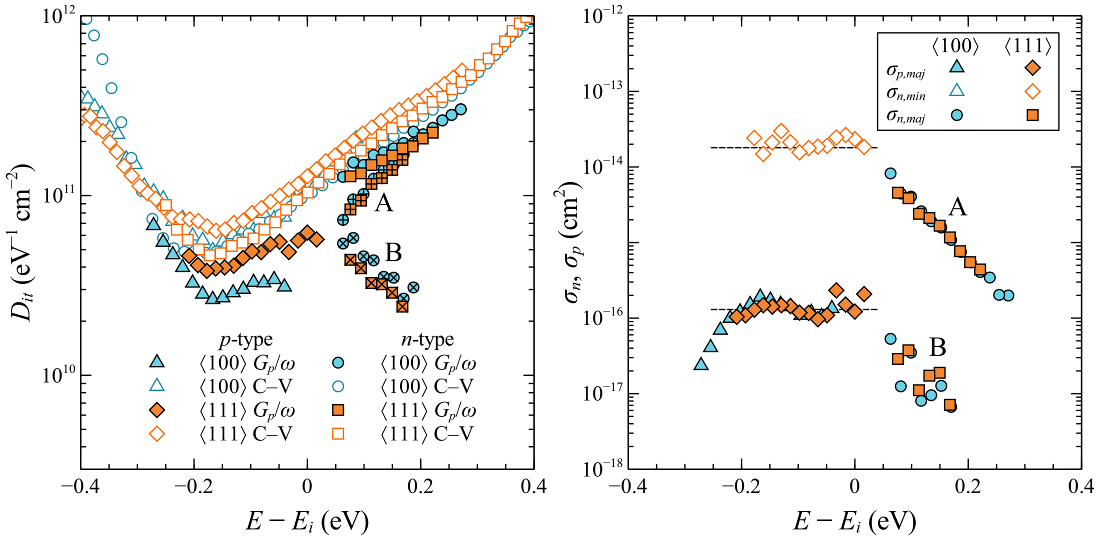

(a) **(b)**

Figure 8.6: Apparent a) D_{it}, and b) σ_p and σ_n, determined by the conductance method for ⟨100⟩ and ⟨111⟩ Si surfaces (p- and n-type) passivated by APCVD Al_2O_3. For n-type surfaces the conductance signal could be resolved into two separate contributions, labelled A and B. D_{it} determined by C–V measurements is also shown. Dashed lines show the values of σ_p and σ_n extracted for the dominant defect in the lower half of the bandgap as described in Section 4.2.

independent. In order to establish whether any such dependence exists, apparent capture cross-sections were determined for both ⟨100⟩ and ⟨111⟩ samples by the conductance method, in the same way as described in Chapter 4. Fig. 8.6 shows the resulting apparent capture cross-sections values and associated defect distributions. It is clear that there is outstanding agreement both between the values determined for the different orientations, and between these and the data presented in Chapter 4. In most cases it was not possible to determine minority carrier capture cross-sections with any confidence, because the low interface state density results in much greater noise in the conductance data at low frequencies. However, the values of σ_n determined for the p-type ⟨111⟩ sample are in good agreement with those determined in Chapter 4 for a ⟨100⟩ substrate. For the n-type samples a secondary conductance peak may be distinguished at low frequencies, consistent with the results of Chapter 4. This is attributed to a species of interface state with very low σ_n, and its resulting apparent properties are included in Fig. 8.6. Again, no significant difference between the data for ⟨100⟩ and ⟨111⟩ surfaces is observed.

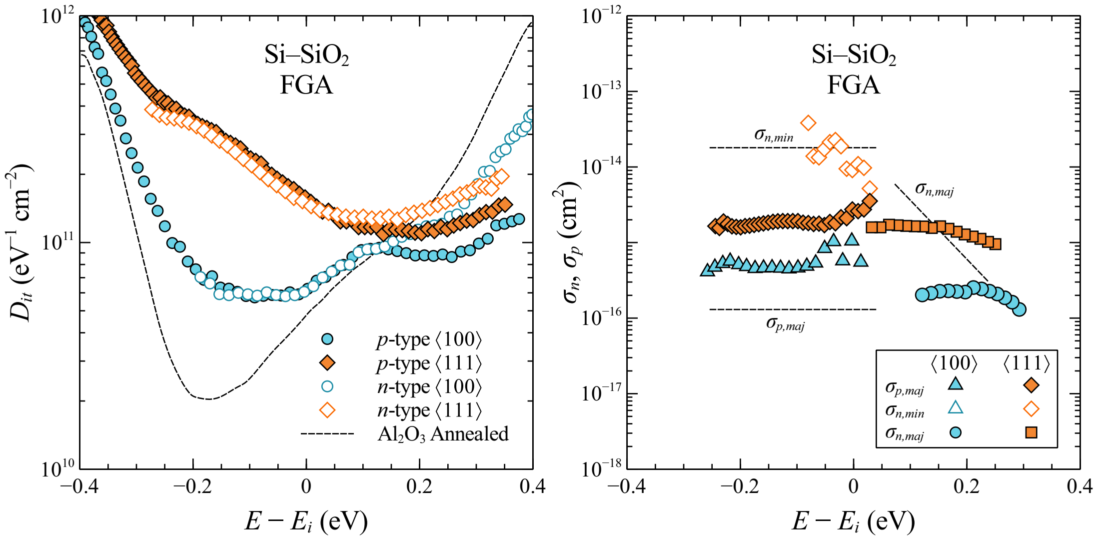

(a) **(b)**

Figure 8.7: a) D_{it} and b) σ_p and σ_n vs energy, for ⟨100⟩ and ⟨111⟩ Si surfaces passivated by thermally grown SiO_2 after annealing in forming gas. Data are shown for both p- and n-type substrates. The values of D_{it}, σ_p and σ_n measured for the Si–Al_2O_3 interface (independent of orientation) are indicated by dashed lines for ease of comparison.

Comparison to SiO_2

The remarkable orientation-independence of D_{it} for Al_2O_3-passivated silicon surfaces, shown in Fig. 8.5, may be contrasted with the case of thermal SiO_2, where D_{it} is well known to be strongly dependent on substrate orientation [203]–[206]. Fig. 8.7a shows D_{it} vs energy for the same ⟨100⟩ and ⟨111⟩ substrates described in Table 8.2, passivated by thermal SiO_2. The SiO_2 layer was grown at 1000 °C in dry O_2 to a thickness of 20 nm on the ⟨100⟩ surfaces (closer to 27 nm for the ⟨111⟩ surfaces due to the higher growth rate for this orientation). A standard anneal in forming gas (5 % H_2, 95 % Ar) at 400 °C for 30 min was subsequently performed to reduce the interface state density prior to metallisation. The major point to be noted in Fig. 8.7a is the significant difference between the shape of the Si–SiO_2 interface state distributions for the different orientations. Most obviously, the ⟨111⟩ surface exhibits a prominent shoulder feature or hump in the lower part of the bandgap, consistent with that noted by other authors [151], [213], that is absent in the ⟨100⟩ distribution, which instead possesses a minimum in this region (the ⟨100⟩ distribution may be compared with those reported by [214]).

The second point that should be taken from Fig. 8.7a is the significant difference between the shape of the D_{it} distributions observed for silicon surfaces passivated by Al_2O_3 and SiO_2, regardless of surface orientation. The ⟨100⟩ distribution for SiO_2, with its minimum in the lower part of the bandgap, is most similar to that of Al_2O_3, but even in this case the difference from the orientation-independent distribution characteristic of Al_2O_3 is sufficiently marked that the two distributions must be considered distinct.

This impression is further reinforced by a comparison of the apparent capture cross-sections measured for the Si–SiO_2 and Si–Al_2O_3 interfaces. Fig. 8.7b shows apparent σ_p and σ_n for the ⟨100⟩ and ⟨111⟩ Si substrates passivated by thermal SiO_2. It is clear that both σ_p and σ_n are significantly different for the ⟨100⟩ and ⟨111⟩ surfaces, and that the values measured for neither orientation match those determined for the Si–Al_2O_3 interface. We note that the values measured for σ_n on the ⟨111⟩ surface are in good agreement with those of Deuling *et al.* [215].

The assumption that the Si–Al_2O_3 interface is essentially the same as that of thermal Si–SiO_2, which is sometimes made on the basis of the observed SiO_x interlayer (see Section 1.2), is thus an unwarranted oversimplification: the two interfaces must be considered electrically distinct. This is not to dismiss the evidence for the existence of some sort of SiO_x interlayer, which appears fairly convincing (indeed, we shall present evidence for its presence in our own samples in Section 9.1.3), only to say that the electrical properties of the interface are clearly not solely determined by the presence such an interlayer, but also by the overlying Al_2O_3 film. It should be remembered that the electrical interface need not coincide with an atomically sharp physical interface, but may extend some atomic lengths into the dielectric. The Si–SiO_x–Al_2O_3 structure, if such it is, ought therefore to be considered as an interfacial system in its own right, and not merely as a Si–SiO_2 or Si–SiO_x interface with an incidental capping layer of Al_2O_3.

Summary

Investigations of the electrical properties of the ⟨100⟩ and ⟨111⟩ Si–Al_2O_3 interface reveal that the silicon surface orientation significantly influences the density of fixed charge Q_f. Q_f for ⟨111⟩ surfaces may be either higher or lower than for ⟨100⟩ surfaces depending on the Al_2O_3 deposition parameters and subsequent thermal processing. On the other hand the Si–Al_2O_3 interface state properties (energetic distribution and capture cross-sections) are shown to be entirely independent of orientation. This is in marked contrast to the situation at other known silicon–dielectric interfaces, particularly the case of thermal SiO_2. The level of agreement is such that the ⟨100⟩ and ⟨111⟩ Si–Al_2O_3 interfaces must be considered electrically indistinguishable.

8.3 Conclusions

The influence of surface orientation and morphology on interface properties and recombination at the Si–Al_2O_3 interface is shown to be relatively limited compared to the situation for other common materials such as SiO_2 and SiN_x. Additional recombination at textured surfaces, beyond that expected from the increase in surface area, amounts to a factor of less than 1.5, while recombination at ⟨111⟩ surfaces is only slightly higher than that at ⟨100⟩ surfaces for annealed APCVD films. This robust passivation performance on various surfaces is in keeping with the minimal doping-dependence of interface properties demonstrated in Chapter 7, and is yet another remarkable property of Al_2O_3 that makes it especially suited to passivating the varied surfaces found in actual devices. Differences in recombination at ⟨100⟩ and ⟨111⟩ surfaces passivated by Al_2O_3 can be entirely attributed to differences in insulator fixed charge, which depend on processing details, since interface state properties are independent of orientation. This latter unexpected result points to a distinctive Si–Al_2O_3 interface structure which must be treated separately from those formed by other well-known dielectrics such as SiO_2 and SiN_x.

Chapter 9

Relationship Between Al_2O_3 Bulk and Interface Properties

> *If you want to understand function, study structure.*
>
> — Francis Crick
>
> WHAT MAD PURSUIT: A PERSONAL VIEW OF SCIENTIFIC DISCOVERY

Surface passivation is directly related to the chemical structure and composition of the silicon–insulator interface. However, the chemical properties of the interface, as an essentially two-dimensional feature, are not easily measured, still less those of the various electronic states, which occupy only a small fraction of interfacial sites. On the other hand, the bulk properties of the Al_2O_3 film are readily accessible, and it seems reasonable to suppose that these may be closely correlated with the interface properties. Thus, the bulk properties of the Al_2O_3 films are of significant interest not only in themselves, but because of the light they may shed on interface properties. In this chapter, information derived from infrared absorption (FTIR), dielectric, and optical measurements of the bulk films are discussed, and where possible related to the composition and structure of the films and to the electrical properties of the interface. In each case the bulk properties are characterised as a function of deposition temperature, with the measurements generally corresponding directly to the measurements of the temperature-dependent interface properties described in Section 5.1.

9.1 Structure and composition

The properties of any thin film are closely related to its chemical structure and composition. Changes in the bulk structure and composition of Al_2O_3 are likely to be reflected in related changes at the Si–Al_2O_3 interface. Therefore, by correlating structural and compositional changes in the films with changes in the electrical properties of the interface, we can expect to gain a deeper understanding of the physical origin of the various electronic states that determine the passivation quality. In this section we discuss structural and compositional information derived from Fourier transform infrared spectroscopy (FTIR) measurements and its relation to interface properties.

9.1.1 Infrared absorption measurements

FTIR measurements can provide a wealth of information on the compositional and structural properties of thin films. FTIR spectra plot the infrared absorbance of the film as a function of photon energy (conventionally expressed as a wavenumber with units of cm^{-1}). Absorption occurs at frequencies corresponding to the vibrational modes of the various chemical groups present, resulting in absorption peaks at characteristic energies that can be related to the composition and bonding configuration within the film.

A number of authors have reported FTIR measurements of passivating Al_2O_3 films on silicon [38], [41], [55], [69], [216]–[220]. Most analysis has focussed on possible correlations between absorption by Si–O bonds and the extent of chemical passivation, which however remain inconclusive. In a very recent paper, Kühnhold *et al.* [220] went significantly further by presenting evidence of a correlation between Al coordination number and the concentration of insulator fixed charge Q_f for PECVD Al_2O_3. Our own data for APCVD Al_2O_3, presented in this section, will be shown to provide significant support for this hypothesis.

FTIR measurements were performed using a Bruker VERTEX 80v vacuum FTIR spectrometer over the range of 400 to $4000\,\mathrm{cm}^{-1}$ with a $2\,\mathrm{cm}^{-1}$ resolution. Each measurement was taken from the average of 128 scans. Films to be examined were deposited on one side of a double-side-polished $\langle 100 \rangle$ FZ silicon wafer, cleaned in the normal way. A bare portion of the same wafer was used as a background reference in order to distinguish those parts of the absorption due to the Al_2O_3 film from those due to the substrate. Baseline correction of the resulting absorbance spectra was performed using spline interpolation between

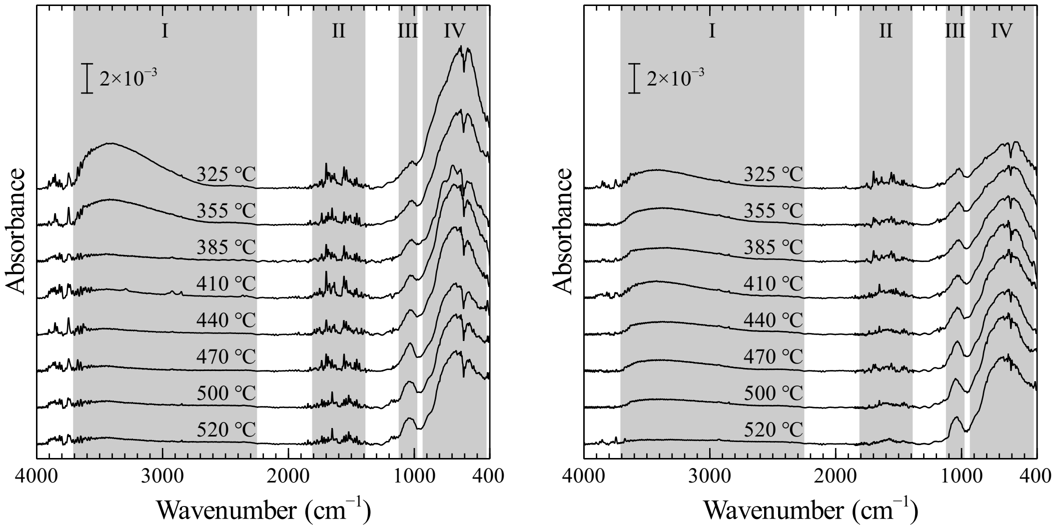

(a) H_2O **(b)** O_2

Figure 9.1: FTIR absorption spectra for Al_2O_3 films deposited from TEDA-TSB and either a) H_2O or b) O_2 with deposition temperature as a parameter. Shaded regions indicate the principle absorption bands.

known zero-absorption points.

FTIR spectra for Al_2O_3 films deposited at various temperatures from TEDA-TSB and either H_2O or O_2 are shown in Fig.9.1. These films were co-deposited with the lifetime and C–V samples described in Section 5.1. In the following sections the detailed assignment of the various absorption features will be discussed, followed by an analysis of the trends in the data and possible correlations with interface passivation properties.

9.1.2 Band assignments

In examining the FTIR spectra of Al_2O_3 (Fig. 9.1), several prominent features are readily discernible (summarised in Table 9.1). Firstly there is a broad and strong peak centred around 700 cm^{-1}. This peak is associated with various Al–O bonds and is the characteristic signature of Al_2O_3 [221], [230]–[234]. The small but distinct peak observed at 1020–1040 cm^{-1} is generally associated with Si–O–Si bonds, pointing to the presence of a thin interfacial SiO_x layer. Between 1350 and 1800 cm^{-1} a cluster of sharp peaks associated with various carbon-oxygen bonds appears. These, and some scattered carbon-related peaks present at higher wavenumbers, can be attributed to un-reacted ligands from the organometallic

Table 9.1: Main absorption bands in the FTIR spectra of Al_2O_3. Band region numbers refer to Fig. 9.1

Band Region	Range (cm^{-1})	Assignment	References
I	2250–3800	O–H	[221], [222]
	2360, 2850, 2920, 3290	C–H (C_2H_5, C_4H_9)	[223], [224]
II	1350–1800	C=O, O–C–O	[225]–[227]
III	1000–1100	Si–O–Si	[228], [229]
IV	400–950	Al–O, O–Al–O	[221], [230]–[234]

precursor. Finally there is a broad feature between 2250 and 3800 cm^{-1}, and peaking at 3420 cm^{-1}, associated with hydroxyl (O–H) groups in the bulk of the film.

Al–O Bonds

Broadly speaking, the Al–O absorption band around 700 cm^{-1} may be divided into two regions due to the contributions of Al atoms in different bonding configurations. The higher wavenumber component is due to vibrations within fourfold-coordinated AlO_4 tetrahedra, in which each Al atom has four oxygen atoms as its nearest neighbours, while absorption at lower wavenumbers is due to sixfold-coordinated AlO_6 octahedra. The higher frequency of absorption by AlO_4 is due to shorter Al–O bond lengths, which result in a higher vibrational frequency [230]. Al is present in both configurations in amorphous Al_2O_3.

A detailed assignment of the vibrational modes contributing to the main Al–O absorption band is complicated by the fact that close coupling between bands at similar frequencies leads to a smearing out and broadening of the individual peaks [230]. The absorption spectrum of the H_2O sample deposited at 385 °C shows the most well-developed structure of any of the spectra in the region between 400 and 950 °C (Fig. 9.2). A number of peak features may be clearly distinguished, and these are summarised in Table 9.2, together with data on identifiable features for spectra at higher and lower temperatures, and with literature data. Good agreement is obtained with literature data for various hydrated alumina, boehmite (AlO(OH)), and mullite ($3Al_2O_3{\cdot}SiO_2$) compounds [221], [231]–[234]. While there is some disagreement within the literature as to the detailed assignments of these peaks, the identification of those above 700 cm^{-1} as due to tetrahedral AlO_4, and those below 650 cm^{-1} as due to octahedral AlO_6, is relatively uncontroversial.

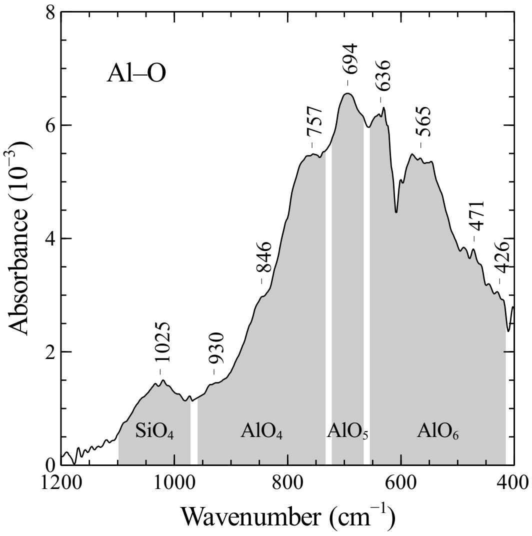

Figure 9.2: Location of peak features in the main Al–O absorption band of Al_2O_3 deposited from TEDA-TSB and H_2O at 385 °C.

On the other hand, the absorption peak around 690 cm^{-1}, which appears prominently in Fig. 9.2, is not apparent in the data of [221], [231]–[234]. It appears distinctly as a peak for several of the films deposited at 385 °C or above, while in other cases only a broad absorption band appears in this region and it is not possible to distinguish individual features. One possibility is that the peak at 690 cm^{-1} relates to stretching modes in five-fold-coordinated AlO_5 polyhedra. A significant absorption peak near 690 cm^{-1} has been observed by several authors for the aluminosilicate andalusite (Al_2SiO_4) [235]–[237], in which Al is distributed equally between five- and six-fold coordinated sites (AlO_5 and AlO_6) [238]. This peak is not observed for the compositionally identical orthosilicates sillimanite and kyanite, which do not feature AlO_5 coordination [238]. An absorption peak appearing around 670 cm^{-1} in SiO_2-Al_2O_3 glasses prepared by fast-quenching was also identified as AlO_5 by [239] by comparison with nuclear magnetic resonance (NMR) measurements. Molecular dynamics simulations suggest that a significant fraction of Al in amorphous Al_2O_3 is found in AlO_5 sites [240]–[246]. The assignment of an AlO_5 Al–O stretching mode at 694 cm^{-1}, intermediate between those of AlO_4 and AlO_6, would be consistent with the relative Al–O bond lengths within each polyhedra, which determine the vibrational frequency [230], [243].

Table 9.2: Positions and assignment of individual absorption features in the 400–1200 cm^{-1} range for Al_2O_3 deposited at 325 385, and 500 °C from TEDA-TSB and H_2O (385 °C spectrum shown in Fig. 9.2). Peak positions reported in the literature for various aluminate compounds are shown for comparison. Assignments are based on those of [221], [231]–[234].

This Work			Literature				Assignment
325 °C	385 °C	500 °C	(a)	(b)	(c)	(d)	
1017	1025	1038	–	–	–	988	Si–O–Si stretch (SiO_4)
–	930*	917*	–	925	–	909	Al–O stretch (AlO_4)
–	846*	–	886*	845	880	828	
742*	757	750*	762	770	761	737	O–Al–O bend (AlO_4)
674*	694	687	–	–	–	–	Al–O stretch (AlO_5)
639	636	644	637	630	616	620	Al–O stretch (AlO_6)
573	565	577	570	570	–	578	
–	471*	488*	487	470*	491	482	O–Al–O bend (AlO_6)
–	426*	423*	420	–	405	–	

* = shoulder

a) transition alumina formed by the dehydration of boehmite gel at 400 °C [231]

b) boehmite powder formed by hydrolysis of ATSB [221]

c) commercial boehmite powder [232]

d) 3:1 Al:Si mullite ($3Al_2O_3{\cdot}SiO_2$) [233]

Si–O–Si Bonds

The small but prominent peak appearing around 1020–1040 cm^{-1} is most likely due to the presence of an interfacial silicon oxide (SiO_x) layer. It is close to the 1060–1080 cm^{-1} peak position associated with the transverse optical asymmetric stretching mode of the Si–O–Si bridging bond between SiO_4 tetrahedra found in thermally grown SiO_2 [228], [229]. It is known that the absorption peak of this mode shifts to lower wavenumbers as the SiO_2 film thickness is decreased below about 5 nm, which has been explained by sub-stoichiometry (excess Si) in the interfacial SiO_x within 0.6 Å to 1.6 Å of the Si surface [228], [229]. A shift to lower wavenumbers can also occur as a result of the presence of Al [247]. Coupled with the other evidence for the existence of a thin interfacial SiO_x layer at the Si–Al_2O_3 interface (Section 1.2), the assignment of this peak to interfacial SiO_x appears quite plausible. Other authors examining FTIR measurements of Al_2O_3

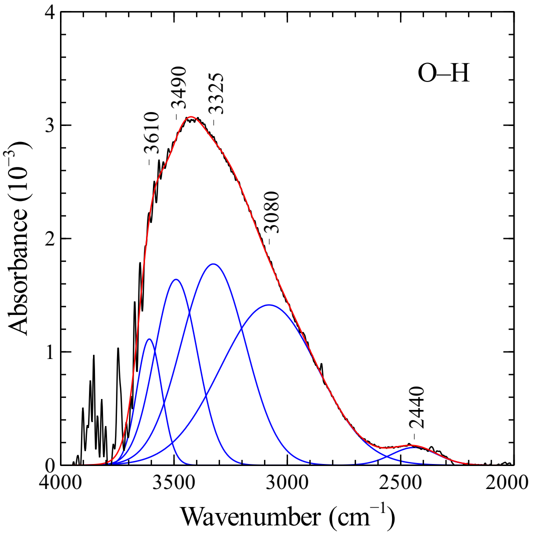

Figure 9.3: FTIR absorbance spectrum in the region of the O–H absorption band for Al_2O_3 deposited from TEDA-TSB and H_2O at 325 °C, showing the deconvolution into Gaussian components.

on silicon surfaces have made a similar assignment of this peak [40], [55], [69], [216]–[218]. Comparison with the data of [229] suggests an implied SiO_x thickness in the range of 5 Å to 8 Å for the examined films, or 3–5 Si–O bond lengths.

O–H Bonds

In order to distinguish the major contributions to the broad O–H absorption band, least-squares fitting was performed using the sum of multiple Gaussian distributions, taking the minimum number of such distributions necessary to provide a satisfactory fit to the data. Based on this analysis, the O–H absorption band may be resolved into at least five Gaussian components, centred at 2440, 3080, 3325, 3490, and 3610 cm^{-1} (Fig. 9.3). Similar peak values are obtained by applying the same procedure to the data of other samples. The 3080 and 3325 cm^{-1} distributions correspond to the broad features reported at 3050 and 3300 cm^{-1} by [221] in hydrated amorphous alumina, and present as distinct peaks at 3090 and ~3300 cm^{-1} in the spectra of crystalline boehmite [231], [232], [248], while the peaks at 3490 and 3610 cm^{-1} are probably due to a combination and broadening of the individual peaks observed at 3405, 3412, 3520, 3540, 3590, 3610, and 3658 cm^{-1} [221]. On the basis of molecular dynamics simulations of hydroxylated alumina, Adiga *et al.* [244] identified vibrational peaks at 3482 and 3608 cm^{-1} due to stretching vibrations of singly and doubly coordinated

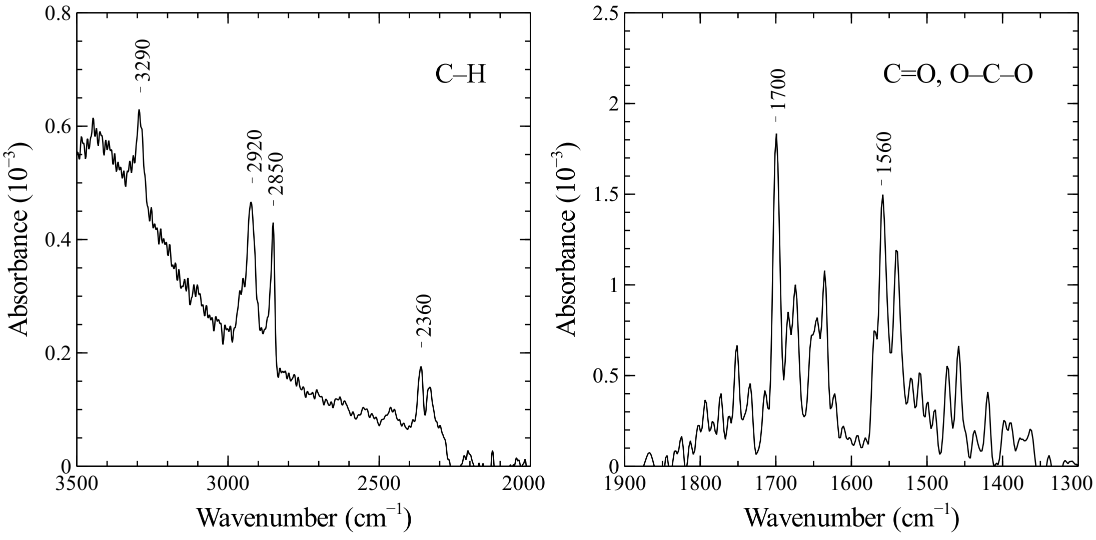

(a) (b)

Figure 9.4: FTIR absorbance spectrum of Al_2O_3 deposited from TEDA-TSB and H_2O at 410 °C, showing absorption peaks attributed to a) C–H and b) C=O and O–C–O bonds. The former peaks are superimposed on the broader O–H absorption peak.

(bridging) O–H groups respectively, which are uncannily close to the locations of these latter peaks. The broad but low feature at 2440 cm^{-1} seems likely to be related to O–H vibrational modes, since its intensity scales with that of the other O–H peaks, but does not appear to have been remarked by other authors.

Carbon-related bonds

A number of significant peaks can be associated with various carbon-related species present in the films. A doubly peaked feature at 2850 and 2920 cm^{-1}, appears prominently for some samples within the broader O–H absorption band. This feature is similar to that observed for the C–H bonds of methyl groups (CH_3) adsorbed on alumina surfaces [223], but its pronounced double-peak structure suggests that it is more likely related to ethyl (C_2H_5) or butyl (C_4H_9) groups [224], both of which are present in the TEDA-TSB precursor. Other features observed less frequently in this range, including a single peak at 3290 cm^{-1}, and an apparently double-peaked structure around 2360 cm^{-1}, are less readily identified, but are likely to also relate to carbon bonding within residual organic ligands derived from the TEDA-TSB precursor. These features are most apparent in the absorption spectrum for Al_2O_3 deposited at 410 °C from H_2O, shown in Fig. 9.4a.

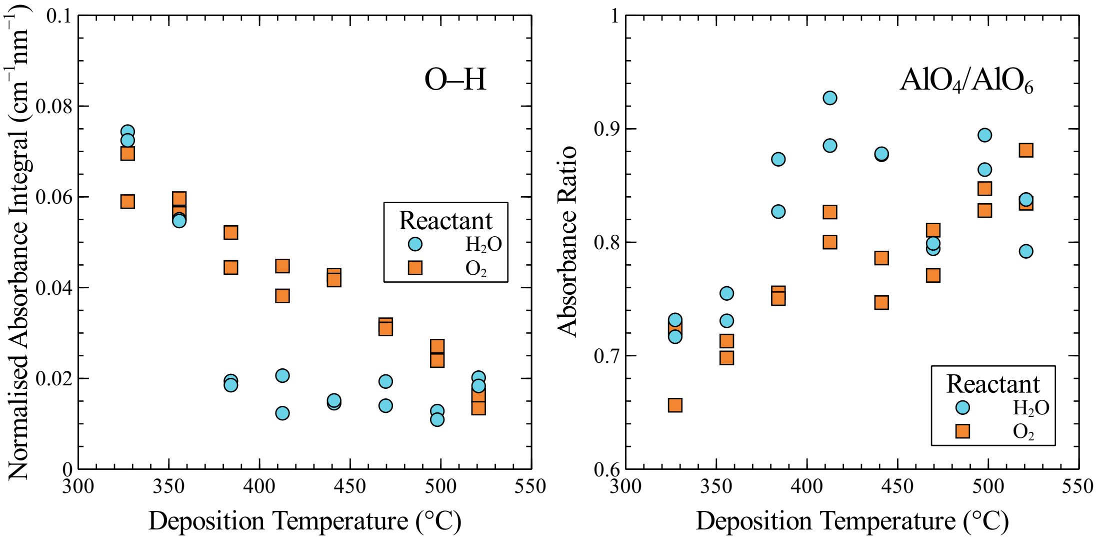

(a) (b)

Figure 9.5: a) Evolution of O–H concentration with deposition temperature, as indicated by the integral of absorbance in the 2700–3700 cm^{-1} range, normalised to film thickness. b) Ratio of absorbance due to Al in tetrahedral sites (750–850 cm^{-1}) to that due to Al in octahedral sites (500–600 cm^{-1}), showing the shift of Al coordination with deposition temperature.

The cluster of sharp peaks observed for all samples in the 1350 to 1800 cm^{-1} range, and decreasing somewhat in intensity with deposition temperature, can be attributed predominantly to carbon-oxygen bonds (C=O, O–C–O) [225]–[227]. The relative intensity of these peaks varies from sample to sample, but in most cases two prominent peaks are observed near 1560 and 1700 cm^{-1}. A typical example is shown in Fig. 9.4b. Similar clusters of sharp absorbance peaks are observed in a comparable energy range for various organic molecules in the gas phase [224].

9.1.3 Trends and discussion

A number of trends may be observed in the data of Fig. 9.1. The most obvious of these is a significant reduction in the intensity of the O–H absorption band with increasing deposition temperature. Fig. 9.5a plots the integrated absorbance between 2700 and 3700 cm^{-1} as a function of deposition temperature, normalised to film thickness. For the H_2O films a large O–H concentration is present at the lowest temperatures, but decreases sharply between 355 and 385 °C, indicating significant hydrogen desorption. Above 385 °C a low but roughly constant O–H concentration remains up to at least 520 °C. For the O_2 films the O–H concentration at low temperatures is essentially identical to that of the H_2O films, but there is no abrupt decrease in concentration between 355 and 385 °C. Instead the O–H concentration decreases roughly linearly with increasing T_{dep}, reaching a similar value as the H_2O films at $T_{dep} = 520\,°C$. This marked difference in behaviour must be attributed to the distinct deposition reactions taking place for the different reactants.

The second major trend relates to the Al–O absorption band. Fig. 9.1 reveals a clear shift in the shape of this band with increasing deposition temperature, with an increase in the intensity of absorption at higher wavenumbers. From Tables 9.1 and 9.2, and Fig. 9.2, it is clear that this represents an increase in the concentration of Al in tetrahedral sites (AlO_4) relative to octahedral sites (AlO_6). By taking the ratio of the integrated spectrum between 750 and 850 cm^{-1} to that between 500 and 600 cm^{-1}, we obtain a measure of the AlO_4/AlO_6 coordination ratio. This is plotted in Fig. 9.5b, which clearly shows an increase in the relative proportion of AlO_4 sites with increasing T_{dep}.

Molecular dynamics simulations indicate that in the absence of hydroxyl species, Al in amorphous Al_2O_3 is predominantly tetrahedrally coordinated [240]–[246]. The degree of octahedral coordination increases with increasing crystallinity through the transition phases (e.g. γ-, δ- and θ-Al_2O_3), finally reaching 100% octahedral coordination in the fully crystalline and stable α-Al_2O_3 (corundum) phase. The shift in Al coordination fraction between the transition phases is thought to occur mainly by the migration of Al cations between interstitial sites within a stable O lattice. These transitions however, occur above the range of temperatures studied here.

On the other hand, it is well established that aluminium hydroxyls such as boehmite (γ-AlO(OH)) feature solely octahedral Al coordination [231], [249], and that the structure shifts towards tetrahedral coordination upon dehydration. Therefore, the higher degree of octahedral coordination found at low deposition temperatures may be attributed to the influence of hydoxyl groups (O–H), which are present in greater concentration in these films. Indeed, the shift in Al coordination closely mirrors the reduction in O–H concentration shown in Fig. 9.5a. This is illustrated in Fig. 9.6, where the two sets of data are plotted against each other.

The shift in absorption to higher wavenumbers therefore represents an increase in the relative concentration of tetrahedrally coordinated Al (AlO_4) at the expense

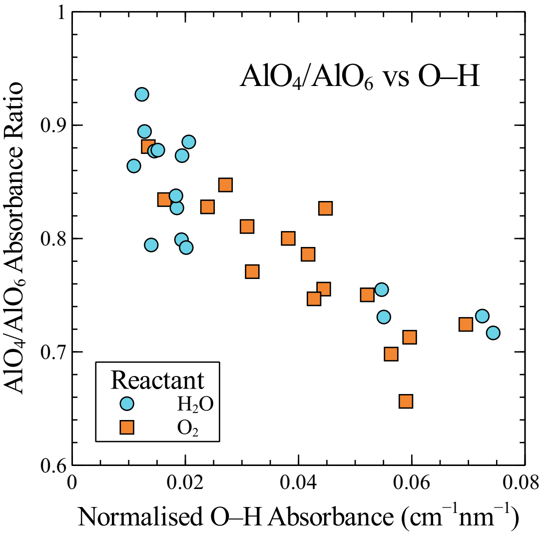

Figure 9.6: AlO_4/AlO_6 absorbance ratio versus normalised O–H concentration. Data taken from Figs. 9.5a and 9.5b.

of more highly coordinated groups, and is related to the removal of hydroxyl species at temperatures above 355 °C. A similar increase in the intensity of the high-wavenumber component of the main Al–O absorption band with increasing temperature, as well as a reduction of absorption due to O–H and C–O groups, was also observed by other authors [127], [129], [131], [222], [231], [250], [251].

Tetrahedrally coordinated Al located near the Si-Al_2O_3 interface has been proposed as a possible origin of the fixed negative charge in Al_2O_3 [26]. It is therefore interesting to observe that there appears to be a correlation between the ratio of AlO_4 and AlO_6 bonding in the bulk of the film, and the fixed charge concentration Q_{tot} determined by C–V measurements (Fig. 5.2). The lowest fixed charge concentration Q_{tot} in the films deposited from H_2O is found in those deposited at the lowest two temperatures, which are also those with the lowest AlO_4 to AlO_6 absorbance ratio, while the highest ratio and largest Q_{tot} are both measured for $T_{dep} = 410\,°C$.

The correlation is even more striking when one compares the post-annealing values of Q_{tot} for the films deposited above 355 °C, i.e. those in which the pre-annealing O–H concentration is small. Even the somewhat unexpected dip in charge of the film deposited at 470 °C is reflected in a similar dip in the pre-annealing ratio of AlO_4 to AlO_6 absorbance for the same film. Fig. 9.7 plots Q_{tot} obtained before and after annealing against the AlO_4 to AlO_6 absorbance ratio of the as-deposited films. In this case Q_{tot} was determined at midgap rather

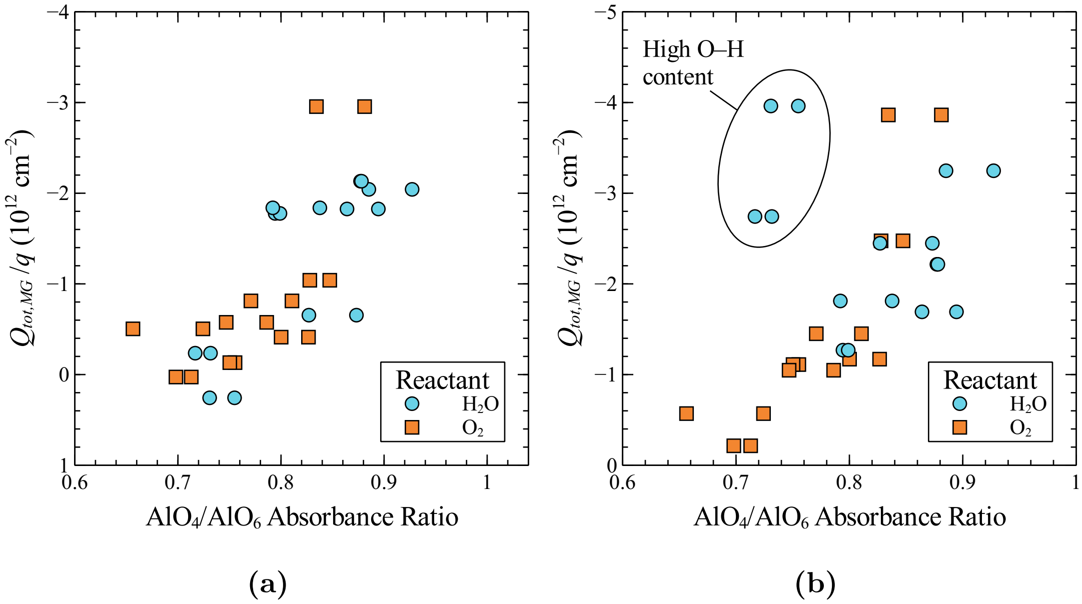

Figure 9.7: a) Pre- and b) post-annealed total insulator charge Q_{tot}, determined at midgap, as a function of the pre-annealed AlO_4 to AlO_6 absorbance ratio.

than flatbands, since this is believed to provide a better approximation of the fixed charge component Q_f for samples with significant Q_{it}, enabling a proper comparison of samples with widely differing D_{it}. There is a clear and strong trend of increasing Q_{tot} with increasing AlO_4/AlO_6 ratio for films deposited from both H_2O and O_2. Prominent exceptions after annealing are the samples deposited at the lowest two temperatures from H_2O, which as noted before contain a significant O–H concentration prior to annealing. It seems reasonable to suppose that a significant change in the Al coordination within these films occurs together with the removal of hydroxyl species upon annealing. This could account for the large increase in Q_{tot} observed after annealing for these films. As noted at the start of this section, similar conclusions concerning the correlation between AlO_4 concentration and Q_f were recently drawn by [220].

The other interface property important to surface passivation is the interface defect density D_{it}. Several authors have reported a correlation between the intensity of the Si–O–Si absorption peak found between 1000 and 1100 cm^{-1} and the degree of surface passivation [38], [55], [216]–[218], which has been attributed to the role of the interfacial SiO_x layer in the chemical passivation of the Si surface.

Gaussian deconvolution was used to isolate this feature from the main Al–O absorption band in our data. Its peak frequency increases from less than 1020 cm^{-1} to around 1040 cm^{-1} with increasing deposition temperature (Fig. 9.8),

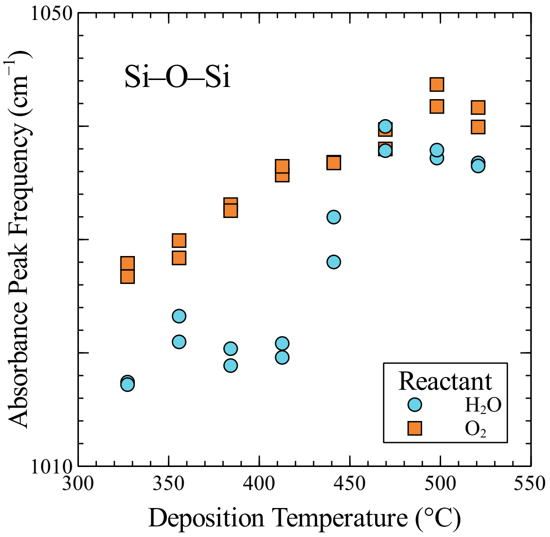

Figure 9.8: Peak frequency of the Si–O–Si absorption peak as a function of deposition temperature for films deposited from H_2O and O_2.

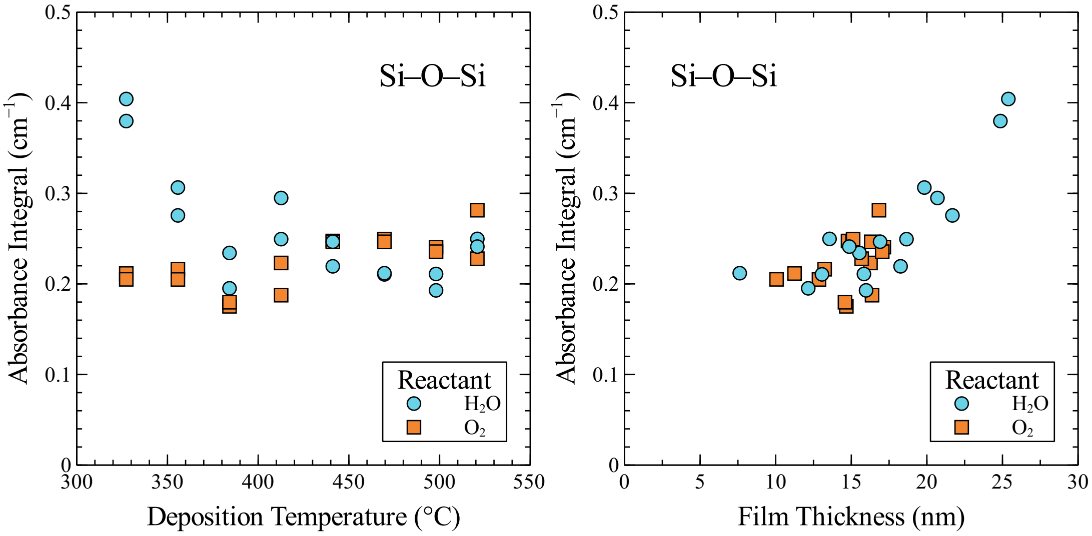

(a) **(b)**

Figure 9.9: Integrated intensity of the Si–O–Si absorption peak as a function of a) deposition temperature and b) film thickness, for films deposited from H_2O and O_2.

which may indicate an increase in the degree of stoichiometry (from SiO towards SiO_2). A similar shift with increasing annealing temperature was reported by [220]. Contrary to the above cited authors, but in agreement with [220], no correlation between peak intensity and surface passivation was observed. Indeed, the absorption feature is just as prominent in the films deposited with O_2, which have a high density of interface states. Rather, the integrated absorbance of the peak appears to scale closely with film thickness (Fig. 9.9b). It is not clear whether this is consistent with its assignment to an interfacial SiO_x. Alternative assignments could include the stretching mode of Al–OH, which is known to occur at around $1070\,cm^{-1}$ in boehmite [232], [248], although this appears inconsistent with the change in intensity of the O–H absorption peak centred at $3450\,cm^{-1}$ at higher temperatures.

In summary, FTIR measurements reveal that Al_2O_3 films deposited at low temperature from H_2O contain significant hydrogen in the form of hydroxyl groups (O–H). They also feature a structure in which Al atoms tend to occupy more highly coordinated (octahedral) sites in the oxygen lattice. Hydroxyl groups are largely removed at temperatures above 355 °C, coinciding with a shift of Al coordination to a predominantly tetrahedral configuration (AlO_4), which generally continues as temperature is increased. Increasing AlO_4 content is correlated with the increase of negative charge revealed by C–V measurements, which provides support for the assignment of interfacial AlO_4 as the chemical origin of the fixed negative charge centres in Al_2O_3. On the other hand, there is no apparent correlation of absorption features with the density of interface states (D_{it}). The intensity of the peak commonly associated with interfacial SiO_x increases with film thickness, but is not correlated with passivation quality.

The correlation between AlO_4 content and Q_{tot} may provide clues on suitable processing routes to achieve desired charge concentrations, since the variation of Al coordination with processing conditions in Al_2O_3 has been fairly well studied, at least for crystalline films.

9.2 Dielectric properties

The dielectric properties of the Al_2O_3 films are of interest in themselves for electronic applications, but they can also shed light on compositional and structural changes in the films and their relation to interface properties. The property of interest is the relative dielectric permittivity ϵ_r and its variation with frequency. The permittivity of a dielectric material describes the ability of charges within it to polarise in response to an electric field. Such polarisation can occur either on the scale of molecular dipoles (e.g. H_2O), by inter-atomic bond stretching between ionic species (e.g. Al^{3+}, O^{2-}), or within atoms by displacement of the electron

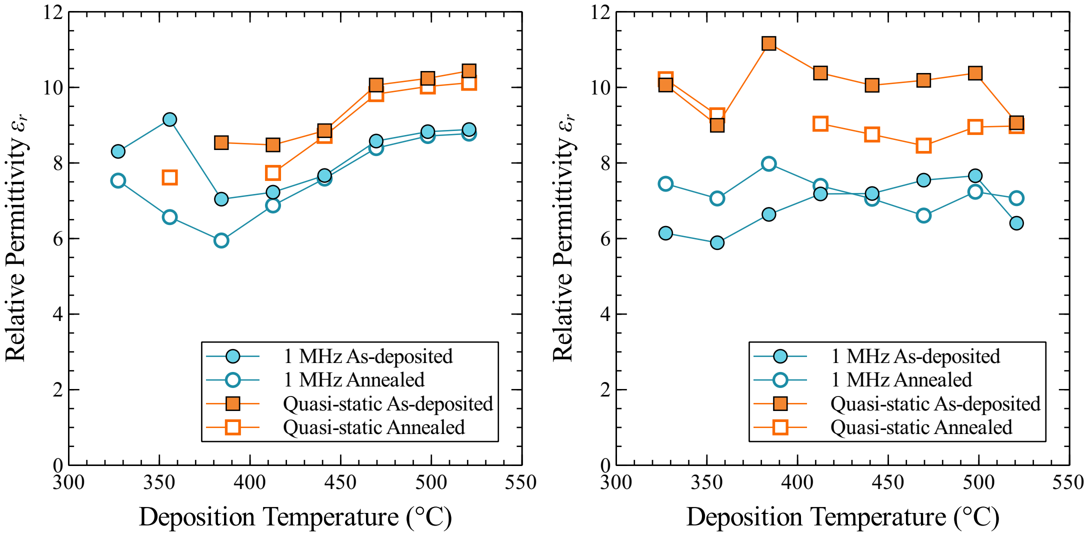

(a) (b)

Figure 9.10: Relative permittivity ϵ_r of APCVD Al_2O_3 as a function of deposition temperature for films deposited with a) H_2O and b) O_2 as reactants.

cloud with respect to the nucleus. As such, the resulting permittivity is highly sensitive to the structure and composition of the films.

The relative permittivity was calculated via Equation (A.9) using the insulator capacitance determined from C–V measurements, with film thickness determined as described in Section 3.3. When possible, the permittivity was determined under both high-frequency (1 MHz) and quasi-static conditions. Fig. 9.10 shows the variation of relative permittivity with deposition temperature for films deposited from H_2O and O_2, which correspond to the D_{it} and Q_{tot} measurements of Fig. 5.2. It can be seen that permittivity varies significantly with deposition temperature.

For the H_2O films at the lowest two temperatures (325 and 355 °C), ϵ_r is significantly increased relative to films deposited at slightly higher temperatures. This is likely due to the contribution of dipolar hydroxyl species which are present in significantly greater concentrations at low T_{dep} (Section 9.1). It is well known that such species contribute significantly to permittivity [252]. After annealing, ϵ_r of films deposited at lower temperatures (less than 410 °C) is substantially reduced, which probably relates to the removal of hydroxyl groups at elevated temperatures.

Above 355 °C, ϵ_r increases with temperature from 7.0 at 385 °C to 8.9 at 520 °C (1 MHz), with the steepest increase occurring between 440 and 470 °C. This transition could relate to the restructuring of the Al–O lattice apparent from FTIR measurements. For instance, theoretical modelling has suggested that certain lowly coordinated Al and O sites contribute disproportionately to lattice polarisation and resultant permittivity [253]. These sites are characterised by local bonding environments that feature weak inter-atomic interactions in at least one vibrational axis. It may be that these types of sites become more prevalent in films deposited at higher temperatures. Given that the sites in question, whatever their nature, contribute to the permittivity, they are likely to be Raman-active, so that Raman scattering measurements may be able to cast more light on them. It is notable that the increase in permittivity appears to be correlated with the shift of the Si–O–Si absorption peak to higher frequencies (Fig. 9.8), which features a major transition over a similar temperature range.

For the films deposited from O_2, the behaviour of the permittivity with deposition temperature shows some similarities to the case of H_2O. ϵ_r generally increases with increasing T_{dep} for the as-deposited films, from ~6 at the lowest temperatures to ~7.6 at 470 to 500 °C (values at 1 MHz). The abrupt increase in ϵ_r at low temperatures seen for H_2O is not present, which is consistent with the attribution of this feature to the contribution of hydroxyl groups, since the sharp rise in O–H concentration present in H_2O films at low T_{dep} is absent in the O_2 films (Fig. 9.5a). ϵ_r also does not increase to the same extent as for H_2O above 440 °C.

The behaviour of ϵ_r after annealing for the O_2 films is unlike that of H_2O. ϵ_r increases at low T_{dep} and decreases at higher T_{dep}, with a transition between 410 and 440 °C. This behaviour strikingly mirrors that of D_{it} determined on the same samples (Fig. 5.2). The obvious question, given that both values are determined from the same measurement, is whether the correlation is the result of systematic error. While the direct dependence of D_{it} at midgap on errors in C_i is slight, a systematic error in the determination of the gate area could produce such a correlation. This, however, appears unlikely to be the case, since all gate areas were individually determined by the same method.

The frequency dispersion of the permittivity, as seen in the ratio between the quasi-static and high frequency values of ϵ_r (Fig. 9.11), is significantly greater for the O_2 films than for those deposited from H_2O. It decreases with increasing T_{dep} and after annealing, especially for the O_2 films. At these frequencies, dispersion is mainly due to dipolar species such as O–H groups. This appears to be consistent with the relative concentrations of O–H groups observed in H_2O and O_2 films and their decrease with T_{dep} (Fig. 9.5a). As it was not possible to measure low frequency capacitance for the H_2O films at low T_{dep}, the existence of the strong

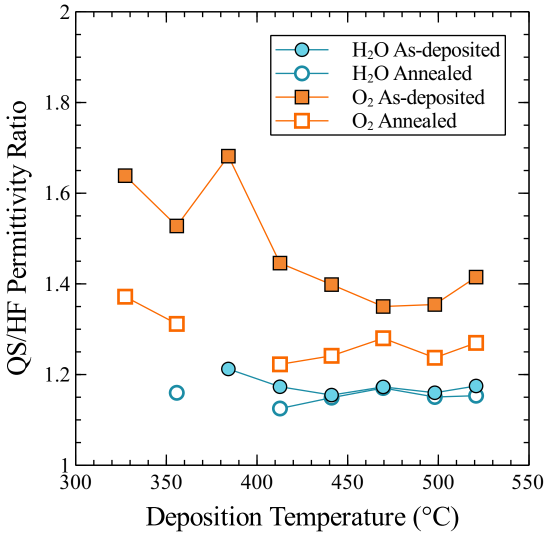

Figure 9.11: Ratio of quasi-static permittivity to permittivity at 1 MHz, as a function of deposition temperature.

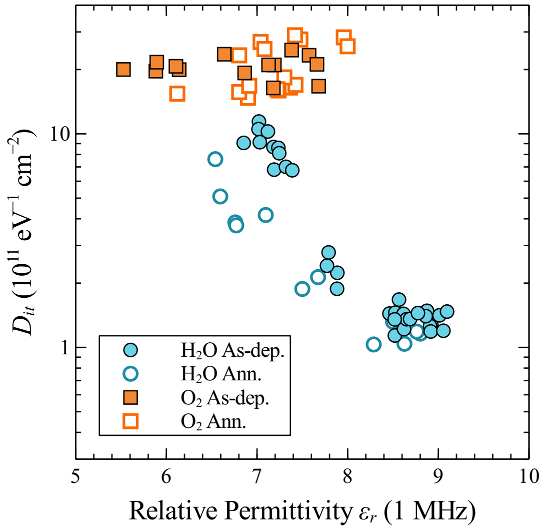

Figure 9.12: D_{it} versus relative permittivity at 1 MHz for Al_2O_3 films deposited from H_2O and O_2.

frequency dispersion expected for these films on this basis cannot be confirmed.

For the films deposited from H_2O, the increase of permittivity with temperature appears to be correlated with the reduction of D_{it}, which was measured for the same samples (Fig. 5.2). D_{it} is plotted against ϵ_r at 1 MHz in Fig. 9.12 for both H_2O and O_2 films. An essentially monotonic trend of decreasing D_{it} with increasing ϵ_r is apparent for the H_2O films, while the O_2 films, with higher

D_{it}, are clustered at lower values of ϵ_r. It should be remembered that ϵ_r consists of contributions from several physically distinct sources, and that even if one of these is genuinely correlated to D_{it}, others may be independent. ϵ_r of the O_2 films, for instance, will include a larger contribution from O–H dipoles than that of any of the H_2O films shown in Fig. 9.12. In addition, the H_2O films at low T_{dep}, which have large ϵ_r for the same reason, are also known to have high D_{it}. The observed trend is very suggestive though, and the possible correlation between high-permittivity lattice configurations and the reduction of interface state density certainly warrants further investigation.

9.3 Optical properties

The optical properties of Al_2O_3 over the wavelength range of the solar spectrum determine its effectiveness as an anti-reflection coating or rear reflector in solar photovoltaic devices. Therefore, for such applications it is important that these properties be accurately determined. Previous studies have reported values of the refractive index n typically ranging between 1.5 and 1.7 for amorphous Al_2O_3 [16], [33], [39], [127], [129], [131], [137], [250], [254]–[259]. For comparison, crystalline corundum (α-Al_2O_3) has $n = 1.77$ [260], while the hydrated crystalline aluminate boehmite (γ-AlO(OH)) has $n = 1.65$ [261].

In order to establish the frequency dispersion of the optical constants for APCVD Al_2O_3, variable angle (55, 65, and 75°) ellipsometry measurements of thicker (80 and 110 nm) Al_2O_3 films were performed over a wide spectral range (192 nm to 1688 nm) using a J.A. Woollam M-2000D ellipsometer. The use of thicker films substantially reduces error in the subsequent extraction of film properties. The relatively thick films were deposited on polished ⟨100⟩ Si wafers from TEDA-TSB and H_2O using the 355 °C temperature profile with a belt speed of 2 IPM.

Fitting of ellipsometry data was performed using a single term Tauc-Lorentz model [262] for the dielectric function of the films. For the silicon substrate, the values recommended by [263] were used (these were derived from the data of [264] in the range of interest). Good fits of the data could be obtained in this way, as shown in Fig. 9.13, with some disagreement at high energies. The parameters of the fits, along with the extracted optical properties, are listed in Table 9.3. These include an average refractive index of $n = 1.53$ at 633 nm and apparent bandgap $E_{g,TL} = 4.5$ eV.

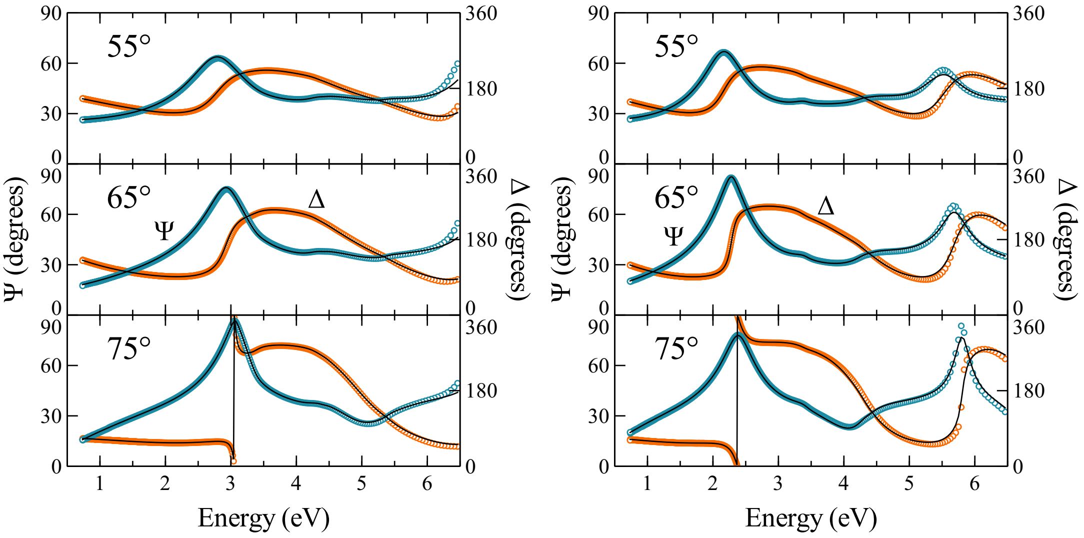

(a) (b)

Figure 9.13: Variable angle ellipsometry measurements of a) 82 nm and b) 111 nm thick APCVD Al_2O_3 films. Symbols show measured data, while lines show the modelled fit.

Table 9.3: Parameters of the Tauc–Lorentz fits of ellipsometry data shown in Fig. 9.13. t_i = film thickness, n = refractive index, $E_{g,TL}$ = Tauc–Lorentz bandgap. The value of $\epsilon(\infty)_{TL}$ was constrained to 1 for the fits.

		Value		
Parameter	Units	Sample 1	Sample 2	Average
t_i	nm	82.0	110.9	
n (633 nm)		1.546	1.515	1.531
$E_{g,TL}$	eV	4.48	4.59	4.53
$\epsilon_1(\infty)_{TL}$		1	1	1
A_{TL}	eV	44.0	42.9	43.4
$E_{0,TL}$	eV	12.5	11.8	12.2
C_{TL}	eV	1.40	1.41	1.40

The resulting refractive index n and extinction coefficient k are shown as a function of wavelength in Fig. 9.14 for both samples. The dependence of n on wavelength can be accurately described over the range of the measurement

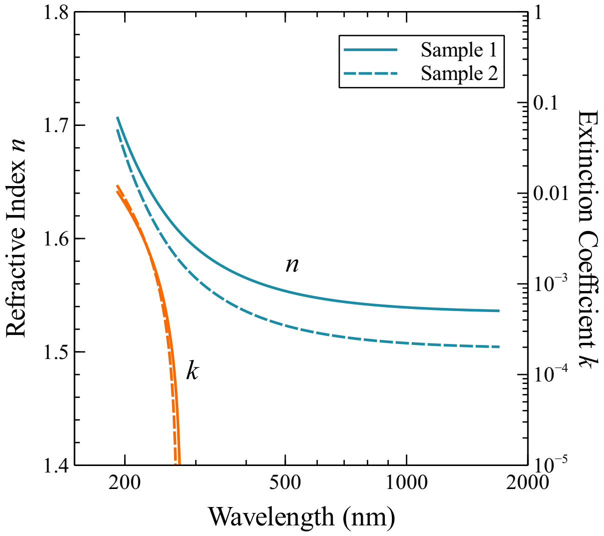

Figure 9.14: Refractive index n and extinction coefficient k of APCVD Al_2O_3 as a function of wavelength (on a log scale), derived from fits to the data of Fig. 9.13.

Table 9.4: Parameters of the Sellmeier dispersion equation for the refractive index (Equation (9.1)).

Parameter	A	B	C (µm^2)
1	1.1416	1.2132	1.1661×10^{-2}
2	1.1267	1.1314	1.3069×10^{-2}
Average	1.1342	1.1723	1.2365×10^{-2}

(192 nm to 1688 nm) using the Sellmeier equation with a single dispersion term:

$$n^2 = A + \frac{B\lambda^2}{\lambda^2 - C}, \tag{9.1}$$

where the values of A, B, and C are given in Table 9.4.

In a separate experiment, the dependence of refractive index on deposition temperature was evaluated by simultaneous fitting of ellipsometry and reflectance spectra (polarised and unpolarised) at multiple angles of incidence, measured on the samples used for the FTIR measurements of Section 9.1 (deposited with H_2O as reactant). The use of both reflectance and ellipsometry data increases the information content on which the fit is based, resulting in greater confidence in the accuracy of the extracted parameters, especially for thinner films. Variable angle ellipsometry measurements were performed as before at 55, 65, and 75° over a wavelength range of 192 nm to 1688 nm. Spectral reflectance was measured for

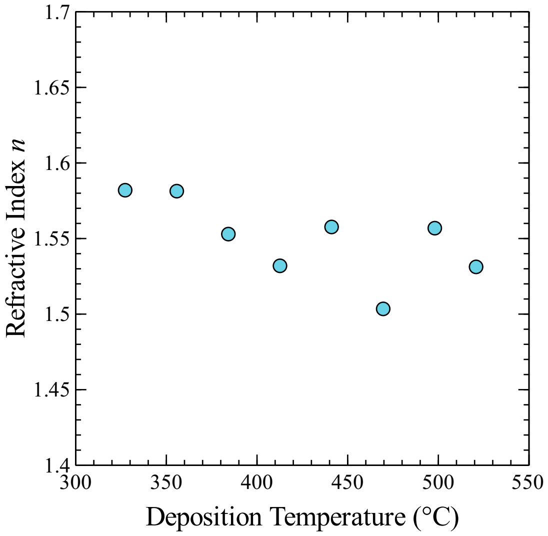

Figure 9.15: Refractive index n of APCVD Al_2O_3 deposited from TEDA-TSB and H_2O as a function of deposition temperature.

p- and s-polarised light between 250 and 1200 nm at angles of incidence of 10, 40, and 60° using a PerkinElmer Lambda 1050 UV/Vis/NIR spectrophotometer equipped with an Automated Reflectance/Transmittance Analyser (ARTA) attachment [265]. Additional unpolarised normal-incidence reflection measurements were performed between 199 and 1100 nm using a Filmetrics F20 thin film measurement system. Simultaneous fitting of all spectra was performed as before using the Tauc–Lorentz model for the dielectric function. Fitting was limited to wavelengths below 900 nm, since data at higher wavelengths was affected by reflection from the polished rear side of the sample.

Fig. 9.15 shows n at 633 nm determined in this way as a function of deposition temperature. n is close to 1.58 for the two lowest temperatures, then decreases somewhat between 355 and 385 °C. Values at higher temperatures generally lie between 1.53 and 1.56 (neglecting the outlier at 470 °C), with an average value of 1.54, and no apparent trend with deposition temperature. The higher value of n for the lowest temperature films is consistent with the fact that film density (and therefore refractive index) is observed to increase with increasing Al coordination in molecular dynamics simulations [240]. The higher refractive index of the films at the lowest two temperatures can therefore be related to their higher fraction of AlO_6 octahedra (Fig. 9.5b).

Table 9.5: Summary of key trends in compositional, structural, electrical, and optical bulk properties, together with their correlations with each other and with interface properties.

Quantity	Trend with T_{dep}	Correlated with	Figs.
O–H conc.	$\searrow$	AlO_4/AlO_6 ratio, ϵ_r	9.5a, 9.6
AlO_4/AlO_6 ratio	$\nearrow$	Q_{tot}, O–H conc., ϵ_r	9.5b, 9.6, 9.7
Si–O–Si peak pos.	$\nearrow$	ϵ_r	9.8
Si–O–Si conc.	$\rightarrow$	t_i	9.9
ϵ_r	$\nearrow$	O–H conc., AlO_4/AlO_6 ratio, Si–O–Si peak pos., D_{it}	9.10, 9.12
n	$\searrow$	O–H conc., AlO_4/AlO_6 ratio	9.15

9.4 Conclusions

Measurements of Al_2O_3 bulk properties reveal a number of interesting trends and correlations with interface properties. The reduction of O–H concentration with increasing deposition temperature is accompanied by a structural shift in which Al increasingly occupies tetrahedral AlO_4 sites in the oxygen lattice in preference to more highly coordinated sites. The relative concentration of tetrahedrally coordinated Al in the bulk of the films is found to correlate strongly with the concentration of fixed charge, which supports the attribution of this charge to near-interfacial AlO_4. The existence of an interfacial SiO_x layer is observed in all cases, but its presence is not correlated with the quality of chemical passivation. Rather, decreasing D_{it} is correlated with the increase in permittivity at higher temperatures, suggesting a link between those conditions which give rise to strong lattice polarisation in the bulk film and those which produce a low density of interface states. Table 9.5 summarises the main trends and correlations. The significantly different behaviour observed for different precursor–reactant systems highlights the sensitivity of film properties to the chemistry of the deposition process.

Chapter 10

Conclusion

"Begin at the beginning," the King said very gravely, "and go on till you come to the end: then stop."

— Lewis Carroll
ALICE IN WONDERLAND

The contributions of this thesis fall into three major areas: 1) those that deepen the current understanding of semiconductor–dielectric interfaces and semiconductor surface recombination and passivation mechanisms in general; 2) those relating to the properties and characteristics of Al_2O_3 as a surface-passivating material for crystalline silicon; and 3) those relating to APCVD specifically as a low-cost, high-throughput deposition method for Al_2O_3 passivation layers, enabling industrial application to photovoltaic devices. A summary of the major conclusions in each of these areas is given here. Further conclusions not mentioned here may be found in the final sections of Chapters 4–9.

This thesis presented the most thorough characterisation of semiconductor surface passivation to date. Specifically, it was shown in Chapter 4 that the various contributions to the distribution of interface states could be distinguished, and their capture cross-sections for minority as well as majority carriers determined, by the application of the extended conductance method in combination with a novel sophisticated analysis taking into account the distinction between apparent and real capture cross-sections. Furthermore, the direct link between the interface properties measured by such electrical characterisation techniques and the carrier lifetime determined by photoconductance measurements was strongly confirmed, by showing that the latter could be accurately predicted from the former via physical theory for both p- and n-type surfaces with a wide range of dopant concentrations, without the use of any free variables (see especially Chapters 4 and 7). Thus it was experimentally demonstrated for the first time that a thorough analysis of semiconductor–dielectric interface properties can be used to determine the recombination rate at that interface, and that this determination can be made for arbitrary surface doping and injection level.

Investigations of the surface passivation properties of Al_2O_3 provide a remarkably consistent picture, and emphasise both its robustness and its distinctiveness as a surface passivation layer. Excellent agreement between the interface state distribution and capture cross-sections measured for Al_2O_3 films deposited by different techniques, and under different deposition conditions (Chapter 4), provide strong evidence that the nature of the Al_2O_3 interface is essentially independent of the means of its formation. Furthermore, these properties are also remarkably insensitive to the characteristics of the silicon surface itself. Chapter 7 showed that the interface properties of Al_2O_3 are independent of the surface dopant concentration at diffused surfaces (in contrast to the situation reported for thermal SiO_2), while it was found in Chapter 8 that the influence of orientation and morphology on recombination are relatively slight compared to the case for other dielectrics. Perhaps most remarkably, it was shown in Chapter 8 that while the fixed charge concentration varies somewhat between $\langle 100\rangle$ and $\langle 111\rangle$ surfaces, the interface state distribution and capture cross-sections are entirely independent of the silicon surface orientation. These results highlight the distinctive nature of the Si–Al_2O_3 interface, and demonstrate the suitability of Al_2O_3 for passivating the varied surfaces found in actual devices.

It was shown in Chapters 4 and 7 that recombination at the Si–Al_2O_3 interface is generally dominated by two species of interface state: one donor-, and one acceptor-like. Recombination is generally dominated by the former, except at heavily doped n-type surfaces. It was shown that the properties of these states may be used to accurately predict recombination at Al_2O_3-passivated surfaces. Meanwhile, Chapter 9 provided strong support for tetrahedrally coordinated AlO_4 in the vicinity of the Si–Al_2O_3 interface as the origin of the negative fixed charge of Al_2O_3.

Regarding the practical implementation of Al_2O_3 passivation, this thesis contained the first clear demonstration of surface passivation by Al_2O_3 deposited by APCVD, a low-cost, high-throughput method suitable for industrial applications. It was shown in Chapters 4–8 that APCVD Al_2O_3 is capable of providing excellent surface passivation, comparable to the best results reported for Al_2O_3 deposited by other methods. Two non-pyrophoric Al precursors were investigated, together with various co-reactants. Best results were achieved with optimised films deposited from TEDA-TSB and H_2O, while a proof-of-concept demonstration of ATSB as an alternative, low-cost, single-source precursor, suited to CVD, was given in Chapter 5. The passivation provided by APCVD Al_2O_3 was shown to be thermally stable when exposed to the conditions used in manufacturing conventional silicon solar cells, actually improving after a high-temperature firing step, while the best passivation properties could be achieved by the use of a short RTA at moderate temperatures following deposition (Chapter 6). The properties achieved in the latter case were exceptionally good, with $J_0 = 7\,\mathrm{fA\,cm^{-2}}$, $D_{it} = \sim 5 \times 10^{10}\,\mathrm{eV^{-1}\,cm^{-2}}$, and $Q_{tot} = -3.3 \times 10^{12}\,\mathrm{cm^{-2}}$. These results are comparable to or better than the best values reported in the literature for Al_2O_3 deposited by other techniques.

Finally, we report that the APCVD Al_2O_3 films described in this thesis have recently been demonstrated as surface-passivating layers in two different solar cell structures. Best efficiencies of 21.6 % were achieved for small-area front-junction n-type cells fabricated at ANU [81], and 21.3 % for 6 inch rear-junction n-type cells fabricated in collaboration with the Interuniversity Microelectronics Centre (IMEC) (the design of these cells has been reported in [80]), both incorporating Al_2O_3 passivation of the boron-doped $p+$ region. The latter results are presented in Fig. 10.1, where they are compared to similarly processed cells featuring passivation by thermal SiO_2 or ALD Al_2O_3. These results, together with those recently reported by [266], provide a proof of concept for the implementation of APCVD Al_2O_3 into industrial solar cells.

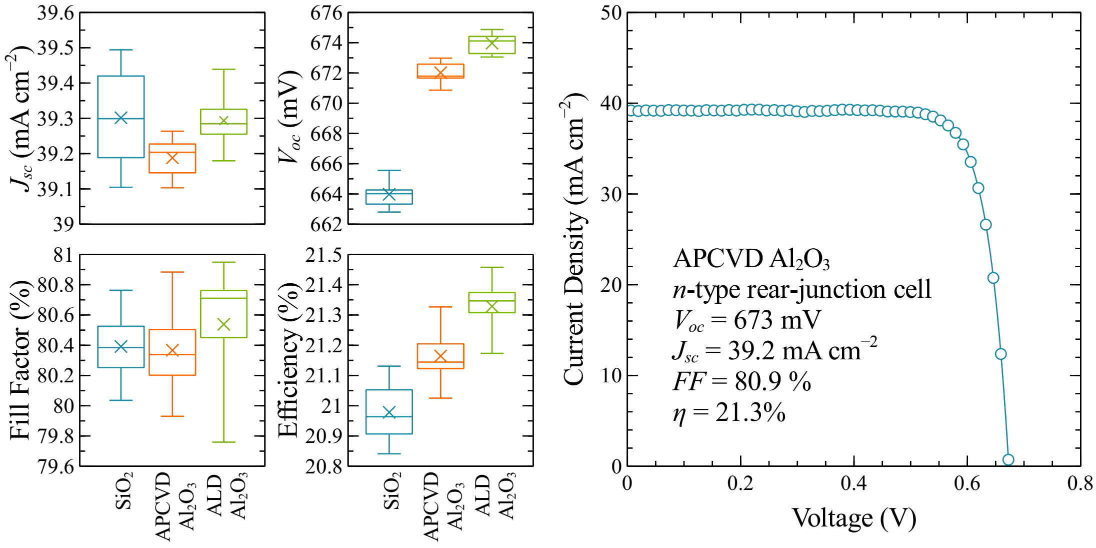

(a) (b)

Figure 10.1: a) Short circuit current density J_{sc}, open circuit voltage V_{oc}, fill factor FF, and efficiency η of n-type, rear-junction cells with the $p+$ region passivated by either thermal SiO_2, or Al_2O_3 deposited by APCVD or spatial ALD. The cells were fabricated at IMEC as described in [80], except for the deposition of the APCVD passivation layer, which was performed at ANU. While the efficiency of the cells with APCVD films was limited by a non-optimal front-side anti-reflection coating (seen in the lower J_{sc}), their high V_{oc}, which is very close to that of the ALD samples, shows the potential of APCVD Al_2O_3 for surface passivation on a device level. Fig. 10.1b shows the I–V characteristics of the best APCVD cell.

Appendix A

Capacitance–Voltage Measurements

C–V measurements are a powerful tool for the characterisation of thin-film dielectrics and their interfaces with semiconductors. Extensive use of such measurements is made in this work. This appendix describes the principles underlying C–V measurements, and details the analysis used to extract material parameters of interest. For a more thorough discussion of the theoretical basis, the interested reader is referred to the definitive work of Nicollian and Brews [8].

A.1 Principles

A.1.1 The MIS capacitor

The sample structure used for C–V measurements is the MIS capacitor, shown in Fig. A.1. This structure typically consists of a semiconductor wafer substrate covered on one side with a thin-film dielectric layer, over which is deposited a metal gate contact which defines the device area. The structure is contacted ohmically at the semiconductor rear and at the gate, which form the two electrodes of the capacitor.

C–V measurements of MIS structures probe the variation of the spatially extended charge distribution in the semiconductor (the space-charge region) in response to a time-varying voltage applied to the metal gate. This charge mirrors charges present at the semiconductor–insulator interface and in the insulator itself, as well as in the gate contact, and C–V measurements therefore contain information about the charge centres that give rise to each of these contributions.

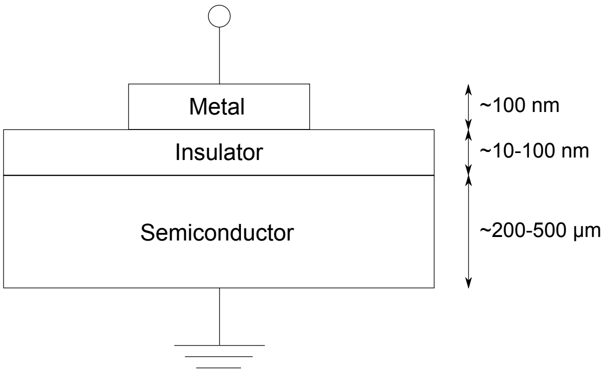

Figure A.1: Schematic of the MIS structure used in C–V measurements. Typical dimensions are indicated.

The capacitive response of each of these charge components—the free charge in the semiconductor, interface-trapped charge, and insulator charge—possesses a characteristic dependence on the semiconductor surface potential and on the frequency of potential variations. Thus, by measuring the C–V characteristics of a given device across a range of gate bias voltages at both high and low frequencies, the various charge contributions may be distinguished.

Furthermore, since the relationship between the semiconductor charge distribution and the gate bias is influenced by the ionised dopant concentration in the semiconductor, as well as the dielectric properties of the insulator layer, C–V measurements also contain information about these device properties. In the following sections we describe how these various parameters influence the measured C–V characteristics, and how they may be systematically extracted from experimental C–V data.

A.1.2 Basic equations

Fig. A.2 shows schematically the energy band diagram of the MIS capacitor under bias, along with the corresponding distribution of the various charges. The semiconductor potential $\phi(x)$ is defined by $q\phi(x) \equiv E_F - E_i(x)$, while the value of $\phi(x)$ in the semiconductor bulk ($x \to \infty$) is called the bulk potential ϕ_b. The gate voltage V_g designates the potential applied to the gate contact with respect to the grounded semiconductor substrate, while ψ_s is the induced potential at the semiconductor surface relative to ϕ_b.

The charge Q_g induced at the metal gate by the applied V_g is balanced by the insulator fixed charge Q_f, interface trapped charge Q_{it}, and semiconductor

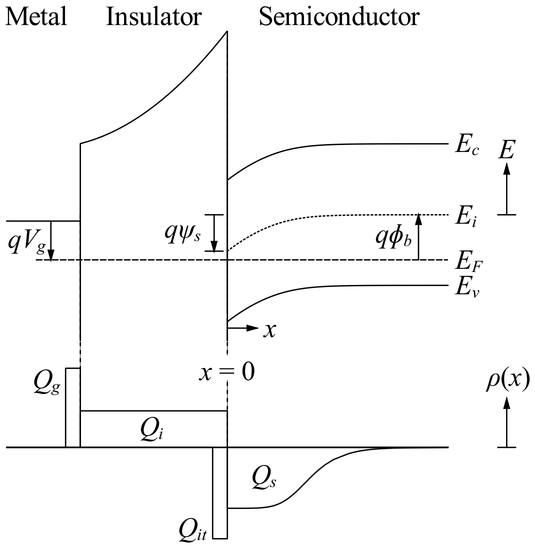

Figure A.2: Energy band diagram and associated charge distribution ($\rho(x)$) diagram of the (p-type) MIS capacitor under bias (depletion), showing the relationship between the various potentials and charges described in the text. Arrows pointing down (up) denote positive (negative) potentials.

charge Q_s. Charge neutrality dictates that

$$Q_g(\psi_s) + Q_s(\psi_s) + Q_f + Q_{it}(\psi_s) = 0\,, \tag{A.1}$$

where the dependence of the various charges on ψ_s has been indicated.

V_g is related to ψ_s and to the charge by

$$V_g = -\frac{Q_s + (1 + x_c/t_i)Q_f + Q_{it}}{C_i/A} + \psi_s + W_{ms}\,, \tag{A.2}$$

where x_c is the location of the insulator charge centroid relative to the semiconductor–insulator interface, C_i is the insulator capacitance, A is the area of the metal gate, and W_{ms} is the work-function difference between the metal gate and the semiconductor bulk. It will be convenient to define a flatband voltage V_{fb}, as the gate voltage corresponding to $\psi_s = 0$. In this case we also have $Q_s = 0$, so that

$$V_{fb} = \frac{(1 + x_c/t_i)Q_f + Q_{it}}{C_i/A} + W_{ms}\,. \tag{A.3}$$

The small-signal differential capacitance C of the MIS capacitor is defined by

$$C(V_g) \equiv \frac{dQ_g}{dV_g}A\,. \tag{A.4}$$

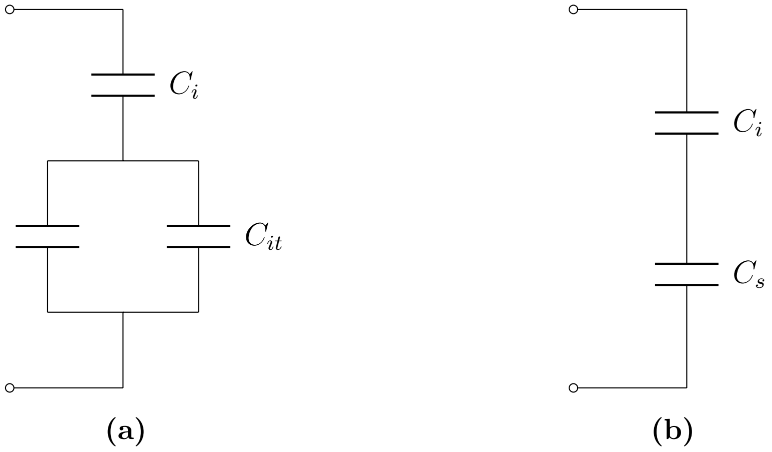

Figure A.3: a) Low frequency, and b) high frequency equivalent circuits of the MIS capacitor.

Similarly the semiconductor capacitance C_s and interface state capacitance C_{it} are defined by

$$C_s(\psi_s) \equiv -\frac{dQ_s}{d\psi_s}A\,, \tag{A.5}$$

$$C_{it}(\psi_s) \equiv -\frac{dQ_{it}}{d\psi_s}A\,. \tag{A.6}$$

The insulator fixed charge is assumed to be independent of ψ_s ($dQ_f/d\psi_s = 0$), so that no capacitive component is associated with this charge.

Combining (A.4)–(A.6) with (A.1) and (A.2), and using $dQ_f/d\psi_s = 0$, the total low-frequency capacitance C_{lf} of the MIS capacitor is related to its components by

$$C_{lf}^{-1} = C_i^{-1} + (C_s + C_{it})^{-1}\,. \tag{A.7}$$

The corresponding low-frequency equivalent circuit of the MIS capacitor is shown in Fig. A.3a. The insulator capacitance C_i is connected in series with the parallel combination of the semiconductor capacitance C_s and the interface state capacitance C_{it}. At high frequencies, interface states are unable to follow variations in the Fermi level, and (A.7) is reduced to

$$C_{hf}^{-1} = C_i^{-1} + C_s^{-1}\,, \tag{A.8}$$

with the corresponding equivalent circuit shown in Fig. A.3b.

The insulator capacitance C_i is given by

$$C_i = \epsilon_i A/t_i\,, \tag{A.9}$$

where ϵ_i is the insulator permittivity, and t_i is the insulator thickness. It is common to refer to an equivalent oxide thickness (EOT), given by calculating t_i from (A.9) with ϵ_i equal to the value for thermal SiO$_2$ ($3.9 \times \epsilon_0$) [97].

Assuming that D_{it} is a slowly varying function of energy, C_{it} is simply related to D_{it} by

$$C_{it}(\psi_s) = qAD_{it}(\psi_s)\,. \tag{A.10}$$

Finally, assuming Fermi–Dirac statistics apply, Q_s is given by

$$\begin{aligned} Q_s = (2kT\epsilon_s)^{1/2}\Bigg\{ & N_c\left[F_{3/2}\left(\frac{E_F - E_c + q\psi_s}{kT}\right) - F_{3/2}\left(\frac{E_F - E_c}{kT}\right)\right] + \\ & N_v\left[F_{3/2}\left(\frac{E_v - E_F - q\psi_s}{kT}\right) - F_{3/2}\left(\frac{E_v - E_F}{kT}\right)\right] + \\ & (N_A - N_D)\left(\frac{q}{kT}\psi_s\right)\Bigg\}^{1/2}. \end{aligned} \tag{A.11}$$

In the low-frequency case, C_s is then found by substituting Q_s from (A.11) in (A.5):

$$\begin{aligned} C_s(\psi_s) = \frac{q\epsilon_s A}{Q_s}\Bigg[& N_c F_{1/2}\left(\frac{E_F - E_c + q\psi_s}{kT}\right) - \\ & N_v F_{1/2}\left(\frac{E_v - E_F - q\psi_s}{kT}\right) + N_A - N_D\Bigg]. \end{aligned} \tag{A.12}$$

For Boltzmann (non-degenerate) statistics, the Fermi integrals in (A.11) and (A.12) may be replaced with exponential functions.

Fig. A.4 shows low-frequency capacitance C_{lf} vs gate voltage V_g, calculated from (A.2), (A.7), (A.9), (A.11), and (A.12), with D_{it}, Q_f, and $W_{ms} = 0$. In accumulation and strong inversion, C_s is large, and C_{lf} approaches C_i, while in depletion and weak inversion C_{lf} is limited by the much smaller value of C_s.

At high frequencies both the inversion layer charge and the interface state charge are unable to follow the AC voltage signal, but do follow changes in the gate bias (although spatial redistribution of the inversion layer charge in response to the AC signal does occur). As a result the high-frequency capacitance C_{hf} saturates at a low value in strong inversion rather than increasing as for low frequencies, as shown in Fig. A.4. The resulting expression for C_s is somewhat more complex than for the low-frequency case, and we do not attempt to provide a derivation here. Exact expressions for the non-degenerate case are given by Nicollian and Brews [8].

Thus, to the first approximation, C_i is independent of the applied bias and frequency (though see the following section on the frequency dispersion of the

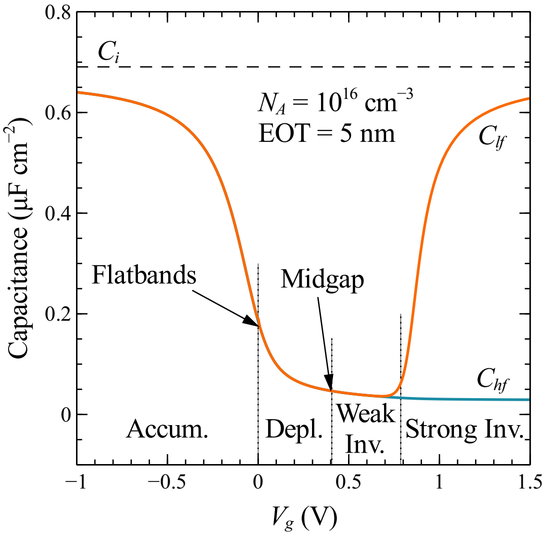

Figure A.4: Modelled ideal C–V curve (no interface states, $V_{fb} = 0\,\mathrm{V}$) of a silicon MIS capacitor at low and high frequencies. The voltage ranges corresponding to accumulation, depletion, weak inversion, and strong inversion are indicated.

permittivity), while C_s and C_{it} are strong functions of both. These different dependencies may be exploited in order to determine the value of each component.

A.2 Measurement corrections

Measured C–V data is subject to systematic errors and non-idealities that must be taken into account to allow an accurate analysis. This section details the correction procedure applied to measured C–V data in this work.

A.2.1 Parallel and series representations

The complex admittance measured by the LCR meter is a vector quantity with real and imaginary components that can be described using a number of equivalent representations. In general for C–V analysis it is most conveniently described as the parallel combination of one capacitive and one conductive component. We shall refer to the measured values of these components as C_{mp} and G_{mp} respectively. The corresponding equivalent circuit is shown in Fig. A.5a.

In some situations, however, it is useful to convert this representation into an equivalent series form, with capacitive and resistive components C_{ms} and R_{ms}, as shown in Fig. A.5b. The following set of relationships may be used to convert

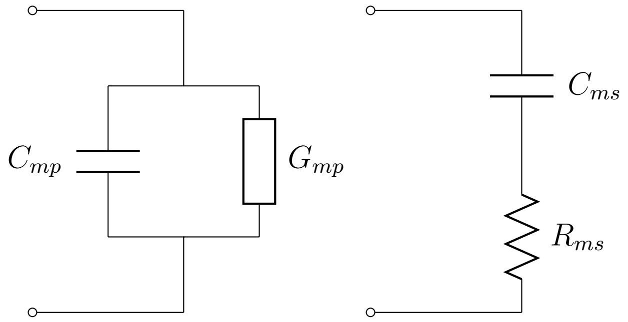

Figure A.5: a) Parallel and b) series equivalent circuits.

between the two equivalent forms.

$$C_{ms} = \frac{G_{mp}^2 + \omega^2 C_{mp}^2}{\omega^2 C_{mp}}\,, \tag{A.13}$$

$$R_{ms} = \frac{G_{mp}}{G_{mp}^2 + \omega^2 C_{mp}^2}\,, \tag{A.14}$$

$$C_{mp} = \frac{C_{ms}}{1 + (\omega R_{ms} C_{ms})^2}\,, \tag{A.15}$$

$$G_{mp} = \frac{1}{R_{ms} + (\omega^2 R_{ms} C_{ms}^2)^{-1}}\,. \tag{A.16}$$

A.2.2 Parasitic circuit elements

A real C–V measurement contains contributions from parasitic elements external to the MIS sample, arising from non-idealities in the measurement system, wires, probes, rear contact, and chuck. These may be described by additional elements in the equivalent circuit of the measurement, as shown in Fig. A.6. Parasitic elements which may be present include parallel capacitance and conductance due to the measurement setup (C_{pp} and G_{pp}), contact capacitance and resistance (C_c and R_c), and equivalent series resistance and inductance (R_s and L). C_{pp} and G_{pp} are corrected for by calibration of the capacitance meter, while C_c and R_c can be made negligible with proper ohmic contacting. This leaves R_s and L as generally non-negligible parasitic elements that must be evaluated and corrected for in careful measurements.

The equivalent series resistance R_s is usually due largely to the resistance of the semiconductor bulk between the rear contact and the edge of the space-charge region. The effect of R_s is to decrease C_{mp} and increase G_{mp} at high frequencies. R_s is most straightforwardly determined from the admittance in accumulation. In strong accumulation, the resistance contribution of interface states is shunted

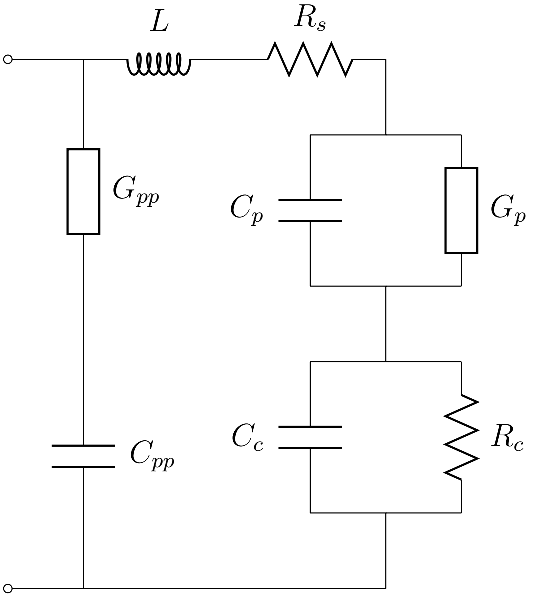

Figure A.6: a) Full equivalent circuit corresponding to the C–V measurement, including parasitic elements of the measurement system.

by the large semiconductor capacitance, and $R_s = R_{ms}$, where R_{ms} may be determined from (A.14) [8].

In addition to series resistance, series inductance L within the measurement circuit is often a significant source of error, acting to increase the measured capacitance at high frequencies. Like R_s, L is most easily determined in accumulation, where the impedance of the device itself is minimised. Unlike R_s however, L cannot be determined from measurements at a single frequency, since L appears in series with the device capacitance. Instead, measurements at two or more frequencies must be used to distinguish the inductive and capacitive components through their different frequency dependence.

Fig. A.7 shows an example of the determination of L by this method. C_{ms} is measured as a function of frequency in accumulation, and L is determined by fitting the measured capacitance with an equivalent circuit model including a frequency-dependent capacitance (see the later part of this section on the frequency dispersion of the permittivity) in series with an inductance. For the measurement system used in this work, L was found to be a function of the capacitance of the device under test. This dependence was assessed by evaluating L for capacitor test structures with nominal capacitances ranging from 47 to 1000 pF, in the same way as shown in Fig. A.7. The results are plotted in Fig. A.8 as a function of C_{ms}^{-1}. It was found that L possessed a linear dependence on C_{ms}^{-1},

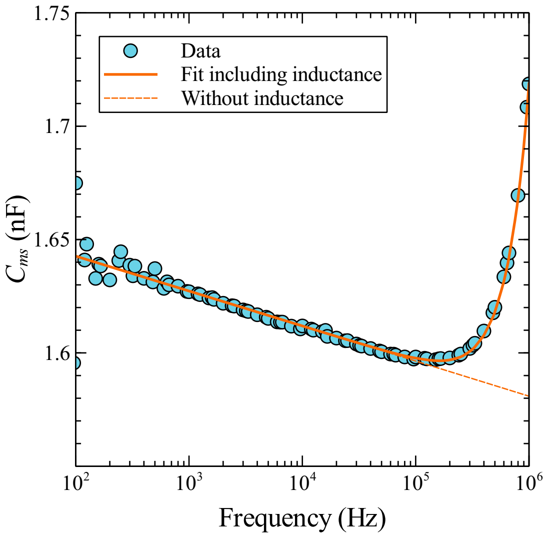

Figure A.7: Experimental C_{ms} vs frequency f for an n-type Al_2O_3 MIS sample in accumulation. Fits using an equivalent circuit model with and without the inclusion of series inductance are also shown. The linear slope of C_{ms} with $\log f$ at lower frequencies is due to frequency dispersion of the insulator permittivity. At higher frequencies, C_{ms} increases sharply due to inductance.

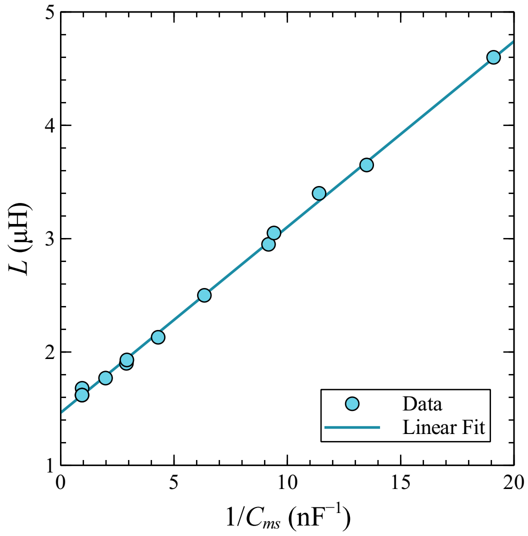

Figure A.8: Equivalent series inductance L vs $1/C_{ms}$ for capacitor test structures with a range of nominal capacitances, measured by the system used in this work.

given by

$$L = a + bC_{ms}^{-1}\,, \tag{A.17}$$

where $a = 1.46\,\mu\mathrm{H}$ and $b = 1.65 \times 10^{-16}\,\mathrm{F\,H}$.[1] Rather than assess L in each individual case, this empirical relationship was subsequently used to determine L for samples measured with this system.

The measured admittance is most straightforwardly corrected for equivalent series resistance and inductance by first converting to its series form via (A.13) and (A.14). Corrected series resistance and capacitance R'_{ms} and C'_{ms} may then be calculated from

$$R'_{ms} = R_{ms} - R_s\,, \tag{A.18}$$

and

$$\frac{1}{C'_{ms}} = \frac{1}{C_{ms}} + \omega^2 L\,. \tag{A.19}$$

Corrected parallel capacitance C'_{mp}, and conductance G'_{mp}, may subsequently be calculated from C'_{ms} and R'_{ms} via (A.15) and (A.16). These values are those used in subsequent analysis.

A.2.3 Quasi-static capacitance correction

While the low-frequency capacitance is not subject to the same parasitic effects as the high-frequency measurement, it can suffer from other sources of error. Because of the practical difficulties in performing true low-frequency AC capacitance measurements,[2] the "low-frequency" capacitance is instead commonly measured using the linear voltage-ramp method (a so-called "quasi-static" capacitance[3]) [267]. In this method, the capacitance is calculated from the displacement current I_d that flows in response to a linear voltage sweep with sweep rate dV_g/dt, using the relationship $C = I_d(dV_g/dt)^{-1}$. However, besides the displacement current, additional contributions to the measured current may be present due either to leakage current between the semiconductor and the gate, or to uncompensated background current within the measurement system. These currents may be distinguished from the displacement current by the fact that they are independent

---

[1] We note that the values of a and b are likely to depend on the details of the measurement setup, and would therefore need to be newly determined if significant changes were made to this setup.

[2] It should be noted that "low-frequency" is defined relative to the response of the interface states and the semiconductor minority carriers. At low-frequency these should be in thermal equilibrium with the surface potential over the full C–V curve. This condition is usually not achieved at the low-frequency limit of typical AC capacitance meters at room temperature.

[3] The term "quasi-static" is generally used elsewhere in this work when referring to low-frequency C–V measurements performed by the voltage-ramp method.

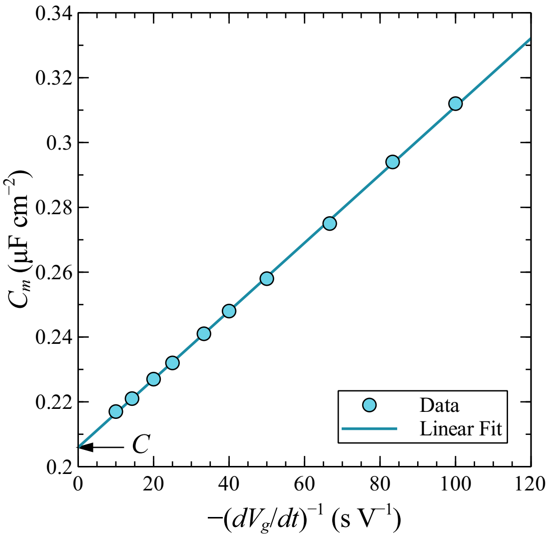

Figure A.9: Quasi-static capacitance measured for an Al_2O_3 MIS capacitor in accumulation, as a function of the inverse voltage sweep rate. The corrected device capacitance is found from the intercept of the linear fit at $(dV_g/dt)^{-1} = 0$.

of the sweep rate, and thus constitute a static current I_s. In the presence of such currents the measured capacitance C_m may be expressed as [268], [269]

$$C_m = C + I_s(dV_g/dt)^{-1} \,. \tag{A.20}$$

Equation (A.20) implies that the corrected capacitance C may be determined from measurements at two or more different sweep rates. Fig. A.9 shows this graphically by plotting experimentally determined C_m as a function of inverse sweep rate for a p-type Al_2O_3 MIS capacitor in accumulation. As expected from (A.20), C_m shows a linear dependence on $(dV_g/dt)^{-1}$, with a slope equal to I_s (in this particular case I_s can be shown to be due to the measurement system rather than to leakage current). The corrected device capacitance C is given by the intercept at $(dV_g/dt)^{-1} = 0$.

In general, measurements at two different sweep rates are sufficient to correct the quasi-static capacitance for static current contributions via (A.20).[4] Fig. A.10 shows examples of such a correction applied to experimental quasi-static C–V data. This procedure is routinely applied to C–V measurements presented in this work.

---

[4] Alternatively, I_s may also be determined by separate current–voltage measurements.

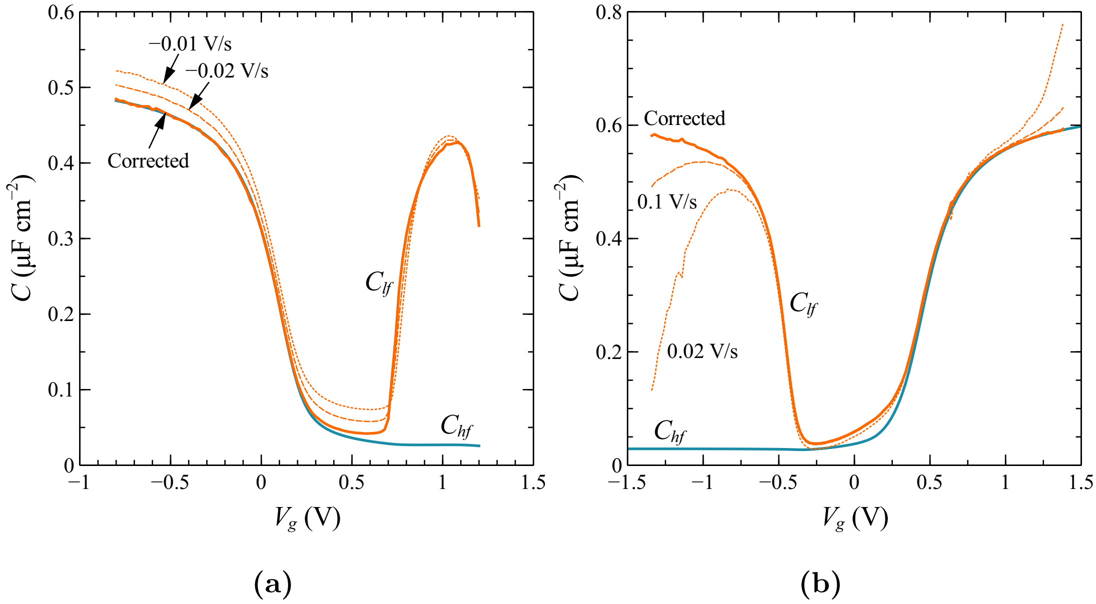

(a) **(b)**

Figure A.10: Experimental examples of the use of quasi-static C–V measurements at different sweep rates to correct for the effects of a) non-zeroed background current within the measurement system, and b) leakage current through the dielectric.

A.2.4 Permittivity frequency dispersion

In conventional C–V analysis it is implicitly assumed that C_i is independent of the measurement frequency, so that high- and low-frequency (or quasi-static) C–V measurements may be directly compared. In fact, the insulator permittivity is usually significantly frequency-dependent in the frequency range of the measurement, due to broad frequency dispersion of the (dipolar) dielectric response. This may readily be observed by measuring the accumulation capacitance as a function of frequency, as shown in Fig. A.7. Such frequency dispersion of the permittivity is a general feature of dielectric materials [270], and is well-attested for Al_2O_3 [16], [20], [271]. As a consequence, the accumulation capacitance measured at low frequencies or under quasi-static conditions is expected to be greater than that measured at high frequencies.[5]

Therefore, in comparing measurements made at high and low frequencies, we need to take into account that C_i is frequency-dependent. The simplest way of doing this is to adjust one or other measurement for the difference in C_i. For C–V analysis, we are primarily interested in the static (zero frequency) permittivity,

---

[5] While this is indeed commonly observed in experimental data within the literature, it is typically attributed to measurement error when it is noted at all.

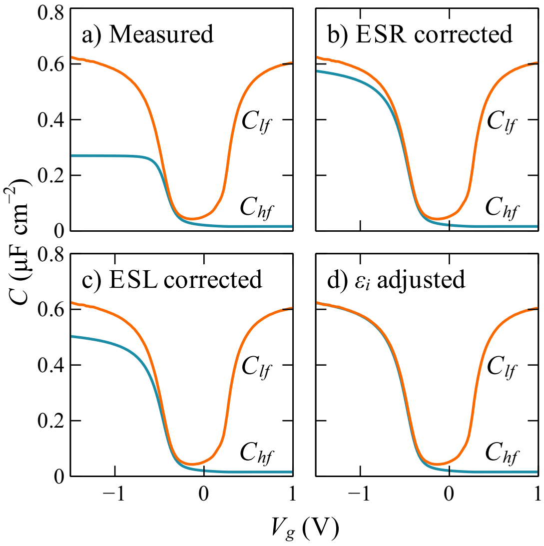

Figure A.11: Example of correction procedure applied to experimental high-frequency (1 MHz) capacitance. The measured parallel capacitance is shown a) without corrections, b) after correction for equivalent series resistance and c) inductance, and d) after adjusting for the frequency dispersion of the insulator permittivity via (A.21).

since this is the value which is relevant for the determination of the insulator fixed charge Q_f from the flatband voltage shift. This value is most closely approached under the conditions of the low-frequency or quasi-static capacitance measurement. Therefore we choose to calculate an adjusted high-frequency capacitance C'_{hf} according to

$$C'_{hf} = \left(C_{hf}^{-1} + C_{i,lf}^{-1} - C_{i,hf}^{-1}\right)^{-1} , \tag{A.21}$$

where $C_{i,hf}$ and $C_{i,lf}$ are the insulator capacitances at high and low frequencies respectively. The value of $C_{i,lf}^{-1} - C_{i,hf}^{-1}$ in (A.21) is chosen such that $C'_{hf} = C_{lf}$ in strong accumulation. Fig. A.11 shows an example of such an adjustment applied to experimental data.

A.3 Parameter extraction

Having corrected the experimental data for measurement errors and inconsistencies, we next wish to analyse it in order to extract various physical parameters of interest. These include the insulator capacitance, dopant concentration, flatband voltage (and by extension, the insulator charge), and the interface state density. This section describes the procedure used to extract these parameters in this

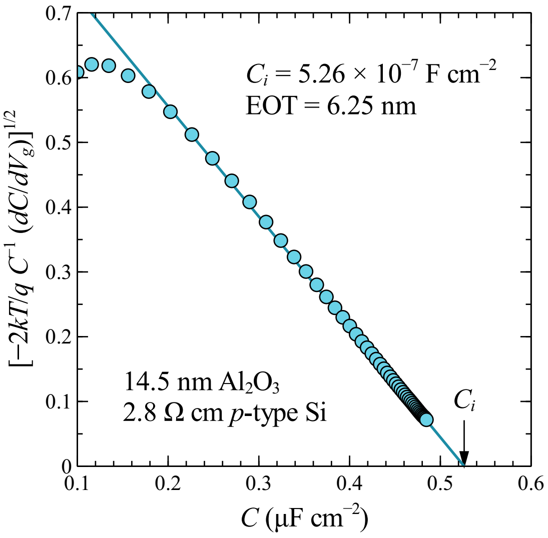

Figure A.12: Example of C_i extraction from experimental C–V data via Equation (A.22).

work.

A.3.1 Insulator capacitance

In the expression for the high-frequency MIS capacitance (Equation (A.8)), the insulator capacitance C_i appears in series with the semiconductor capacitance C_s. In order to extract C_i it is therefore necessary to make some assumption about C_s. Most commonly, it is assumed that $C_s \gg C_i$ in strong accumulation, so that C_i is simply given by the maximum measured capacitance in accumulation. This approximation is commonly used because of its simplicity, and is reasonable for thicker dielectrics ($\gtrapprox$ 100 nm), for which C_i is small. However, it becomes an increasingly poor approximation as insulator thickness is decreased, especially for high-κ materials.

A number of more sophisticated approximations have been proposed for extraction of C_i [272]–[277]. In this work we use that of McNutt and Sah [273], as extended by Walstra and Sah [275]. These authors derived the following expression for C_i based on the Boltzmann approximation for the carrier statistics in strong accumulation:

$$C_i = C\left[1 - \left(-2\frac{kT}{q}C^{-1}\frac{dC}{dV_g}\right)^{1/2}\right]^{-1}. \tag{A.22}$$

Equation (A.22) implies that a plot of $(-2kT/qC^{-1}(dC/dV_g))^{1/2}$ versus C in non-

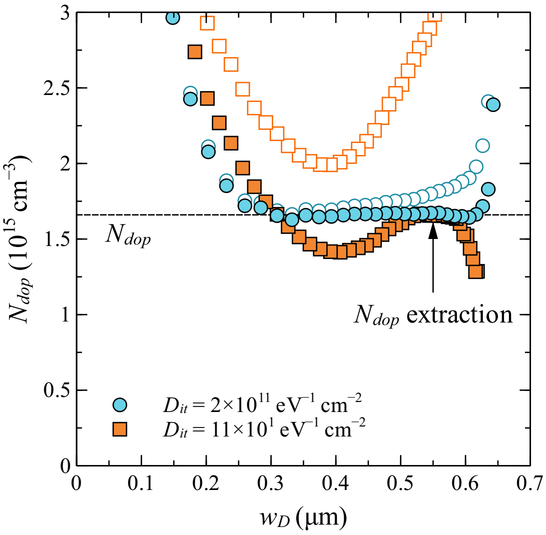

Figure A.13: Experimental N_{dop} profiles calculated using Equations (A.23) and (A.24). Data are shown for two samples processed on the same p-type substrate with different Al_2O_3 films, distinguished by the value of D_{it} at midgap. Closed (open) symbols show N_{dop} with (without) correction for stretch-out due to interface states.

degenerate strong accumulation will have a slope of $-C_i^{-1}$ and an intercept of C_i at $dC/dV_g = 0$. In practice, the value derived from the intercept is significantly less sensitive to the assumed carrier statistics, and is therefore preferred. Fig. A.12 shows an experimental example of such a plot, together with the fit used to extract C_i. For this sample, use of (A.22) to determine C_i results in a value 8 % higher than the maximum measured capacitance. The relative difference increases as film thickness is reduced. Equation (A.22) is still an approximation, because it is based on Boltzmann statistics, and hence neglects degeneracy and surface quantisation effects. Because of this, it is still expected to underestimate C_i, though to a significantly lesser extent than when C_i is taken as equal to the maximum measured capacitance.

A.3.2 Dopant concentration

The dopant concentration N_{dop} is most accurately determined from the slope of the capacitance in depletion, according to [8]

$$N_{dop} = 2\left[q\epsilon_s A^2 \frac{d}{dV_g}\left(\frac{1}{C_{hf}^2}\right)\right]^{-1}\left(\frac{1 - C_{lf}/C_i}{1 - C_{hf}/C_i}\right), \tag{A.23}$$

where the latter term accounts for voltage stretch-out due to interface states. The corresponding depletion layer width w_D is given by

$$w_D = \epsilon_s A(C_{hf}^{-1} - C_i^{-1})\,. \tag{A.24}$$

Using (A.23) and (A.24), N_{dop} may be plotted as a function of distance from the semiconductor surface.

Fig. A.13 shows N_{dop} vs w_D calculated in this way for samples with two different Al_2O_3 films fabricated on the same $8.2\,\Omega\,\mathrm{cm}$ p-type substrate. The apparent rise of N_{dop} near the surface is due to the failure of the depletion approximation—which underlies Equations (A.23) and (A.24)—for small departures from flatbands [8]. The subsequent dip in N_{dop}, visible most prominently for the sample with higher D_{it}, is due to the distortion of the 1 MHz high-frequency capacitance by interface state response near flatbands [8]. Its magnitude thus depends on D_{it}. N_{dop} should be extracted from the flat part of the profile following the dip. Fig. A.13 also shows that neglecting the interface state correction term in (A.23) results in significant error in the apparent N_{dop}, especially as D_{it} increases.

A.3.3 Flatband voltage and charge

A widely used method of determining V_{fb} is to calculate the theoretical capacitance at flatbands from C_i and N_{dop} using (A.8) and (A.12), and then to find the voltage corresponding to this capacitance on the experimental high-frequency C–V curve. This method is commonly used because of its simplicity. However, it is subject to systematic error due to the failure of the high-frequency assumption at flatbands for typical measurement frequencies. That is, interface state response at flatbands is non-zero, and $C_{it} > 0$. This results in systematic over(under)estimation of V_{fb} for p-type (n-type) substrates. This error increases with increasing D_{it}.

As proposed by [8], a better point of comparison is the capacitance in depletion, where interface state response is slower, and the assumption of high-frequency conditions is more usually valid. The most straightforward way to make this comparison is to calculate a gate voltage V_{g0} corrected for stretch-out due to interface states

$$V_{g0} = \int_{V_{fb}}^{V_g} \frac{C_i + C_s}{C_i + C_s + C_{it}}\, dV\,. \tag{A.25}$$

We begin by calculating V_{g0} from (A.25) making an arbitrary initial guess for V_{fb}. By plotting $1/C^2$ vs V_{g0} calculated in this way, and an ideal $1/C^2$ vs V_{g0}

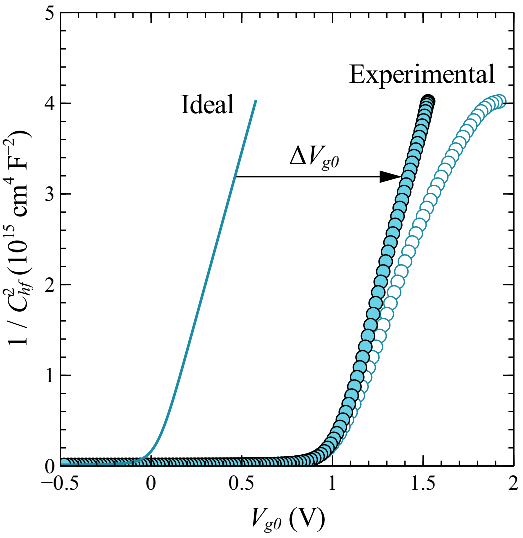

Figure A.14: Example of experimental determination of ΔV_{g0} using (A.25). Closed (open) symbols show experimental data plotted against V_{g0} (V_g), where the latter is uncorrected for stretch-out due to interface states.

calculated from (A.2), (A.8), and (A.12), with D_{it}, Q_f, and $W_{ms} = 0$, we should obtain two parallel linear curves in depletion, with a slope given by $2(q\epsilon_s N_{dop})^{-1}$. We label the voltage shift of the measured plot relative to the ideal plot ΔV_{g0}. V_{fb} is then found as the value of V_g for which V_{g0} calculated from (A.25) is equal to ΔV_{g0}. Fig. A.14 shows an experimental example of the determination of ΔV_{g0} in this manner.

To make use of (A.25) to determine V_{fb}, we must know C_{it} as a function of gate voltage. The formulation given by [8] for V_{g0} uses C_{it} derived from the combined high–low frequency capacitance method [278]. This has the advantage of allowing an explicit determination of V_{g0}, since D_{it} determined by this method is independent of V_{fb}. However, it results in systematic error in V_{fb}, due to the fact that D_{it} near flatbands is systematically underestimated by this method. In this work, we instead use D_{it} calculated from (A.29) for the purpose of determining (A.25). Since D_{it} from (A.29) depends on V_{fb}, this approach requires an iterative solution, but it avoids systematic error in V_{fb}.

From (A.3), V_{fb} is related to the insulator fixed charge Q_f and interface state trapped charge Q_{it} by

$$V_{fb} = \frac{(1 + x_c/t_i)Q_f + Q_{it}}{C_i/A} + W_{ms}\,. \tag{A.26}$$

Assuming $x_c = 0$ (i.e. Q_f is located at the semiconductor–dielectric interface), we may write

$$Q_{tot} = Q_f + Q_{it} = \frac{C_i}{A}(V_{fb} - W_{ms})\,. \tag{A.27}$$

Given V_{fb}, Equation (A.27) may thus be used to assess the sum of Q_f and Q_{it}, designated Q_{tot}. When Q_{it} is negligible (e.g. for samples with low D_{it}), $Q_{tot} \approx Q_f$.

The metal–semiconductor work-function difference W_{ms} is given by

$$W_{ms} = \phi_m - (\phi_s - \phi_b)\,, \tag{A.28}$$

where ϕ_m and ϕ_s are the metal and semiconductor work-functions (the latter defined with respect to E_i), and ϕ_b is the semiconductor bulk potential which is determined by the dopant concentration. The values of ϕ_m and ϕ_s used in this work are those recommended by Kawano [212] of 4.23 V for Al, 4.71 V for intrinsic $\langle 100\rangle$ Si, and 4.79 V for intrinsic $\langle 111\rangle$ Si.

A.3.4 Interface state density

From (A.7) and (A.10), D_{it} may be related to the low-frequency (quasi-static) capacitance C_{lf} by [152]

$$qAD_{it}(\psi_s) = C_{it} = (C_{lf}^{-1} - C_i^{-1})^{-1} - C_s(\psi_s)\,. \tag{A.29}$$

C_s in (A.29) may be calculated using (A.12), following determination of $\psi_s(V_g)$. The latter may be calculated from the low-frequency C–V curve via [152]

$$\psi_s(V_g) = \int_{V_{fb}}^{V_g} \left(1 - \frac{C_{lf}}{C_i}\right)\, dV\,. \tag{A.30}$$

Alternatively, C_s may be determined directly from the difference between C_{lf} and C_{hf}. Combining (A.8) with (A.29) leads to [278]

$$qAD_{it}(\psi_s) = C_{it} = (C_{lf}^{-1} - C_i^{-1})^{-1} - (C_{hf}^{-1} - C_i^{-1})^{-1}\,. \tag{A.31}$$

This has the advantage of avoiding the need to calculate C_s theoretically. However the use of (A.31) results in systematic underestimation of D_{it} near flatbands due to non-zero interface state response at practical measurement frequencies [8]. D_{it} determined by (A.29) is more accurate in this range.

D_{it} can also be calculated from the voltage stretch-out of the high-frequency C–V curve as described by Terman [279]. However, this method is also subject to significant error near flatbands due to non-zero interface state response, and additionally requires accurate knowledge of the dopant concentration, which cannot be determined reliably from C_{hf} alone when interface states are present [8]. Consequently, the use of (A.29) or even (A.31) to determine D_{it} is preferable. The former is used in this thesis.

A.3.5 General procedure

The general procedure followed in this work for parameter extraction from corrected C–V data is as follows:

1. C_i is determined from (A.22).
2. N_{dop} is determined from (A.23).
3. An initial guess value for V_{fb} is determined using the theoretical flatband capacitance calculated from (A.8) and (A.12).
4. $\psi_s(V_g)$ is determined from (A.30).
5. $D_{it}(\psi_s)$ is determined from (A.29).
6. V_{fb} is determined from (A.25).
7. Steps 4–6 are iterated to determine V_{fb} and $D_{it}(\psi_s)$ self-consistently.
8. Q_{tot} is evaluated from V_{fb} and C_i via (A.27).

Appendix B

The Conductance Method

The C–V method (Appendix A) may be used to evaluate the energetic distribution of interface states, but provides only limited information concerning their capture cross-sections, which determine their effectiveness as recombination centres. For this purpose, other, related techniques must be employed, such as DLTS (which examines the temperature dependence of time-domain capacitance transients), or measurements of the MIS parallel conductance as a function of frequency. The latter technique, generally referred to as the conductance method, is the subject of this appendix.

The use of the conductance method to determine interface state properties was pioneered by Nicollian and Goetzberger [143], [144], and subsequently employed by numerous authors, particularly for the characterisation of the Si–SiO$_2$ interface. A detailed exposition of the method, together with a comprehensive survey of work up to that date, was given by [8].

We first briefly describe the principles of the method, before presenting the relevant theory and equations. Following Cooper and Schwartz [148], we include minority carrier effects in our treatment of the equivalent circuit of the interface states. These are usually neglected, which unnecessarily limits the range of validity of the method. The derivation of the equations closely follows that of [148], except that here full expressions for all of the elements of the equivalent circuit are given explicitly rather than simply implied.

B.1 Principles

The principle of the conductance method is based on the energy loss that occurs when interface state capture and emission occurs out of phase with an AC variation of the surface Fermi level. At low frequencies, the interface states are able to change their occupancy in response to Fermi-level variations in order to maintain equilibrium, and no energy loss occurs. At very high frequencies, Fermi-level variations occur too quickly for the interface states to follow at all, so that energy loss is again zero. However, at intermediate frequencies, interface state response occurs out of phase with the applied signal, leading to energy loss as electrons transition from higher to lower energy states.

This energy loss manifests as an increase of the small-signal parallel conductance G_p of the MIS capacitor. The component of G_p due to the interface state branch of the MIS equivalent circuit, designated $\langle G_p \rangle$, is given by

$$\frac{\langle G_p \rangle}{\omega} = \frac{\omega C_i^2 G_p}{G_p^2 + \omega^2 (C_i - C_p)^2} \, . \tag{B.1}$$

When plotted as $\langle G_p \rangle / \omega$ vs frequency on a log scale, this contribution forms a peaked function with a peak frequency corresponding to the time constant for majority carrier capture, and an integrated area proportional to the interface state density. The peak width is broadened relative to that expected from single-time-constant behaviour due to short-range statistical fluctuations of the surface potential, described by the standard deviation of surface potential σ_s. Minority carrier contributions alter the shape of the peak at lower frequencies.

Parameter extraction requires fitting such experimental $\langle G_p \rangle / \omega$ data over a range of frequencies with a numerical model. The following section describes the equivalent circuit model used for this purpose.

B.2 Equivalent circuit

The small-signal equivalent circuit of the MIS capacitor including an energetic distribution of interface states is shown in Fig. B.1. Each state may exchange charge with the valence and conduction bands via capture resistances R_{ps} and R_{ns} for holes and electrons, and may store charge on a capacitance C_{it} connected to the displacement current line of the semiconductor. C_I and C_D are the capacitances of the inversion layer and depletion region respectively. The values of R_{ps}, R_{ns}, and C_{it} are given by

$$R_{ps} = \left(\frac{q}{kT} q A D_{it} f_t \sigma_p v_{th} p_s \right)^{-1} \, , \tag{B.2}$$

$$R_{ns} = \left(\frac{q}{kT} q A D_{it} (1 - f_t) \sigma_n v_{th} n_s \right)^{-1} \, , \tag{B.3}$$

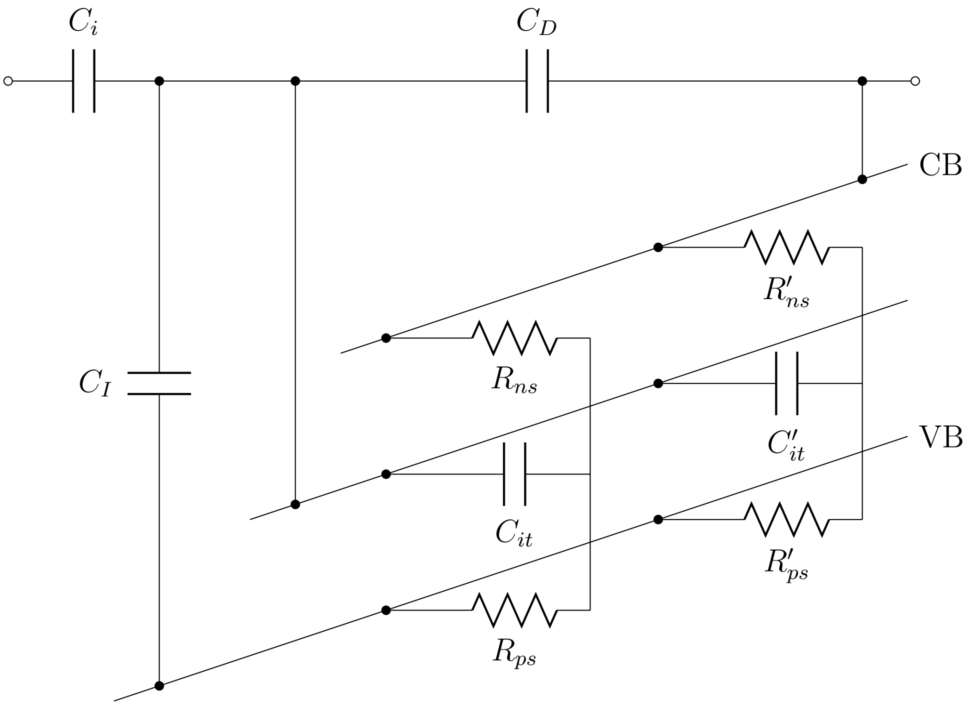

Figure B.1: Equivalent circuit of the (n-type) MIS capacitor with a distribution of interface states throughout the semiconductor bandgap (in this case two states are shown, but an arbitrary number may be present).

$$C_{it} = \frac{q}{kT} qAD_{it} f_t(1 - f_t)\,, \tag{B.4}$$

where

$$f_t = \left(1 + \exp\left(\frac{E_t - E_F}{kT}\right)\right)^{-1} \tag{B.5}$$

is the Fermi occupation function for interface states of energy E_t.

By performing a Y-Δ transformation, the equivalent circuit of Fig. B.1 becomes a parallel network of lumped admittance elements Y_{dp}, Y_{dn}, and Y_{pn} as shown in Fig. B.2. These elements are given by

$$Y_{dp} = \frac{j\omega R_{ns} C_{it}}{R_{ns} + R_{ps} + j\omega R_{ns} R_{ps} C_{it}}\,, \tag{B.6}$$

$$Y_{dn} = \frac{j\omega R_{ps} C_{it}}{R_{ns} + R_{ps} + j\omega R_{ns} R_{ps} C_{it}}\,, \tag{B.7}$$

$$Y_{pn} = \frac{1}{R_{ns} + R_{ps} + j\omega R_{ns} R_{ps} C_{it}}\,. \tag{B.8}$$

The total lumped admittance between each node may then simply be calculated as the sum of the individual Y_{dp}, Y_{dn}, and Y_{pn} elements (i.e. $Y_{dp} + Y'_{dp} + Y''_{dp} + \ldots$).

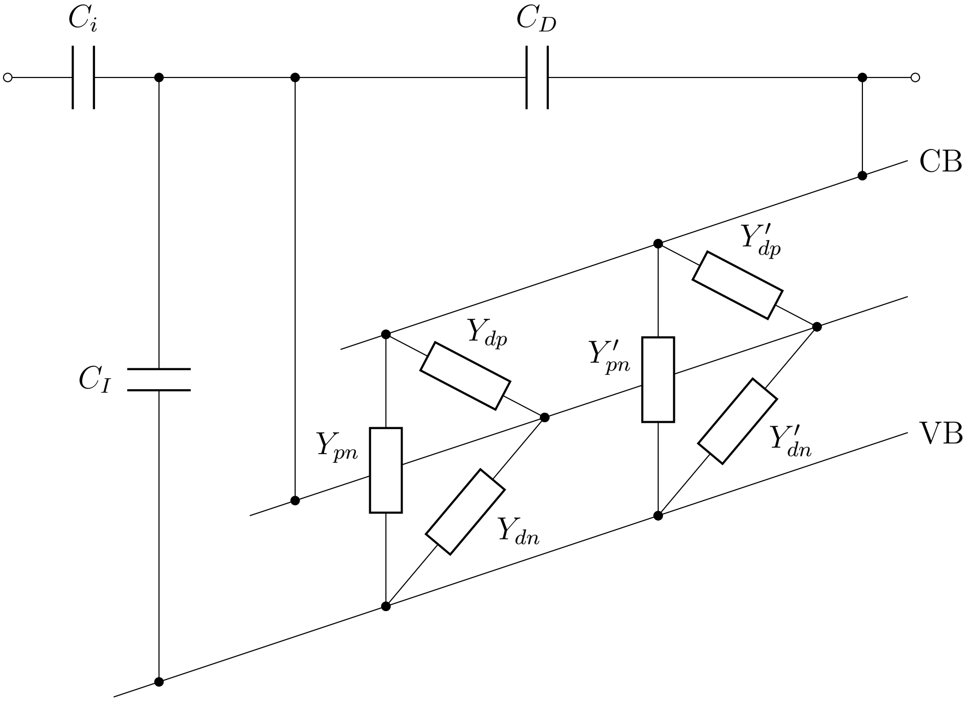

Figure B.2: Parallel equivalent circuit of the (n-type) MIS capacitor following a Y-Δ transformation.

Because each admittance depends both on the interface state energy and on the surface carrier concentration (which varies locally due to surface potential fluctuations), this involves a double integration over both bandgap energy and surface potential, where the latter integral is weighted by the surface potential probability density function $P(\psi_s)$, where

$$P(\psi_s) = (2\pi\sigma_s^2)^{-1/2} \exp\left[-(kT/q)^{-2}\frac{(\psi_s - \bar{\psi}_s)^2}{2\sigma_s^2}\right] , \tag{B.9}$$

$\bar{\psi}_s$ is the mean surface potential, and σ_s^2 is the variance of band bending in units of kT/q. Writing the real and imaginary parts of these admittances separately, we have

$$\frac{G_{dp}}{\omega} = \int_{-\infty}^{\infty}\int_{E_v}^{E_c} \frac{\omega R_{ps}C_{it}}{(1 + R_{ps}/R_{ns})^2 + (\omega R_{ps}C_{it})^2} C_{it}P(\psi_s)\, dE_t\, d\psi_s\, , \tag{B.10}$$

$$C_{dp} = \int_{-\infty}^{\infty}\int_{E_v}^{E_c} \frac{1 + R_{ps}/R_{ns}}{(1 + R_{ps}/R_{ns})^2 + (\omega R_{ps}C_{it})^2} C_{it}P(\psi_s)\, dE_t\, d\psi_s\, , \tag{B.11}$$

$$\frac{G_{dn}}{\omega} = \int_{-\infty}^{\infty}\int_{E_v}^{E_c} \frac{\omega R_{ns}C_{it}}{(1 + R_{ns}/R_{ps})^2 + (\omega R_{ns}C_{it})^2} C_{it}P(\psi_s)\, dE_t\, d\psi_s\, , \tag{B.12}$$

$$C_{dn} = \int_{-\infty}^{\infty} \int_{E_v}^{E_c} \frac{1 + R_{ns}/R_{ps}}{(1 + R_{ns}/R_{ps})^2 + (\omega R_{ns} C_{it})^2} C_{it} P(\psi_s) \, dE_t \, d\psi_s \, , \tag{B.13}$$

$$G_{pn} = \int_{-\infty}^{\infty} \int_{E_v}^{E_c} \frac{R_{ns} + R_{ps}}{(R_{ns} + R_{ps})^2 + (\omega R_{ns} R_{ps} C_{it})^2} P(\psi_s) \, dE_t \, d\psi_s \, , \tag{B.14}$$

$$C_{pn} = \int_{-\infty}^{\infty} \int_{E_v}^{E_c} \frac{R_{ns} R_{ps} C_{it}}{(R_{ns} + R_{ps})^2 + (\omega R_{ns} R_{ps} C_{it})^2} P(\psi_s) \, dE_t \, d\psi_s \, . \tag{B.15}$$

Finally, the total semiconductor admittance including the interface states is given (for n-type doping) by

$$Y_s = j\omega C_D + Y_{dn} + \left[(j\omega C_I + Y_{dp})^{-1} + Y_{pn}^{-1} \right]^{-1} \, . \tag{B.16}$$

Solving for the real and imaginary components gives

$$\langle G_p \rangle = G_{dn} + \frac{\begin{array}{c}(G_{dp} + G_{pn}) \left[G_{dp} G_{pn} - \omega^2 C_{pn} (C_I + C_{dp}) \right] \\ + \, \omega^2 (C_I + C_{dp} + C_{pn}) \left[G_{dp} C_{pn} + G_{pn} (C_I + C_{dp}) \right]\end{array}}{(G_{dp} + G_{pn})^2 + \omega^2 (C_I + C_{dp} + C_{pn})^2} \, , \tag{B.17}$$

and

$$\langle C_p \rangle = C_D + C_{dn} + \frac{\begin{array}{c}(G_{dp} + G_{pn}) \left[G_{dp} C_{pn} + G_{pn} (C_I + C_{dp}) \right] \\ - \, (C_I + C_{dp} + C_{pn}) \left[G_{dp} G_{pn} - \omega^2 C_{pn} (C_I + C_{dp}) \right]\end{array}}{(G_{dp} + G_{pn})^2 + \omega^2 (C_I + C_{dp} + C_{pn})^2} \, . \tag{B.18}$$

Analogous expressions apply for the case of p-type doping.

In order to determine D_{it}, σ_p, σ_n, and σ_s, by the conductance method, these parameters must be adjusted to provide a good fit between $\langle G_p \rangle / \omega$ calculated from Equation (B.17), and experimental data measured over a range of frequencies. In this work, automated least-squares fitting of $\langle G_p \rangle / \omega$ data was performed using the Levenberg–Marquardt algorithm. Interface states at different energies are probed by performing measurements over a range of gate biases in depletion and weak inversion. C_I is generally negligible at these biases and thus may be neglected when calculating $\langle G_p \rangle / \omega$ from (B.17). The surface potential ψ_s must be determined independently as a function of gate bias using C–V measurements, as described in Appendix A. This may then be used to calculate p_s and n_s in (B.2) and (B.3).

B.3 General procedure

The general procedure followed in this work for parameter extraction from conductance measurements is as follows:

1. High- and low-frequency C–V curves are measured, and C_i, N_{dop}, and $\psi_s(V_g)$ are determined as described in Appendix A.

2. G_p and C_p are measured as a function of frequency at a bias in depletion or weak inversion (correcting for parasitic effects as described in Appendix A).

3. $\langle G_p \rangle / \omega$ vs ω is determined from (B.1).

4. A theoretical $\langle G_p \rangle / \omega$ vs ω curve is calculated from (B.17), using initial guess values for D_{it}, σ_p, σ_n, and σ_s.

5. D_{it}, σ_p, σ_n, and σ_s are determined by varying their values using a non-linear least-squares solver (Levenberg–Marquardt) in order to minimise the mean squared error between the measured and modelled $\langle G_p \rangle / \omega$ vs ω.

6. Steps 2–5 are repeated to determine D_{it}, σ_p, σ_n, and σ_s for a range of energies in the bandgap.

List of Publications

Significant parts of this thesis are based on work previously published in the following papers:

L. E. Black *et al.*, "Surface passivation of crystalline silicon by APCVD aluminium oxide," in *Proc. 26th European Photovoltaic Solar Energy Conf.*, Hamburg, Germany, 2011, pp. 1120–1124.

L. E. Black and K. R. McIntosh, "Surface passivation of c-Si by atmospheric pressure chemical vapor deposition of Al_2O_3," *Applied Physics Letters*, vol. 100, 202107, 2012.

L. E. Black and K. R. McIntosh, "Modeling recombination at the Si–Al_2O_3 interface," *IEEE Journal of Photovoltaics*, vol. 3, pp. 936–943, 2013.

L. E. Black *et al.*, "Safe and inexpensive Al_2O_3 deposited by APCVD with single-source precursor," in *Proc. 28th European Photovoltaic Solar Energy Conf.*, Paris, France, 2013, pp. 1068–1072.

L. E. Black *et al.*, "Thermal stability of silicon surface passivation by APCVD Al_2O_3," *Solar Energy Materials and Solar Cells*, vol. 120, Part A, pp. 339–345, 2014.

L. E. Black *et al.*, "Effect of boron concentration on recombination at the p-Si–Al_2O_3 interface," *Journal of Applied Physics*, vol. 115, 093707, 2014.

L. E. Black *et al.*, "The influence of orientation and morphology on the passivation of crystalline silicon surfaces by Al_2O_3," *Energy Procedia*, vol. 55, pp. 750–756, 2014.

Bibliography

[1] P. Lolgen, C. Leguijt, J. Eikelboom, R. Steeman, W. Sinke, L. Verhoef, P. Alkemade, and E. Algra, “Aluminium back-surface field doping profiles with surface recombination velocities below 200 cm/s,” in *Proc. 23rd IEEE Photovoltaic Specialists Conf.*, 1993, pp. 236–242.

[2] S. Narasimha, A. Rohatgi, and A. Weeber, “An optimized rapid aluminum back surface field technique for silicon solar cells,” *IEEE Transactions on Electron Devices*, vol. 46, pp. 1363–1370, 1999.

[3] S. Bowden, D. Kim, C. Honsberg, and A. Rohatgi, “Rapid thermal processing for front and rear contact passivation,” in *Proc. 29th IEEE Photovoltaic Specialists Conf.*, 2002, pp. 410–413.

[4] S. Peters, “Rapid thermal processing of crystalline silicon materials and solar cells,” PhD thesis, Universität Konstanz, 2004.

[5] R. Bock, J. Schmidt, and R. Brendel, “Effective passivation of highly aluminum-doped p-type silicon surfaces using amorphous silicon,” *Applied Physics Letters*, vol. 91, 112112, 2007.

[6] S. Gatz, K. Bothe, J. Müller, T. Dullweber, and R. Brendel, “Analysis of local Al-doped back surface fields for high efficiency screen-printed solar cells,” *Energy Procedia*, vol. 8, pp. 318–323, 2011.

[7] J. Müller, K. Bothe, S. Gatz, H. Plagwitz, G. Schubert, and R. Brendel, “Contact formation and recombination at screen-printed local aluminum-alloyed silicon solar cell base contacts,” *IEEE Trans. Electron Devices*, vol. 58, pp. 3239–3245, 2011.

[8] E. H. Nicollian and J. R. Brews, *MOS (Metal Oxide Semiconductor) Physics and Technology.* New York: John Wiley & Sons, 1982.

[9] E. H. Poindexter, “MOS interface states: Overview and physicochemical perspective,” *Semiconductor Science and Technology*, vol. 4, pp. 961–969, 1989.

[10] A. G. Aberle, S. Glunz, and W. Warta, "Impact of illumination level and oxide parameters on Shockley–Read–Hall recombination at the Si–SiO_2 interface," *Journal of Applied Physics*, vol. 71, pp. 4422–4431, 1992.

[11] S. W. Glunz, D. Biro, S. Rein, and W. Warta, "Field-effect passivation of the SiO_2–Si interface," *Journal of Applied Physics*, vol. 86, pp. 683–691, 1999.

[12] J. Schmidt and A. G. Aberle, "Carrier recombination at silicon–silicon nitride interfaces fabricated by plasma-enhanced chemical vapor deposition," *Journal of Applied Physics*, vol. 85, pp. 3626–3633, 1999.

[13] S. Dauwe, L. Mittelstädt, A. Metz, and R. Hezel, "Experimental evidence of parasitic shunting in silicon nitride rear surface passivated solar cells," *Progress in Photovoltaics*, vol. 10, pp. 271–278, 2002.

[14] M. J. Kerr, "Surface, emitter and bulk recombination in silicon and development of silicon nitride passivated solar cells," PhD thesis, The Australian National University, 2002.

[15] D. Macdonald and L. J. Geerligs, "Recombination activity of interstitial iron and other transition metal point defects in p- and n-type crystalline silicon," *Applied Physics Letters*, vol. 85, pp. 4061–4063, 2004.

[16] J. A. Aboaf, "Deposition and properties of aluminum oxide obtained by pyrolytic decomposition of an aluminum alkoxide," *Journal of the Electrochemical Society*, vol. 114, pp. 948–952, 1967.

[17] A. Waxman and K. H. Zaininger, "Al_2O_3-silicon insulated gate field effect transistors," *Applied Physics Letters*, vol. 12, pp. 109–110, 1968.

[18] C. A. T. Salama, "RF sputtered aluminum oxide films on silicon," *Journal of the Electrochemical Society*, vol. 117, pp. 913–917, 1970.

[19] T. Tsujide, S. Nakanuma, and Y. Ikushima, "Properties of aluminum oxide obtained by hydrolysis of $AlCl_3$," *Journal of the Electrochemical Society*, vol. 117, pp. 703–708, 1970.

[20] M. T. Duffy and A. G. Revesz, "Interface properties of Si-(SiO_2)-Al_2O_3 structures," *Journal of the Electrochemical Society*, vol. 117, pp. 372–377, 1970.

[21] M. Duffy, J. Carnes, and D. Richman, "Dielectric and interface properties of pyrolytic aluminum oxide films on silicon substrates," *Metallurgical Transactions*, vol. 2, pp. 667–672, 1971.

[22] T. Tanaka and S. Iwauchi, "Interface characteristics of the reactively sputtered Al_2O_3-Si structure," *Japanese Journal of Applied Physics*, vol. 8, pp. 730–738, 1969.

[23] K. Jaeger and R. Hezel, "A novel thin silicon solar cell with Al_2O_3 as surface passivation," in *Proc. 18th IEEE Photovoltaic Specialists Conf.*, Las Vegas, USA, 1985, pp. 1752–1753.

[24] R. Hezel and K. Jaeger, "Low-temperature surface passivation of silicon for solar cells," *Journal of the Electrochemical Society*, vol. 136, pp. 518–523, 1989.

[25] G. Agostinelli, P. Vitanov, Z. Alexieva, A. Harizanova, H. F. W. Dekkers, S. De Wolf, and G. Beaucarne, "Surface passivation of silicon by means of negative charge dielectrics," in *Proc. 19th European Photovoltaic Solar Energy Conf.*, Paris, France, 2004, pp. 132–134.

[26] G. Agostinelli, A. Delabie, P. Vitanov, Z. Alexieva, H. F. W. Dekkers, S. D. Wolf, and G. Beaucarne, "Very low surface recombination velocities on p-type silicon wafers passivated with a dielectric with fixed negative charge," *Solar Energy Materials and Solar Cells*, vol. 90, pp. 3438–3443, 2006.

[27] B. Hoex, S. B. S. Heil, E. Langereis, M. C. M. v. d. Sanden, and W. M. M. Kessels, "Ultralow surface recombination of c-Si substrates passivated by plasma-assisted atomic layer deposited Al_2O_3," *Applied Physics Letters*, vol. 89, 042112, 2006.

[28] G. Dingemans and W. M. M. Kessels, "Status and prospects of Al_2O_3-based surface passivation schemes for silicon solar cells," *Journal of Vacuum Science and Technology A*, vol. 30, 040802, 2012.

[29] B. Hoex, J. Schmidt, R. Bock, P. P. Altermatt, M. C. M. v. d. Sanden, and W. M. M. Kessels, "Excellent passivation of highly doped p-type Si surfaces by the negative-charge-dielectric Al_2O_3," *Applied Physics Letters*, vol. 91, 112107, 2007.

[30] B. Hoex, M. C. M. v. d. Sanden, J. Schmidt, R. Brendel, and W. M. M. Kessels, "Surface passivation of phosphorous-diffused n+-type emitters by plasma-assisted atomic-layer deposited Al_2O_3," *Physica Status Solidi RRL*, vol. 6, pp. 4–6, 2012.

[31] A. Richter, S. W. Glunz, F. Werner, J. Schmidt, and A. Cuevas, "Improved quantitative description of Auger recombination in crystalline silicon," *Physical Review B*, vol. 86, 165202, 2012.

[32] L. E. Black, K. M. Provancha, and K. R. McIntosh, "Surface passivation of crystalline silicon by APCVD aluminium oxide," in *Proc. 26th European Photovoltaic Solar Energy Conf.*, Hamburg, Germany, 2011, pp. 1120–1124.

[33] L. E. Black and K. R. McIntosh, "Surface passivation of c-Si by atmospheric pressure chemical vapor deposition of Al_2O_3," *Applied Physics Letters*, vol. 100, 202107, 2012.

[34] S. Miyajima, J. Irikawa, A. Yamada, and M. Konagai, "Hydrogenated aluminum oxide films deposited by plasma enhanced chemical vapor deposition for passivation of p-type crystalline silicon," in *Proc. 23rd European Photovoltaic Solar Energy Conf.*, Valencia, Spain, 2008.

[35] P. Saint-Cast, D. Kania, M. Hofmann, J. Benick, J. Rentsch, and R. Preu, "Very low surface recombination velocity on p-type c-Si by high-rate plasma-deposited aluminum oxide," *Applied Physics Letters*, vol. 95, 151502, 2009.

[36] S. Miyajima, J. Irikawa, A. Yamada, and M. Konagai, "High quality aluminum oxide passivation layer for crystalline silicon solar cells deposited by parallel-plate plasma-enhanced chemical vapor deposition," *Applied Physics Express*, vol. 3, 012301, 2010.

[37] T.-T. Li and A. Cuevas, "Effective surface passivation of crystalline silicon by rf sputtered aluminum oxide," *Physica Status Solidi RRL*, vol. 3, pp. 160–162, 2009.

[38] X. Zhang and A. Cuevas, "Plasma hydrogenated, reactively sputtered aluminium oxide for silicon surface passivation," *Physica Status Solidi RRL*, vol. 7, pp. 619–622, 2013.

[39] M. Aguilar-Frutis, M. Garcia, and C. Falcony, "Optical and electrical properties of aluminum oxide films deposited by spray pyrolysis," *Applied Physics Letters*, vol. 72, pp. 1700–1702, 1998.

[40] M. Aguilar-Frutis, M. Garcia, C. Falcony, G. Plesch, and S. Jimenez-Sandoval, "A study of the dielectric characteristics of aluminum oxide thin films deposited by spray pyrolysis from $Al(acac)_3$," *Thin Solid Films*, vol. 389, pp. 200–206, 2001.

[41] J. Benick, A. Richter, A. Li, N. E. Grant, K. R. McIntosh, Y. Ren, K. J. Weber, M. Hermle, and S. W. Glunz, "Effect of a post-deposition anneal on Al_2O_3/Si interface properties," in *Proc. 35th IEEE Photovoltaic Specialists Conf.*, Honolulu, Hawaii, 2010, pp. 000 891–000 896.

[42] G. Dingemans, N. M. Terlinden, D. Pierreux, H. B. Profijt, M. C. M. v. d. Sanden, and W. M. M. Kessels, "Influence of the oxidant on the chemical and field-effect passivation of Si by ALD Al_2O_3," *Electrochemical and Solid State Letters*, vol. 14, H1–H4, 2011.

[43] F. Werner, B. Veith, D. Zielke, L. Kühnemund, C. Tegenkamp, M. Seibt, R. Brendel, and J. Schmidt, "Electronic and chemical properties of the c-Si/Al_2O_3 interface," *Journal of Applied Physics*, vol. 109, 113701, 2011.

[44] P. Saint-Cast, D. Kania, R. Heller, S. Kuehnhold, M. Hofmann, J. Rentsch, and R. Preu, "High-temperature stability of c-Si surface passivation by thick PECVD Al_2O_3 with and without hydrogenated capping layers," *Applied Surface Science*, vol. 258, pp. 8371–8376, 2012.

[45] D. Schuldis, A. Richter, J. Benick, and M. Hermle, "Influence of different post deposition treatments on the passivation quality and interface properties of thermal ALD Al_2O_3 capped by PECVD SiN_x," in *Proc. 27th European Photovoltaic Solar Energy Conf.*, 2012, pp. 1933–1937.

[46] B. Veith, T. Dullweber, M. Siebert, C. Kranz, F. Werner, N.-P. Harder, J. Schmidt, B. F. P. Roos, T. Dippell, and R. Brendel, "Comparison of ICP-AlO_x and ALD-Al_2O_3 layers for the rear surface passivation of c-Si solar cells," *Energy Procedia*, vol. 27, pp. 379–384, 2012.

[47] F. Werner, A. Cosceev, and J. Schmidt, "Interface recombination parameters of atomic-layer-deposited Al_2O_3 on crystalline silicon," *Journal of Applied Physics*, vol. 111, 073710, 2012.

[48] L. E. Black and K. R. McIntosh, "Modeling recombination at the Si–Al_2O_3 interface," *IEEE Journal of Photovoltaics*, vol. 3, pp. 936–943, 2013.

[49] W. Liang, K. J. Weber, D. Suh, S. P. Phang, J. Yu, A. K. McAuley, and B. R. Legg, "Surface passivation of boron-diffused p-type silicon surfaces with (100) and (111) orientations by ALD Al_2O_3 layers," *IEEE Journal of Photovoltaics*, vol. 3, pp. 678–683, 2013.

[50] L. E. Black, T. Allen, and K. R. McIntosh, "Safe and inexpensive Al_2O_3 deposited by APCVD with single-source precursor," in *Proc. 28th European Photovoltaic Solar Energy Conf.*, Paris, France, 2013, pp. 1068–1072.

[51] F. Werner and J. Schmidt, “Manipulating the negative fixed charge density at the c-Si/Al_2O_3 interface,” *Applied Physics Letters*, vol. 104, 091604, 2014.

[52] L. E. Black, T. Allen, K. R. McIntosh, and A. Cuevas, “Effect of boron concentration on recombination at the *p*-Si–Al_2O_3 interface,” *Journal of Applied Physics*, vol. 115, 093707, 2014.

[53] L. E. Black, T. Allen, A. Cuevas, K. R. McIntosh, B. Veith, and J. Schmidt, “Thermal stability of silicon surface passivation by APCVD Al_2O_3,” *Solar Energy Materials and Solar Cells*, vol. 120, Part A, pp. 339–345, 2014.

[54] P. Saint-Cast, Y.-H. Heo, E. Billot, P. Olwal, M. Hofmann, J. Rentsch, S. W. Glunz, and R. Preu, “Variation of the layer thickness to study the electrical property of PECVD Al_2O_3 / c-Si interface,” *Energy Procedia*, vol. 8, pp. 642–647, 2011.

[55] B. Hoex, J. J. H. Gielis, M. C. M. v. d. Sanden, and W. M. M. Kessels, “On the c-Si surface passivation mechanism by the negative-charge-dielectric Al_2O_3,” *Journal of Applied Physics*, vol. 104, 113703, 2008.

[56] M. M. Mandoc, M. L. C. Adams, G. Dingemans, N. M. Terlinden, M. C. M. v. d. Sanden, and W. M. M. Kessels, “Corona charging and optical second-harmonic generation studies of the field-effect passivation of c-Si by Al_2O_3 films,” in *Proc. 35th IEEE Photovoltaic Specialists Conf.*, Honolulu, Hawaii, 2010.

[57] P. Saint-Cast, A. Richter, E. Billot, M. Hofmann, J. Benick, J. Rentsch, R. Preu, and S. W. Glunz, “Very low surface recombination velocity of boron doped emitter passivated with plasma-enhanced chemical-vapor-deposited AlO_x layers,” *Thin Solid Films*, vol. 522, pp. 336–339, 2012.

[58] R. S. Johnson, G. Lucovsky, and I. Baumvol, “Physical and electrical properties of noncrystalline Al_2O_3 prepared by remote plasma enhanced chemical vapor deposition,” *Journal of Vacuum Science and Technology A*, vol. 19, pp. 1353–1360, 2001.

[59] N. M. Terlinden, G. Dingemans, M. C. M. v. d. Sanden, and W. M. M. Kessels, “Role of field-effect on c-Si surface passivation by ultrathin (2–20 nm) atomic layer deposited Al_2O_3,” *Applied Physics Letters*, vol. 96, 112101, 2010.

[60] K. R. McIntosh, L. E. Black, S. C. Baker-Finch, T. C. Kho, and Y. Y. Wan, "Determination of the magnitude and centroid of the charge in a thin-film insulator by CV and Kelvin probe measurements," *Energy Procedia*, vol. 15, pp. 162–170, 2012.

[61] G. Dingemans, R. Seguin, P. Engelhart, M. C. M. v. d. Sanden, and W. M. M. Kessels, "Silicon surface passivation by ultrathin Al_2O_3 films synthesized by thermal and plasma atomic layer deposition," *Physica Status Solidi RRL*, vol. 4, pp. 10–12, 2010.

[62] A. Richter, J. Benick, M. Hermle, and S. W. Glunz, "Excellent silicon surface passivation with 5 å thin ALD Al_2O_3 layers: Influence of different thermal post-deposition treatments," *Physica Status Solidi RRL*, vol. 5, pp. 202–204, 2011.

[63] J. M. Rafí, M. Zabala, O. Beldarrain, and F. Campabadal, "Deposition temperature and thermal annealing effects on the electrical characteristics of atomic layer deposited Al_2O_3 films on silicon," *Journal of the Electrochemical Society*, vol. 158, G108–G114, 2011.

[64] S. Bordihn, I. Kiesow, V. Mertens, P. Engelhart, J. W. MÅ¸ller, and W. M. M. Kessels, "Impact of the deposition and annealing temperature on the silicon surface passivation of ALD Al_2O_3 films," *Energy Procedia*, vol. 27, pp. 396–401, 2012.

[65] J. Benick, A. Richter, M. Hermle, and S. W. Glunz, "Thermal stability of the Al_2O_3 passivation on p-type silicon surfaces for solar cell applications," *Physica Status Solidi RRL*, vol. 3, pp. 233–235, 2009.

[66] G. Dingemans, P. Engelhart, R. Seguin, F. Einsele, B. Hoex, M. C. M. v. d. Sanden, and W. M. M. Kessels, "Stability of Al_2O_3 and Al_2O_3/a-SiN_x:H stacks for surface passivation of crystalline silicon," *Journal of Applied Physics*, vol. 106, 114907, 2009.

[67] B. Vermang, X. Loozen, C. Allebé, J. John, E. v. Kerschaver, J. Poortmans, and R. Mertens, "Characterization and implementation of thermal ALD Al_2O_3 as surface passivation for industrial Si solar cells," in *Proc. 24th European Photovoltaic Solar Energy Conf.*, Hamburg, Germany, 2009, pp. 1051–1054.

[68] J. Schmidt, B. Veith, and R. Brendel, "Effective surface passivation of crystalline silicon using ultrathin Al_2O_3 films and Al_2O_3/SiN_x stacks," *Physica Status Solidi RRL*, vol. 3, pp. 287–289, 2009.

[69] A. Richter, S. Henneck, J. Benick, M. Hörteis, M. Hermle, and S. W. Glunz, "Firing stable Al_2O_3/SiN_x layer stack passivation for the front side boron emitter of n-type silicon solar cells," in *Proc. 25th European Photovoltaic Solar Energy Conf.*, Valencia, Spain, 2010, pp. 1453–1459.

[70] B. Veith, F. Werner, D. Zielke, R. Brendel, and J. Schmidt, "Comparison of the thermal stability of single Al_2O_3 layers and Al_2O_3/SiN_x stacks for the surface passivation of silicon," *Energy Procedia*, vol. 8, pp. 307–312, 2011.

[71] B. Vermang, H. Goverde, A. Lorenz, A. Uruena, J. Das, P. Choulat, E. Cornagliotti, A. Rothschild, J. John, J. Poortmans, and R. Mertens, "On the blistering of Al_2O_3 passivation layers for Si solar cells," in *Proc. 26th European Photovoltaic Solar Energy Conf.*, Hamburg, Germany, 2011, pp. 1129–1131.

[72] B. Vermang, H. Goverde, A. Lorenz, A. Uruena, G. Vereecke, J. Meersschaut, E. Cornagliotti, A. Rothschild, J. John, J. Poortmans, and R. Mertens, "On the blistering of atomic layer deposited Al_2O_3 as Si surface passivation," in *Proc. 37th IEEE Photovoltaic Specialists Conf.*, Seattle, USA, 2011, pp. 3562–3567.

[73] L. Hennen, E. H. A. Granneman, and W. M. M. Kessels, "Analysis of blister formation in spatial ALD Al_2O_3 for silicon surface passivation," in *Proc. 38th IEEE Photovoltaic Specialists Conf.*, Austin, USA, 2012, pp. 1049–1054.

[74] S. Kühnhold, B. Kafle, L. Kroely, P. Saint-Cast, M. Hofmann, J. Rentsch, and R. Preu, "Impact of thermal treatment on PECVD Al_2O_3 passivation layers," *Energy Procedia*, vol. 27, pp. 273–279, 2012.

[75] W. Liang, K. J. Weber, and A. F. Thomson, "Effective SiN_x:H capping layers on 1-nm Al_2O_3 for p+ surface passivation," *IEEE Journal of Photovoltaics*, vol. 4, pp. 1405–1412, 2014.

[76] J. Benick, B. Hoex, M. C. M. v. d. Sanden, W. M. M. Kessels, O. Schultz, and S. W. Glunz, "High efficiency n-type Si solar cells on Al_2O_3-passivated boron emitters," *Applied Physics Letters*, vol. 92, 253504, 2008.

[77] J. Schmidt, A. Merkle, R. Bock, P. P. Altermatt, A. Cuevas, N.-P. Harder, B. Hoex, R. v. d. Sanden, E. Kessels, and R. Brendel, "Progress in the surface passivation of silicon solar cells," in *Proc. 23rd European Photovoltaic Solar Energy Conf.*, Valencia, Spain, 2008.

[78] J. Benick, B. Hoex, G. Dingemans, W. M. M. Kessels, A. Richter, M. Hermle, and S. W. Glunz, "High-efficiency n-type silicon solar cells with front side boron emitter," in *Proc. 24th European Photovoltaic Solar Energy Conf.*, Hamburg, Germany, 2009, pp. 863–870.

[79] P. Saint-Cast, J. Benick, D. Kania, L. Weiss, M. Hofmann, J. Rentsch, R. Preu, and S. W. Glunz, "High-efficiency c-Si solar cells passivated with ALD and PECVD aluminum oxide," *IEEE Electron Device Letters*, vol. 31, pp. 695–697, 2010.

[80] E. Cornagliotti, A. Sharma, L. Tous, L. Black, A. Uruena De Castro, M. Aleman, F. Duerinckx, R. Russell, P. Choulat, J. John, B. Dielissen, R. Gortzen, and J. Szlufcik, "Large area n-type c-Si solar cells featuring rear emitter and efficiency beyond 21%," in *Proc. 6th World Conf. Photovoltaic Energy Conversion*, Kyoto, Japan, 2014.

[81] Y. Wan, C. Samundsett, T. Kho, J. McKeon, L. Black, D. Macdonald, A. Cuevas, J. Sheng, Y. Sheng, S. Yuan, C. Zhang, Z. Feng, and P. J. Verlinden, "Towards industrial advanced front-junction n-type silicon solar cells," in *Proc. 40th IEEE Photovoltaic Specialist Conf.*, 2014, pp. 0862–0865.

[82] A. R. Chowdhuri, C. G. Takoudis, R. F. Klie, and N. D. Browning, "Metalorganic chemical vapor deposition of aluminum oxide on Si: Evidence of interface SiO_2 formation," *Applied Physics Letters*, vol. 80, pp. 4241–4243, 2002.

[83] R. Kuse, M. Kundu, T. Yasuda, N. Miyata, and A. Toriumi, "Effect of precursor concentration in atomic layer deposition of Al_2O_3," *Journal of Applied Physics*, vol. 94, pp. 6411–6416, 2003.

[84] H. Lee, T. Tachibana, N. Ikeno, H. Hashiguchi, K. Arafune, H. Yoshida, S.-i. Satoh, T. Chikyow, and A. Ogura, "Interface engineering for the passivation of c-Si with O_3-based atomic layer deposited AlO_x for solar cell application," *Applied Physics Letters*, vol. 100, 143901, 2012.

[85] V. Naumann, M. Otto, R. B. Wehrspohn, M. Werner, and C. Hagendorf, "Interface and material characterization of thin ALD-Al_2O_3 layers on crystalline silicon," *Energy Procedia*, vol. 27, pp. 312–318, 2012.

[86] A. Stesmans and V. V. Afanas'ev, "Si dangling-bond-type defects at the interface of (100)Si with ultrathin layers of SiO_x,Al_2O_3, and ZrO_2," *Applied Physics Letters*, vol. 80, pp. 1957–1959, 2002.

[87] J. Schmidt, F. Werner, B. Veith, D. Zielke, R. Bock, V. Tiba, P. Poodt, F. Roozeboom, T.-T. A. Li, A. Cuevas, and R. Brendel, “Industrially relevant Al_2O_3 deposition techniques for the surface passivation of Si solar cells,” in *Proc. 25th European Photovoltaic Solar Energy Conf.*, Valencia, Spain, 2010, pp. 1130–1133.

[88] I. Cesar, E. Granneman, P. Vermont, E. Tois, P. Manshanden, L. Geerligs, E. Bende, A. Burgers, A. Mewe, Y. Komatsu, and A. Weeber, “Excellent rear side passivation on multi-crystalline silicon solar cells with 20 nm uncapped Al_2O_3 layer: Industrialization of ALD for solar cell applications,” in *Proc. 35th IEEE Photovoltaic Specialists Conf.*, 2010, pp. 000 044–000 049.

[89] E. H. A. Granneman, P. Vermont, V. Kuznetsov, M. Coolen, and K. Vanormelingen, “High-throughput, in-line ALD Al_2O_3 system,” in *Proc. 25th European Photovoltaic Solar Energy Conf.*, Valencia, Spain, 2010.

[90] P. Poodt, A. Lankhorst, F. Roozeboom, K. Spee, D. Maas, and A. Vermeer, “High-speed spatial atomic-layer deposition of aluminum oxide layers for solar cell passivation,” *Advanced Materials*, vol. 22, pp. 3564–3567, 2010.

[91] F. Werner, W. Stals, R. Görtzen, B. Veith, R. Brendel, and J. Schmidt, “High-rate atomic layer deposition of Al_2O_3 for the surface passivation of Si solar cells,” *Energy Procedia*, vol. 8, pp. 301–306, 2011.

[92] P. Vitanov, X. Loozen, A. Harizanova, T. Ivanova, and G. Beaucarne, “A study of sol-gel deposited Al_2O_3 films as passivating coatings for solar cells application,” in *Proc. 23rd European Photovoltaic Solar Energy Conf*, Valencia, Spain, 2008, pp. 1596–1599.

[93] P. Vitanov, A. Harizanova, T. Ivanova, and T. Dimitrova, “Chemical deposition of Al_2O_3 thin films on Si substrates,” *Thin Solid Films*, vol. 517, pp. 6327–6330, 2009.

[94] H.-Q. Xiao, C.-L. Zhou, X.-N. Cao, W.-J. Wang, L. Zhao, H.-L. Li, and H.-W. Diao, “Excellent passivation of p-type Si surface by sol-gel Al_2O_3 films,” *Chinese Physics Letters*, vol. 26, 088102, 2009.

[95] J.-Y. Hung, J.-C. Wang, S.-W. Chen, T.-C. Chen, Y.-S. Lin, C.-H. Ku, and C.-C. Wen, “Back-side AlO_x passivation material and technology for the application of high efficiency (20%) and low cost PERC solar cells,” in *Proc. 40th IEEE Photovoltaic Specialists Conf.*, 2014, pp. 3308–3312.

[96] Y.-S. Lin, J.-Y. Hung, T.-C. Chen, C.-H. Ku, J.-C. Wang, S.-W. Chen, J.-J. Lee, and C.-C. Wen, "Effect of post deposition annealing of printed AlO_x film on PERC solar cells," in *Proc. 40th IEEE Photovoltaic Specialists Conf.*, 2014, pp. 0615–0618.

[97] S. M. Sze, *Semiconductor Devices: Physics and Technology*, 3rd Edition. Hoboken, NJ: John Wiley & Sons, 2002.

[98] R. F. Pierret, *Advanced semiconductor fundamentals*, 2nd ed. Pearson Education, 2003.

[99] P. Würfel, *Physics of solar cells: From basic principles to advanced concepts*, 2nd ed. Wiley-VCH, 2009.

[100] A. G. Aberle, *Crystalline Silicon Solar Cells: Advanced Surface Passivation and Analysis*. Sydney, Australia: Centre for Photovoltaic Engineering, University of New South Wales, 1999.

[101] G. Declerck, R. V. Overstraeten, and G. Broux, "Measurement of low densities of surface states at the Si–SiO_2-interface," *Solid-State Electronics*, vol. 16, pp. 1451–1460, 1973.

[102] A. Cuevas and D. Yan, "Misconceptions and misnomers in solar cells," *IEEE Journal of Photovoltaics*, vol. 3, pp. 916–923, 2013.

[103] M. Atalla, E. Tannenbaum, and E. Scheibner, "Stabilization of silicon surfaces by thermally grown oxides," *The Bell System Technical Journal*, vol. 38, pp. 749–783, 1959.

[104] P. Van Halen and D. L. Pulfrey, "Accurate, short series approximations to Fermi–Dirac integrals of order $-1/2$, $1/2$, 1, $3/2$, 2, $5/2$, 3, and $7/2$," *Journal of Applied Physics*, vol. 57, pp. 5271–5274, 1985.

[105] ——, "Erratum: "Accurate, short series approximations to Fermi–Dirac integrals of order $-1/2$, $1/2$, 1, $3/2$, 2, $5/2$, 3, and $7/2$"," *Journal of Applied Physics*, vol. 59, pp. 2264–2265, 1986.

[106] M. A. Green, "Intrinsic concentration, effective densities of states, and effective mass in silicon," *Journal of Applied Physics*, vol. 67, pp. 2944–2954, 1990.

[107] K. Misiakos and D. Tsamakis, "Accurate measurements of the silicon intrinsic carrier density from 78 to 340 K," *Journal of Applied Physics*, vol. 74, pp. 3293–3297, 1993.

[108] R. J. Van Overstraeten, H. J. DeMan, and R. P. Mertens, “Transport equations in heavy doped silicon,” *IEEE Transactions on Electron Devices*, vol. 20, pp. 290–298, 1973.

[109] J. del Alamo and R. Swanson, “The physics and modeling of heavily doped emitters,” *IEEE Transactions on Electron Devices*, vol. 31, pp. 1878–1888, 1984.

[110] K. McIntosh and P. Altermatt, “A freeware 1D emitter model for silicon solar cells,” in *Proc. 35th IEEE Photovoltaic Specialists Conf.*, 2010, pp. 002 188–002 193.

[111] R. Seiwatz and M. Green, “Space charge calculations for semiconductors,” *Journal of Applied Physics*, vol. 29, pp. 1034–1040, 1958.

[112] R. B. M. Girisch, R. P. Mertens, and R. F. De Keersmaecker, “Determination of Si–SiO_2 interface recombination parameters using a gate-controlled point-junction diode under illumination,” *IEEE Transactions on Electron Devices*, vol. 35, pp. 203–222, 1988.

[113] K. R. McIntosh and L. E. Black, “On effective surface recombination parameters,” *Journal of Applied Physics*, vol. 116, 014503, 2014.

[114] W. Shockley and W. T. Read, “Statistics of the recombinations of holes and electrons,” *Physical Review*, vol. 87, pp. 835–842, 1952.

[115] R. N. Hall, “Electron-hole recombination in germanium,” *Physical Review*, vol. 87, p. 387, 1952.

[116] D. E. Kane and R. M. Swanson, “Measurement of the emitter saturation current by a contactless photoconductivity decay method,” in *Conf. Rec. 18th IEEE Photovoltaic Specialists Conf.*, Las Vegas, USA, 1985, pp. 578–583.

[117] S. E. Potts, G. Dingemans, C. Lachaud, and W. M. M. Kessels, “Plasma-enhanced and thermal atomic layer deposition of Al_2O_3 using dimethylaluminum isopropoxide, $[Al(CH_3)_2(\mu\text{-}O^iPr)]_2$, as an alternative aluminum precursor,” *Journal of Vacuum Science and Technology A*, vol. 30, 021505, 2012.

[118] J. H. Rogers, A. W. Apblett, W. M. Cleaver, A. N. Tyler, and A. R. Barron, “Dimethylaluminium alkoxides: A physico-chemical investigation,” *J. Chem. Soc., Dalton Trans.*, pp. 3179–3187, 1992.

[119] M.-M. Sovar, D. Samélor, A. N. Gleizes, and C. Vahlas, “Aluminium tri-iso-propoxide: Shelf life, transport properties, and decomposition kinetics for the low temperature processing of aluminium oxide-based coatings,” *Surface and Coatings Technology*, vol. 201, pp. 9159–9162, 2007.

[120] I. Nasution, A. Velasco, and H.-j. Kim, “Atmospheric pressure chemical vapor deposition mechanism of Al_2O_3 film from $AlCl_3$ and O_2,” *Journal of Crystal Growth*, vol. 311, pp. 429–434, 2009.

[121] A. W. Laubengayer and W. F. Gilliam, “The alkyls of the third group elements. I. Vapor phase studies of the alkyls of aluminum, gallium and indium,” *Journal of the American Chemical Society*, vol. 63, pp. 477–479, 1941.

[122] J. P. McCullough, J. F. Messerly, R. T. Moore, and S. S. Todd, “Trimethylaluminum: Thermodynamic functions in the solid and liquid states, 0-380°k.; vapor pressure, heat of vaporization, and entropy in the ideal gas state,” *The Journal of Physical Chemistry*, vol. 67, pp. 677–679, 1963.

[123] M. Fulem, K. Růžička, V. Růžička, E. Hulicius, T. Šimeček, K. Melichar, J. Pangrác, S. A. Rushworth, and L. M. Smith, “Vapor pressure of metal organic precursors,” *Journal of Crystal Growth*, vol. 248, pp. 99–107, 2003.

[124] S. S. Lee, E.-S. Lee, S. H. Kim, B. K. Lee, and S. J. Jeong, “Non-stoichiometric AlO_x films prepared by chemical vapor deposition using dimethylaluminum isopropoxide as single precursor and their non-volatile memory characteristics,” *Bulletin of the Korean Chemical Society*, vol. 33, pp. 2207–2212, 2012.

[125] J. T. Viola, D. W. Seegmiller, A. A. Fannin, and L. A. King, “Vapor pressure of aluminum chloride systems. 1. Vapor pressure and triple point of pure aluminum chloride,” *Journal of Chemical & Engineering Data*, vol. 22, pp. 367–370, 1977.

[126] R. C. Wilhoit, “Vapor pressures of some aluminum alkoxides,” *The Journal of Physical Chemistry*, vol. 61, pp. 114–116, 1957.

[127] V. A. C. Haanappel, H. D. v. Corbach, T. Fransen, and P. J. Gellings, “Properties of alumina films prepared by low-pressure metal-organic chemical vapour deposition,” *Surface and Coatings Technology*, vol. 72, pp. 13–22, 1995.

[128] R. G. Gordon, K. Kramer, and X. Liu, "Chemical vapor deposition and properties of amorphous aluminum oxide films," *Materials Research Society Symposium Proceedings*, vol. 446, pp. 383–388, 1997.

[129] V. A. C. Haanappel, H. D. v. Corbach, T. Fransen, and P. J. Gellings, "Properties of alumina films prepared by atmospheric pressure metal-organic chemical vapour deposition," *Surface and Coatings Technology*, vol. 63, pp. 145–153, 1994.

[130] V. A. C. Haanappel, H. D. van Corbach, T. Fransen, and P. J. Gellings, "The pyrolytic decomposition of aluminium-tri-sec-butoxide during chemical vapour deposition of thin alumina films," *Thermochimica Acta*, vol. 240, pp. 67–77, 1994.

[131] V. A. C. Haanappel, J. B. Rem, H. D. v. Corbach, T. Fransen, and P. J. Gellings, "Properties of alumina films prepared by metal-organic chemical vapour deposition at atmospheric pressure in the presence of small amounts of water," *Surface and Coatings Technology*, vol. 72, pp. 1–12, 1995.

[132] H. Nagel, C. Berge, and A. G. Aberle, "Generalized analysis of quasi-steady-state and quasi-transient measurements of carrier lifetimes in semiconductors," *Journal of Applied Physics*, vol. 86, pp. 6218–6221, 1999.

[133] J. Brody, A. Rohatgi, and A. Ristow, "Guidelines for more accurate determination and interpretation of effective lifetime from measured quasi-steady-state photoconductance," in *Proc. 11th Workshop on Crystalline Silicon Solar Cell Materials and Processes*, Estes Park, Colorado, 2001, pp. 163–167.

[134] H. Flietner, W. Füssel, N. D. Sinh, and H. Angermann, "Density of states and relaxation spectra of etched, H-terminated and naturally oxidized si-surfaces and the accompanied defects," *Applied Surface Science*, vol. 104/105, pp. 342–348, 1996.

[135] T. Hattori, S. Iwauchi, K. Nagano, and T. Tanaka, "Effect of heat treatment on the interface characteristics in reactively sputtered Al_2O_3-Si structures," *Japanese Journal of Applied Physics*, vol. 10, pp. 203–207, 1971.

[136] D.-G. Park, H.-J. Cho, K.-Y. Lim, C. Lim, I.-S. Yeo, J.-S. Roh, and J. W. Park, "Characteristics of n^+ polycrystalline-Si/Al_2O_3/Si metal–oxide–semiconductor structures prepared by atomic layer chemical vapor

deposition using Al(CH_3)$_3$ and H_2O vapor," *Journal of Applied Physics*, vol. 89, pp. 6275–6280, 2001.

[137] S. Carmona-Tellez, J. Guzman-Mendoza, M. Aguilar-Frutis, G. Alarcon-Flores, M. Garcia-Hipolito, M. A. Canseco, and C. Falcony, "Electrical, optical, and structural characteristics of Al_2O_3 thin films prepared by pulsed ultrasonic sprayed pyrolysis," *Journal of Applied Physics*, vol. 103, 034105, 2008.

[138] A. Laades, H.-P. Sperlich, M. Bähr, U. Stürzebecher, C. A. Diaz Alvarez, M. Burkhardt, H. Angermann, M. Blech, and A. Lawerenz, "On the impact of interfacial SiO_x-layer on the passivation properties of PECVD synthesized aluminum oxide," *Physica Status Solidi C*, vol. 9, pp. 2120–2123, 2012.

[139] F. Kersten, A. Schmid, S. Bordihn, J. W. Müller, and J. Heitmann, "Role of annealing conditions on surface passivation properties of ALD Al_2O_3 films," *Energy Procedia*, vol. 38, pp. 843–848, 2013.

[140] B. Liao, R. Stangl, T. Mueller, F. Lin, C. S. Bhatia, and B. Hoex, "The effect of light soaking on crystalline silicon surface passivation by atomic layer deposited Al_2O_3," *Journal of Applied Physics*, vol. 113, 024509, 2013.

[141] M. Kuhn and E. H. Nicollian, "Nonequilibrium effects in quasi–static MOS measurements," *Journal of the Electrochemical Society*, vol. 118, pp. 370–373, 1971.

[142] S. R. Hofstein and G. Warfield, "Physical limitations on the frequency response of a semiconductor surface inversion layer," *Solid-State Electronics*, vol. 8, pp. 321–341, 1965.

[143] E. H. Nicollian and A. Goetzberger, "MOS conductance technique for measuring surface state parameters," *Applied Physics Letters*, vol. 7, pp. 216–219, 1965.

[144] ——, "The Si–SiO_2 interface – electrical properties as determined by the metal-insulator-silicon conductance technique," *The Bell System Technical Journal*, vol. 46, pp. 1055–1133, 1967.

[145] J. Schmidt, F. M. Schuurmans, W. C. Sinke, S. W. Glunz, and A. G. Aberle, "Observation of multiple defect states at silicon–silicon nitride interfaces fabricated by low-frequency plasma-enhanced chemical vapor deposition," *Applied Physics Letters*, vol. 71, pp. 252–254, 1997.

[146] K. R. McIntosh, S. C. Baker-Finch, N. E. Grant, A. F. Thomson, S. Singh, and I. D. Baikie, “Charge density in atmospheric pressure chemical vapor deposition TiO_2 on SiO_2-passivated silicon,” *Journal of the Electrochemical Society*, vol. 156, G190–G195, 2009.

[147] S. Steingrube, P. P. Altermatt, D. S. Steingrube, J. Schmidt, and R. Brendel, “Interpretation of recombination at c-Si/SiN_x interfaces by surface damage,” *Journal of Applied Physics*, vol. 108, 014506, 2010.

[148] J. A. Cooper Jr. and R. J. Schwartz, “Electrical characteristics of the SiO_2–Si interface near midgap and in weak inversion,” *Solid-State Electronics*, vol. 17, pp. 641–654, 1974.

[149] N. Taoka, T. Yamamoto, M. Harada, Y. Yamashita, N. Sugiyama, and S. Takagi, “Importance of minority carrier response in accurate characterization of Ge metal-insulator-semiconductor interface traps,” *Journal of Applied Physics*, vol. 106, 044506, 2009.

[150] H. Preier, “Contributions of surface states to MOS impedance,” *Applied Physics Letters*, vol. 10, pp. 361–363, 1967.

[151] W. Füssel, M. Schmidt, H. Angermann, G. Mende, and H. Flietner, “Defects at the Si/SiO_2 interface: Their nature and behaviour in technological processes and stress,” *Nuclear Instruments and Methods in Physics Research Section A: Accelerators, Spectrometers, Detectors and Associated Equipment*, vol. 377, pp. 177–183, 1996.

[152] C. N. Berglund, “Surface states at steam-grown silicon-silicon dioxide interfaces,” *IEEE Transactions on Electron Devices*, vol. 13, pp. 701–705, 1966.

[153] M. Schöfthaler, R. Brendel, G. Langguth, and J. H. Werner, “High-quality surface passivation by corona-charged oxides for semiconductor surface characterization,” in *Proc. 1st World Conf. Photovoltaic Energy Conversion*, vol. 2, Waikoloa, Hawaii, USA, 1994, pp. 1509–1512.

[154] S. Dauwe, J. Schmidt, A. Metz, and R. Hezel, “Fixed charge density in silicon nitride films on crystalline silicon surfaces under illumination,” pp. 162–165, 2002.

[155] W. E. Jellett and K. J. Weber, “Accurate measurement of extremely low surface recombination velocities on charged, oxidized silicon surfaces using a simple metal-oxide-semiconductor structure,” *Applied Physics Letters*, vol. 90, 042104, 2007.

[156] K. J. Weber, H. Jin, C. Zhang, N. Nursam, W. E. Jellett, and K. R. McIntosh, "Surface passivation using dielectric films: How much charge is enough?" In *Proc. 24th European Photovoltaic Solar Energy Conf.*, 2009, pp. 534–537.

[157] T. C. Kho, S. C. Baker-Finch, and K. R. McIntosh, "The study of thermal silicon dioxide electrets formed by corona discharge and rapid-thermal annealing," *Journal of Applied Physics*, vol. 109, 053108, 2011.

[158] M. J. Kerr and A. Cuevas, "Recombination at the interface between silicon and stoichiometric plasma silicon nitride," *Semiconductor Science and Technology*, vol. 17, pp. 166–172, 2002.

[159] ——, "Very low bulk and surface recombination in oxidized silicon wafers," *Semiconductor Science and Technology*, vol. 17, pp. 35–38, 2002.

[160] B. Vermang, H. Goverde, V. Simons, I. De Wolf, J. Meersschaut, S. Tanaka, J. Joachim, J. Poortmans, and R. Mertens, "A study of blister formation in ALD Al_2O_3 grown on silicon," in *Proc. 38th IEEE Photovoltaic Specialists Conf.*, Austin, USA, 2012, pp. 1135–1138.

[161] B. Veith, T. Ohrdes, F. Werner, R. Brendel, P. P. Altermatt, N.-P. Harder, and J. Schmidt, "Injection dependence of the effective lifetime of n-type Si passivated by Al_2O_3: An edge effect?" *Solar Energy Materials and Solar Cells*, vol. 120, Part A, pp. 436–440, 2014.

[162] S. Joos, A. Herguth, U. Hess, J. Ebser, S. Seren, B. Terheiden, and G. Hahn, "Light induced curing (LIC) of passivation layers deposited on native silicon oxide," *Energy Procedia*, vol. 27, pp. 349–354, 2012.

[163] D. Macdonald, J. Tan, and T. Trupke, "Imaging interstitial iron concentrations in boron-doped crystalline silicon using photoluminescence," *Journal of Applied Physics*, vol. 103, 073710, 2008.

[164] D. Macdonald, T. Roth, P. N. K. Deenapanray, T. Trupke, and R. A. Bardos, "Doping dependence of the carrier lifetime crossover point upon dissociation of iron-boron pairs in crystalline silicon," *Applied Physics Letters*, vol. 89, 142107, 2006.

[165] T. C. Kho, L. E. Black, and K. R. McIntosh, "Degradation of Si–SiO_2 interfaces during rapid thermal annealing," in *Proc. 24th European Photovoltaic Solar Energy Conf.*, Hamburg, Germany: WIP, Munich, 2009, 2009, pp. 1586–1590.

[166] J. Snel, “The doped Si/SiO_2 interface,” *Solid-State Electronics*, vol. 24, pp. 135–139, 1981.

[167] M. Y. Ghannam, R. Mertens, R. De Keersmaecker, and R. Van Overstraeten, “Electrical characterization of the boron-doped Si-SiO_2 interface,” *IEEE Transactions on Electron Devices*, vol. 32, pp. 1264–1271, 1985.

[168] H. Jin, W. E. Jellett, Z. Chun, K. J. Weber, A. W. Blakers, and P. J. Smith, “The effect of boron diffusions on the defect density and recombination at the (111) silicon-silicon oxide interface,” *Applied Physics Letters*, vol. 92, 122109, 2008.

[169] R. King, R. Sinton, and R. Swanson, “Studies of diffused phosphorus emitters: Saturation current, surface recombination velocity, and quantum efficiency,” *IEEE Transactions on Electron Devices*, vol. 37, pp. 365–371, 1990.

[170] R. R. King and R. Swanson, “Studies of diffused boron emitters: Saturation current, bandgap narrowing, and surface recombination velocity,” *IEEE Transactions on Electron Devices*, vol. 38, pp. 1399–1409, 1991.

[171] A. Cuevas, P. A. Basore, G. Giroult-Matlakowski, and C. Dubois, “Surface recombination velocity of highly doped n-type silicon,” *Journal of Applied Physics*, vol. 80, pp. 3370–3375, 1996.

[172] A. Cuevas, M. Stuckings, J. Lau, and M. Petravic, “The recombination velocity of boron diffused silicon surfaces,” in *Proc. 14th European Photovoltaic Solar Energy Conf.*, Barcelona, Spain: HS Stephens, Falmerston, UK, 1997, 1997, pp. 2416–2419.

[173] P. P. Altermatt, J. O. Schumacher, A. Cuevas, M. J. Kerr, S. W. Glunz, R. R. King, G. Heiser, and A. Schenk, “Numerical modeling of highly doped Si:P emitters based on Fermi–Dirac statistics and self-consistent material parameters,” *Journal of Applied Physics*, vol. 92, pp. 3187–3197, 2002.

[174] A. Cuevas, M. J. Kerr, and J. Schmidt, “Passivation of crystalline silicon using silicon nitride,” in *Proc. 3rd World Conf. Photovoltaic Energy Conversion*, Osaka, Japan, 2003, pp. 913–918.

[175] P. P. Altermatt, H. Plagwitz, R. Bock, J. Schmidt, R. Brendel, M. J. Kerr, and A. Cuevas, “The surface recombination velocity at boron-doped emitters: Comparison between various passivation techniques,” in *Proc. 21st European Photovoltaic Solar Energy Conf.*, Dresden, Germany: WIP, Munich, 2006, 2006, pp. 647–650.

[176] S. Duttagupta, F. Lin, K. D. Shetty, A. G. Aberle, and B. Hoex, “Excellent boron emitter passivation for high-efficiency Si wafer solar cells using AlO_x/SiN_x dielectric stacks deposited in an industrial inline plasma reactor,” *Progress in Photovoltaics: Research and Applications*, vol. 21, pp. 760–764, 2012.

[177] F.-J. Ma, S. Duttagupta, M. Peters, G. S. Samudra, A. G. Aberle, and B. Hoex, “Numerical modelling of silicon p+ emitters passivated by a PECVD AlO_x/SiN_x stack,” *Energy Procedia*, vol. 33, pp. 104–109, 2013.

[178] S. Duttagupta, F.-J. Ma, S. F. Lin, T. Mueller, A. G. Aberle, and B. Hoex, “Progress in surface passivation of heavily doped n-type and p-type silicon by plasma-deposited AlO_x/SiN_x dielectric stacks,” *IEEE Journal of Photovoltaics*, vol. 3, pp. 1163–1169, 2013.

[179] A. Richter, J. Benick, and M. Hermle, “Boron emitter passivation with Al_2O_3 and Al_2O_3/SiN_x stacks using ALD Al_2O_3,” *IEEE Journal of Photovoltaics*, vol. 3, pp. 236–245, 2013.

[180] B. Liao, R. Stangl, F. Ma, Z. Hameiri, T. Mueller, D. Chi, A. G. Aberle, C. S. Bhatia, and B. Hoex, “Deposition temperature independent excellent passivation of highly boron doped silicon emitters by thermal atomic layer deposited Al_2O_3,” *Journal of Applied Physics*, vol. 114, 094505, 2013.

[181] D. Yan and A. Cuevas, “Empirical determination of the energy band gap narrowing in highly doped n+ silicon,” *Journal of Applied Physics*, vol. 114, 044508, 2013.

[182] D. B. M. Klaassen, J. W. Slotboom, and H. C. de Graaff, “Unified apparent bandgap narrowing in n- and p-type silicon,” *Solid-State Electronics*, vol. 35, pp. 125–129, 1992.

[183] J. Dziewior and W. Schmid, “Auger coefficients for highly doped and highly excited silicon,” *Applied Physics Letters*, vol. 31, pp. 346–348, 1977.

[184] M. J. Kerr and A. Cuevas, “General parameterization of Auger recombination in crystalline silicon,” *Journal of Applied Physics*, vol. 91, pp. 2473–2480, 2002.

[185] A. S. Grove and D. J. Fitzgerald, "Surface effects on p-n junctions: Characteristics of surface space-charge regions under non-equilibrium conditions," *Solid-State Electronics*, vol. 9, pp. 783–806, 1966.

[186] J. S. Kang and D. K. Schroder, "The pulsed MIS capacitor: A critical review," *Physica Status Solidi A*, vol. 89, pp. 13–43, 1985.

[187] G. Dingemans, N. M. Terlinden, M. A. Verheijen, M. C. M. van de Sanden, and W. M. M. Kessels, "Controlling the fixed charge and passivation properties of Si(100)/Al_2O_3 interfaces using ultrathin SiO_2 interlayers synthesized by atomic layer deposition," *Journal of Applied Physics*, vol. 110, 093715, 2011.

[188] C. Chan, M. Abbott, M. Juhl, B. Hallam, B. Xiao, and S. Wenham, "Assessing the performance of surface passivation using low-intensity photoluminescence characterization techniques," *IEEE Journal of Photovoltaics*, vol. 4, pp. 100–106, 2014.

[189] J. R. Elmiger, R. Schieck, and M. Kunst, "Recombination at the silicon nitride/silicon interface," *Journal of Vacuum Science and Technology A*, vol. 15, pp. 2418–2425, 1997.

[190] J. Schmidt, J. D. Moschner, J. Henze, S. Dauwe, and R. Hezel, "Recent progress in the surface passivation of silicon solar cells using silicon nitride," in *Proc. 19th European Photovoltaic Solar Energy Conf.*, Paris, France, 2004, pp. 391–396.

[191] F. W. Chen, J. E. Cotter, M. Abbott, T.-T. A. Li, and K. Fisher, "The influence of parasitic effects on injection-level-dependent lifetime data," *IEEE Transactions on Electron Devices*, vol. 54, pp. 2960–2968, 2007.

[192] P. J. Cousins, D. H. Neuhaus, and J. E. Cotter, "Experimental verification of the effect of depletion-region modulation on photoconductance lifetime measurements," *Journal of Applied Physics*, vol. 95, pp. 1854–1858, 2004.

[193] K. McIntosh, "A model for the steady-state photoconductance of an abrupt p-n junction semiconductor diode assuming flat quasi-fermi levels," *IEEE Transactions on Electron Devices*, vol. 54, pp. 346–353, 2007.

[194] I. Martin, B. Hoex, M. C. M. Van de Sanden, R. Alcubilla, and W. M. M. Kessels, "The origin of emitter-like recombination for inverted c-Si surfaces," in *Proc. 23rd European Photovoltaic Solar Energy Conf.*, Valencia Spain, 2008, pp. 1388–1392.

[195] F.-J. Ma, G. G. Samudra, M. Peters, A. G. Aberle, F. Werner, J. Schmidt, and B. Hoex, "Advanced modeling of the effective minority carrier lifetime of passivated crystalline silicon wafers," *Journal of Applied Physics*, vol. 112, 054508, 2012.

[196] S. Steingrube, P. P. Altermatt, D. Zielke, F. Werner, J. Schmidt, and R. Brendel, "Reduced passivation of silicon surfaces at low injection densities caused by H-induced defects," in *Proc. 25th European Photovoltaic Solar Energy Conf.*, Valencia, Spain, 2010.

[197] M. Kessler, T. Ohrdes, P. P. Altermatt, and R. Brendel, "The effect of sample edge recombination on the averaged injection-dependent carrier lifetime in silicon," *Journal of Applied Physics*, vol. 111, 054508, 2012.

[198] D. Macdonald and A. Cuevas, "Reduced fill factors in multicrystalline silicon solar cells due to injection-level dependent bulk recombination lifetimes," *Progress in Photovoltaics: Research and Applications*, vol. 8, pp. 363–375, 2000.

[199] M. Abbott, G. Scardera, K. R. McIntosh, and A. Meisel, "Simulation of emitter doping profiles formed by industrial $POCl_3$ processes," in *Proc. 39th IEEE Photovoltaic Specialists Conf.*, Tampa, FL, 2013, pp. 1383–1388.

[200] B. Min, H. Wagner, A. Dastgheib-Shirazi, A. Kimmerle, H. Kurz, and P. P. Altermatt, "Heavily doped Si:P emitters of crystalline Si solar cells: Recombination due to phosphorus precipitation," *Physica Status Solidi RRL*, vol. 8, pp. 680–684, 2014.

[201] C.-T. Sah, P. C. H. Chan, C.-K. Wang, R.-Y. Sah, K. Yamakawa, and R. Lutwack, "Effect of zinc impurity on silicon solar-cell efficiency," *IEEE Transactions on Electron Devices*, vol. 28, pp. 304–313, 1981.

[202] A. C. Wang, L. S. Lu, and C. T. Sah, "Electron capture at the two acceptor levels of a zinc center in silicon," *Physical Review B*, vol. 30, pp. 5896–5903, 1984.

[203] E. Arnold, J. Ladell, and G. Abowitz, "Crystallographic symmetry of surface state density in thermally oxidized silicon," *Applied Physics Letters*, vol. 13, pp. 413–416, 1968.

[204] T. Satô, Y. Takeishi, and H. Hara, "Effects of crystallographic orientation on mobility, surface state density, and noise in p-type inversion layers on oxidized silicon surfaces," *Japanese Journal of Applied Physics*, vol. 8, pp. 588–598, 1969.

[205] S. C. Vitkavage, E. A. Irene, and H. Z. Massoud, "An investigation of Si–SiO_2 interface charges in thermally oxidized (100), (110), (111), and (511) silicon," *Journal of Applied Physics*, vol. 68, pp. 5262–5272, 1990.

[206] S. Ogata, S. Ohno, M. Tanaka, T. Mori, T. Horikawa, and T. Yasuda, "SiO_2/Si interfaces on high-index surfaces: Re-evaluation of trap densities and characterization of bonding structures," *Applied Physics Letters*, vol. 98, 092906, 2011.

[207] S. C. Baker-Finch and K. McIntosh, "The contribution of planes, vertices, and edges to recombination at pyramidally textured surfaces," *IEEE Journal of Photovoltaics*, vol. 1, pp. 59–65, 2011.

[208] H. C. Sio, S. P. Phang, Y. Wan, W. Liang, T. Trupke, S. Cao, D. Hu, Y. Wan, and D. Macdonald, "The influence of crystal orientation on surface passivation in multi-crystalline silicon," in *Proc. 39th IEEE Photovoltaic Specialists Conf.*, 2013, pp. 1770–1775.

[209] S. C. Baker-Finch, "Rules and tools for understanding, modelling and designing textured silicon solar cells," PhD thesis, The Australian National University, 2012.

[210] L. E. Black, T. C. Kho, K. R. McIntosh, and A. Cuevas, "The influence of orientation and morphology on the passivation of crystalline silicon surfaces by Al_2O_3," *Energy Procedia*, vol. 55, pp. 750–756, 2014.

[211] Y. Komatsu, D. Harata, E. W. Schuring, A. H. Vlooswijk, S. Katori, S. Fujita, P. R. Venema, and I. Cesar, "Calibration of electrochemical capacitance-voltage method on pyramid texture surface using scanning electron microscopy," *Energy Procedia*, vol. 38, pp. 94–100, 2013.

[212] H. Kawano, "Effective work functions for ionic and electronic emissions from mono- and polycrystalline surfaces," *Progress in Surface Science*, vol. 83, pp. 1–165, 2008.

[213] H. Flietner, W. Füssel, and N. D. Sinh, "Interface states of the Si/SiO_2 system and their separation in groups," *Physica Status Solidi A*, vol. 43, K99–K101, 1977.

[214] L. Do Thanh and P. Balk, “Elimination and generation of Si–SiO_2 interface traps by low temperature hydrogen annealing,” *Journal of the Electrochemical Society*, vol. 135, pp. 1797–1801, 1988.

[215] H. Deuling, E. Klausmann, and A. Goetzberger, “Interface states in si–SiO_2 interfaces,” *Solid-State Electronics*, vol. 15, pp. 559–571, 1972.

[216] T.-T. A. Li, “Surface passivation of crystalline silicon by sputtered aluminium oxide,” PhD thesis, The Australian National University, 2010.

[217] T.-T. A. Li and A. Cuevas, “Role of hydrogen in the surface passivation of crystalline silicon by sputtered aluminum oxide,” *Progress in Photovoltaics: Research and Applications*, vol. 19, pp. 320–325, 2011.

[218] T.-T. A. Li, S. Ruffell, M. Tucci, Y. Mansoulié, C. Samundsett, S. D. Iullis, L. Serenelli, and A. Cuevas, “Influence of oxygen on the sputtering of aluminum oxide for the surface passivation of crystalline silicon,” *Solar Energy Materials and Solar Cells*, vol. 95, pp. 69–72, 2011.

[219] A. Richter, J. Benick, M. Hermle, and S. W. Glunz, “Reaction kinetics during the thermal activation of the silicon surface passivation with atomic layer deposited Al_2O_3,” *Applied Physics Letters*, vol. 104, 061606, 2014.

[220] S. Kühnhold, P. Saint-Cast, B. Kafle, M. Hofmann, F. Colonna, and M. Zacharias, “High-temperature degradation in plasma-enhanced chemical vapor deposition Al_2O_3 surface passivation layers on crystalline silicon,” *Journal of Applied Physics*, vol. 116, 054507, 2014.

[221] P. Colomban, “Structure of oxide gels and glasses by infrared and Raman scattering Part 1: Alumina,” *Journal of Materials Science*, vol. 24, pp. 3002–3010, 1989.

[222] Y.-C. Kim, H.-H. Park, J. S. Chun, and W.-J. Lee, “Compositional and structural analysis of aluminum oxide films prepared by plasma-enhanced chemical vapor deposition,” *Thin Solid Films*, vol. 237, pp. 57–65, 1994.

[223] A. C. Dillon, A. W. Ott, J. D. Way, and S. M. George, “Surface chemistry of Al_2O_3 deposition using $Al(CH_3)_3$ and H_2O in a binary reaction sequence,” *Surface Science*, vol. 322, pp. 230–242, 1995.

[224] P. M. Chu, F. R. Guenther, G. C. Rhoderick, and W. J. Lafferty, “The NIST quantitative infrared database,” *Journal of Research of the National Institute of Standards and Technology*, vol. 104, pp. 59–81, 1999.

[225] D. N. Goldstein, J. A. McCormick, and S. M. George, "Al_2O_3 atomic layer deposition with trimethylaluminum and ozone studied by in situ transmission FTIR spectroscopy and quadrupole mass spectrometry," *The Journal of Physical Chemistry C*, vol. 112, pp. 19 530–19 539, 2008.

[226] E. Langereis, J. Keijmel, M. C. M. van de Sanden, and W. M. M. Kessels, "Surface chemistry of plasma-assisted atomic layer deposition of Al_2O_3 studied by infrared spectroscopy," *Applied Physics Letters*, vol. 92, 231904, 2008.

[227] T. O. Kääriäinen and D. C. Cameron, "Plasma-assisted atomic layer deposition of Al_2O_3 at room temperature," *Plasma Processes and Polymers*, vol. 6, S237–S241, 2009.

[228] R. A. B. Devine, "Structural nature of the Si/SiO_2 interface through infrared spectroscopy," *Applied Physics Letters*, vol. 68, pp. 3108–3110, 1996.

[229] K. T. Queeney, M. K. Weldon, J. P. Chang, Y. J. Chabal, A. B. Gurevich, J. Sapjeta, and R. L. Opila, "Infrared spectroscopic analysis of the Si/SiO_2 interface structure of thermally oxidized silicon," *Journal of Applied Physics*, vol. 87, pp. 1322–1330, 2000.

[230] P. Tarte, "Infra-red spectra of inorganic aluminates and characteristic vibrational frequencies of AlO_4 tetrahedra and AlO_6 octahedra," *Spectrochimica Acta*, vol. 23A, pp. 2127–2143, 1967.

[231] G. K. Priya, P. Padmaja, K. G. K. Warrier, A. D. Damodaran, and G. Aruldhas, "Dehydroxylation and high temperature phase formation in sol-gel boehmite characterized by Fourier transform infrared spectroscopy," *Journal of Materials Science Letters*, vol. 16, pp. 1584–1587, 1997.

[232] A. Boumaza, L. Favaro, J. Lédion, G. Sattonnay, J. B. Brubach, P. Berthet, A. M. Huntz, P. Roy, and R. Tétot, "Transition alumina phases induced by heat treatment of boehmite: An X-ray diffraction and infrared spectroscopy study," *Journal of Solid State Chemistry*, vol. 182, pp. 1171–1176, 2009.

[233] D. Voll, P. Angerer, A. Beran, and S. H., "A new assignment of IR vibrational modes in mullite," *Vibrational Spectroscopy*, vol. 30, pp. 237–243, 2002.

[234] K. J. D. MacKenzie, "Infrared frequency calculations for ideal mullite ($3Al_2O_3\bullet SiO_2$)," *Journal of the American Ceramic Society*, vol. 55, pp. 68–71, 1972.

[235] K. Iishi, E. Salje, and C. Werneke, “Phonon spectra and rigid-ion model calculations on andalusite,” *Physics and Chemistry of Minerals*, vol. 4, pp. 173–188, 1979.

[236] S. W. Kieffer, “Thermodynamics and lattice vibrations of minerals: 2. Vibrational characteristics of silicates,” *Reviews of Geophysics and Space Physics*, vol. 17, pp. 20–34, 1979.

[237] B. Winkler and W. Buehrer, “Lattice dynamics of andalusite: Prediction and experiment,” *Physics and Chemistry of Minerals*, vol. 17, pp. 453–461, 1990.

[238] P. McMillan and B. Piriou, “The structures and vibrational spectra of crystals and glasses in the silica-alumina system,” *Journal of Non-Crystalline Solids*, vol. 53, pp. 279–298, 1982.

[239] B. T. Poe, P. F. McMillan, C. A. Angell, and R. K. Sato, “Al and Si coordination in SiO_2–Al_2O_3 glasses and liquids: A study by NMR and IR spectroscopy and MD simulations,” *Chemical Geology*, vol. 96, pp. 333–349, 1992.

[240] G. Gutiérrez and B. Johansson, “Molecular dynamics study of structural properties of amorphous Al_2O_3,” *Physical Review B*, vol. 65, 104202, 2002.

[241] V. V. Hoang and S. K. Oh, “Simulation of structural properties and structural transformation of amorphous Al_2O_3,” *Physica B: Condensed Matter*, vol. 352, pp. 73–85, 2004.

[242] M. Prokhorskii, A. Fofanov, L. Aleshina, and E. Nikitina, “Structure of amorphous oxide Al_2O_3: Results of a molecular-dynamics experiment,” *Crystallography Reports*, vol. 49, pp. 631–634, 2004.

[243] S. P. Adiga, P. Zapol, and L. A. Curtiss, “Atomistic simulations of amorphous alumina surfaces,” *Physical Review B*, vol. 74, 064204, 2006.

[244] ——, “Structure and morphology of hydroxylated amorphous alumina surfaces,” *The Journal of Physical Chemistry C*, vol. 111, pp. 7422–7429, 2007.

[245] R. Lizárraga, E. Holmström, S. C. Parker, and C. Arrouvel, “Structural characterization of amorphous alumina and its polymorphs from first-principles XPS and NMR calculations,” *Physical Review B*, vol. 83, 094201, 2011.

[246] S. Davis and G. Gutiérrez, "Structural, elastic, vibrational and electronic properties of amorphous Al_2O_3 from ab initio calculations," *Journal of Physics: Condensed Matter*, vol. 23, 495401, 2011.

[247] L. Stoch and M. Åšroda, "Infrared spectroscopy in the investigation of oxide glasses structure," *Journal of Molecular Structure*, vol. 511–512, pp. 77–84, 1999.

[248] M. C. Stegmann, D. Vivien, and C. Mazieres, "Etude des modes de vibration infrarouge dans les oxyhydroxides d'aluminium boehmite et diaspore," *Spectrochimica Acta*, vol. 29A, pp. 1653–1663, 1973.

[249] I. Levin and D. Brandon, "Metastable alumina polymorphs: Crystal structures and transition sequences," *Journal of the American Ceramic Society*, vol. 81, pp. 1995–2012, 1998.

[250] Y. Catherine and A. Talebian, "Plasma deposition of aluminum oxide films," *Journal of Electronic Materials*, vol. 17, pp. 127–134, 1988.

[251] R. Rinaldi and U. Schuchardt, "On the paradox of transition metal-free alumina-catalyzed epoxidation with aqueous hydrogen peroxide," *Journal of Catalysis*, vol. 236, pp. 335–345, 2005.

[252] K. Murase, "Dielectric constant of silicon dioxide deposited by atmospheric-pressure chemical vapor deposition using tetraethylorthosilicate and ozone," *Japanese Journal of Applied Physics*, vol. 33, pp. 1385–1389, 1994.

[253] H. Momida, T. Hamada, Y. Takagi, T. Yamamoto, T. Uda, and T. Ohno, "Theoretical study on dielectric response of amorphous alumina," *Physical Review B*, vol. 73, 054108, 2006.

[254] H. Kumagai, K. Toyoda, M. Matsumoto, and M. Obara, "Comparative study of Al_2O_3 optical crystalline thin films grown by vapor combinations of $Al(CH_3)_3/N_2O$ and $Al(CH_3)_3/H_2O_2$," *Japanese Journal of Applied Physics*, vol. 32, pp. 6137–6140, 1993.

[255] Y. Kim, S. M. Lee, C. S. Park, S. I. Lee, and M. Y. Lee, "Substrate dependence on the optical properties of Al_2O_3 films grown by atomic layer deposition," *Applied Physics Letters*, vol. 71, pp. 3604–3606, 1997.

[256] K. Kukli, M. Ritala, M. Leskelä, and J. Jokinen, "Atomic layer epitaxy growth of aluminum oxide thin films from a novel $Al(CH_3)_2Cl$ precursor and H_2O," *Journal of Vacuum Science and Technology A*, vol. 15, pp. 2214–2218, 1997.

[257] D.-H. Kuo, B.-Y. Cheung, and R.-J. Wu, "Growth and properties of alumina films obtained by low-pressure metal–organic chemical vapor deposition," *Thin Solid Films*, vol. 398-399, pp. 35–40, 2001.

[258] M. D. Groner, F. H. Fabreguette, J. W. Elam, and S. M. George, "Low-temperature Al_2O_3 atomic layer deposition," *Chemistry of Materials*, vol. 16, pp. 639–645, 2004.

[259] P. Kumar, M. K. Wiedman, C. H. Winter, and I. Avrutsky, "Optical properties of Al_2O_3 thin films grown by atomic layer deposition," *Applied Optics*, vol. 48, pp. 5407–5412, 2009.

[260] I. H. Malitson, "Refraction and dispersion of synthetic sapphire," *Journal of the Optical Society of America*, vol. 52, pp. 1377–1379, 1962.

[261] D. R. Lide, Ed., *CRC Handbook of Chemistry and Physics*, 85th Edition. Boca Raton, FL: CRC Press, 2005.

[262] G. E. Jellison and F. A. Modine, "Parameterization of the optical functions of amorphous materials in the interband region," *Applied Physics Letters*, vol. 69, pp. 371–373, 1996.

[263] D. E. Aspnes, "Optical properties," in *Properties of crystalline silicon*, R. Hull, Ed., London: INSPEC, the Institution of Electrical Engineers, 1999.

[264] C. M. Herzinger, B. Johs, W. A. McGahan, J. A. Woollam, and W. Paulson, "Ellipsometric determination of optical constants for silicon and thermally grown silicon dioxide via a multi-sample, multi-wavelength, multi-angle investigation," *Journal of Applied Physics*, vol. 83, pp. 3323–3336, 1998.

[265] P. van Nijnatten, "An automated directional reflectance/transmittance analyser for coating analysis," *Thin Solid Films*, vol. 442, pp. 74–79, 2003.

[266] A. Metz, D. Adler, S. Bagus, H. Blanke, M. Bothar, E. Brouwer, S. Dauwe, K. Dressler, R. Droessler, T. Droste, M. Fiedler, Y. Gassenbauer, T. Grahl, N. Hermert, W. Kuzminski, A. Lachowicz, T. Lauinger, N. Lenck, M. Manole, M. Martini, R. Messmer, C. Meyer, J. Moschner, K. Ramspeck, P. Roth, R. Schönfelder, B. Schum, J. Sticksel, K. Vaas, M. Volk, and K.

Wangemann, “Industrial high performance crystalline silicon solar cells and modules based on rear surface passivation technology,” *Solar Energy Materials and Solar Cells*, vol. 120, Part A, pp. 417–425, 2014.

[267] M. Kuhn, “A quasi-static technique for MOS C-V and surface state measurements,” *Solid-State Electronics*, vol. 13, pp. 873–885, 1970.

[268] B. Monderer and A. A. Lakhani, “Measurement of the quasi-static C-V curves of an MIS structure in the presence of charge leakage,” *Solid-State Electronics*, vol. 28, pp. 447–451, 1985.

[269] J. Schmitz, M. H. H. Weusthof, and A. J. Hof, “Leakage current correction in quasi-static C-V measurements,” in *Proc. International Conf. Microelectronic Test Structures*, IEEE Electron Devices Soc, 2004, pp. 179–181.

[270] A. K. Jonscher, “Dielectric relaxation in solids,” *Journal of Physics D: Applied Physics*, vol. 32, R57, 1999.

[271] S. Rüße, M. Lohrengel, and J. Schultze, “Ion migration and dielectric effects in aluminum oxide films,” *Solid State Ionics*, vol. 72, Part 2, pp. 29–34, 1994.

[272] J. Maserjian, G. Petersson, and C. Svensson, “Saturation capacitance of thin oxide MOS structures and the effective surface density of states of silicon,” *Solid-State Electronics*, vol. 17, pp. 335–339, 1974.

[273] M. J. McNutt and C. T. Sah, “Determination of the MOS oxide capacitance,” *Journal of Applied Physics*, vol. 46, pp. 3909–3913, 1975.

[274] S. V. Walstra and C.-T. Sah, “Thin oxide thickness extrapolation from capacitance-voltage measurements,” *IEEE Transactions on Electron Devices*, vol. 44, pp. 1136–1142, 1997.

[275] ——, “Extension of the McNutt-Sah method for measuring thin oxide thicknesses of MOS devices,” *Solid-State Electronics*, vol. 42, pp. 671–673, 1998.

[276] E. Vincent, G. Ghibaudo, G. Morin, and C. Papadas, “On the oxide thickness extraction in deep-submicron technologies,” in *Proc. IEEE International Conf. Microelectronic Test Structures*, 1997, pp. 105–110.

[277] G. Ghibaudo, S. Bruyere, T. Devoivre, B. DeSalvo, and E. Vincent, "Improved method for the oxide thickness extraction in MOS structures with ultrathin gate dielectrics," *IEEE Transactions on Semiconductor Manufacturing*, vol. 13, pp. 152–158, 2000.

[278] R. Castagné and A. Vapaille, "Description of the SiO_2–Si interface properties by means of very low frequency MOS capacitance measurements," *Surface Science*, vol. 28, pp. 157–193, 1971.

[279] L. M. Terman, "An investigation of surface states at a silicon/silicon oxide interface employing metal–oxide–silicon diodes," *Solid-State Electronics*, vol. 5, pp. 285–299, 1962.